UNIVERSITÀ DEGLI STUDI DI NAPOLI "FEDERICO II"
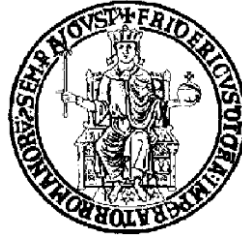
Corso di Dottorato in Ingegneria Elettrica

Dipartimento di Ingegneria Elettrica e Tecnologie dell'Informazione

TESI DI DOTTORATO

THREE-DIMENSIONAL EFFECTS OF ELECTROMAGNETIC FIELDS IN TOKAMAK PLASMAS

Tutor: Dottorando:

Prof. Raffaele Albanese   Ing. Simone Minucci

PhD Coordinator:

Prof. Claudio Serpico

XXVII Ciclo

Contents

Conclusions

References

Acknowledgements

Abstract

The problem of the energy harvesting to face the more and more increasing energy demand is currently challenging. The higher part of our electrical energy (about 80%) is produced by thermoelectrical power plants, which exploit the so-called *Non-renewable energy resources* (e.g. oil and gas), whose re-growth rate lasts millions of years and are so to be considered as in a fixed amount.

On the other hand, the *Renewable energy resources* are not reduced by their exploitation. For instance, solar and wind energy are obviously both permanent renewable resources, because the energy flow is lower than the energy storage, contrary to the oil resource, where the flow exceeds its natural re-growth rate.

Recalling that the renewable energy resources are not able to cover the energy needs (they are often used for the *Peak Shaving* and not to cover the basis energy demand), it is clear that a new energy resource is necessary to meet the increased energy demand. Moreover, it has to be non-polluting, renewable and continuously available with no interruptions (unlike solar and wind energy, which are affected by the presence of sunlight and wind).

This new energy source can be the *Nuclear Fusion Energy*, a new kind of energy resource that exploits the energy released by the collision and the fusion of two light atoms (such as hydrogen or its isotopes), according to Einstein equation and the mass-energy balance. Although controlled fusion is extremely technologically challenging, a fusion power plant would offer significant advantages over the existing renewable and non-renewable energy sources, such as the practically infinite fuel supply, the absence or air pollution or greenhouses gas during normal operations and the absence of the risk of a nuclear meltdown.

The collision of two nuclei can occur if and only if their kinetic energy is high enough to overcome the energy barrier opposing the fusion reaction, due to the long-range Coulomb repulsion. Therefore, the hydrogen gas is heated up to very high temperatures (one hundred million degrees and even more), reaching the *Plasma* state.

Because of this temperature range, the plasma must be confined and must not touch any structure, in order to avoid yielding heat loads as well as mechanical loads. The *Tokamak* is a fusion machine aimed at the plasma confinement by means of a magnetic field generated by a set of coils surrounding the plasma itself. In principle, the plasma is supposed to be toroidal shaped during normal operations, but this symmetrical condition is ideal, because of many effects which may lead to a non-axisymmetric perturbation of the plasma column.

For these reasons, this PhD thesis is devoted to the analysis of some non-axisymmetric plasma perturbations, their effects during the plasma operations and their modelling. The PhD thesis is divided as follows:

1. The first chapter is a brief overview of the main principles the controlled thermonuclear fusion is based on, focusing on the plasma confinement inside a tokamak, the additional heating and the roadmap towards the fusion energy.

2. The second chapter describes the diamagnetic flux evaluation in ITER tokamak for the estimation of the poloidal beta in the presence of non-axisymmetric effects. In particular, the COMPFLUX procedure used for the analysis is presented, then the effects of the main three-dimensional effects are evaluated and the performance of the compensation system is assessed.

3. The third chapter shows the electromechanical effects due to non-axisymmetric halo currents in ITER tokamak. After discussing the mathematical model, the mechanical effects in terms of forces and torques on the structures surrounding the plasma are evaluated.

4. The fourth chapter is devoted to the flux-density field lines tracing and to the identification of non-axisymmetric plasmas. The mathematical model and the procedures developed for the analysis are presented. Afterwards,

the standard and geometrical integrators are compared with reference to test cases for which analytical solutions based on the use of Clebsch potentials are available. Finally, the field line tracing technique is used for the non-axisymmetric plasma boundary reconstruction and a novel technique for the 3-D plasma identification is presented and validated.

5. The fifth chapter reports the main conclusions regarding all the topics dealt with this PhD thesis.

Chapter 1

Introduction to the Thermonuclear Fusion

This chapter illustrates a brief overview of the most important aspect of the *Controlled Thermonuclear Fusion*: the basic principles, the most important features and the evolution of the nuclear fusion technology are introduced to set a framework for what is described in the following chapters.

1.1   Towards the energy of the future: Controlled Thermonuclear Fusion

The estimations about the worldwide population growth show that by half of the present century it will double while the need for energy will be triple.

Taking into account that the most part of energy sources come from the limited primary sources our planet produced in millions of years (for instance oil, carbon and gas), their overexploitation would cause such a pollution to upset the entire ecosystem, yielding the problem of finding a sure, green and plentiful enough resource.

Renewable energy resources (e.g. hydroelectric energy) offer many advantages, are able to satisfy parts of our energy needs, but will never be able to replace all fossil fuels, as for Italy, where the energy production from these sources is around 10% of the national energy one. This percentage makes hard the achievement of any target foreseen in the Kyoto Protocol.

The solution to the energy demand can only come by a portfolio of many options including improvements in the energy efficiency and renewable energy, nuclear fission and carbon extraction and use.

The *Nuclear fusion* can be a long-term solution to the energy-supplying problem. As the fusion fuel is the hydrogen (and its isotopes), there is a theoretically infinite storage in oceans, seas and lakes, providing so much high quantities to make millions of reactors work for millions of years.

While deuterium is widely spread in nature, tritium is not. Moreover, because of its short decay time, tritium is an unstable atom, thus the decision to produce it by reactions between neutrons and lithium (widely present in nature).

Among the many nuclear fusion advantages, we can list:

1. fuel inexhaustibility;

2. the fusion products (helium and neutrons) are not radioactive elements as the tritium is (however, radioactivity problems are present, first of all because tritium is involved in the reaction and secondly because high speed neutrons hit the structures of the reactor, with the possibility of activated them);

3. the fuel quantity needed to nuclear fusion is very low and there is no chain reaction.

Like nuclear fission, nuclear fusion too is based on mass – energy transformation, as stated in the well-known Einstein Equation:

$$E = mc^2 \tag{I.1}$$

Products' atomic mass is not equal to that of the reagents and this mass defect is turned into products' kinetic energy; therefore, the mass – energy balances can be verified if and only if both the reagents' and products' masses and kinetic energies are taken into account, as follows:

$$E_R + m_R c^2 = E_P + m_P c^2 \tag{I.2}$$

Considering that the mass converted in energy is about 1‰ – 1% of the reagents', if 1 kg of fuel is involved into the reaction, the energy produced is about 10^{14} J: the result is a huge energy production to be converted in electrical energy, using just 1 litre of water.

Another nuclear fusion important advantage is the safety, if compared with the nuclear fission, where the atomic bomb effect should be avoided. In fission reactors, uranium bars are put inside a liquid that slows the fission reactions in case of wrong control actions, which bring to dangerous situations, as the core fusion. On the other hand, fusion reactions use a very low fuel quantity, with a

very low release of energy and radioactivity in case a dangerous situation should occur. It is worth noticing that tritium is the unique radioactive material involved in the fusion reactions and is characterized by a half-life time lasting some days, differently from the materials activated by fast neutron, whose half-life time is comparable with that of the activated materials in nuclear fission.

Among all the objectives the nuclear fusion achieved, the JET (Joint European Torus) in Great Britain, produced 16 MW Nuclear Fusion Power, even though using 25 MW, towards the end of the eighties, when the so called c*old fusion* was announced to the world. Nowadays the *Break-Even Point* (operational condition in which the nuclear fusion power is equal to the electrical power absorbed) is not achieved yet. Introducing the *Energy Amplification Factor* (Q), defined as the ratio between the nuclear fusion power and power need to sustain nuclear fusion reactions, we can say that the Break-Even Point is reached when $Q = 1$.

To better understand the meaning of the Energy Amplification Factor, let us consider the balance equation between deuterium and tritium involved in a nuclear fusion reaction:

$$D + T \rightarrow {}^4He + n + 17.6 Mev \qquad\qquad (I.3)$$

where:

➢ D is the Deuterium;

➢ T is the Tritium;

➢ ⁴He is the Helium 4;

➢ N is the neutron;

➢ *Mev* is the kinetic energy produced by the fusion reaction, measured in Megaelectronvolts ($1eV = 1.602 \cdot 10^{-19} J$, since e is the elementary charge of a proton).

Having no electrical charge, the neutrons are shot against the walls, releasing the thermal energy to the surrounding structures, heating them; this thermal energy can be recovered by using coils and heat exchangers and then used to produce electrical energy.

As regards the ⁴He atoms (in the following, they will be named *alpha particles*), they have their own electric charge, so they are confined inside the Vacuum Vessel, giving their energy to other particles and allowing other fusion

reactions. As consequence, once a certain energetic threshold is reached and exceeded, this process can continue with no interruptions; the only condition to satisfy is the insertion of new fuel, i.e. deuterium and tritium, and the extraction of the exhausted alpha particles that already gave their energy to the other particles.
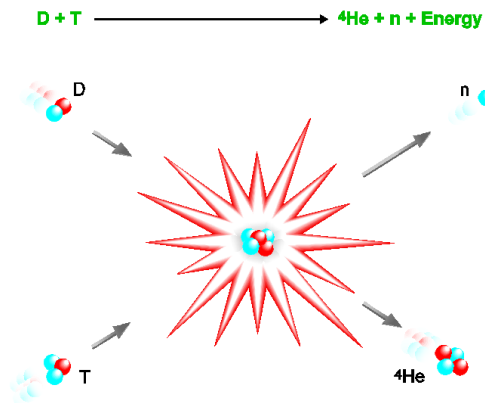
Fig. I.1: Nuclear Fusion Reaction

When the alpha particles satisfy the total energy requirement for the sustainability of the fusion reactions, the fusion reaction reaches a condition named *Ignition*: the plasma is heated by the energy released by the alpha particles, no more electrical energy has to be absorbed by the electrical grid and the Energy Amplification factor tends to infinite.

This was ITER's first goal (International Tokamak Experimental Reactor), but a little way down the road, it was reduced to an Energy Amplification Factor ranging from 5 to10.

1.2   Plasma confinement

Differently from the nuclear fission reaction, where a high energy neutron is shot on an atom, splitting it in others lighter atoms and releasing energy, in nuclear fusion reactions two electrically charged particles must hit and fuse, overcoming the Coulomb repulsion.

Recalling the expression of the energy of a particle moving into the electrostatic field generated by a still one, it is clear that the kinetic energy it

needs to have to approach the electrostatic source to a few Angstrom distance is huge, resulting in a speed being a non-negligible fraction of the speed of the light.

To guarantee such a high kinetic energy, it is necessary to heat the D-T mixture up to 100 million of degrees (about 5-6 times the temperature of the sun), so to reach the *Plasma* state.

This is not the unique condition to ensure for a correct fusion reaction: in fact, considering a high enough kinetic energy so to let them to collide, the particles must do it showing their entire cross section. It is clear that the probability that this condition is satisfied is very low, so as the probability that a collision generates a correct fusion reaction, because of the very small cross section of the particles.

For this reason, it is necessary that a high number of particles per unit volume be involved in the fusion reactions, so that the starting fusion probability is proportional to the product of reagent densities.

Finally, it is also necessary that the interaction time of the particles is long enough to allow the nuclear fusion reactions to start: it is worth noticing that if the plasma is heated up to 100 million of degrees, the particles will move with a speed about of $10000 \frac{km}{s}$, and the time they spend in a $1 cm^3$ volume is about $10^{-12} s$.

From these considerations, it is clear that the number density of the reagents is inversely proportional to their interaction time; therefore, a criterion linking the confinement time and particle densities is necessary and can be derived from some energetic considerations.

First, let us consider that it is possible to heat a plasma up to a temperature of the order of 10 keV instead of 100 keV, thanks to the quantum tunnelling through the Coulomb barrier. For equal deuterium and tritium number densities, the thermonuclear power per unit volume generated by the fusion reactions is:

$$P = \frac{1}{4} n^2 <\sigma v> \Delta E \qquad (I.4)$$

where:

- n is the particle density;
- $<\sigma v>$ is the reaction rate, being σ the collisional cross section and v the relative speed of the colliding particles;

- ΔE is the energy released after the collision.

About the fifth part of this power is transferred to the alpha particles, which increase their kinetic energy, while the 80% is carried by the neutrons. Taking into account all the energy losses (e.g. due to radiation and transmission to the structures surrounding the plasma), in 1957 Lawson introduced a relation between the Thermonuclear Power Gain and the product of the Confinement Time and the numeric density of the particles. He also expressed the power available to heat the plasma as function of the total power leaving the plasma [1] as follows:

$$n \cdot \tau \geq \frac{3k_B T}{\frac{\eta}{4(\eta - 1)} < \sigma v > \Delta E - \alpha\sqrt{T}} \qquad (I.5)$$

being:

- k_B the Boltzmann constant;
- T the plasma temperature;
- η an efficiency factor.

Choosing η=1/3, as Lawson did, we get the condition for magnetically confined plasmas known as *Lawson Criterion*:

$$N \cdot \tau_E \geq 10^{20} m^3 s^{-1} \qquad (I.6)$$

After having introduced the criterion of fusion reactions for a plasma to burn, in the following, the main techniques to confine it inside the reactor are depicted. The *magnetic confinement* is based on the motion of a charged particle in a Flux Density Field; if it has an initial speed with both the perpendicular and parallel components to the field lines, the trajectory it covers is a helix around the flux density field lines, whose radius is the so named *Larmor Radius*:

$$r_L = \frac{mv_\perp}{qB} \qquad (I.7)$$

This consideration led to the first idea to design a fusion machine as a linear solenoid, as in Fig. I.2:
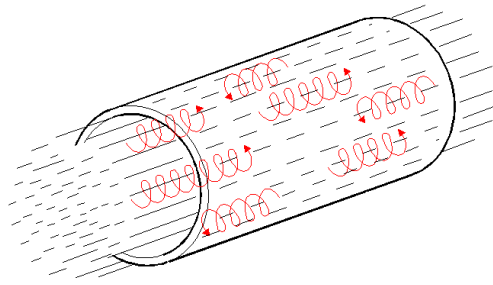
Fig. I.2: Straight solenoid and particles trajectories around the flux density field lines

This design was quickly abandoned because of the edge losses in terms of non-contained particles, so as for the *Magnetic Mirrors* [1] (they were much more lower than those of the straight solenoid, because of the edge additional solenoids that increased the magnetic field). For these reasons, a *Toroidal Solenoid* named *Tokamak* (**TO**роидальная **КА**мера с **МА**гнитными **К**атушками) was proposed at the beginning of fifties [2], so that particles cannot get out of it, if the drift effects are neglected.
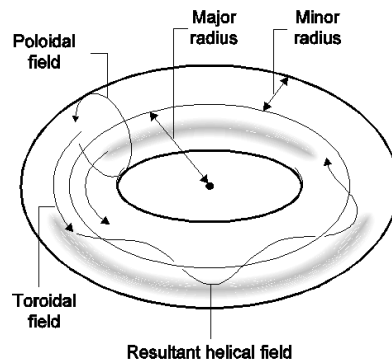
Fig. I.3: Magnetic confinement in a toroidal solenoid

Besides the magnetic confinement (the gravitational confinement used into the stars cannot be used on the earth because the gravity force is very low and vertically directed), the *inertial confinement* can be used to contain the plasma. This technique is based on the creation of the plasma by irradiating a frozen pellet consisting of a D-T mixture, by means of high power laser beams. The ionization reactions heat and compress the pellet, making it to overcome the threshold between solid matter and plasma (the state the pellet reaches is named *Hot Dense Matter* [3]), reaching thermonuclear temperatures and densities 1000 times higher than that of the solid matter and finally blowing up.

Once heated the particles need some nanosecond to leave the pellet ($\tau \geq 10^{-11} s$) because of their inertia, being able to interact with the other particles during this time interval.

On the other side, typical magnetically confined plasma densities require a containment time of a few seconds.

1.2.1 Drift Effects in Magnetically Confined Plasmas in Tokamaks

It is well known that in a toroidally continuous solenoid there is no magnetic field anywhere except for the region inside the solenoid itself, where it is toroidally directed and decreases with the radial coordinate.

Therefore, the charged particles move in an inhomogeneous magnetic field [1], and the Larmor radius (I.7) is linearly proportional to the radial position of the charged particle. As consequence of the study of the particles' motion via integration of D'Alembert equation (the electrical and magnetic forces balance the inertial force), we note that the particles are affected by a *Gradient Drift.* For this reason, they do not return in their starting position after one turn along the circumference whose centre is on the flux density field line and whose radius is r_L.
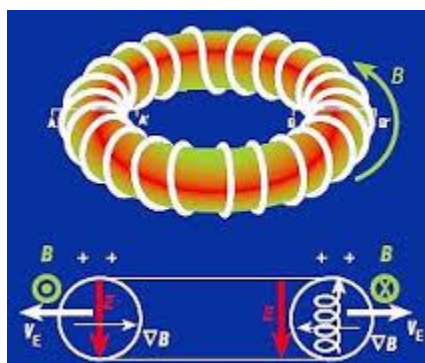
Fig. I.4: Particles Gradient Drift

Besides the gradient drift, another drift component is the *Curvature Drift* due to the Centrifugal Force acting on the charged particles and pushing them outside the torus.

At last, also the *Electrical Drift* affects the plasma particles and depends on the electrical charges separation generated by the previous effects (positive and negative charges have gradient drifts in different directions): the electrical charges displacement generates an electrical field whose force must be taken into account into the force balance equation.

Since the magnetic flux density magnitude is about few Teslas and the particles' speed is several thousand kilometres per second, the drift time is not compatible with the Lawson's Criterion; therefore, the charged particles must not have drifts along a unique direction to face the drift effects.

This condition can be achieved by changing the topology of the magnetic flux density field lines, by adding the field generated by an axisymmetric loop current placed inside the Vacuum Vessel to the toroidal field. It not possible to place a current inside the chamber because of plasma hot temperature, so the idea to induce a current in it via electromagnetic induction, thus exploiting the high plasma conductivity.

Basing on these suppositions, a Tokamak has a *Central Solenoid* around the vacuum vessel, acting like the primary winding of a transformer that induce an electromotive force on the plasma; the following figure Fig. I.5 shows a sketch of the main coils inside a tokamak.
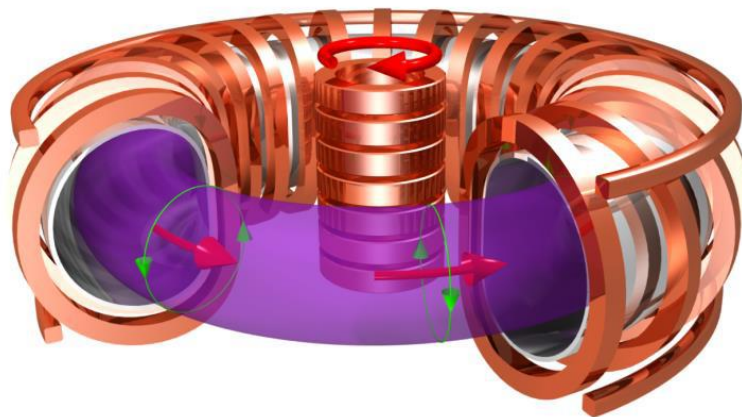
Fig. I.5: Tokamak coils

At last, to prevent the radial expansion of the plasma column, a vertical magnetic field has to be superposed: this need is due to the absence of a Stress Tensor in the plasma balancing the Lorentz expansion force. Additional magnetic

fields are needed for the plasma shaping and control; the vertical and shaping fields are produced by the *Poloidal Field Coils* (*PFCs*).

1.3   Plasma Heating

Plasma current in tokamaks is not good enough to heat the D-T mixture up to 100 million degrees required for the gas in the vacuum chamber to turn into plasma and for the fusion reactions to occur; moreover, the hot plasma must then be sustained at these temperatures in a controlled way in order to extract energy.

Generally, Tokamaks can rely on some additional heating sources that work in concert to provide the input heating power required to bring the plasma to the temperature necessary for fusion [4].

Ultimately, in the hopeful hypothesis of ignition operative condition, the external heating can then be strongly reduced or switched off altogether; in fact, an ignited plasma is an essential step to reaching the goal of fusion power generation, because at least 50% of the energy needed to drive the fusion reaction is generated internally

Fig. I.6 shows the sketch of the additional heating systems detailed in the following.
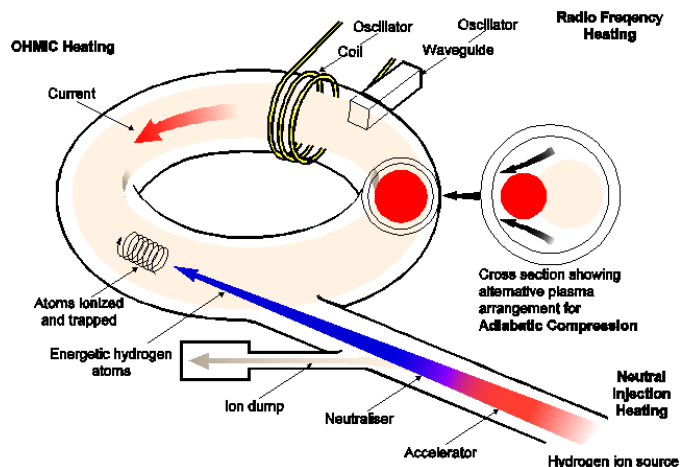
Fig. I.6: Plasma Additional Heating

1.3.1 Heating Transformer

The heating transformer was already examined in Section 1.2.1: the magnetic flux time variation generated by the current flowing in its windings creates an electromotive force into the plasma; the plasma current starts flowing and heats it via Joule dissipation.

1.3.2 RF Heating

It is based on the radiation on the plasma of an electromagnetic wave with a frequency ranging in the Radio Frequencies.

Being *v* the particles' speed while moving on a spiral around magnetic field lines, it is possible to define the ratio between the velocity and the radial coordinate of the particles as *Cyclotron Frequency*.

This is a very important parameter because it is related to the temperature of the particles and to the magnetic field value at their position; therefore, if an electromagnetic wave is radiated on the plasma, it possible to approximatively know the plasma region heated.

Usually three frequencies are used, depending on the magnetic flux density field and the kind of particles the plasma consists of:

➢ *Electron Cyclotron*: cyclotron frequency for electrons;

➢ *Ion Cyclotron*: cyclotron frequency for ions;

➢ *Lower Hybrid*: it is based on the presence of other particles with different speeds (temperatures).

1.3.3 Heating by Neutron Beam Injection (NBI)

This technique consists in accelerating neutrons outside the Vacuum Vessel and making them collide with the plasma particles; in this way, they yield kinetic energy to the plasma, heating it.

Neutrons are used because they have no electric charge, and so are not deflected by the magnetic field barrier used for plasma containment; thus the problem of their acceleration by using no particles accelerators based on

magnetic fields. Actually, the charged particles are accelerated and then neutralized before entering into the vessel, even though this results in a decrease of their kinetic energy.

Fig. I.7 shows a conceptual sketch of the Neutral Beam Injector:
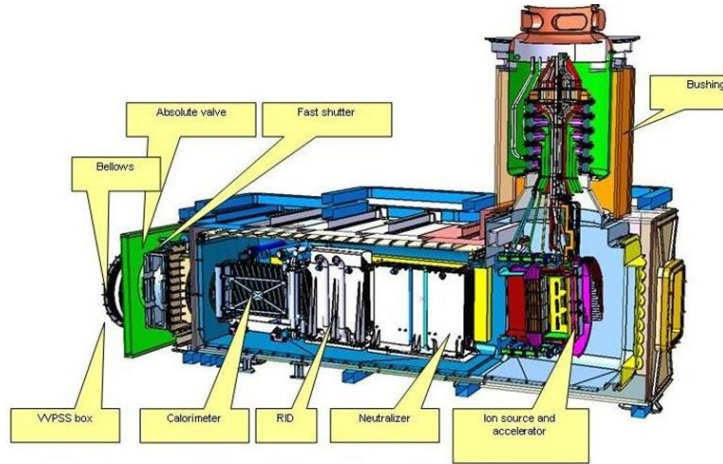
Fig. I.7: Neutral Beam Injector section

NBI heating generates also a secondary effect. If the particle beam is directed in the poloidal plane, it does not affect the toroidal plasma current. Otherwise, the neutral beam would impact the plasma particles yielding them a toroidal component of the velocity and modifying the toroidal plasma current, resulting in an enhanced heating by Joule dissipation; this effect is named *Current Drive*.

1.3.4   Heating by Adiabatic Compression

It is based on *Adiabatic Compression Principle*: if a perfect gas is subjected to a very fast compression, the heat losses and the thermal exchanges are negligible; therefore, the pressure and the temperature increase.

1.4 The Fusion Roadmap: Towards the Fusion Power Plants

Because of a combined effect of population growth and energy consumption pro capita of OECD parties increase, a long-term perspective on fusion is mandatory.

For these reasons, a *Fast Track* approach [5] to the fusion energy was defined in 2001; on such basis, a program aimed at fusion electricity by 2050 was defined in the Fusion Roadmap developed in 2013 [6], based on the following three points:

- ITER (**I**nternational **T**okamak **E**xperiamental **R**eactor) tokamak: a fundamental step towards the fusion energy production;
- DEMO (**DEMO**nstration power plant) tokamak: a prototype for a power-producing fusion reactor between ITER and the commercial fusion power plant;
- IFMIF (**I**nternational **F**usion **M**aterials **I**rradiation **F**acility): a step for material qualification under intense neutron irradiation.

The roadmap foresees three periods having the following main objectives:

1. Horizon 2020 (2014-2020):
   - Construct ITER within scope, schedule and cost;
   - Secure the success of future ITER operation;
   - Prepare the ITER generation of scientists, engineers and operators;
   - Lay the foundation of the fusion power plant;
   - Promote innovation and EU industry competitiveness.
2. Second period (2021-2030): Exploit ITER up to its maximum performance and prepare DEMO construction.
3. Third period (2031-2050): complete the ITER exploitation, construct, and operate DEMO.

Being DEMO the only step between ITER and fusion power plants [7], it has to:

- Produce few hundreds MWs of net electricity for the grid;
- Breed the amount of tritium it needs;

- Demonstrate the feasibility of all the technologies for the construction of the future fusion power plants.

For the same reason, DEMO's operating scenarios will have to be as far as possible extrapolated from ITER, to meet its goals.
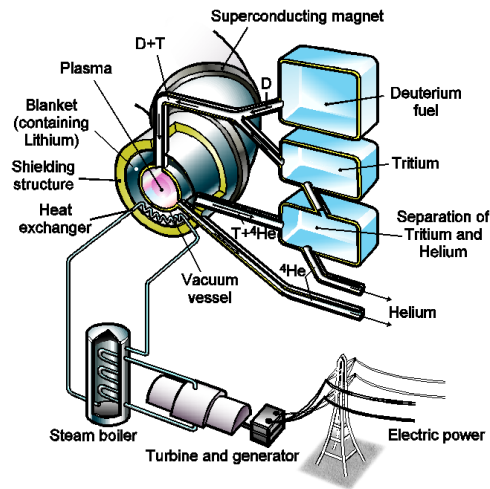
Fig. I.8: Fusion Power Plant conceptual sketch

However, the feasible realisation of fusion power plants energy aimed to the energy production has to face many challenges:

1. Plasmas must be confined at temperatures many times higher than that of the sun, requiring a *magnetic confinement of the plasma*; the plasma operative conditions are developed ad hoc for ITER tokamak and will definitively require enhances to meet the requirements for DEMO.

2. The power necessary to the plasmas sustainment at so high temperatures is exhausted in the region of the divertor, withstanding huge heat loads with new type of plasma-facing materials and exhausting systems; the born of a technically feasible solution for the *heat exhaust* is still challenging in DEMO.

3. The research of new *Neutron resistant materials* is also challenging for DEMO, since they are asked to be able to withstand up to 14MeV neutron flux, preserving their structural and thermal properties, to ensure efficient electricity production and adequate plant availability.

4. *Tritium self-feeding* is mandatory for DEMO, which will burn about 0.4kg of tritium per operational day.

5. The *Operative Safety* is also mandatory for DEMO, which must prevent any accident and guarantee a safe evacuation to all people involved in its operation in the worst case; thus, the development of solutions to reduce the tritium quantity involved into the process.

6. The *Integrated DEMO Design* as consequence of the combination of all fusion technologies will guarantee a smoother path to its realization, especially thanks to the ITER construction, with a high level of reliability of the tokamak.

7. In order to be competitive on the electrical energy market, fusion electricity must show *low costs*; even though this is not the primary goal for DEMO, its pursuing needs to be an important target for the fusion power plants in terms of economic aspects.

For all the seven missions listed, appropriate risk mitigation strategies and technical solutions were defined and well assessed.

There is also an eighth mission, specifically addressed to the Stellarators: despite of the tokamaks, they show an intrinsic plasma stability due to the magnetic field configuration, being a possible alternative solution to the tokamak. Because their physics is not mature enough to produce electricity by 2050, the mission id devoted to *bring the stellarator line to maturity*.
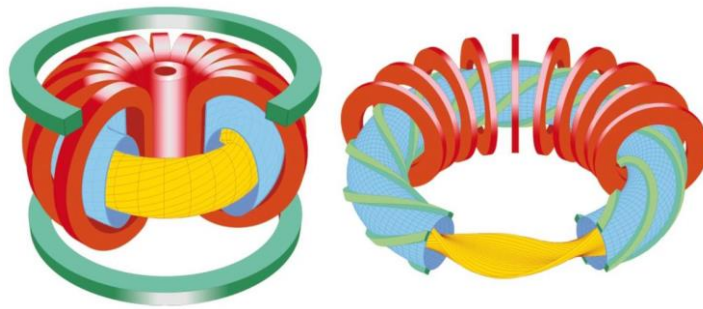
Fig. I.9: Comparison between a tokamak (left) and a stellarator (right)

It is clear that large *theory and modelling effort* for all the mission will be important to provide the capability of the results extrapolation for DEMO tokamak, also dedicating special previsions to the high-performance computing and related supporting activities

Chapter 2

Diamagnetic flux measurements for poloidal beta estimation in the presence of non-axisymmetric effects in ITER Tokamak

In this chapter, the computational model used for the simulated measurements performed by the magnetic field and flux sensors is shown [8]-[9]; then, the problem of the measurement of the diamagnetic flux and the compensation of spurious signals and errors generated by the external magnetic pollution is tackled, highlighting their effects in terms of the poloidal beta estimation [10].

2.1 COMPFLUX: a numerical suite for the electromagnetic analysis of a Tokamak

2.1.1 Why the COMPFLUX Procedure

The measurement of many physical plasma parameters as the poloidal beta, the safety factor and the confinement time is necessary in tokamaks to enhance their performances.

For these purposes, the diagnostic systems consisting of local sensors and coils are designed. They are deputed to measure the magnetic flux density field along prescribed directions and the magnetic fluxes linked with the coils respectively, in presence of several kinds of electromagnetic sources, as the currents flowing into the active coils and into the passive structures of the machine and/or ferromagnetic materials.

Of course, the actual measurements are different from the ideal ones, being they affected by errors due to a not perfect matching of the actual tokamak structures with respect to the nominal design. The measurements are also affected by imperfections of the sensor geometries like:

- not perfect positioning or alignment of the field sensors (the actual measurement is performed at a different point and/or along a different direction with respect to the nominal one);
- rotations, shifts or random deformations of the flux sensors with respect to the nominal geometry (the actual measurement depends on the actual shape of the sensor).

These errors dynamically change during the operations because of the thermal and electromechanical loads acting on the tokamak structure; therefore, many sensitivity analyses are necessary to get the tolerance bounds of the deviations both of the sensors' and other structures' geometries with respect to the ideal design.

The COMPFLUX peocedure was so designed, tested and validated with the aim to perform full and fast sensitivity analyses of the magnetic field and flux sensors.

It consists of three main parts:

1. *Preprocessor*: its main task is to define the field sensors, the axisymmetric flux sensors and the 3-D flux sensors;
2. *Processor*: its main task is to calculate Magnetic Flux Density Field B and Magnetic Vector Potential A generated by the sources at the output points defined by the preprocessor;
3. *Postprocessor*: its main task is to calculate the Magnetic Flux Density Field B and the Magnetic Vector Potential A via interpolation, in other points out of the original set provided in the preprocessor.

The electromagnetic sources can be magnets, conductors of any geometry and massive axisymmetric coils of rectangular section, each of them treated by a set of filamentary currents located in optimal way by using the Gauss quadrature rule.

2.1.2 COMPFLUX processor

The COMPFLUX processor [9] is aimed to the calculation of the magnetic flux density field and vector potentials at the sensors' points; their computation is analytically performed by means of the Biot-Savart Law for both the massive axisymmetric coils and the non-axisymmetric coils.

As regards the magnetic materials, if saturated, the COMPFLUX processor partitions them in spheres, in such a way that the total volume is kept (Fig. II.1), and calculates the magnetization vector for each sphere. The hypothesis of magnetic saturation allows to model a sphere of radius r_{sf} and uniform magnetization $\boldsymbol{M_{sf}}$ as a magnetic dipole whose magnetic moment is assigned and then to superpose all the contributions to obtain the total magnetic field and potential at the sensors' positions.
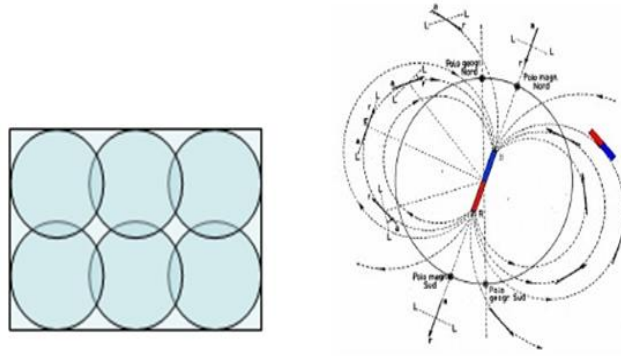
Fig. II.1: Magnetic material partitioned in spheres (left) and model of a single sphere as a magnetic dipole (right)

The magnetic moment associated to each sphere can be easily calculated with the following formula:

$$\boldsymbol{m} = \frac{4}{3}\pi r_{sf}^3 \mathbf{M_{sf}} \tag{II.1}$$

Thus, the value at each point of the space of the scalar potential, vector potential and magnetic field associated to the magnetic dipole are respectively:

$$\Phi(\vec{r}) = \frac{\mu_0}{4\pi}\frac{\boldsymbol{m}\cdot\hat{r}}{\left|\vec{r}-\hat{r}_{sf}\right|^2} \tag{II.2}$$

$$A(\vec{r}) = \frac{\mu_0}{4\pi} \frac{\boldsymbol{m} \times \hat{r}}{|\vec{r} - \hat{r}_{sf}|^2} \qquad (\text{II.3})$$

$$H(\vec{r}) = \frac{1}{4\pi |\vec{r} - \hat{r}_{sf}|^3} \left(\frac{3(\boldsymbol{m} \cdot \hat{r})\hat{r}}{|\vec{r} - \hat{r}_{sf}|^2} - \boldsymbol{m} \right) \qquad (\text{II.4})$$

If the magnetic material is not saturated, an iterative procedure based on Newton contractions is used [11].

At last, once the magnetic vector potential is known, the flux linked with a closed line γ is computed via its circulation along the flux sensor's geometry via Simpson's rule: the line γ is divided in Nγ evenly spaced arcs and the circulation of the vector potential is approximated for each of them by the sum of the following three contributions:

$$\Phi_\gamma = \oint_\gamma A \cdot \hat{t}dl =$$

$$= \sum_{j=1}^{N_\gamma} \frac{A(\mathbf{x}_{j,0}) \cdot d\mathbf{x}_{j,0}}{6} + \frac{2A(\mathbf{x}_{j,0.5}) \cdot d\mathbf{x}_{j,0.5}}{3} + \frac{A(\mathbf{x}_{j,1}) \cdot d\mathbf{x}_{j,1}}{6} \qquad (\text{II.5})$$

According to a parabolic approximation:

$$\begin{aligned}
d\mathbf{x}_{j,0.5} &= \mathbf{x}_{j+1} - \mathbf{x}_j \\
d\mathbf{x}_{j,0} &= -\mathbf{x}_{j+1} + 4\mathbf{x}_{j+0.5} - 3\mathbf{x}_j \\
d\mathbf{x}_{j,1} &= 3\mathbf{x}_{j+1} - 4\mathbf{x}_{j+0.5} - \mathbf{x}_j
\end{aligned} \qquad (\text{II.6})$$

where $\mathbf{x}_j$ is the arc starting point, $\mathbf{x}_{j+1}$ the arc end point, and $\mathbf{x}_{j+0.5}$ the mid-point of the arc.

The COMPFLUX built-in processor can also be replaced by other numerical procedures' processors, if necessary; in the following, the main characteristics of the CARIDDI [11]-[12]-[13] and MISTIC [14] processors are summarized.

2.1.3   The CARIDDI processor

CARIDDI is a 3-D integral code well assessed to solve numerically the time-domain Maxwell equations in the magneto-quasi-stationary limit.

The electric vector potential $\boldsymbol{T}$ ($\boldsymbol{J} = \nabla \times \boldsymbol{T}$) is the unknown field of the numerical formulation so to automatically impose that the current density field $\boldsymbol{J}$ in the conductive domain Ω_D is divergence-free and its normal component is continuous.

Moreover, using the edge elements for the numerical expansion of the electric vector potential, it is possible to use a numerical gauge based on the tree–cotree decomposition of the edges of the mesh; the advantage is that the discrete unknowns are the only line integrals along the co-tree branches.

The final discretized model to be solved resembles a high order LR network:

$$\underline{\underline{L}}\frac{d\underline{I}}{dt} + \underline{\underline{R}}\,\underline{I} = \underline{V_c} \tag{II.7}$$

where:

$$R_{i,j} = \int_{\Omega_D} \eta \boldsymbol{w}_i \cdot \boldsymbol{w}_j d\Omega \tag{II.8}$$

$$L_{i,j} = \frac{\mu_0}{4\pi} \int_{\Omega_D} \int_{\Omega_D} \frac{\boldsymbol{w}_i(\boldsymbol{r}) \cdot \boldsymbol{w}_j(\boldsymbol{r}')}{|\boldsymbol{r} - \boldsymbol{r}'|} d\Omega d\Omega' \tag{II.9}$$

$$V_{c,i} = -\int_{\Omega_S} \frac{\partial \boldsymbol{A}_c}{\partial t} \cdot \boldsymbol{w}_i d\Omega; \quad \boldsymbol{A}_c = \frac{\mu_0}{4\pi} \int_{\Omega_S} \frac{\boldsymbol{J}_c(\boldsymbol{r}',t)}{|\boldsymbol{r} - \boldsymbol{r}'|} d\Omega' \tag{II.10}$$

where $\boldsymbol{w}_i$ is the shape function of the weak formulation and $\mathbf{J}_c$ is the impressed current density into the source domain Ω_S.

Note that the resistance matrix $\underline{\underline{R}}$ is symmetric and sparse, whose elements $R_{i,j}$ do not vanish only if the i-th and j-th unknowns share the same mesh element. On the other hand, the inductance matrix $\underline{\underline{L}}$ is symmetric and full because the $L_{i,j}$ coefficients keep into account the long-distance interactions between the unknowns.

The CARIDDI and CARIDDI-MAG [15] codes are able to calculate the magnetic flux linked with a flux loop via time integration of the electromotive force, but paying a very high computational cost, due to the time integration itself and the need a solid model of the loop. On the other hand, the COMPFLUX procedure calculates the flux linked with the flux loop via circulation of the magnetic vector potential at the points of the sensor itself, thus implying a much lower computational load.

2.1.4 The MISTIC processor

MISTIC is a Matlab-based code designed to compute the magnetic field maps at a generic set of field points, generated by coils of arbitrary shape. The code is based on the analytical expression of the flux density and the vector potential for "current sticks"; the massive coils of arbitrary shape are partitioned in a suitable number of sticks, then the superposition principle is used to compute the total field and vector potential.
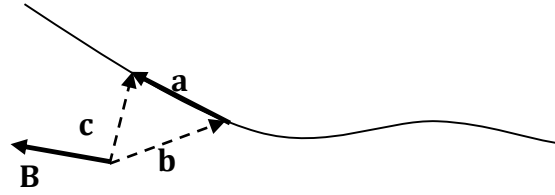
Fig. II.2: Magnetic flux density field generated by a current stick

With reference to Fig. II.2, we have:

$$\boldsymbol{B}_{stick} = \mu_0 \frac{I}{4\pi} \frac{\boldsymbol{c} \times \boldsymbol{a}}{\|\boldsymbol{c} \times \boldsymbol{a}\|} \left(\frac{\boldsymbol{a} \cdot \boldsymbol{c}}{\|\boldsymbol{c}\|} - \frac{\boldsymbol{a} \cdot \boldsymbol{c}}{\|\boldsymbol{b}\|} \right) \qquad \text{(II.11)}$$

$$\boldsymbol{A}_{stick} = \mu_0 \frac{I}{4\pi} \widehat{\boldsymbol{a}} \log \left(\frac{\|\boldsymbol{c}\| + \|\boldsymbol{b}\| + \|\boldsymbol{a}\|}{\|\boldsymbol{c}\| + \|\boldsymbol{b}\| - \|\boldsymbol{a}\|} \right) \qquad \text{(II.12)}$$

2.1.5 COMPFLUX postprocessor

The COMPFLUX procedure allows to carry out the sensitivity analyses in case of perturbations of the field sensors' position or of the flux sensors' geometry with respect to the nominal one.

These analyses usually require the knowledge of the vector potential and magnetic field values at a huge number of points, being very expensive in terms of CPU load; thus the idea of computing $\boldsymbol{B}$ and $\boldsymbol{A}$ only at a limited set of field points and interpolating them in the remaining set.

Essentially, the full map of the vector potential in the nearness of the nominal curve of each flux sensor is reconstructed by interpolating the values computed at the points of four auxiliary curves (see Fig. II.3) with a third order interpolation.
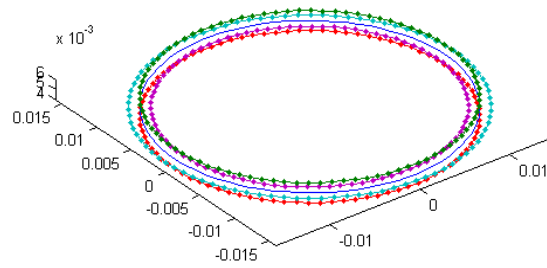
Fig. II.3: The four auxiliary curves (dotted) around the actual flux sensor (solid blue) for the reconstruction of the Vector Potential map

The same procedure is adopted for the reconstruction of the magnetic flux density field in the proximity of the nominal field sensor; the interpolation is carried out by using the evaluation of the **B** field in the six points surrounding the nominal sensor, obtained by a fixed magnitude displacement along the coordinates axes (1 mm in Fig. II.4).
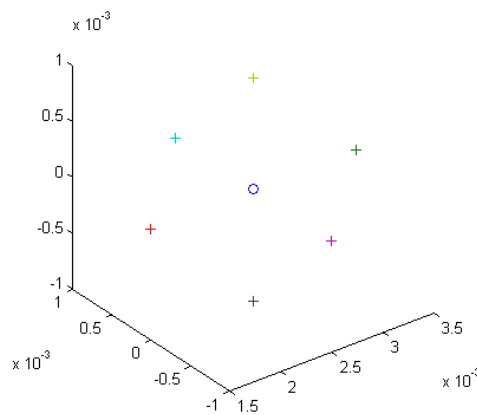
Fig. II.4: The six auxiliary points (crosses) around the actual field sensor (bubble) used for the reconstruction of the Flux Density Field

In this way, sensitivity analyses for many set of perturbations of both flux and field sensors are executable with low computational cost, because only a single electromagnetic study (carried out by any processor among COMPFLUX, CARIDDI or MISTIC) is necessary.

2.1.6 Test cases and Validation & Assessment

2.1.6.a Flux computation in 2-D axisymmetric geometry in presence of magnetic material

We consider the axisymmetric configuration reported in Fig. II.5 consisting of one coil with a uniformly distributed 100 A current and of a linear magnetized (μ_r=10) material ring.
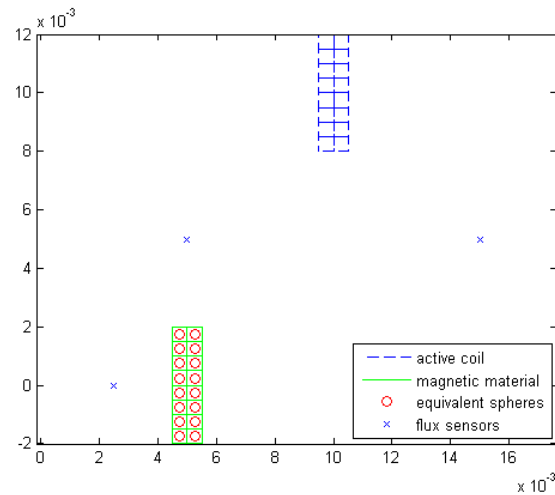
Fig. II.5: Test #1 - The 2D axisymmetric geometry

The total flux is computed in three different points, both in absence and in presence of the magnetic material, using the following procedures:

1. SOLENOID (an analytical code based on the elliptical integrals) [16];
2. the Finite Elements Method commercial code COMSOL Multiphysics [17];
3. COMPFLUX;
4. MISTIC;
5. CARIDDI.

The magnetic ring is modelled by $(N_r = 2) \times (N_z = 8) \times (N_\phi = 90)$ magnetic; the following Tab. II.1 and Tab. II.2 report the obtained results:

Tab. II.1: Test #1 – Flux computation in absence of magnetic materials

r [m]	5.0e-3	1.5e-2	2.5e-3
z [m]	5.0e-3	5.0e-3	0.0e+0
SOLENOID [Vs]	3.5170e-7	1.1882e-6	4.3480e-8
COMSOL [Vs]	3.5170e-7	1.1882e-6	4.3481e-8
COMPFLUX [Vs]	3.5171e-7	1.1879e-6	4.3478e-8
CARIDDI [Vs]	3.5173e-7	1.1860e-6	4.3432e-8
MISTIC [Vs]	3.5170e-7	1.1879e-6	4.3477e-8

Tab. II.2: Flux computation in presence of magnetic materials

r [m]	5.0e-3	1.5e-2	2.5e-3
z [m]	5.0e-3	5.0e-3	0.0e+0
COMSOL [Vs]	3.6685e-7	1.2114e-6	3.3654e-8
COMPFLUX [Vs]	3.6657e-7	1.2111e-6	3.3706e-8
CARIDDI [Vs]	3.6645e-7	1.2089e-6	3.3740e-8

2.1.6.b   Flux computation in 3-D geometry

The second test case is the problem proposed in [18], whose geometry is illustrated in Fig. II.6; the aim is the evaluation of the flux linked with the central wire when the upper and lower wires are fed.
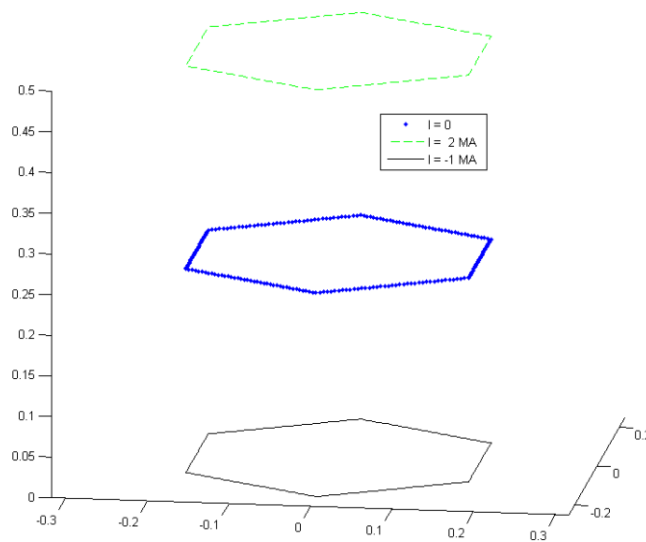
Fig. II.6: Test #2 – Flux computation in 3-D geometry

The side of each hexagonal wire is 20 *cm* long and the mutual distance is 25 *cm*. Hereafter, the results obtained with the COMPFLUX, CARIDDI and MISTIC processor are listed and compared with the analytic result given in [18]:

Tab. II.3: Flux linked with the hexagonal wire

COMPFLUX [Vs]	0.05366
CARIDDI [Vs]	0.05366
MISTIC [Vs]	0.05366
ANALYTIC [Vs]	0.05367

2.1.6.c Flux linked with the diamagnetic loop generated by poloidal and toroidal field coils and magnetic inserts

In this test case a full 3-D electromagnetic problem is faced, where both the poloidal and toroidal field coils are fed, with the additional presence of ferromagnetic inserts (Fig. II.7).
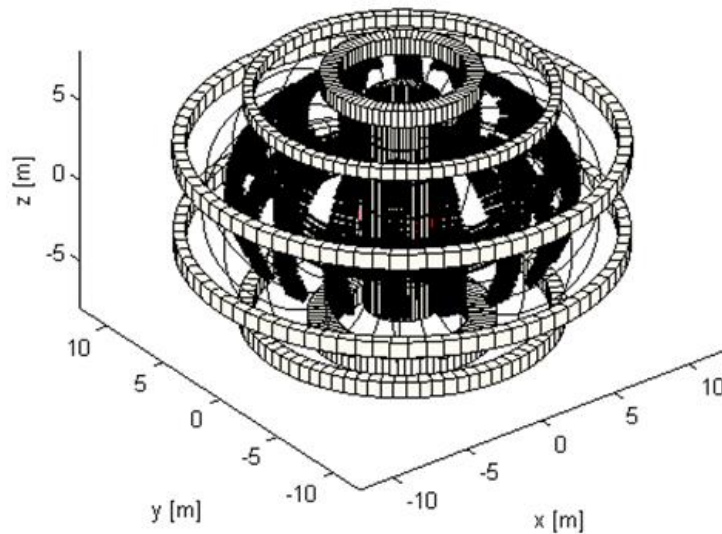
Fig. II.7: Test #3 – Solid model of the PF and TF coils and magnetic inserts

The results obtained by using both CARIDDI-MAG and COMPFLUX processors are reported below:

1. CARIDDI-MAG processor: 262.7309 Vs;
2. COMPFLUX processor: 262.7295 Vs

The ferromagnetic inserts are modelled as a set of spheres, as described in Section 2.1.2 and the CARIDDI code is used for the computation of the magnetization vector field of the inserts.

The total flux linked with the diamagnetic loop is the sum of the three contributions due to the TF Coils, the PF Coils and the Ferromagnetic Inserts; Tab. II.4 summarizes the single contributions for each processor.

Tab. II.4: Test #3 - Contributions of the PF Coils, TF Coils and Ferromagnetic Inserts

	COMPFLUX	CARIDDI
TF Coils Flux [Vs]	262.1319	262.1359
PF Coils Flux [Vs]	1.115e-16	0
Ferromagnetic Inserts Flux [Vs]	0.5975 Vs	0.5950

2.2   Diamagnetic Flux Measurement

Diamagnetic diagnostics are commonly used in tokamaks to measure the time variation of toroidal flux repelled by the plasma, as well as to estimate several plasma physical quantities, as the total diamagnetic energy content, plasma's confinement time or the poloidal beta β_p. In particular, a precise estimation of the mentioned parameters is relevant to improve the quality of the plasma discharges in terms of plasma current flatness and safety factor profiles [19]-[20].

The diamagnetic diagnostic system consists of a main diamagnetic loop for the diamagnetic flux measurement and a compensation coils system aimed to cancel the many polluting terms from the measure carried out by the main sensor. The measured value is the total toroidal flux Φ, which is the sum of the plasma diamagnetic (or paramagnetic) flux and several other quantities (see section 2.2.6) which are to be compensated by using both the compensation coils system [21]-[22], to meet the accuracy requirements. The compensation system, in fact, is aimed to extract the diamagnetic flux from the total toroidal flux linked with the main diamagnetic loop.
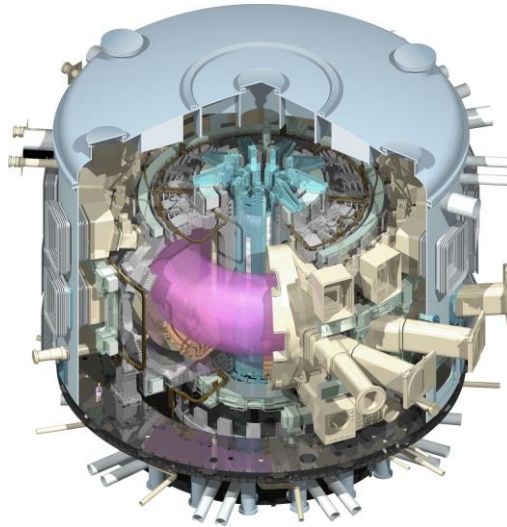
Fig. II.8: 3-D Rendering of ITER Tokamak (Courtesy of ITER organization)

In the following, the design of the diamagnetic diagnostics system in ITER tokamak (Fig. II.8) will be described and its performances will be assessed.

2.2.1   Sensors

The diamagnetic diagnostic system in ITER tokamak consists of the five sets of sensors listed below:

- main diamagnetic loops;
- inner diamagnetic compensation coils;
- outer diamagnetic compensation coils;
- diamagnetic saddles;
- TF coils (back-up).

In the following, the nominal design of each kind of sensor will be illustrated.

2.2.1.a   Main diamagnetic loop

This loop is installed on the inner shell of the Vacuum Vessel and is characterized by a total poloidal extension of $30\ m^2$; a set of three in-vessel main diamagnetic loops are present in ITER tokamak, placed in the poloidal sections

with $\varphi = 16\ deg$, $\varphi = 136\ deg$ and $\varphi = 256\ deg$, to take into account the toroidal average of the measured quantities [23].

The presence of some obstacles in the poloidal section (e.g. ports and ribs) forces the sensor to bypass them, moving also in the toroidal direction (see Fig. II.9), then linking also the magnetic field perpendicular to the vacuum vessel. To compensate this effect, each sensor consists of the series of two loops, surrounding the obstacles on both sides.
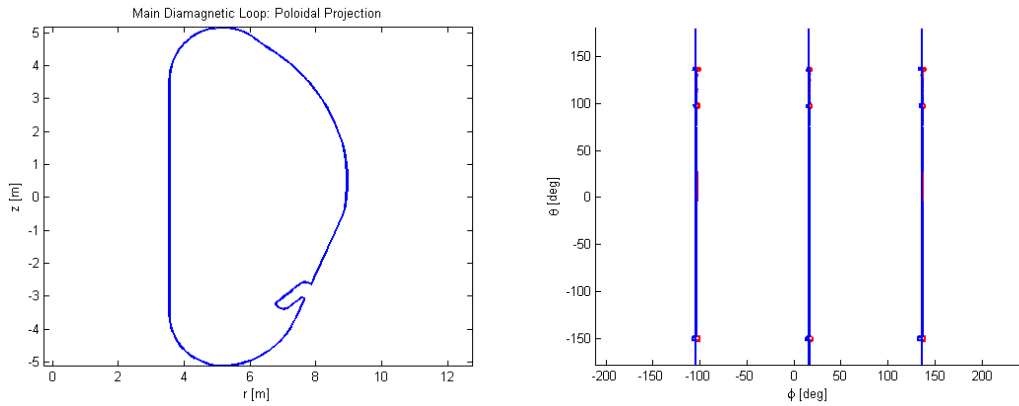
Fig. II.9: Main diamagnetic loop nominal geometry

The main diamagnetic loops measure the total toroidal flux via time integration of the loop voltage measured at its terminals.

2.2.1.b   Inner Diamagnetic Compensation Coils

Three pairs of toroidal pick-up coils [24], 120 degrees apart and located under the Outer Triangular Support are used in ITER tokamak as Inner Diamagnetic Compensation Coils, each of them measuring the toroidal field.

The two pick-up coils of each set are placed at either sides of a port and each sensor is square shaped (see Fig. II.10) with each side 81 mm long (2 layers of 150 turns for an effective area of 1.97 m² each).
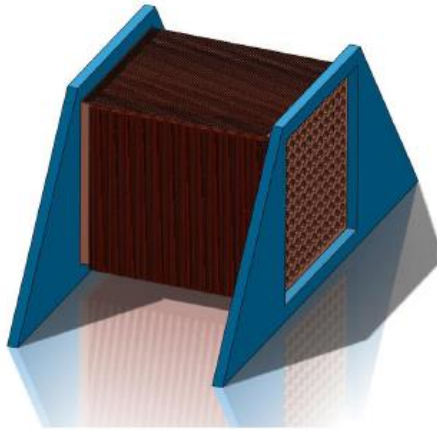
Fig. II.10: Isometric view of an Inner Diamagnetic Compensation Coil (courtesy of ITER and RFX organizations)

2.2.1.c   Outer Diamagnetic Compensation Coils

They are used in combination with the inner coils in paragraph 2.2.1.b to compensate the effects of the poloidal currents induced into the vacuum vessel.
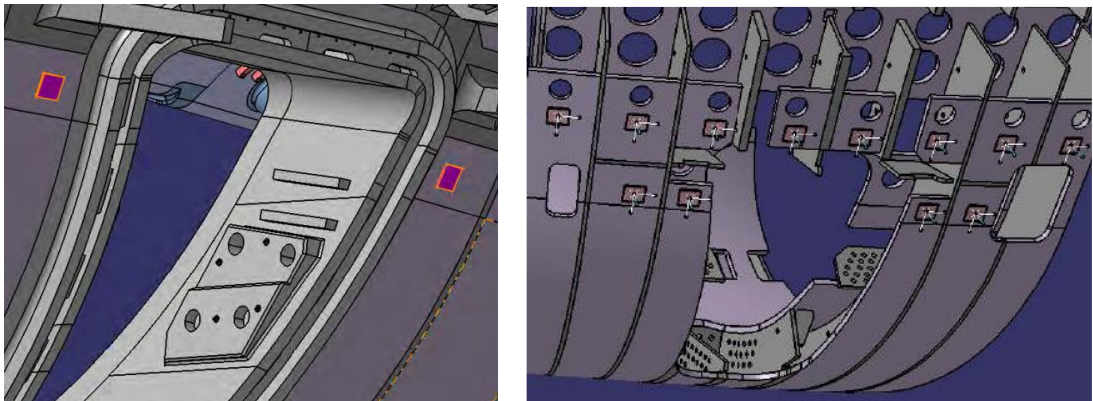
Fig. II.11: Detail of a Lower Outer Diamagnetic Compensation Coil (courtesy of ITER and RFX organizations).

In ITER there are two sets of pick-up coils measuring the toroidal field and having an overall effective area of 20 m^2: the Upper Set consists of 8 square shaped sensors and the Lower Set which consists of 4 square shaped sensors.

2.2.1.d   Diamagnetic Saddles

Three sets of two saddles are placed at the top and the bottom sides of the main diamagnetic loops.

They are called to compensate the effects of the vertical field, which might be significant whether the two parts of a main diamagnetic loop are not symmetric with respect to the poloidal plane.
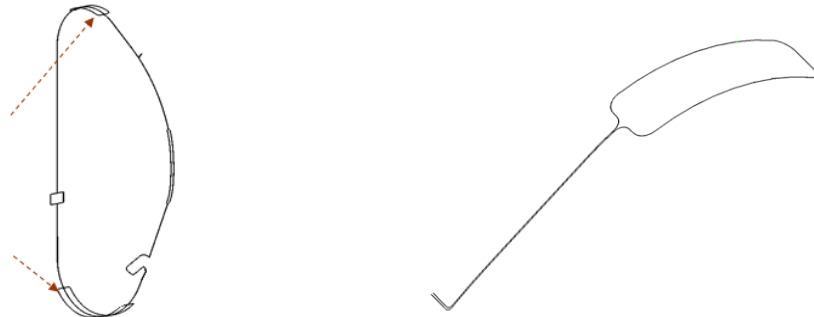
Fig. II.12: Diamagnetic saddles in ITER: locations with respect to the main diamagnetic loop (left) and detail of an upper diamagnetic saddle with its tail

In the following, the tiles of each diamagnetic saddle were neglected and the flux sensors considered as closed; in this way, the measure it carries out, that is the flux linked with it, was simulated by calculating the circulation of the magnetic vector potential along its path and not by calculating the time integral of the voltage across its terminals.

2.2.1.e   Toroidal Field Coils

Being magnetically coupled with the poloidal plasma current, the currents flowing into the Toroidal Field Coils or the voltages across their terminals can be used as back-up measurements of the diamagnetic flux [25]-[26].

2.2.2   General assumptions

To carry out the diamagnetic flux estimation, the general assumption hereafter summarized [27] were adopted:

- the ITER operative scenario is described in terms of the time history of the currents in the active coils (Poloidal & Toroidal Field Coils) and in the plasma;

- the diamagnetic loops are considered as ideal sensors [28]-[29], i.e. measuring the linked magnetic flux with no errors nor delays; in practice,

they carry out the measure of the time integral of the magnetic flux time derivative, which differs from the actual flux by a constant (the time integration usually starts before plasma breakdown, when the TF coils are already energized);

- the plasma is modelled with a suitable number of axisymmetric filamentary currents (carrying prescribed time-varying toroidal currents) and an axisymmetric poloidal current distribution placed on the shell of a toroidal surface located inside the vacuum vessel (it generates the same plasma diamagnetic flux as calculated by CREATE-NL or assigned in the scenario);

- the symmetry module of the overall structure spans no more than 40 deg toroidally, with a specular (left-right) symmetry at the poloidal mid-plane of the symmetry module itself;

The magnetic sources taken into account in the present study are the:

- Active Coils (Poloidal Field Coils and Central Solenoid) and Toroidal Field Coils (both in nominal geometry and affected by the assembly/manufacturing errors and dynamic deformations [30]-[31]);

- Plasma;

- Non-axisymmetric coils, e.g. ELM coils;

- Bus bars & feeders of conductors in main field coils winding packs;

- Ferromagnetic inserts, Netural Beam Injector iron and other iron components in the blanket modules;

- Eddy currents (mainly in Vacuum Vessel, blanket and divertor cassette) in various operating conditions.

Some of these effects just produce an offset that can be automatically removed by the time integration of the diamagnetic loop voltage (as large part of the polluting terms due to the TF Coils and the Ferromagnetic Inserts). Some other can be compensated by a linear combination of the error sources (as the current in a PF coil that is not perfectly circular). The others can be compensated by using the whole set of diamagnetic measurements and suitable compensation formulas.

The many components are considered with their nominal geometry at Operative Temperature (OT) and the affected by the following deviations:

- Static deviations at the flat-top, to characterize the assembly errors and thermal effects;
- Dynamic deviation (including thermal expansion) in normal operation scenarios and during fast transients (e.g. ELMs).

As regards the sensors located on the vacuum vessel, also the thermal expansion and the deformation of the vessel itself are to be considered among the possible deviations occurring [32].

The whole set of error sources and related operational conditions taken in account is here summarized:

1. FERROMAGNETIC INSERTS:
   a. Only TF Coil;
   b. Nominal Flat Top Scenario;
   c. Radial Field without plasma and TF Coil;
   d. Vertical Field without plasma and TF Coil.

2. TEST BLANKET MODULES IRON:
   a. Only TF Coil;
   b. Nominal Flat Top Scenario;
   c. Radial Field without plasma and TF Coil;
   d. Vertical Field without plasma and TF Coil.

3. NBI IRON:
   a. Only TF Coil;
   b. Nominal Flat Top Scenario;
   c. Radial Field without plasma and TF Coil;
   d. Vertical Field without plasma and TF Coil.

4. NON-AXISYMMETRIC COILS:
   a. ELM COILS (single currents,9 dofs in 3 sectors, $f = 0 \, \& \, f \rightarrow \infty$).

5. EDDY CURRENTS:
   a. Disruptions (Major Disruptions, Vertical Displacement Events-UPward, Vertical Displacement Events-DOWNward);
   b. Toroidal Field Discharge;
   c. Control Actions (ELM, L-H Transitions).

6. SINGLE PERTURBATION ON PF, CS & TF COILS:

    a. Tilting;

    b. Ellipticity;

    c. Horizontal Shifts.

7. BUS BARS & FEEDERS:

    a. $f = 0$.

In Tab. II.5, we detail the plasma current and the related plasma flux, the total poloidal and toroidal components of the eddy currents induced into the Vacuum Vessel and the required accuracy for the diamagnetic flux measurement, in the most meaningful instants for each considered scenario:

Tab. II.5: Main data about the Operative Conditions related to the considered transients

Case	I_p [MA]	Φ_p [Vs]	Required accuracy [mVs]	Total Eddy Currents [MA]
BD + Rampup	0 @ 0.783 s 0 @ 0.900 s 0.5 @ 1.296 s 1.0 @ 1.835 s	0 0 0 0.01	10 10 10 10	1.9 (tor) 1.8 (tor) 1.2 (tor) 0.55 (tor)
ELM	15	0.42	117	<0.1 (pol), <0.1 (tor)
VDE up fast cat. II	15 @ 0.6382 s <1 @ 0.6875 s	2.3 ~0	690 60	-1.1 (pol), -12 (tor) 0.49 (pol) , -11 (tor)
VDE down slow cat. III	15 @ 0.683 s <1 @ 1.100 s	3.2 0.3	960 90	-1.6 (pol), 3.4 (tor) 0.38 (pol), -4.9 (tor)
MD UP	15 @ 0.0101 s <1 @ 0.1000 s	2.3 ~0	690 60	-1.0 (pol), 0.75 (tor) 0.40 (pol), -13 (tor)
TFD	-	-	117	9 (pol)

The fast transients are simulated using the CARIDDI code under the main assumptions reported in [27].

2.2.3 Effects of error sources and geometrical imperfections on diamagnetic sensor measurements

2.2.3.a Ideal sensors and electromagnetic sources

We consider the nominal configuration depicted in Tab. II.6 and shown in Fig. II.9:

Tab. II.6: Nominal configuration of the Active Coils (geometry and current)

Coil	R [m]	Z [m]	NI [MAt]	ΔR [m]	ΔZ [m]
CS3U	1.696	5.435	4.0269	0.734	2.12
CS2U	1.696	3.265	-1.2381e+001	0.734	2.12
CS1U	1.696	1.095	-2.2304e+001	0.734	2.12
CS1L	1.696	-1.075	-2.2304e+001	0.734	2.12
CS2L	1.696	-3.245	-1.0468e+001	0.734	2.12
CS3L	1.696	-5.415	5.5449	0.734	2.12
PFC1	3.943	7.574	4.1181	0.959	0.984
PFC2	8.285	6.540	-3.0219	0.580	0.715
PFC3	11.992	3.275	-4.9790	0.696	0.954
PFC4	11.963	-2.234	-4.3668	0.638	0.954
PFC5	8.391	-6.727	-7.3434	0.812	0.954
PFC6	4.334	-7.466	1.5220e+001	1.559	1.107
TFC	-	-	18*9.112	-	-
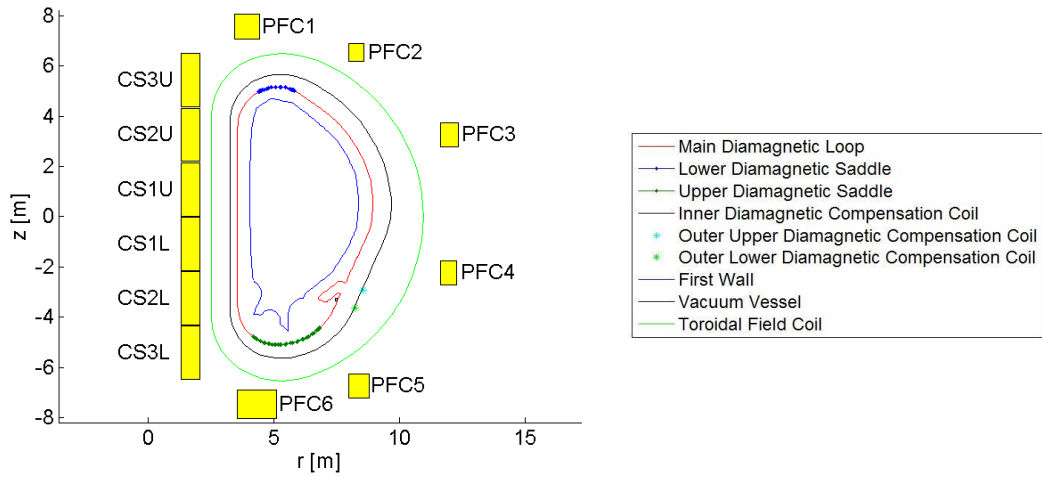
Fig. II.13: Poloidal view of ITER Tokamak diagnostic system, active coils and Vacuum Vessel.

The measurements carried out by the nominal sensors are simulated in Tab. II.7; it is worth noting that these signals can mostly be compensated.

Tab. II.7: Diamagnetic Measurements in ideal configuration (toroidal average)

Sensor	Signal
diamagMainH	255.794 Vs
diamagSadUpH	-0.381 Vs
diamagSadLoH	-1.501 Vs
diaCompInH	4.386 T
diaCompOutUH	3.83 T
diaCompOutLH	4.322 T

2.2.3.b   Effects of non-ideal PF and CS coils

The analysis described in this section is based on the following static 3-D deviations from the nominal geometry:

- 3 *mm* shift along a coordinate axis;
- 5 *mm* ellipticity for PF1, PF2, PF5, PF6, and 7mm ellipticity for PF3 and PF4 along x and y;
- 5 *mm* warping for PF1, PF2, PF5, PF6, and 7mm warping for PF3 and PF4 along z;
- 6 *mm* shift along x and y axis and from 0.5 for linearly to 4mm for CS3U and CS3L along z axis;
- 6 *mm* ellipticity along x and y;
- 4 *mm* warping along z;

In the following, the percentage errors on the estimated signals with respect to the nominal case in Tab. II.7 are reported; note that their toroidal averages are obviously not significant (the largest effects are shown in Tab. II.8), if compared with the local effects (Tab. II.9):

Tab. II.8: Percentage error in sensors signals in the presence of deformed PFCs & CSCs (toroidal averages)

Sensor	Maximum Percentage Error	EM Source Deformed	EM Sources Deformation
Main Diamagnetic Loop	7e-8%	PF1	5 mm warping along z axis
Diamagnetic Saddles	0.05%	CS2	6 mm shift along x axis
Inner Compensation Coils	8e-7%	CS4	6 mm shift along x axis
Outer Compensation Coils	6e-7%	PF1	3 mm shift along y axis

Tab. II.9: Percentage error in sensors signals in the presence of deformed PFCs & CSCs (local effects)

Sensor	Sensor #	Maximum Percentage Error	EM Source Deformed	EM Sources Deformation
Main Diamagnetic Loop	16 deg – Left	0.002%	CS4	6 mm shift along z axis
Diamagnetic Saddles	256 deg – Lower	0.1%	PF6	3mm shift along y axis
Inner Compensation Coils	30 deg – Right	0.004%	PF5	3mm shift along x axis
Outer Compensation Coils	30 deg – #4	0.005%	PF5	3mm shift along x axis

2.2.3.c Effects of non-ideal TF coils

As regards the Toroidal Field Coils, it is worth noticing that they are non-axisymmetric conductors even in nominal geometry, because of the need of the some space along the toroidal direction (e.g. to install the ports necessary to the remote handling and other operations). This forces the TF Coils to be a not toroidally continuous solenoid (in ITER there will be 18 TFCs).

Besides this consideration, the following 3-D deviations from nominal geometry are considered:

- 4 mm shift along all coordinate axis;
- 0.3 $mrad$ rotation around x axis, and 0.6 $mrad$ rotations around y and z axis;
- random deformation (obtained by a 5 mm shift of one control point via spline interpolation).

Apart from the Diamagnetic Saddles, the effect on the signals obtained by the toroidal averages of the diamagnetic measurements is not significant (Tab. II.10) if compared with the local effects (Tab. II.11):

Tab. II.10: Percentage error in sensors signals in the presence of deformed TFCs (toroidal averages)

Sensor	Maximum Percentage Error	EM Source Deformed	EM Sources Deformation
Main Diamagnetic Loop	0.14%	TF1	4 mm shift along y axis
Diamagnetic Saddles	33%	TF2	5mm shift along y axis of the 2nd control point
Inner Compensation Coils	0.045%	TF4	4 mm shift along y axis
Outer Compensation Coils	0.06%	TF2	5 mm shift along z axis of the 4th control point

Tab. II.11: Percentage error in sensors signals in the presence of deformed TFCs (local effects)

Sensor	Sensor #	Maximum Percentage Error	EM Source Deformed	EM Sources Deformation
Main Diamagnetic Loop	16 deg – Right	0.19%	TF1	4 mm shift along y axis
Diamagnetic Saddles	16 deg – Upper	34%	TF2	5mm shift along y axis of the 2nd control point
Inner Compensation Coils	30 deg – Left	0.5%	TF2	5mm shift along y axis of the 4th control point
Outer Compensation Coils	30 deg - #2	2%	TF2	5mm shift along y axis of the 4th control point

2.2.3.d   Effects of non-axisymmetric coils

The effects of the ELM coils (Fig. II.14) on the set of diamagnetic diagnostics is here analysed.
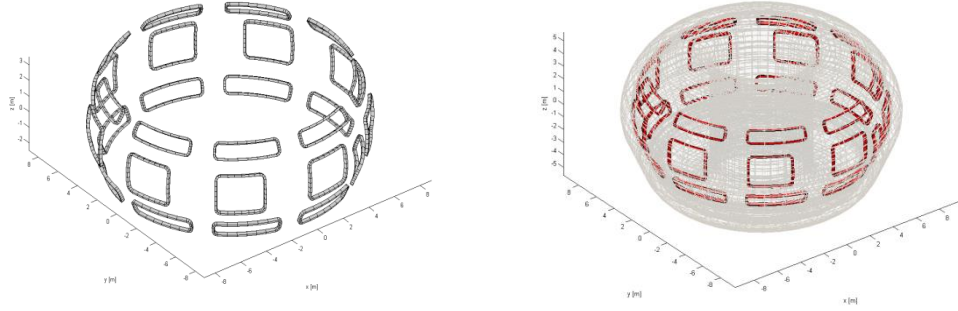
Fig. II.14: ELM coils model for static analysis (left) and model of vessel and ELM coils for the analysis in the presence of eddy currents.

We considered 27 coils (9 upper, 9 lower, and 9 middle ELM coils) and the analyses were carried out feeding one coil at a time with a 15 kA current (this is the current limit per coil); the effects on the toroidal average of the signals coming from the three main diamagnetic loops are shown in Fig. II.15.
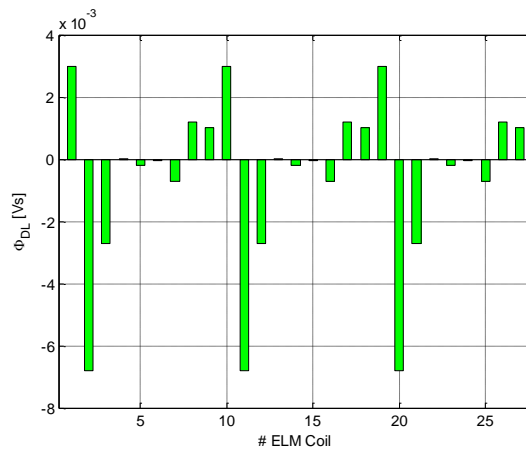
Fig. II.15: Spurious signal of the main diamagnetic loop in presence of a 15 kA current in each ELM coil (toroidal averages)

The worst effect is expected when the coils #2, 11 and 20 (middle ELM coils in the 1st, 4th and 7th sector respectively) are fed, yielding a spurious signal of $-6.8\ mVs$.

This signal is caused by a large influence (about 20 mVs) on the closest loop (at 16 deg) and negligible effects (two orders of magnitude smaller) on the other ones (at 136 deg and 256 deg). When all the coils are fed, the mean value of the signal is 0.6 mVs and the standard deviation is 2.4 mVs.

Fig. II.16 shows the influence of the ELM coils on the diamagnetic saddle loops:

46
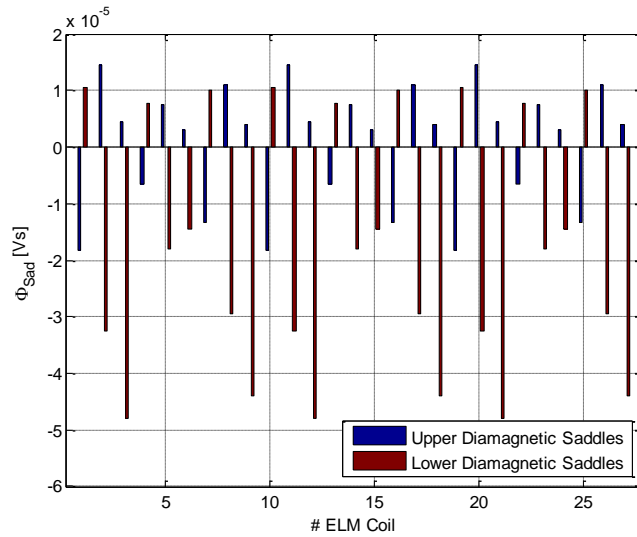
Fig. II.16: Spurious signal of the diamagnetic saddle loops in presence of a 15 kA current in each ELM coil (toroidal averages)

The worst effects are estimated on the lower saddle loops and do not exceed 50 μVs when feeding the coils #3, 12 and 21 (lower ELM coil in the 1st, 4th and 7th sector respectively).

The influence on the diamagnetic compensation coils (both inner and outer) is shown in Fig. II.17.
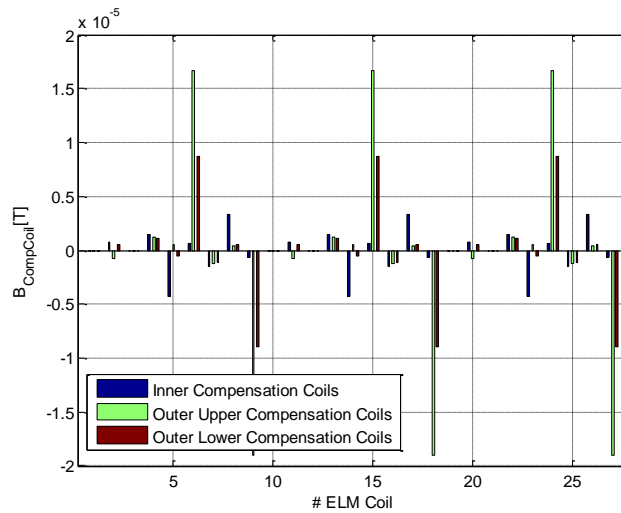
Fig. II.17: Spurious signal of the diamagnetic compensation coils in presence of a 15 kA current in each ELM coil (toroidal averages)

The worst effects are expected on the upper outer diamagnetic compensation coils and do not exceed 20 μT, when coils #6, 9, 15, 18, 24 and 27 (lower coils in the 2nd, 3rd, 5th, 6th, 8th and 9th sectors) are fed. The effect on the

lower outer diamagnetic compensation coils is smaller (not exceeding less than 10 μT), while the influence on the inner diamagnetic compensation coils (less than 5 μT) is even smaller.

During the transient phases the spurious signals are reduced thanks to the effects of the eddy currents flowing into the passive structures, very close both to the sources (the ELM coils) and the sensors (the diamagnetic diagnostics). Fig. II.18 shows that the effects of the eddy currents on the spurious signal of the main diamagnetic loop is beneficial (about 70%), while Fig. II.19 shows the effects on the other diamagnetic diagnostics.
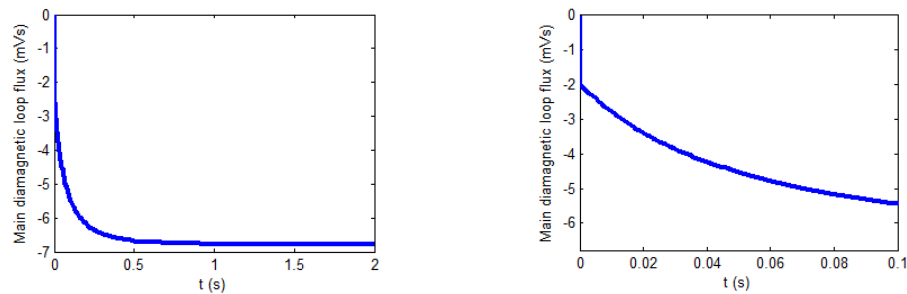
Fig. II.18: Spurious signal of the main diamagnetic loop in the presence of 15 kA step in ELM coil #2 (middle model coil in the first sector): whole transient (left) and zoom in the initial phase (right).
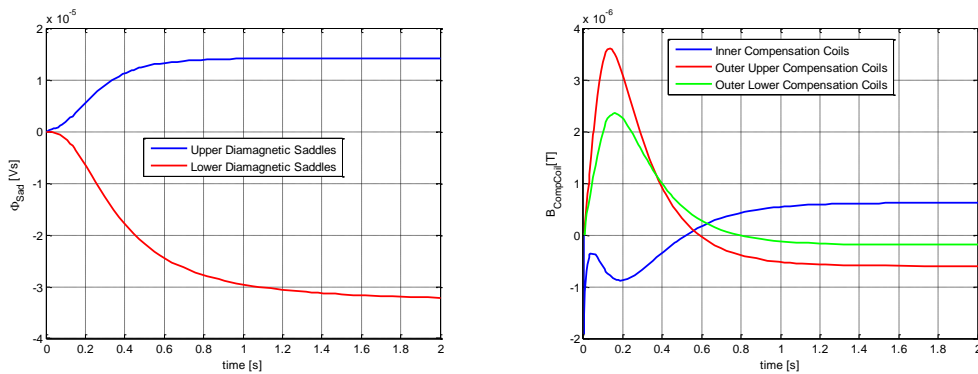
Fig. II.19: Spurious signal of the diamagnetic saddle loops and the diamagnetic compensation coils in the presence of 15 kA step in ELM coil #2 (middle ELM coil in the first sector).

2.2.3.e Effects of feeders

The bus bars and the feeders (Fig. II.20) are the connection between the electrical grid (after the many conversion stages) and the winding packs of the coils of the tokamak and are so aimed to feed them:
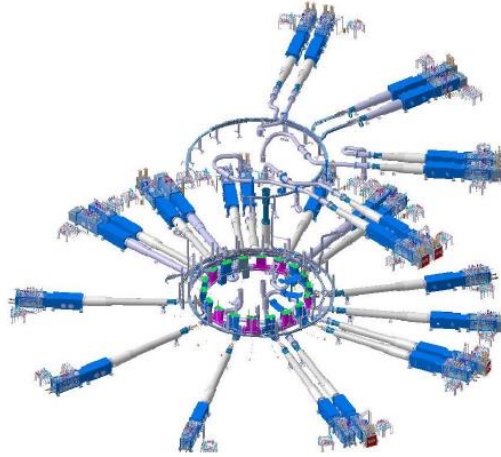
Fig. II.20: Overview of ITER coils feeders systems (Courtesy of ITER Organization)

Their effects on the diamagnetic sensors measurements are very small and are here summarized (toroidal average and local effects):

Tab. II.12: Effect of the feeders on the diamagnetic diagnostics (toroidal average & local effect)

Diamagnetic Sensor	Measured Signal (Toroidal Average)	Measured Signal (Local Effect)
Main Diamagnetic Loops	3.5 mVs	5.8 mVs
Upper Diamagnetic Saddles	-85 µVs	-90 µVs
Lower Diamagnetic Saddles	-1 mVs	-1.1 mVs
Inner Compensation Coils	49 µT	78 µT
Outer Upper Compensation Coils	42 µT	70 µT
Outer Lower Compensation Coils	40 µT	61 µT

2.2.3.f Effects of ferromagnetic inserts, NBI iron and test blanket modules

Three kinds of ferromagnetic materials were considered in the following analysis to evaluate their effect on the diamagnetic diagnostics: ferromagnetic inserts (Fig. II.21a), test blanket modules (Fig. II.21b) and neutral beam injector (Fig. II.21c), operating in the following four configurations:

- FLAT TOP CONFIGURATION: (Standard 15 MA Scenario @296.1 s: $I_p = 15\ MA$, $R_p = 6.19\ m$, $Z_p = 0.498\ m$, $I_{TF} = 68kA$);

- TF COILS ENERGIZED ($68\ kA$) + RADIAL FIELD: (PF3-PF4 energized, yielding $B_r = -0.6\ T$ @ $R = 6.2\ m$);

- ONLY TF COILS ENERGIZED (68 kA):
  - NBI: $\Delta\Phi_{DL} = -93 \div 30 \ \mu Vs, \ \Delta B_\varphi = -44 \div 39 \ \mu T$;
  - FI: $\Delta\Phi_{DL} = -0.25 \ Vs, \ \Delta B_\varphi = -25 \div 26 \ mT$;
  - BLK: $\Delta\Phi_{DL} = 5 \div 112 \ mVs, \ \Delta B_\varphi = -950 \div 400 \ \mu T$;
- TF COILS ENERGIZED (68 kA) + VERTICAL FIELD: (PF3-PF4 energized, yielding $B_z = -0.6 \ T \ @ \ R = 6.2m$).

The following figures show the ferromagnetic components listed above and their effect in terms of flux density field at the points of the diamagnetic diagnostics:
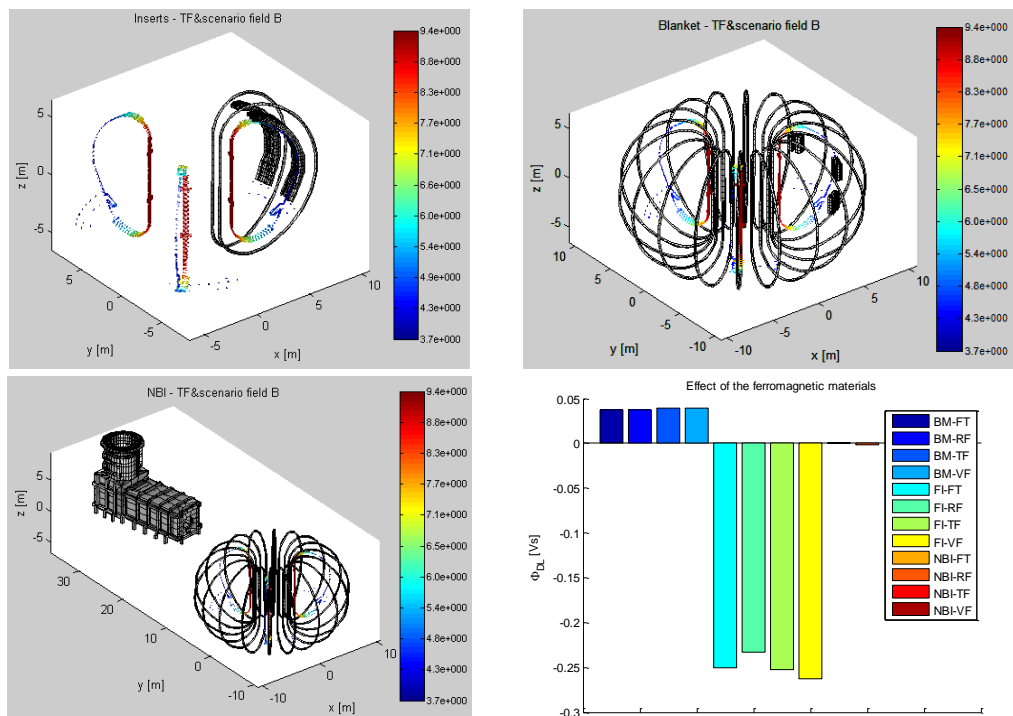
Fig. II.21: Effects of the ferromagnetic inserts (FI, top-left), test blanket modules (BM, top right), Neutron Beam Injector (NBI, down-left) and spurious signal of the main diamagnetic loop in the following operative conditions: flat-top (FT), only TFCs energized (TF), TFCs energized & Radial Field (RF) and TFCs energized & Vertical Field (VF).

Fig. II.21 shows the effects of the ferromagnetic components on the diamagnetic measurements; the largest effect is due to the ferromagnetic inserts (about 250 mVs), while those of NBI are negligible.

However, taking into account that the time integration of the diamagnetic loop voltage starts at the beginning of the pulse, this effect is limited to about

$50\ mVs$, thanks to the effect of the rotation of the magnetization vector when the poloidal field changes.

This effect can be experimentally estimated (with suitable test pulses for CSCs and PFCs pick up and plasma current pick-up at different values of the toroidal field) and then partially compensated for other pulses.

2.2.4   Non-ideal sensors with ideal electromagnetic sources

2.2.4.a   Effects of PF/TF/CS coils

Referring to the nominal configuration described in Section 2.2.3.a, the following variations deformations for the flux sensors (Main Diamagnetic Loops and Diamagnetic Saddles) are considered:

- Var1: 0.1 deg rotation around r axis ($z = 0$);
- Var:2 0.1 deg rotation around z axis ($r = 0$);
- Var3: 0.1 deg rotation around z axis ($r = R_0 = 6\ m$);
- Var4: $0\ deg, 45\ deg, 90\ deg, 135\ deg$ random deformation and spline interpolation;
- Var5: $0\ deg, 45\ deg, 90\ deg, 135\ deg$ random deformation and spline interpolation.

On the other hand, the nominal geometry of the field sensors (Inner Compensation Coils and Outer Lower & Upper Compensation Coils), is perturbed as follows:

- Var1: 1 deg rotation of the normal of the sensor around z axis;
- Var2: 1 deg rotation of the normal of the sensor around r axis;
- Var3: 10 mm variation in radial direction of the position of the sensor;
- Var4: 10 mm variation in vertical direction of the position of the sensor;
- Var5: 1 deg rotation around z axis.

With these classes of deformation, we intend to group all the possible deformations occurring to the sensors because of manufacturing and installation errors, considering their maximum deviations.

The effects on the signals obtained by the toroidal averages of the diamagnetic measurements (Tab. II.13) are not significant if compared with the effects on the single sensors (Tab. II.14):

Tab. II.13: Percentage error in deformed sensors signals (toroidal averages)

Sensor	Maximum Percentage Error	Sensors Deformation
Main Diamagnetic Loop	0.27%	Var. 5
Diamagnetic Saddles	4.8%	Var. 5
Inner Compensation Coils	0.3%	Var.2
Outer Compensation Coils	1.5%	Var. 5

Tab. II.14: Percentage error in deformed sensors signals (local effects)

Sensor	Sensor #	Maximum Percentage Error	Sensors Deformation
Main Diamagnetic Loop	136 deg – Left	0.63%	Var. 5
Diamagnetic Saddles	256 deg – Upper	7.8%	Var. 4
Inner Compensation Coils	150 deg – Left	0.55%	Var. 5
Outer Compensation Coils	30 deg - #1	2.69%	Var. 5

2.2.4.b Effects of the toroidal plasma current

In such analysis, the plasma is modelled as an axisymmetric filamentary current, located at the centroid ($R = 6.2\ m,\ Z = 0.4\ m$), and carrying a $15\ MA$ current.

The following Tab. II.15 shows that the largest effect on the main diamagnetic loop is about $26\ mVs$ for a $0.1\ deg$ tilt of the loop around the z-axis; the measurement is slightly affected by the position of the plasma current centroid, as the main diamagnetic loop signal variation changes by $20\ mVs/m$ along r and $2\ mVs/m$ along z.

Tab. II.15: Effects of a 15 *MA* filamentary plasma located at the plasma centroid with ideal and non-ideal diamagnetic sensors

Case	Ideal	Var1	Var2	Var3	Var4	Var5
Main Diamagnetic Loops [Vs]	-9.8E-12	-0.02622	-3.8E-07	-3E-08	-0.00238	0.004039
Upper Diamagnetic Saddles [Vs]	0.209647	0.209647	0.209647	0.209111	0.210378	0.209661
Lower Diamagnetic Saddles [Vs]	0.630263	0.630602	0.630263	0.629523	0.627304	0.632257
Inner Compensation Coils [T]	-7.1E-12	0.00902	0.001804	-7E-12	-7.1E-12	-0.00902
Outer Upper Compensation Coils [T]	-5E-12	0.007057	-0.00088	-5E-12	-5E-12	-0.00706
Outer Lower Compensation Coils [T]	-4.5E-12	0.00676	0.000568	-4.5E-12	-4.6E-12	-0.00676

Tab. II.15 also shows that the largest effect on the inner diamagnetic compensation coils is about 9 mT for a tilt of 1 deg of the pick-up coil around the z axis (and slightly less, about 7 mT, for the outer compensation coils). Also this quantity also affected by the position of the plasma current centroid (the signal increases by 2.7 mT/m along R axis and decreases by the same quantity along Z axis).

It is worth noticing that the toroidal plasma current pick up can be experimentally measured (and then at least partially compensated for the other pulses) with two similar plasmas with opposite helicity.

2.2.4.c Thermal expansion of the main diamagnetic loop

During the operations, the temperature in the Vacuum Vessel increases yielding a thermal expansion of the main components, as shown in Fig. II.22. When the assessment of the thermal transient occurs, the temperature of the diamagnetic sensors increases from 37 °C (Room Temperature - RT) to 103 °C (Operating Temperature - OT).
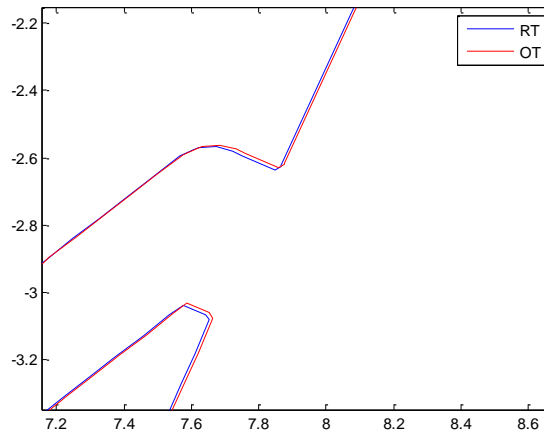
Fig. II.22: Effect of the thermal expansion on the main diamagnetic loop (particular of the Outer Triangular Support)

This phenomenon produces a linear expansion of 0.136% on the diamagnetic loop cross-section that yields a spurious signal of $360\ mVs$ in nominal conditions.

2.2.5 Combined effects of non-ideal sensors with non-ideal electromagnetic sources

At last, a combined deformation effect of both the electromagnetic sources (see Sections 2.2.3.b and 2.2.3.c) and of the sensors (see Section 2.2.4) is considered, to take into account a more realistic situation where both the sources and the sensors are affected by manufacturing and installation errors.

As expected, the effects on the signals obtained by the toroidal averages of the diamagnetic measurements are not significant with respect to the local effects on the single sensors. The following Tab. II.16 and Tab. II.17 show the largest effects due to CS and PF Coils deformations on the deformed diamagnetic sensors:

Tab. II.16: Percentage error in deformed sensors signals in the presence of deformed PFCs & CSCs (toroidal averages)

Sensor	Maximum Percentage Error	EM Source Deformed	EM Sources Deformation	Sensors Deformation
Main Diamagnetic Loop	0.27%	PF6	6 mm ellipticity deformation along x axis	Var. 5
Diamagnetic Saddles	4.88%	CS1	6 mm shift deformation along x axis	Var. 5
Inner Compensation Coils	0.31%	PF4	7mm warping deformation along z axis	Var. 2
Outer Compensation Coils	1.5%	PF5	3mm shift deformation along y axis	Var. 5

Tab. II.17: Percentage error in deformed sensors signals in the presence of deformed PFCs & CSCs (local effects)

Sensor	Sensor #	Maximum Percentage Error	EM Source Deformed	EM Sources Deformation	Sensors Deformation
Main Diamagnetic Loop	136 deg – Left	0.63%	CS3	6 mm shift deformation along y axis	Var. 5
Diamagnetic Saddles	256 deg – Upper	7.8%	CS2	6 mm shift deformation along x axis	Var. 4
Inner Compensation Coils	150 deg – Left	0.55%	PF4	7 mm warping deformation along z axis	Var. 5
Outer Compensation Coils	30 deg - #1	2.69%	PF5	5 mm ellipticity deformation along x axis	Var. 5

As for the ideal sensors case, the effect on the signals obtained by the toroidal averages of the diamagnetic measurements (main diamagnetic loops, inner compensation coils and outer compensation coils) is not significant when the TFCs deformations are considered.

The largest effects on the toroidal averages (Tab. II.18) and local effects (Tab. II.19) of the signals are summarized hereafter:

Tab. II.18: Percentage error in deformed sensors signals in the presence of deformed TFCs (toroidal averages)

Sensor	Maximum Percentage Error	EM Source Deformed	EM Sources Deformation	Sensors Deformation
Main Diamagnetic Loop	0.43%	TF1	4 mm shift deformation along x axis	Var. 5
Diamagnetic Saddles	39.76%	TF2	5 mm shift deformation along x axis of the 2nd control point	Var. 5
Inner Compensation Coils	0.17%	TF4	4 mm shift deformation along x axis	Var. 3
Outer Compensation Coils	0.14%	TF2	5 mm shift deformation along z axis of the 3rd control point	Var. 5

Tab. II.19: Percentage error in deformed sensors signals in the presence of deformed TFCs (local effects)

Sensor	Sensor #	Maximum Percentage Error	EM Source Deformed	EM Sources Deformation	Sensors Deformation
Main Diamagnetic Loop	136 deg – Right	0.84%	TF6	4 mm shift deformation along x axis	Var. 5
Diamagnetic Saddles	256 deg – Upper	41.37%	TF5	5 mm shift deformation along x axis of the sixth control point	Var. 5
Inner Compensation Coils	30 deg – Left	0.64%	TF5	5 mm shift deformation along x axis of the sixth control point	Var. 3
Outer Compensation Coils	30 deg - #1	2.94%	TF2	5 mm shift deformation along x axis of the forth control point	Var. 5

2.2.6 Compensation formulas

The flux linked with the main diamagnetic loop does not consist of the only toroidal flux of the plasma, but it is affected by many polluting terms as depicted in Sections 2.2.3, 2.2.4 and 2.2.5. For this reason, a compensation system is necessary to extract the only flux quantity related to plasma diamagnetism, so to

prevent a wrong measurement of the diamagnetic flux and a consequent wrong estimation of the poloidal beta.

The flux linked with the mail diamagnetic loop is the sum of the following terms:

$$\Phi_{DL} = \Phi_p + \Phi_{TF} + \Phi_{TF_{Tilt}} + \Phi_{TF_{Exp}} + \Phi_{EC} + \Phi_{PF} + \Phi_{PF_{Tilt}} + +\Phi_{I_p} \\ +\Phi_{Iron} + \Phi_{Other}$$ (II.13)

where:

- Φ_{DL} is the flux linked with the main diamagnetic loop;
- Φ_P is the plasma diamagnetic flux;
- Φ_{TF} is the flux generated by the TFCs;
- $\Phi_{Tilt_{TF}}$ is the flux generated by the tilt of the TFC;
- $\Phi_{Exp_{TF}}$ is the flux generated by the TFCs (Thermal & Electromagnetic) expansion;
- Φ_{EC} is the flux generated by the eddy currents flowing into the vacuum vessel;
- Φ_{PF} is the flux generated by the PFCs deformation;
- $\Phi_{Exp_{PF}}$ is the flux generated by the PFCs (Thermal & Electromagnetic) Expansion;
- Φ_{I_p} is the flux generated by the plasma current pick-up;
- Φ_{Iron} is the flux generated by the iron pick-up;
- Φ_{Other} is the flux generated by other coils pick-up (e.g. bus bars and feeders).

The plasma diamagnetic flux can be derived from equation (II.13) while the other terms can be related to other physical quantities (e.g. the currents in the poloidal and toroidal field coils or the plasma current and the eddy currents in the passive structures) and to the measurements of the compensation sensors, as follows:

$$\Phi_{DL} = \int V_{DL} dt$$ (II.14)

$$\Phi_{TF_{Tilt}} = k_{saddle}^T \Phi_{saddle}$$ (II.15)

$$\Phi_{TF} = M_{pol\_TF} I_{TF}$$ (II.16)

$$\Phi_{EC} = k_0^T \Phi_{OutComp} - k_I^T \Phi_{InComp}$$ (II.17)

$$\Phi_{TF_{Exp}} = \alpha_{TF} I_{TF}^3 \qquad \text{(II.18)}$$

$$\Phi_{I_p} = k_{pol}^T B_{pol} \qquad \text{(II.19)}$$

$$\Phi_{PF_{Exp}} = k_{PF}^T I_{TF} \qquad \text{(II.20)}$$

where:

- V_{DL} is the voltage measured at the diamagnetic loop terminals;
- Φ_{Saddle}, $\Phi_{OutComp}$ and Φ_{InComp} are the values of measurements carried out by the diamagnetic saddles, the outer compensation coils and the inner compensation coils, respectively;
- I_{TF} and I_{PF} are the flowing into the Toroidal Field Coils and the Poloidal Field Coils respectively;
- M_{pol_TF} is the mutual inductances between the Poloidal Field Coils and the main diamagnetic loops;
- I_p is the plasma current;
- B_{pol} is the set of poloidal field measurements in the vicinity of the main diamagnetic loop;
- k_{Saddle}^T, k_O^T, k_I^T, k_{pol}^T, k_{PF}^T are proportional coefficients, determined via pseudoinversion using models or experimental data.

It is worth noticing that:

- in (II.14) the integration drift and the pick-up of connection cables are not considered;
- a similar treatment for other coils (e.g. bus bars, feeders, cables) could be adopted as for the Toroidal Field Coils in (II.16);
- the expression (II.17) is preferred to $\Phi_{EC} = \tau_{VV} \frac{d\Phi_{DL}}{dt}$, adopted in the JET reactor (see section 2.2.6.a), where τ_{VV} the Vacuum Vessel electromagnetic time constant;
- in (II.19) the value of the coefficient vector $k^T{}_{pol}$ can be computed from correlations between the poloidal pick-up coil signals and the measure carried out by the main diamagnetic loop;

- the ferromagnetic materials pick-up can be approximated by an offset (it can be cancelled by time-integration of the diamagnetic loop voltage) and a time linear term (it can be treated using a similar expression to (II.19));
- In (II.20) the value of the coefficient vector $k^T{}_{PF}$ can be computed from correlations with dry-runs.

An alternative way to estimate the plasma diamagnetic flux is based on the use of the TF coils; being them magnetically coupled with the plasma, the voltage measured at their terminals consists of the following terms:

$$U_{TF} = R_{TF}I_{TF} + L_{TF}\frac{dI_{TF}}{dt} + M_{TF\_VV}\frac{dI_{Eddy}}{dt} + N_{TF}\frac{d\Phi_p}{dt} \qquad (II.21)$$

where:

- U_{TF} is the applied voltage;
- R_{TF} is the TF Coils resistance (negligible, being them superconductive coils);
- L_{TF} is the TF Coils self-inductance;
- I_{VV} the vacuum vessel current;
- M_{TF_VV} the mutual inductance between the TF Coils and the Vacuum Vessel;
- N_{TF} is the number of turns.

Therefore, the flux Φ_p can be estimated by using the TF Coils like sensors, as follows:

$$\Phi_p = \frac{1}{N_{TF}}\int\left(U_{TF} - L_{TF}\frac{dI_{TF}}{dt} - M_{TF\_VV}\frac{dI_{Eddy}}{dt}\right)dt \qquad (II.22)$$

2.2.6.a   Selection of the compensation formula for the study

The reason of choosing the equation (II.17) instead of the one used for JET tokamak [33] is based on the non-compliance of the hypothesis of the Nyquist-Shannon theorem as regards the poloidal beta sampling time and of the accuracy requirements [23]-[28]-[33].
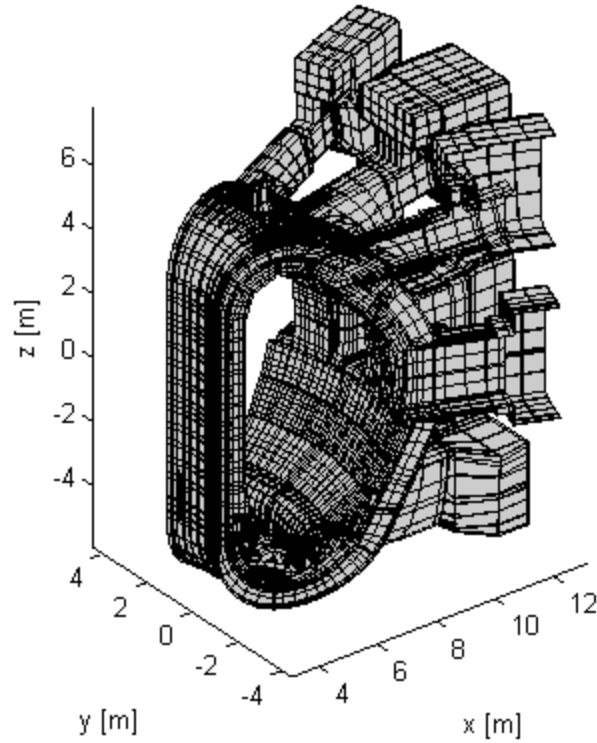
Fig. II.23: ITER mesh of a 20 *deg* sector

Fig. II.23 shows the two vacuum vessel of ITER tokamak for a 20 deg section; it is possible to see that it consists of two shells, which are magnetically coupled with the plasma. Therefore, the flux measured by the main diamagnetic loop is affected also by the currents flowing into the two shells, as follows:

$$\begin{cases} L_{in}\dot{I}_{in} + M_{in-out}\dot{I}_{out} + R_{in}I_{in} = -\dot{\Phi}_p \\ M_{out-in}\dot{I}_{in} + L_{out}\dot{I}_{out} + R_{out}I_{out} = -\dot{\Phi}_p \\ \Phi_{DL} = M_{DL}(I_{in} + I_{out}) + \Phi_p \end{cases} \qquad \text{(II.23)}$$

where

- L_{in} (L_{out}) is the inner (outer) shell self-inductance
- $M_{in-out} = M_{out-in}$ is the mutual inductance between the two shells;
- R_{in} (R_{out}) is the inner (outer) resistance;
- I_{in} (I_{out}) is the current flowing into the inner (outer) shell;
- M_{DL} is the mutual inductance between the Main Diamagnetic Loop and the shells;
- Φ_p is the plasma flux;
- Φ_{DL} is the flux linked with the Main Diamagnetic Loop.

Introducing the matrix notation, equation (II.23) can becomes:

$$\begin{cases} \underline{\dot{I}}_{vv} = -\left(\underline{\underline{L}}_{vv}^{-1} \cdot \underline{\underline{R}}_{vv}\right) \cdot \underline{I}_{vv} - \underline{\underline{L}}_{vv}^{-1} \cdot \underline{\dot{\Phi}}_p \\ \Phi_{DL} = \underline{\underline{M}}_{DL} \cdot \underline{I}_{vv} + \Phi_p \end{cases} \qquad \text{(II.24)}$$

with:

$$\begin{aligned} \underline{\underline{L}}_{vv} &= \begin{bmatrix} L_{in} & M_{in-out} \\ M_{out-in} & L_{out} \end{bmatrix} \\ \underline{\underline{R}}_{vv} &= \begin{bmatrix} R_{in} & 0 \\ 0 & R_{out} \end{bmatrix} \\ \underline{\underline{M}}_{DL} &= \begin{bmatrix} M_{DL} & M_{DL} \end{bmatrix} \\ \underline{I}_{VV} &= \begin{bmatrix} I_{in} \\ I_{out} \end{bmatrix} \\ \underline{\dot{\Phi}}_p &= \begin{bmatrix} \dot{\Phi}_p \\ \dot{\Phi}_p \end{bmatrix} \end{aligned} \qquad \text{(II.25)}$$

The evaluation of the entries of the matrices is carried out by considering that the shells thickness is $\delta = 60\ mm$ and the resistivity at $100\ °C$ temperature is $\eta = 0.8\dfrac{\mu\Omega}{m}$:

$$L_{shell} = \frac{\Phi_{shell}}{I_{TF}} = \frac{B_\phi \cdot \pi a^2 k}{\dfrac{B_\phi \cdot 2\pi R_0}{\mu_0}} \qquad R_{shell} = \eta \frac{2\pi a \sqrt{k}}{2\pi R_0 \cdot 2\delta} \qquad \text{(II.26)}$$

where:

- a is the minor radius;
- R_0 is the major radius;
- k is the vertical elongation.

Therefore, the time constant of the system is $\tau = 0.295s$, obtained from the dynamic matrix $(A = -\underline{\underline{L}}_{vv}^{-1} \cdot \underline{\underline{R}}_{vv})$:

This analytical model is hereafter validated, by comparing it with a simplified model with a Vacuum Vessel consisting only of one shell, whose inductance is the average value of the two shells self-inductance and whose resistance is equivalent to the two shells parallel-resistance:

$$\begin{cases} \underline{\dot{I}}_{vv} = -\dfrac{R_{vv}}{L_{vv}} \cdot \underline{I}_{vv} - \dfrac{1}{L_{vv}} \cdot \dot{\Phi}_p \\ \Phi_{DL} = M_{DL} \cdot I_{vv} + \Phi_p \end{cases} \qquad \text{(II.27)}$$

The time constant is $\tau = 0.306s$, thus agreeing with that of the two shells model.

At last, a further numerical experiment for the evaluation of the time constant was set up. As shown in the second equation of (II.24), the flux liked

with the main diamagnetic loop is the sum of the contribution of the flux generated by the currents flowing into the shells and the plasma flux, that is related to the current flowing into the TFCs (so controllable).

Being the time constant about 300 ms, the current into the TFCs is driven with a triangular wave whose rise-time and fall-time are long enough to let the transient to end (about 5 s each) and whose peak-value is unitary. The evaluation of the flux linked with the main diamagnetic loop can be carried out by evaluating the voltage at its terminals both at half of the rise and fall time.

The average value of the these values does not include that of the TFCs, being symmetrical with respect to the time instant when the Toroidal Field Coils current reverse its time derivative. Therefore, the only quantity related to the eddy currents flowing into the vacuum vessel can be estimated.

The electromagnetic time constant of the system can be calculated as the ratio between the voltage at the sensor's terminals and the flux linked with it. The value obtained from this procedure is $\tau = 0.304\ s$, agreeing with the values calculated with the analytical models.

Therefore, the vacuum vessel acts like a low-pass filter having the time constant about of 300 ms and so cut-off frequency about of 5 Hz; since the sampling time for the poloidal beta β_{pol} ranges from 100 μs to 1 ms (the sampling rate ranges from 1 kHz to 100 kHz), the hypothesis required in Nyquist-Shannon Theorem are not fulfilled.

For this reason, a new type of compensation formula; as the compensation system consists of coils located inside and outside the vacuum vessel, their measurements can be used to extract the flux linked with the main diamagnetic loop due to the eddy currents as follows:

$$\Phi_{EC} = \frac{2\pi}{\mu_0} M_{DL}(R_{in}B_{in} - R_{out}B_{out}) = c^T \cdot \left[B_{in}, B_{out_{up}}, B_{out_{low}}\right] \qquad \text{(II.28)}$$

where:

- μ_0 is the vacuum magnetic permeability;
- M_{DL} is the mutual inductance between diamagnetic loop and the Vacuum Vessel;
- R_{in} and R_{out} are the radial coordinates of the compensation coils;

- B_{in}, $B_{out_{up}}$ and $B_{out_{low}}$ are the pick-up coils measurements;
- c is the set of coefficients.

It is worth noticing that the centre side of equation (II.28) is based on the 2-D axisymmetric assumption, whereas its right side is a generalization to the 3-D case.

Three sets of compensation coefficients were tested and listed below:

Tab. II.20: Compensation Coefficients for Poloidal Eddy Currents Compensation

	R_{in}	R_{out_up}	R_{out_low}
c_1 [m²]	-58.4	67.7	0
c_2 [m²]	-58.4	0	64.3
c_{3d} [m²]	-49.1	56.1	0

where: $M_{DL} = 1.56\,\mu H$, $R_{in} = 7.49\,m$, $R_{out_{up}} = 8.65\,m$ and $R_{out_{low}} = 8.25\,m$. The first triple of coefficients exploits the outer upper compensation coils set (three sets of eight sensors each), the second one uses the outer lower compensation coils set (three sets of four sensors each) whilst the third set uses the outer upper compensation coils set, but takes into account the local 3-D effects (mainly ports) on the signal measured by the inner compensation coils and rescales the signals on the outer sensors.

For this reason, the c_1 and c_2 vectors are calculated with the center side of equation (II.28) whereas the c_3 vector is calculated via pseudo-inversion using both the model and the experimental data.

The compensation formulas were tested and validated for many discharges and hereafter the results obtained on a Major Disruption Upward with Toroidal Field Variation (MD_UP_TFV) and a Vertical Displacement Event Downward with Toroidal Field Variation (VDE_DOWN_TFV) are reported:
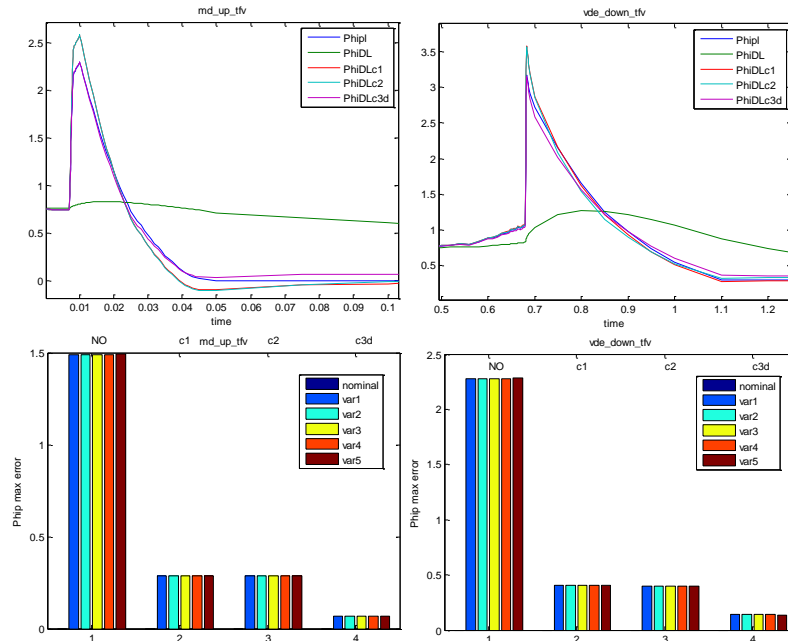
Fig. II.24: Effects of the Compensation formulas with ideal sensors (top: reconstruction of plasma flux time evolution; bottom: maximum errors on plasma flux reconstruction)

In case of ideal sensors there is a very good reconstruction of the plasma flux, but there are significant effects due to the Poloidal Field Variations on both the inner and outer compensation coils, if they are misaligned:
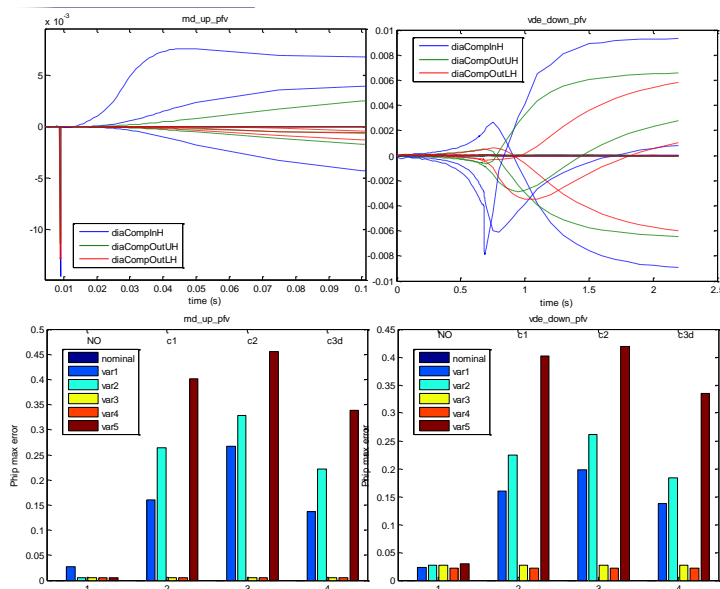
Fig. II.25: Effects of the Compensation formulas with misaligned sensors (up: reconstruction of plasma flux time evolution; down: maximum errors on plasma flux reconstruction)

As regards the fast TF coil discharge, Fig. II.26 shows that the formulas based on the outer upper compensation coils work better (more details are

visible in Fig. II.27). The eddy current contribution is about 13.5 Vs in the fast transient due to Toroidal Field Coils current quench (18 Vs due to the external TF source in 200 ms), and the compensation formulas based on the inner and upper outer compensation coils provide good estimations (within an error of 220 mVs).
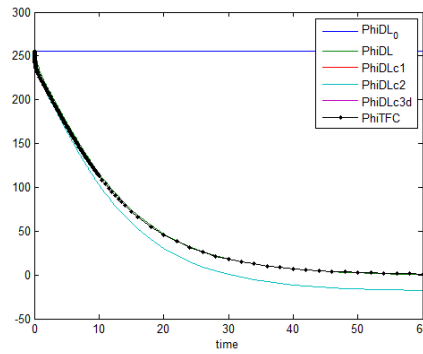
Fig. II.26: The flux linked with the Main Diamagnetic Loop during the Fast TF coil discharge, PhiDL, is compared to the TF coil flux PhiTFC, to the initial flux PhiDL0, and to the three compensated signals PhiDLc1, PhiDLc2 and PhiDLc3d.
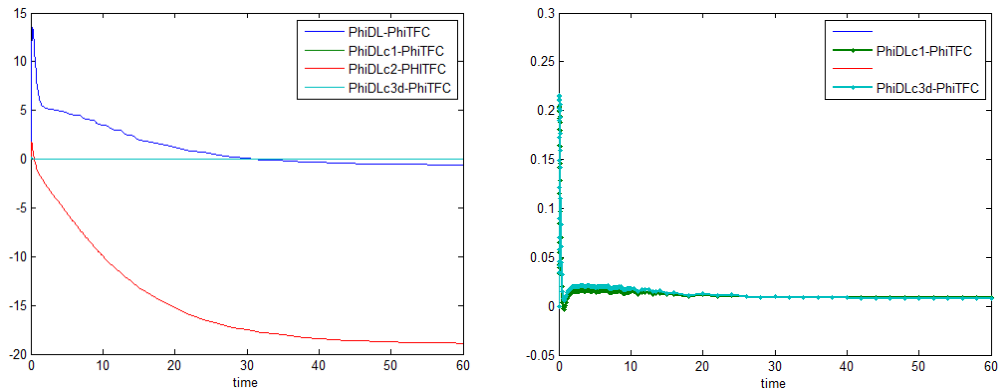
Fig. II.27: The eddy current contribution PhiDL-PhiTFC during the Fast TF coil discharge is compared with the difference from the compensated signals and the flux directly linked to the TF coil currents (zoom into the right figure of the compensation formulas using the outer upper compensation coils).

2.2.7 Application of the Compensation Formulas to mitigate the effects of error sources and geometrical imperfections on diamagnetic sensor measurements

2.2.7.a Ideal sensors and electromagnetic sources in presence of eddy currents

After the validation of the proposed compensation formulas (see Section 2.2.6.a), they were used in many transients, in case of ideal sensors and ideal electromagnetic sources. Tab. II.21 shows the results for each of them:

Tab. II.21: Application of the compensation formulas during the transients with ideal sensors

Case	I_p [MA]	Φ_p [Vs]	Required accuracy [mVs]	Max. error without/with compensation [mVs]
BD + Rampup	0 @ 0.783 s	0	10	<1/<1
	0 @ 0.900 s	0	10	<1/<1
	0.5 @ 1.296 s	0	10	<1/<1
	1.0 @ 1.835 s	0.01	10	<1/<1
ELM	15	420	117	30/3
	15		117	
VDEup fast cat. II	15 @ 0.6382 s	2.3	690	1600/21
	<1 @ 0.6875 s	~0	60	720/46
VDEdown slow cat. III	15 @ 0.683 s	3.2	960	2300/140
	<1 @ 1.100 s	0.3	90	600/80
MD UP	15 @ 0.0101 s	2.3	690	1500/10
	<1 @ 0.1000 s	~0	60	700/70
TFD	-	-	-	13500/220

The effect of the compensation formulas is crucially beneficial in all the transients, apart from plasma breakdown and rump-up and ELM transients where the accuracy requirements are met also without compensation. In the other cases, they are met by compensating the largest part of the polluting signal, mostly due to the toroidal field variation, that is the poloidal currents.

2.2.7.b Non- ideal sensors with ideal EM sources

Tab. II.22 reports the combined effects on the main diamagnetic loop due to the geometrical deviation from the nominal design (tilt, displacement, deformation -2σ-, being σ the standard deviation of the deformation) and to eddy currents:

Tab. II.22: Combined main DL tilt/displacement/deformation (2σ) and eddy current effects

Case	I_p [MA]	Φ_p [Vs]	Req. accuracy [mVs]	$2\sigma =$ $0.1\,deg$ horizontal tilt [mVs]	$2\sigma =$ $0.1\,deg$ vertical tilt [mVs]	$2\sigma =$ $1\,cm$ radial shift [mVs]	$2\sigma =$ $1\,cm$ random deform. [mVs]
BD + Rampup	0 @ 0.783 s	0	10	0.26	~0	0.01	0.44
	0 @ 0.900 s	0	10	0.40	~0	0.01	0.48
	0.5 @ 1.296 s	0	10	0.99	~0	0.01	0.33
	1.0 @ 1.835 s	0.01	10	1.10	0.03	0.03	0.24
ELM	15	420	117	2	2	2	2
VDEup fast cat. II	15 @ 0.6382 s	2.3	690	2.79	0.25	1.41	8.5
	<1 @ 0.6875 s	~0	60	3.42	0.09	0.61	7.7
VDEdown slow cat. III	15 @ 0.683 s	3.2	960	1.12	0.37	2.01	10
	<1 @ 1.100 s	0.3	90	4.31	0.04	0.55	15
MD UP	15 @ 0.0101 s	2.3	690	0.17	0.26	1.30	5.1
	<1 @ 0.1000 s	~0	60	2.20	0.04	0.56	4.5

This analysis clearly shows that:

- the horizontal tilt is more sensitive to the poloidal field (toroidal currents), for instance during the breakdown, the rump-up and the current quench;
- the vertical tilt and the radial shift are more sensitive to the toroidal field (poloidal currents), for instance during the ELM and the thermal quench.

Moreover, the accuracy requirements are met without using the compensation system, during the phases when the significant component of the eddy currents is toroidal (e.g., breakdown & ramp-up). On the contrary, they are met by using the compensation formulas during the fast disruptions, supposing that the compensation coil misalignment is (or can be estimated) within $0.2\,deg$.

Finally, the same analysis is carried out for thermal expansion, noise and integration drift (Tab. II.23) and for various effects, as the combination of the tilt of the sensors with the eddy current effect (Tab. II.24 & Tab. II.25):

Tab. II.23: Effects of thermal expansion, noise and integration drift on the Main Diamagnetic Loop

Case	I_p [MA]	Φ_p [Vs]	Required accuracy [mVs]	Thermal expansion RT→OT [mVs]	Noise 2σ [mVs]	Integration drift 2σ [mVs]
BD + Rampup	0 @ 0.783 s 0 @ 0.900 s 0.5 @ 1.296 s 1.0 @ 1.835 s	0 0 0 0.01	10 10 10 10	360	~0 ~0 0.2 0.4	~0
VDEup fast cat. II	15 @ 0.6382 s <1 @ 0.6875 s	2.3 ~0	690 60	360	4.3	0.2
VDEdown slow cat. III	15 @ 0.683 s <1 @ 1.100 s	3.2 0.3	960 90	360	4.8	0.2
MD UP	15 @ 0.0101 s <1 @ 0.1000 s	2.3 ~0	690 60	360	4.1	0.2

Note that the thermal expansion additional flux can be compensated by monitoring the temperature at each pulse.

Tab. II.24: Various effects on the Main Diamagnetic Loop 1/2

Case	I_p [MA]	Φ_p [Vs]	Required accurracy [mVs]	Ideal sensors [mVs]	Noise & integration drift [mVs]	Main DL tilt + eddy [mVs]	Inner coil tilt + eddy [mVs]
BD + Rampup	0 @ 0.783 s 0 @ 0.900 s 0.5 @ 1.296 s 1.0 @ 1.835 s	0 0 0 0.01	10 10 10 10	0 0 0 0	0 0 0.2 0.4	1 1.1 1.3 1.3	5 5 13 22
ELM	15 15	420	117 117	3	4	2	2
VDEup fast cat. II	15 @ 0.6382 s <1 @ 0.6875 s	2.3 ~0	690 60	21 46	4.3 4.3	9 8	216 233
VDEdown slow cat. III	15 @ 0.683 s <1 @ 1.100 s	3.2 0.3	960 90	140 80	4.8 4.8	10 16	185 191
MD UP	15 @ 0.0101 s <1 @ 0.1000 s	2.3 ~0	690 60	10 70	4.1 4.1	5 5	2 213

Tab. II.25: Various effects on the Main Diamagnetic Loop 2/2

Case	I_p [MA]	Φ_p [Vs]	Required accuracy [mVs]	Ideal sensors [mVs]	OuterUp coil tilt + eddy [mVs]	Inner coil noise [mVs]	OuterUp coil noise [mVs]
BD + Rampup	0 @ 0.783 s 0 @ 0.900 s 0.5 @ 1.296 s 1.0 @ 1.835 s	0 0 0 0.01	10 10 10 10	0 0 0 0	8 9 11 12	29 29 29 29	16 16 16 16
ELM	15 15	420	117 117	3	2	29	16
VDEup fast cat. II	15 @ 0.6382 s <1 @ 0.6875 s	2.3 ~0	690 60	21 46	63 74	29 29	16 16
VDEdown slow cat. III	15 @ 0.683 s <1 @ 1.100 s	3.2 0.3	960 90	140 80	15 86	29 29	16 16
MD UP	15 @ 0.0101 s <1 @ 0.1000 s	2.3 ~0	690 60	10 70	0.1 42	29 29	16 16

2.2.8 Estimation of the Poloidal beta via Diamagnetic Diagnostics

For a given thermonuclear plasma, the *Poloidal Beta* is defined as the ratio between the average plasma's kinetic pressure and the average poloidal magnetic pressure:

$$\beta_p = \frac{\iiint_{V_p} p\, dV}{\iiint_{V_p} \frac{B_{pa}^2}{2\mu_0}\, dV} \tag{II.29}$$

where:

- V_p is the plasma volume;
- B_{pa} is the average value of the poloidal magnetic flux density field (different ways to calculate this parameters lead to different definitions of the poloidal beta).

The average value considered for the following analysis is based on that used in $EFIT^{++}$ [34]-[35]-[36]:

$$B_{pa} = \frac{\oint_{\Gamma_p} B_p \cdot dl}{\oint_{\Gamma_p} dl} \tag{II.30}$$

where Γ_p is the plasma boundary, that is the intersection of ∂V_p with the poloidal plane.

In anisotropic plasmas it is possible to define two components of the poloidal beta associated to the perpendicular $(\beta_{p\perp})$ and parallel $(\beta_{p\parallel})$ pressure, respectively. The poloidal beta is then related to these two components as follows [37]:

$$\beta_p = \frac{2\beta_{p\perp} + \beta_{p\parallel}}{3} \tag{II.31}$$

Let us introduce the following quantities:

$$l_i = \frac{\iiint_{V_p} B_p^2\, dV}{\iiint_{V_p} dV \frac{B_{pa}^2}{2\mu_0}} \tag{II.32}$$

$$\Lambda = \frac{1}{2}\left(\beta_{p\perp} + \beta_{p\parallel}\right) + W_{pt} + \frac{l_i}{2} \tag{II.33}$$

$$\mu_i = \frac{1}{B_{pa}^2 \iiint_{V_p} dV} \iiint_{V_p} (B_{\varphi_0}^2 - B_\varphi^2) dV \tag{II.34}$$

where:

- l_i is the plasma internal inductance (or inductance per unit length);
- μ_i is called diamagnetic parameter.
- Λ is the coefficient of asymmetry of the poloidal field;
- W_{pt} is the energy density associated with the plasma mass motion in the toroidal direction;
- B_φ is the toroidal magnetic flux density field;
- B_{φ_0} is the toroidal magnetic flux density field without the plasma contribution.

Introducing the Shafranov integrals [38], defined as follows:

$$S_1 = \frac{1}{B_{pa}^2 \int_{V_p} dV} \oiint_{\partial V_p} [B_p^2((r - R_0)\boldsymbol{i_r} + z\boldsymbol{i_z})] \cdot \boldsymbol{n} dS \tag{II.35}$$

$$S_2 = \frac{R_0}{B_{pa}^2 \int_{V_p} dV} \oiint_{\partial V_p} B_p^2 \boldsymbol{i_r} \cdot \boldsymbol{n} dS \tag{II.36}$$

$$S_3 = \frac{1}{B_{pa}^2 \iiint_{V_p} dV} \oiint_{\partial V_p} [B_p^2 z \boldsymbol{i_z}] \cdot \boldsymbol{n} dS \tag{II.37}$$

it is possible to rewrite the parameters in (II.32), (II.33) and (II.34), as follows:

$$l_i = \frac{1}{\alpha - 1} \left[0.5 S_1 + 0.5 S_2 \left(1 - \frac{R_t}{R_0} \right) - S_3 \right] \tag{II.38}$$

$$\Lambda = 0.25 S_1 + 0.25 S_2 \left(1 - \frac{R_t}{R_0} \right) \tag{II.39}$$

$$\beta_{p\perp} = 0.5 S_1 + 0.5 S_2 \left(1 + \frac{R_t}{R_0} \right) + \mu_i \tag{II.40}$$

where:

$$R_t = \frac{\iiint_{V_p} (8\pi p + B_p^2 + B_{t0}^2 - B_t^2) dV}{\iiint_{V_p} \frac{1}{r} (8\pi p + B_p^2 + B_{t0}^2 - B_t^2) dV} \tag{II.41}$$

$$\alpha = 2 \frac{\iiint_{V_p} (\boldsymbol{B_p} \cdot \boldsymbol{i_z})^2 dV}{\iiint_{V_p} B_p^2 dV} \tag{II.42}$$

being R_0 a characteristic radius (e.g. the vacuum vessel centre radius). It is worth noticing that the equation (II.41) assumes an isotropic plasma and a negligible rotational mass flow; the general expression for R_t can be found in [39][39].

Under the same hypothesis, it is possible to demonstrate that:

$$\beta_p = \beta_{p\perp} = \beta_{p\parallel} \qquad \text{(II.43)}$$

$$W_{pt} = 0 \qquad \text{(II.44)}$$

so rewriting the parameters in (II.38), (II.39) and (II.40), as follows:

$$\beta_p + \frac{l_i}{2} = 0.25S_1 + 0.25S_2\left(1 + \frac{R_t}{R_0}\right) \qquad \text{(II.45)}$$

$$l_i = \frac{1}{\alpha - 1}\left[0.5S_1 + 0.5S_2\left(1 - \frac{R_t}{R_0}\right) - S_3\right] \qquad \text{(II.46)}$$

$$\beta_p = 0.5S_1 + 0.5S_2\left(1 - \frac{R_t}{R_0}\right) + \mu_i \qquad \text{(II.47)}$$

Once the plasma diamagnetic flux is measured via the diagnostic system, it is possible to estimate the diamagnetic parameter as follows:

$$\mu_i \cong -\frac{4\pi B_{t0} R_0}{B_{pa}^2 V_{pl}}\Delta\Phi \qquad \text{(II.48)}$$

where $\Delta\Phi$ is the diamagnetic flux.

Assuming that the plasma has an elliptic cross-section, equation (II.47) can be simplified as follows:

$$\beta_{DIA}^{(2)} = 1 + \frac{E^2 + 1}{E}\frac{B_{t_0}}{20\pi I_p^2}\Delta\Phi \qquad \text{(II.49)}$$

where E is the plasma elongation.

The range of validity for expressions (II.29) and (II.31) was tested on several static equilibria extracted from the database of the $EFIT^{++}$ code [40]. Assuming no noise affecting the sensors, the code was used for the reconstruction of all the plasma parameters, except for the diamagnetic flux.

In Tab. II.26 we report the actual values of the poloidal beta β_p, the diamagnetic flux $\Delta\Phi$, the required accuracy of the diamagnetic flux measurement ($\varepsilon_{\Delta\Phi}$), the expected error without eddy current compensation ($2\sigma_{\Delta\Phi}$), and the expected error with the eddy current compensation ($2\sigma_{\Delta\Phi_{COMP}}$) in terms of the 2σ confidence interval (σ is the standard deviation).

Tab. II.26: Equilibria and maximum values of expected diamagnetic flux errors (2σ interval)

Eq. #	I_p [MA]	β_p	$\Delta\Phi$ [Vs]	$\varepsilon_{\Delta\Phi}$ [mVs]	$2\sigma_{\Delta\Phi}$ [mVs]	$2\sigma_{\Delta\Phi_{COMP}}$ [mVs]
30	3.00	0.0843	0.0878	5	0	33
50	15.00	0.5937	1.1568	116	5	33
182	15.00	0.6000	1.0346	119	5	33
131	2.53	0.1881	0.0574	4	0	33
230	9.36	2.4752	-1.0743	48	2	33
184	15.00	0.5991	1.0890	119	5	33

In the following Tab. II.27 and Tab. II.28, the confidence intervals on diamagnetic flux shown in Tab. II.26 were mapped to the 2σ confidence intervals on the poloidal beta estimation errors, by applying equations (II.29) and (II.31) respectively. The cases highlighted in red show that the required accuracy bounds are exceeded.

Tab. II.27: Estimation results using equation (II.29)

Eq. #	$\Delta\beta_p$	$\beta_{DIA}^{(1)}$	$\varepsilon_{\beta_{DIA}^{(1)}}$	$2\sigma_{\beta_{DIA}^{(1)}}$	$2\sigma_{\beta_{DIA_{COMP}}^{(1)}}$
30	0.030~0.138	0.086	0.034~0.138	0.086~0.086	-0.257~0.430
50	0.514~0.674	0.617	0.562~0.671	0.614~0.619	0.601~0.632
182	0.520~0.680	0.615	0.560~0.669	0.612~0.617	0.600~0.630
131	0.129~0.247	0.196	0.138~0.255	0.196~0.196	-0.287~0.679
230	2.301~2.649	2.559	2.501~2.617	2.556~2.561	2.519~2.599
184	0.519~0.679	0.618	0.564~0.673	0.616~0.620	0.603~0.633

Tab. II.28: Estimation results using equation (II.31)

Eq. #	$\Delta\beta_p$	$\beta_{DIA}^{(1)}$	$\varepsilon_{\beta_{DIA}^{(2)}}$	$2\sigma_{\beta_{DIA}^{(2)}}$	$2\sigma_{\beta_{DIA_{COMP}}^{(2)}}$
30	0.030~0.138	-0.426	-0.507~-0.345	-0.426~-0.426	-0.962~0.110
50	0.514~0.674	0.553	0.508~0.598	0.551~0.555	0.540~0.566
182	0.520~0.680	0.588	0.540~0.635	0.586~0.590	0.574~0.601
131	0.129~0.247	-0.475	-0.578~-0.372	-0.475~-0.475	-1.323~0.373
230	2.301~2.649	2.052	2.005~2.099	2.050~2.054	2.020~2.085
184	0.519~0.679	0.566	0.519~0.614	0.564~0.568	0.553~0.580

From these analyses it is possible to note that formula (II.29) can be used without the compensation system and the compensation provides out-of-bound estimations, at low poloidal beta values.

On the other hand, the approximated formula (II.31) should not be used at low poloidal beta values in any case.

Chapter 3

Electromechanical effects of non-axisymmetric Halo Currents on ITER tokamak components

In this chapter, the analysis of the electromechanical loads due to asymmetric halo currents on the structures of ITER Tokamak is carried out. After introduction of the mathematical model and the numerical formulation of the problem, it is firstly validated on an axisymmetric halo currents configuration. Finally, the asymmetric analysis is tackled, focusing on the inductive effects too and on the electromechanical loads on the TF Coils [41].

3.1   Introduction

When a disruption occurs during the normal operations of a Tokamak, the loss of the plasma vertical position control generates a so-called *Vertical Displacement Event* (VDE) resulting in the halo current circulation from the plasma into the First Wall through the various in-vessel components, and then back into the plasma.

The halo current interaction with the strong magnetic field inside the tokamak produces mechanical loads that usually are a mandatory design criterion for many of its components, such us the Vacuum Vessel, the divertor and the blanket modules.

The experimental evidence [42] highlights that ITER load specifications should also take into account the occurrence of *Asymmetric Vertical Displacement Events* (AVDEs), which may generate additional concentrated loads in some regions of the tokamak [43]-[44].

For these reasons, the evaluation both of the halo current distributions due to AVDEs and of the subsequent force distributions on the structures surrounding the plasma in ITER tokamak is the principal aim of the activity described hereafter.

The chapter focuses on the simulation of electromagnetic transients, and in particular on the calculation of the electromagnetic loads generated by both the halo and the eddy currents (thus estimating the time-history of torques and net forces among the vacuum vessel and surrounding structures), the volumetric forces components at each time instant and the net forces on the Toroidal Field Coils.

3.2   Numerical Model

The numerical model for the halo currents analyses in presence of AVDEs can be formulated in terms of weak form of the Maxwell equations in magneto-quasistatic limit [11]-[12]-[13] where the displacement current is neglected and by the linear constitutive equation $J = \sigma E$ in the conducting region.

The equation of the finite element method is derived by using the method of mean weighted residuals and therefore introducing the vector W of the weighting functions. In this case, the imposition of the electric constitutive equation in the weak form leads to:

$$\int_{V_c} W \cdot \frac{1}{\sigma} J dV + \frac{d}{dt} \int_{V_c} W \cdot A[J] dV = -\frac{d}{dt} \int_{V_c} W \cdot A_s dV +$$
$$- \sum_{h=1:N_E} \int_{S_h} \phi_h W \cdot \hat{n}\, dS \; \forall W, J \in S \tag{III.1}$$

where S is the subspace of $L^2_{div}(V_c)$ defined by:

$$S = \{J \in L^2_{div}, \nabla \cdot J = 0 \; in \; V_c, J \cdot \hat{n} = 0 \; on \; \partial V_c / S_E\} \tag{III.2}$$

and:

- $L^2_{div}(V_c)$ is the space where both J and $\nabla \cdot J$ belong to $L^2(V_c)$;
- A_s is the vector potential of the magnetic field generated by the external sources;

- **A** is the operator that returns the magnetic vector potential for a prescribed current density (it is based on the Biot-Savart law);

- N_E is the number of electrodes (part of the boundary of the conducting domain), identified by the surface S_E, characterized by the electric potential Φ_h and by an assigned current density distribution $\mathbf{J}_H(\mathbf{r}, t)$.

Expressing **J** in terms of the electric vector potential ($\mathbf{J} = \nabla \times \mathbf{T}$), we choose to represent it as the linear combination of the basis functions

$\boldsymbol{J}_j = \nabla \times \boldsymbol{T}_j \in S : \boldsymbol{J}(\boldsymbol{r}, t) = \sum_j I_j(t) \boldsymbol{J}_j(\boldsymbol{r})$ in V_c, and according to Galerkin's method, the chosen $\boldsymbol{J}_i$'s are the weighting functions.

The condition $\nabla \times \boldsymbol{T}_j \in S$ can be satisfied by using the edge elements as shape functions for $\boldsymbol{T}$, imposing its uniqueness as [11].

Using such assumptions, we get the following ordinary differential equation set:

$$\begin{cases} \underline{\underline{L}} \dfrac{dI}{dt} + \underline{\underline{R}} \cdot \underline{I} + \underline{\underline{P}}^T \cdot \underline{\Phi} = \underline{V}(t) \\ \underline{\underline{P}} \cdot \underline{I} = \underline{\mathcal{I}}_h \end{cases} \tag{III.3}$$

where:

- $\underline{\underline{L}}$ is the fully populated inductance matrix;

- $\underline{\underline{R}}$ is the sparse resistance matrix;

- $\underline{\Phi}$ is the vector of voltages feeding the electrodes;

- $\underline{V}$ is the vector of the external voltages;

- $\underline{\mathcal{I}}_h$ is the vector of the fluxes through all the boundary facets elements;

- $\underline{\underline{P}}$ is the matrix of the fluxes through the mesh facets S_k belonging to ∂V_c and generated by the $\underline{\mathcal{I}}_h$ unknown currents (the entries P_{ij} are zeroes for those unknowns not belonging to the boundary).

These considerations lead to a suitable partitioning of the unknowns as boundary (I_b) and internal (I_i) currents unknowns (the apices b and i stand for boundary and internal region of the conductor domain), thus rewriting the set (III.3) as follows:

$$\begin{cases} \left(\underline{\underline{L}}^{bb} + \Delta t\underline{\underline{R}}^{bb}\right) \cdot \underline{I}_{n+1}^b + \left(\underline{\underline{L}}^{bi} + \Delta t\underline{\underline{R}}^{bi}\right) \cdot \underline{I}_{n+1}^i + \Delta t\underline{\underline{P}}^T \cdot \underline{\Phi}_{n+1} = \\ = \underline{\underline{L}}^{bb} \cdot \underline{I}_n^b + \underline{\underline{L}}^{bi} \cdot \underline{I}_n^i + \Delta t \cdot \underline{V}_{0,n+1}^b \\ \left(\underline{\underline{L}}^{bi} + \Delta t\underline{\underline{R}}^{bi}\right) \cdot \underline{I}_{n+1}^i + \left(\underline{\underline{L}}^{ii} + \Delta t\underline{\underline{R}}^{ii}\right)^T \cdot \underline{I}_{n+1}^i = \\ = \underline{\underline{L}}^{ib} \cdot \underline{I}_n^b + \underline{\underline{L}}^{ii} \cdot \underline{I}_n^i + \Delta t \cdot \underline{V}_{0,n+1}^i \end{cases} \tag{III.4}$$

where:

- the quantity I_{n_x} is the unknown current at generic time instant n_x;

- Φ_n is the set of voltages associated to the boundary facets at generic time instant n (defined by the incidence matrix $\underline{P}$);

- V_{0,n_x} is the set of external voltages at generic time instant n_x;

- I_{0,n_x} is the set of the plasma halo currents imposed at the boundary elements facing the plasma, at generic time instant n_x.

The solution of the (III.4) can be gainfully calculated by changing the variables and defining a new unknown vector $\underline{Z}$ as follows:

$$\underline{I}^b = \underline{\underline{K}} \cdot \underline{Z} + \underline{I}_0 \tag{III.5}$$

where:

- $\underline{\underline{K}}$ is the right null of P;

- $I_0 = \underline{\underline{P}}^\dagger I_h$, where $\underline{\underline{P}}^\dagger$ is the Moore-Penrose pseudo-inverse matrix of $\underline{\underline{P}}$.

Taking into account that:

$$\underline{\underline{K}} \cdot \underline{\underline{P}} \cdot \underline{\Phi} = \left(\underline{\Phi}^T \cdot \underline{\underline{P}} \cdot \underline{\underline{K}}\right) = 0 \tag{III.6}$$

if the set of equations (III.4) is multiplied by $\underline{\underline{K}}^T$, we get:

$$\begin{cases} \underline{\underline{K}}^T \left(\underline{\underline{L}}^{bb} + \Delta t\underline{\underline{R}}^{bb}\right) \cdot \underline{\underline{K}} \cdot \underline{Z}_{n+1} + \underline{\underline{K}}^T \left(\underline{\underline{L}}^{bi} + \Delta t\underline{\underline{R}}^{bi}\right) \cdot \underline{I}_{n+1}^i = \underline{u}_n^b \\ \left(\underline{\underline{L}}^{bi} + \Delta t\underline{\underline{R}}^{bi}\right) \cdot \underline{\underline{K}} \cdot \underline{Z}_{n+1} + \underline{\underline{R}}^{ii} \cdot \underline{I}_{n+1}^i = \underline{u}_n^i \end{cases} \tag{III.7}$$

for suitable right-hand sides u_n^b and u_n^i.

The solution of the set of (III.7) is calculated in two different cases:

- the resistive limit, where the inductive effects are neglected (the L_{ij} terms are not present);

- the dynamic case, where the inductive effects related to the L_{ij} terms are taken into account.

The solver of the resistive limit is very important not only for the resistive solution itself, but for the inductive case too, because it can be used as a preconditioner in the iterative method. The procedure is based on the pseudo-inversion of the matrix $\underline{\underline{A}}_{bb} = \underline{\underline{K}}^T \cdot \underline{\underline{R}}_{bb} \cdot \underline{\underline{K}}$ (related to the boundary DoFs) using a singular value decomposition [45]-[46].

3.3   Assumptions

3.3.1   Reference case

The reference load case considered is a *Slow Downward Vertical Displacement Event* belonging to the third category (in the following VDE DOWN SLOW lin CAT III, whose main parameters are shown in Fig. III.1), and an AVDE assuming an $n = 1$ kink, (it may yield large horizontal forces and peaking factors [43]):
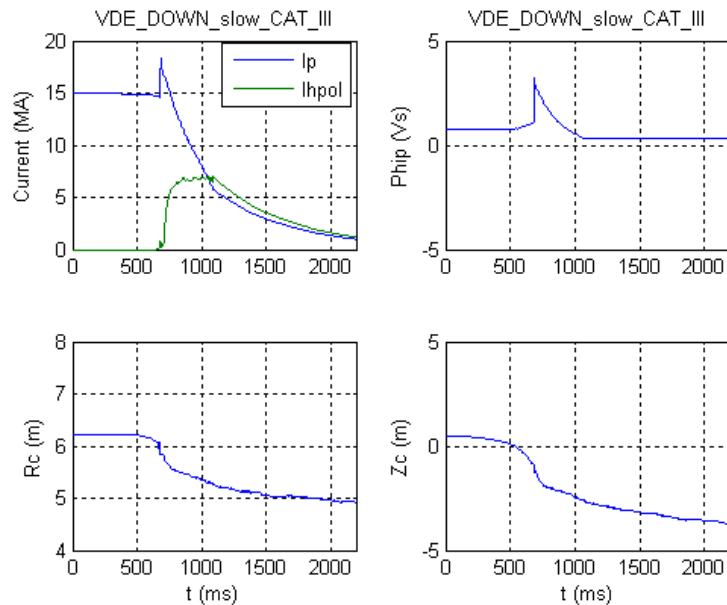
Fig. III.1: Load case VDE DOWN SLOW lin CAT III: plasma current I_p, poloidal halo current I_{hpol}, toroidal flux Phip, radial (R_c) and vertical (Z_c) position of the plasma current centroid.

The axisymmetric analysis is self-consistent because it takes into account both the poloidal field variation due to the plasma current movement and quench and the toroidal field variation due to the diamagnetic flux time history.

As regards the non-axisymmetric analysis, we assume a simplified $n = 1$, $m = 1$ kink mode given by a horizontal displacement $dx(t)$ and a tilt around the x axis $d\theta_x(t)$ and that the asymmetric perturbation starts $10\,ms$ after the thermal quench (when the safety factor at the plasma boundary is about 1.5).

Taking into account the data provided in [47], we consider a pulse for the two perturbation parameters, starting at $t_0 = 690\,ms$ and lasting $dt = 338\,ms$, so that the maximum value of dI_p is $10\% I_p = 1.5\,MA$. The quantity dI_p is given by the non-uniform value of the toroidal plasma current along the toroidal direction and is so defined as follows:

$$dI_p(t) = I_{p_{max}}(\varphi, t) - I_{p_{min}}(\varphi, t) \tag{III.8}$$

The time waveform is bell shaped so that the time integral of dI_p is:

$$\int dI_p(t) dt = 0.6 \cdot dI_{p_{max}} \cdot dt \tag{III.9}$$

During the rectangular pulse, the ratio between dx and $d\theta_x$ is taken so that the ratio between the maximum values of the asymmetric vertical and horizontal displacements is the equal to the elongation:

$$\left|\frac{dz}{dx}\right| = \left|\frac{R_0 \cdot d\theta_x}{dx}\right| = \frac{b}{a} = 2 \tag{III.10}$$

3.3.2 Solid model of the ITER Tokamak

Both the eddy and halo current analyses were carried out by means of the volumetric integral formulation described in [11]-[12] and implemented in the 3-D code CARIDDI, well suited for the eddy currents induced both in massive structures and in thin shells.

The computational domain consists of the only conducting region, including the passive structures of the tokamak facing the plasma region. Therefore, the solid model includes:

- the two Vacuum Vessel shells;
- the ribs;
- the blanket modules below the equatorial plane;

- a simplified model of the divertor (with dome, baffles, targets, cassette body);

- simplified models of the plugs;

- triangular support and copper cladding;

- the electrical connections of the blanket to the vessel;

- an artificial shell which allows the closure of the halo current path inside the vessel.

It is worthy noticing that these components shield the vessel, thus the electromagnetic loads acting on them are transferred to the vessel itself in the inductive phases.

Basing on these assumptions, one mesh was used to assess the axisymmetric model (Fig. III.2) and two additional meshes were used respectively for the VDE analyses (the mesh covering a sector 20 deg wide, $0 \leq \varphi \leq \pi/9$, shown in Fig. III.3 without the upper part of blanket modules) and for the AVDE analyses (the whole torus mesh shown in Fig. III.4):
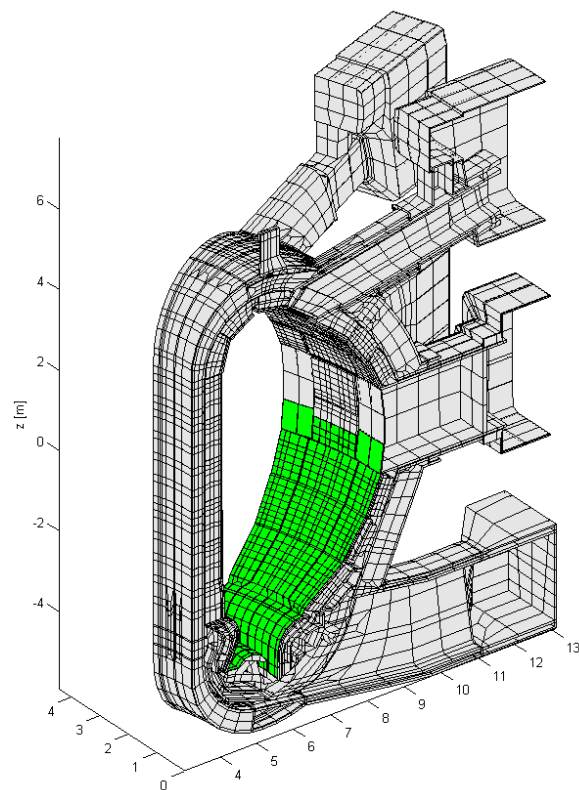
Fig. III.2: Mesh for the validation of the axisymmetric model
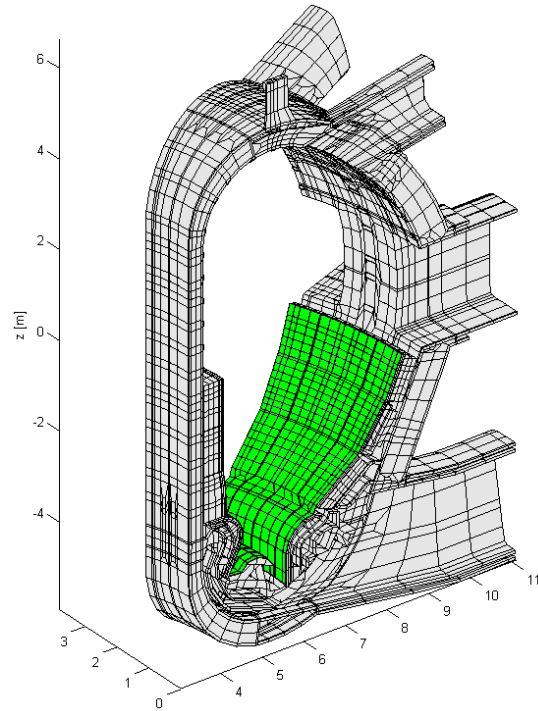
Fig. III.3: Mesh for the 20 deg sector 0≤φ≤π/9 (artificial shell in green).
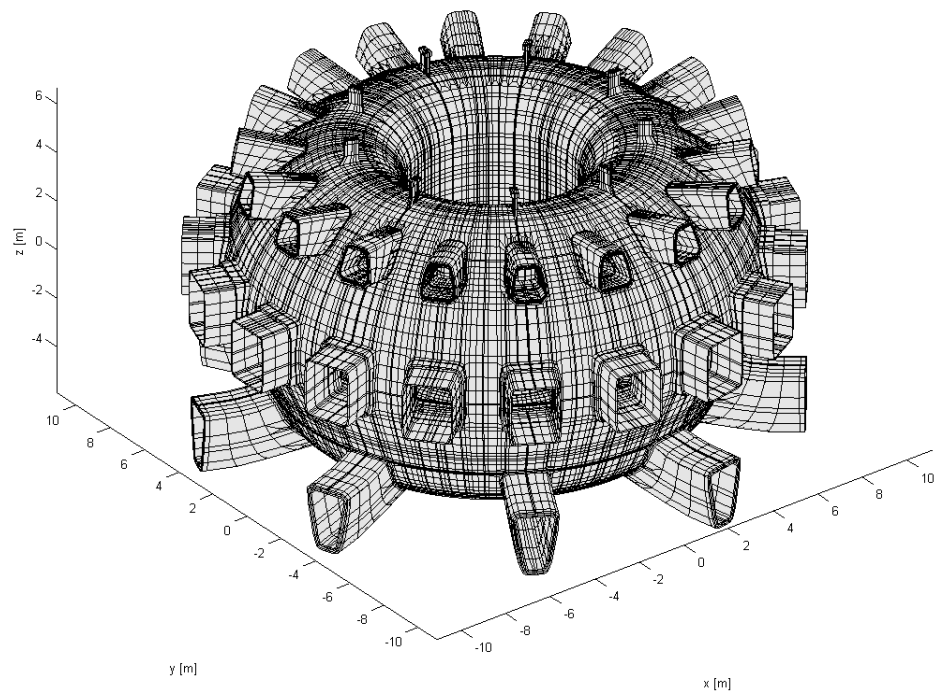
Fig. III.4: Mesh for the whole torus (the artificial shell not visible because inside the VV)

At last, the following Tab. III.1 reports the list of components, with their own equivalent resistivity.

Tab. III.1: List of components and their equivalent resistivity

Component	Resistivity [Ωm]
Vessel inner shell	0.825e-6
Vessel outer shell	0.825e-6
Copper cladding	0.027e-6
Ribs	0.825e-6
Hook	0.825e-6
Connection upper port – vessel	0.825e-6
Connection equatorial port – vessel	0.825e-6
Connection lower port – vessel	0.825e-6
Connection upper port – extension	0.825e-6
Upper port extension	0.825e-6
Upper port plug	0.825e-6
Equatorial port extension	0.825e-6
Equatorial port plug	0.825e-6
Lower port extension (inner)	0.825e-6
Lower port extension (outer)	0.825e-6
Lower port closure	0.825e-6
Rail	0.825e-6
Connection rail – cassette	0.825e-6
Connections cassette – IVT, OVT	0.825e-6
Cassettes	0.825e-6
Inner Vertical Targets (IVT)	0.825e-6
Outer Vertical Targets (OVT)	0.825e-6
Dome	0.825e-6
Connections blankets – vessel	0.825e-6
Blankets: shielding blocks	1.0403e-6
Blankets: connections shielding blocks – front panels	1.0403e-6
Blankets: front panels	1.0403e-6
Artificial shell	0.8e-7 or 0.8e-5

3.4   Eddy and halo current analyses: procedures, models, excitations

Since CARIDDI is based on an integral formulation, the finite elements model used does not include the air and vacuum regions; moreover, the PFCs are supposed to be current driven, hence they are excluded by the finite elements model as well.

When the halo currents are present, the magnetic vector potential $\boldsymbol{A}_{pl}$ and the magnetic flux density field $\boldsymbol{B}_{pl}$ due to the plasma are given by the toroidal and poloidal current densities in the plasma core. The plasma motion and the current quench generate the driving term related to the plasma toroidal current density. In this case, the plasma is approximated as a set of equivalent filaments in fixed positions and driving a current time waveform so as to produce the same poloidal field of the actual plasma (within a prescribed accuracy).

To describe the effects of the poloidal currents in presence of halo currents, a specific treatment is necessary: it is based on the computation of the plasma time evolution using a 2-D axisymmetric approximation, so that the halo current density ($\boldsymbol{J}_{halo}$) injected in each elementary surface ($2\pi r \Delta l$) of the first wall is given by the following expression:

$$2\pi r \Delta l \mu_0 \boldsymbol{J}_{halo} \cdot \hat{n}_w = 2\pi \big[B_\phi(r + \Delta r) \cdot (r + \Delta r) - B_\phi(r) \cdot (r) \big]$$
$$= 2\pi [f(r + \Delta r) - f(r)] \tag{III.11}$$

where:

- $f = r B_\phi$ is the toroidal flux per unit radian at each point of the plasma-first wall interface;
- $\hat{n}_w$ is the unit normal vector at the plasma-first wall interface, directed towards the first wall;
- Δl is the incremental distance along the plasma-first wall interface and $\Delta r = \Delta l \big(\hat{\imath}_\phi \times \hat{n}_w \cdot \hat{\imath}_r \big)$.

In the limit where $\Delta l \to 0$, it results:

$$\boldsymbol{J}_{halo} \cdot \hat{n}_w = \frac{1}{\mu_0 r} \frac{\partial f}{\partial l} \tag{III.12}$$

Being the current density a divergence-free vector field, it is convenient to guarantee its closure with a surface current density sheet related to the normal component of the halo current density at the plasma-first wall interface, $\boldsymbol{J}_{halo} \cdot \hat{n}_w$, by means of the balance equation:

$$\boldsymbol{J}_{halo} \cdot \hat{\boldsymbol{n}}_w = -\nabla \cdot \boldsymbol{J}_\Sigma = -\frac{1}{r} \frac{\partial r J_\Sigma}{\partial l} \tag{III.13}$$

This fictitious surface current density is placed on the artificial shell that is in contact with the first wall and the divertor plates, in order to allow the closure of the halo current path outside the conducting structures placed inside the

vessel. In particular, the same currents injected in each element of the first wall are imposed on the artificial shell, but with opposite direction.

The current distribution is now divergence-free, even though it does not reproduce the flow pattern associated to the plasma behaviour inside the plasma chamber. However, this behaviour can be recovered by computing the axisymmetric poloidal currents flowing inside the plasma when the same artificial shell is used in the 2-D axisymmetric domain.

It is worth noticing that these modified poloidal plasma currents do not generate a magnetic flux density field in the passive structures placed outside the plasma, but only a contribution to the time derivative of the magnetic vector potential that is associated to the time derivative of the toroidal flux $\Phi_T(t)$ linked with the plasma boundary.

In the axisymmetric case, the imposition of the toroidal flux as a source is obtained by exploiting the analogy between $(\boldsymbol{H}, \boldsymbol{J})$ and $(\boldsymbol{A}, \boldsymbol{B})$:

$$\begin{cases} \nabla \times \boldsymbol{B}/\mu_0 = \boldsymbol{J} \\ \nabla \cdot \boldsymbol{B}/\mu_0 = 0 \\ \lim_{r \to \infty} B = 0 \end{cases} \Longleftrightarrow \begin{cases} \nabla \times \boldsymbol{A} = \boldsymbol{B} \\ \nabla \cdot \boldsymbol{A} = 0 \\ \lim_{r \to \infty} A = 0 \end{cases} \tag{III.14}$$

The axisymmetric vector potential $\boldsymbol{A}$ associated to a given $\Phi_T(t)$ can be computed as the poloidal field $\boldsymbol{H}$ generated by a filament that carries an equivalent current equal to the toroidal flux and placed inside the plasma region, e.g. the plasma centroid.

The total field and the flux variation are due to the superposition of both axisymmetric and 3-D halo current sources. Notice that the contribution of the surface current circulating in the 3-D artificial shell is exactly canceled by the surface current flowing at the boundary of the axisymmetric plasma region.

As regards the AVDEs analyses [48], a suitable decomposition of the driving terms is necessary if the mesh not covering the full torus is used. Therefore, the 20 deg mesh is used only for axisymmetric VDE analyses, which include:

1. Poloidal Field Variation (PFV);
2. Toroidal Field Variation (TFV);
3. Halo Currents injected in each element of the first wall and in each element of the artificial shell, as given by (III.5) in the axisymmetric case [49].

The resulting fields can be then superposed thanks to the linearity assumption, being careful to the different boundary conditions:

- *symmetry* for halo and TFV analyses, i.e. $J_n = 0, @\ \varphi = 0$ and rotational symmetry, i.e. $\boldsymbol{J}(r, \varphi + 2k\pi/9, z) = \boldsymbol{J}(r, \varphi, z)$ for any integer k;

- *antisymmetry* for PFV analyses, i.e. $\boldsymbol{J} \times \boldsymbol{n} = 0, @\ \varphi = 0$ and rotational symmetry, i.e. $\boldsymbol{J}(r, \varphi + 2k\pi/9, z) = \boldsymbol{J}(r, \varphi, z)$ for any integer k.

On the other hand, when the $360\ deg$ mesh is used, all the effects can be cumulated and analysed in a single simulation, considering simultaneously all the driving terms.

As regards the only PFV analysis, the driving term is related to the plasma motion and current quench. The plasma is modelled with a set of fixed filamentary sources whose current time waveforms are calculated so as to produce the same poloidal field on the first wall within a reasonable accuracy; the PF coil current waveforms are prescribed.

As regards the only TFV analysis, the PF coil are assumed to be not fed, and the driving term is related to the time dynamics of the magnetic vector potential associated with the toroidal flux in the plasma.

Finally, as regard the only axisymmetric halo current effects, the PF coil are again assumed to be not fed and the driving term is related to the current injected from the plasma into the structure and whose path is closed through the artificial shell.

Since the plasma is axisymmetric, the current is calculated via Ampere's law considering the only toroidal component of the flux density field due to the plasma (that is, $B_\varphi - B_{\varphi_0}$, where B_{φ_0} is the vacuum field, which is assumed to be curl-free).

In the following figures, some parameters of interest of the considered disruption are shown (the 2-D axisymmetric plasma evolution was computed by using the DINA numerical suite [43]-[50]-[51]):
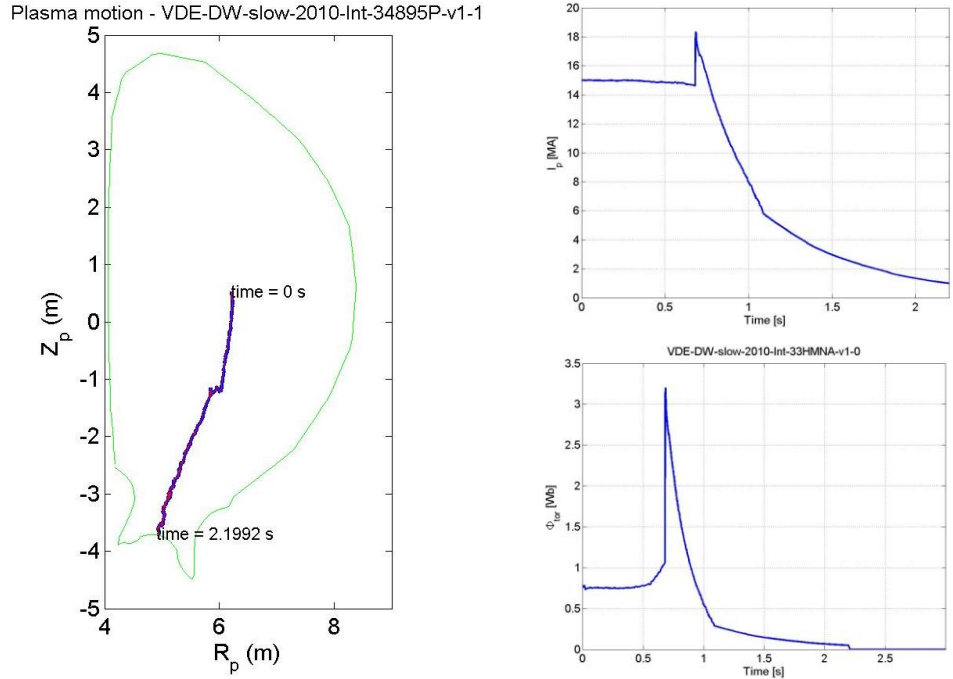
Fig. III.5: VDE_DW_slow_2010. The trajectory of the centroid of the plasma current during the disruption (left), the plasma current evolution as a function of time (top right) and the waveform of the toroidal flux due to the diamagnetic flux variation.
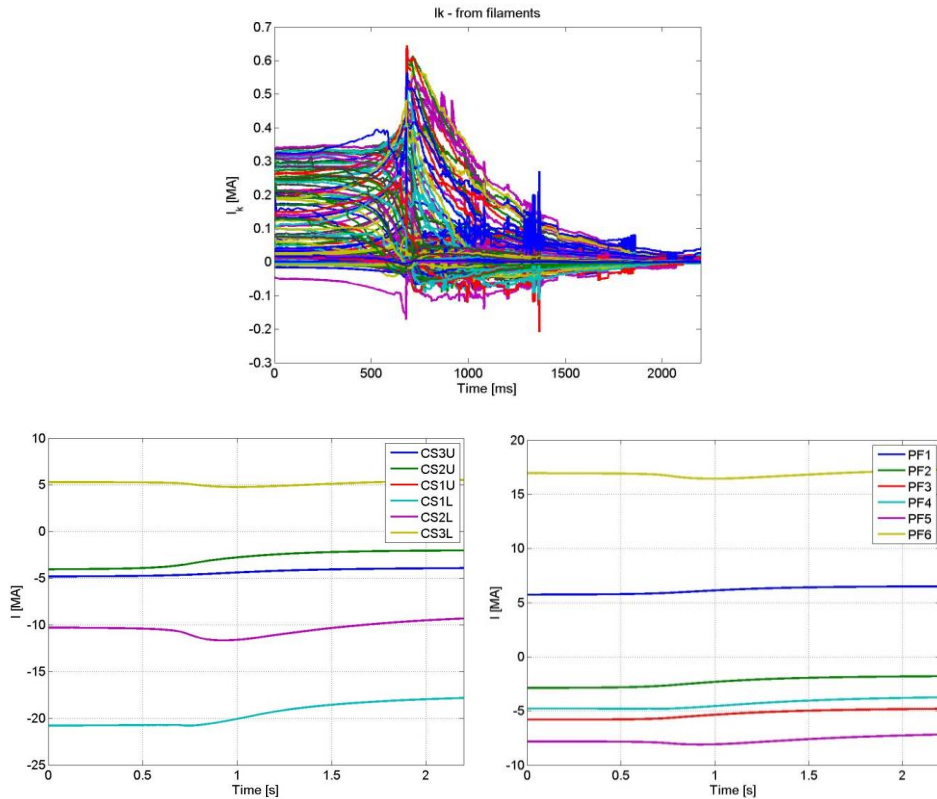
Fig. III.6: VDE_DW_slow_2010. Waveforms of the fixed filamentary currents (up), waveforms of the CS (down left) and PF coils (down right) currents
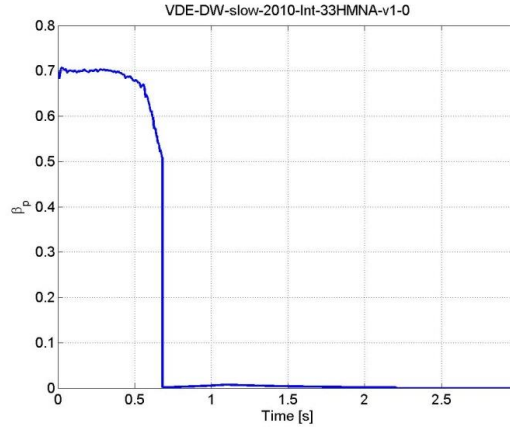
Fig. III.7: VDE_DW_slow_2010: TFV. Poloidal beta as a function of the time
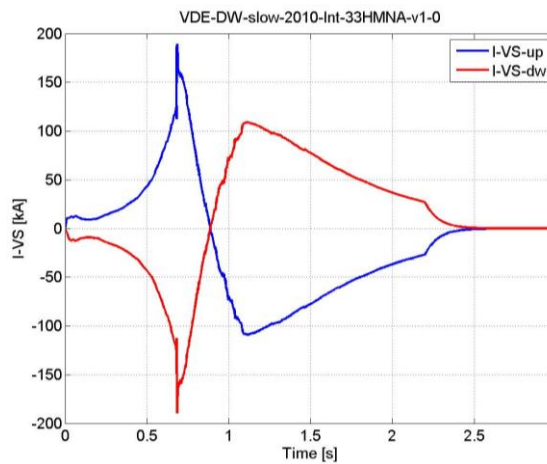
Fig. III.8: VDE_DW_slow_2010. Currents in the VS circuits, including the extrapolation after 2.1992s. The VS circuits are included in the model as current driven circuits.

As regards the AVDEs, they are carried out using the $360 \ deg$ mesh and assuming that:

- the TFV and PFV driving terms are the same as the VDE;
- the halo currents injected into the structure are calculated at each time instant t and:
  - o the reference configuration is rescaled so as to have the toroidal plasma current at each time instant $I_p(t)$ and the total poloidal current equal to the poloidal halo current $I_{h_{pol}}(t)$ multiplied by the factor $\frac{I_p(t)}{I_{h_{tor}}(t)}$, where $I_{h_{tor}}(t)$ is the toroidal halo current flowing at time instant t;
  - o the 2-D axisymmetric first wall is mapped inside the plasma; an image point P_i inside the plasma is associated to each point on the

first wall so as to have the same (rescaled) value of the toroidal flux per radian $f = rB_\varphi$ (the two extrema of the wetted area are mapped into the plasma boundary, whilst the other points of the wetted area are mapped inside).

The following Fig. III.9 shows a comparison between the halo currents distribution both in the VDE and in the AVDE:
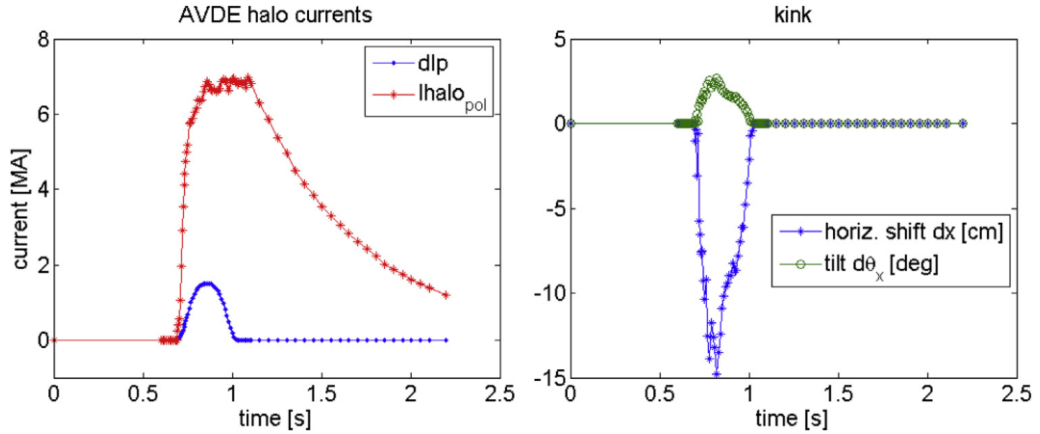
Fig. III.9: Halo currents in the VDE and in the AVDE. Left: total poloidal halo current Ihpol (the same in both VDE and AVDE) and differential current dI$_p$ in the AVDE. Right: kink parameters in the AVDE (up to about 2.7 deg tilt and about 15 cm horizontal shift).

The figure clearly shows that the total poloidal halo current distribution is the same both for the VDE and the AVDE until the kink occurrence. In that very moment, a differential current dI_p arises and is present until the kink's termination.
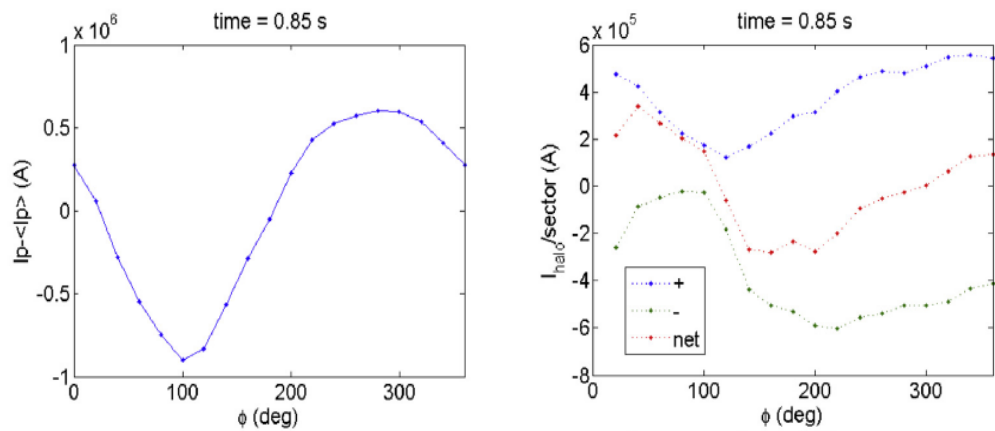
Fig. III.10: Halo currents in the AVDE at time=0.85 s (Ip=11.74MA, Ihpol=6.73 MA, dIp=1.50 MA). Left: variation of the total toroidal plasma current Ip (including halo region) along the toroidal angle. Right: halo currents interesting the various slices of the torus (20 deg wide each).
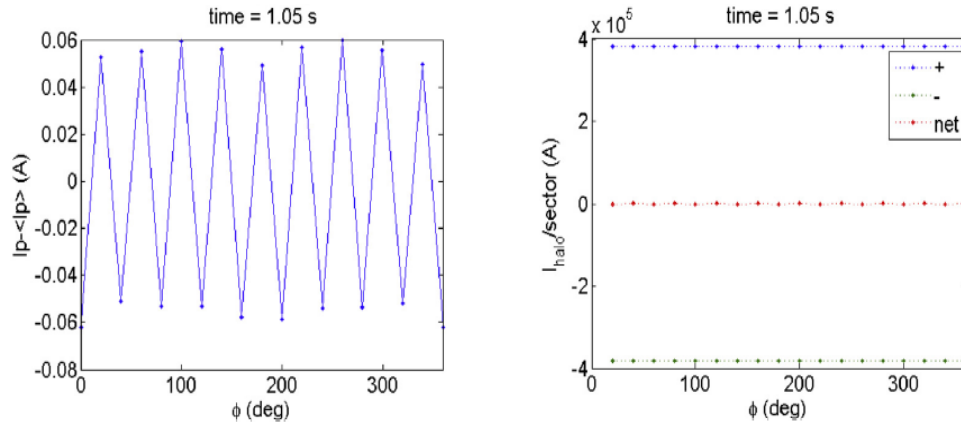
Fig. III.11: Halo currents in the AVDE at time=1.05s (Ip=6.88 MA, Ihpol=6.87 MA, dIp=0). Left: variation of the total toroidal plasma current Ip (including halo region) along the toroidal angle. Right: halo currents interesting the various slices of the torus (20 deg wide each).

In Fig. III.10 the kink perturbation is still acting on the plasma current, thus resulting in a very high variation of the total toroidal plasma current whose order of magnitude is comparable with that of the total plasma current. A halo current net distribution so arises, that is the difference between the current inside and outside the faces of the mesh per each slice. When the perturbation is terminated (Fig. III.11) there is no variation in the total toroidal plasma current and so the net halo current distribution is zero in the toroidal direction.

The following figures show the plasma cross section at the same time instants:
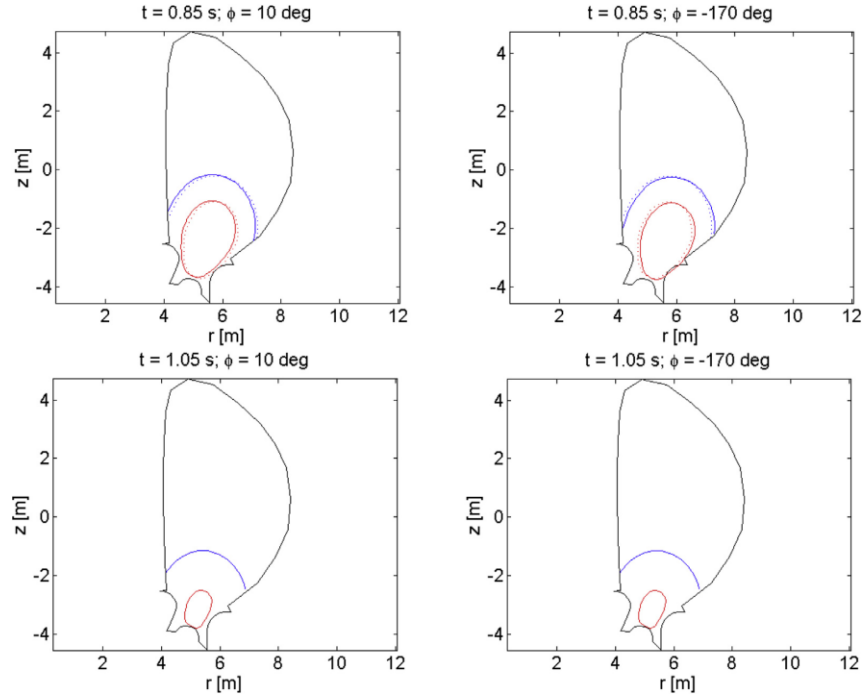
Fig. III.12: Halo currents in the AVDE at time=0.85 s (Ip=11.74MA, Ihpol=6.73 MA, dIp=1.50 MA in the upper row) and at time=1.05 s (Ip=6.88 MA, Ihpol=6.87 MA, dIp=0 in the lower row) - cross section of plasma core (solid red) and halo (solid blue) at φ=10 deg (left) and φ=-170 deg (right); the dashed lines refer to the original axisymmetric plasma.

The figures completely agree with the results in terms of differential current dI_p and toroidal halo current net distribution (Fig. III.11): the plasma cross section in two different poloidal sections is clearly different while the kink acts on the plasma whilst returns to be axisymmetric after the kink expires.

3.5   Axisymmetric Halo Currents Analysis

3.5.1   PFV effects

The driving terms of the PFV analyses are the plasma filaments and the PF coil currents, whilst the vacuum field generated by the TF coils istaken into account as F_0/R with $F_0 = 32.86\,Tm$ for $R < 9m$.

Fig. III.13 shows the vertical force on the vacuum vessel and on all the structures in one sector, as calculated with the $20\,deg$ mesh.
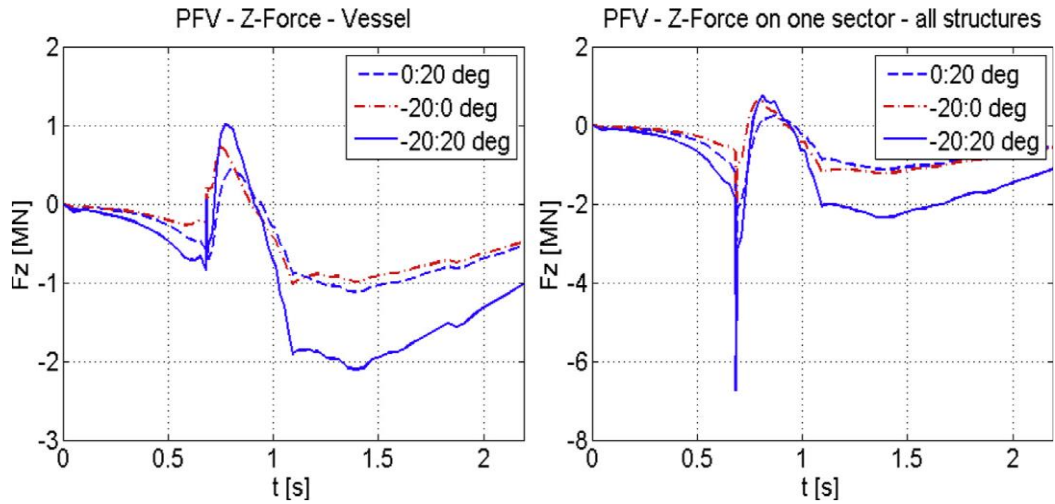
Fig. III.13: Vertical force on the vacuum vessel (up) and on all the structures (down) in one sector due to the eddy currents induced by the PFV.

These results are in agreement with those obtained in [52] and the toroidal current agrees with the simulation of DINA (Fig. III.14), showing that the removal of the upper blanket modules does not affect the global results dramatically.
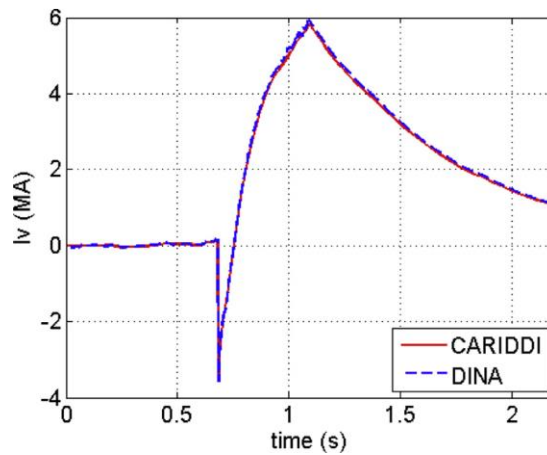
Fig. III.14: VDE_DW_slow_2010. Eddy current induced on the vacuum vessel as a function of time, as computed by DINA and CARIDDI overall 3D structure

At last, Fig. III.15 shows the eddy currents and the electromagnetic force distribution in the vacuum vessel due to the PFV at the final time of the simulation ($t = 2.2\ s$).
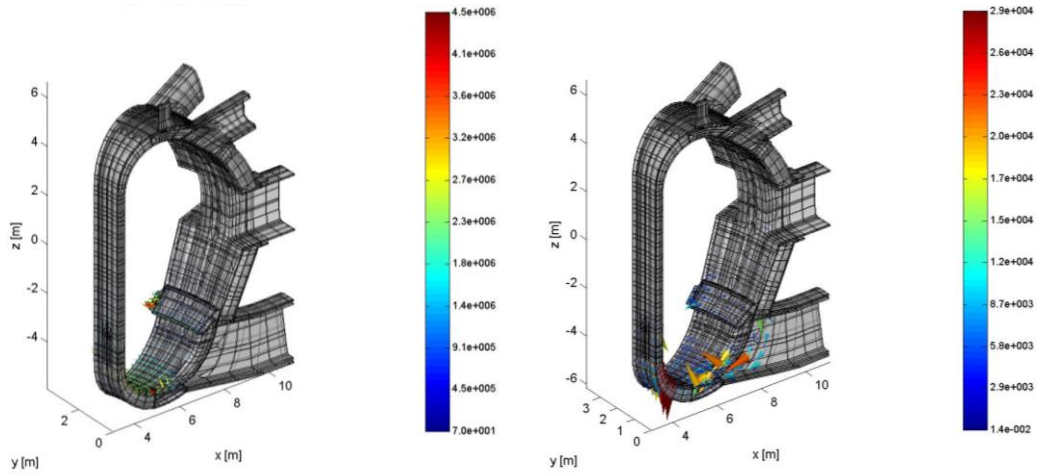
Fig. III.15: Eddy currents (left) and EM force distribution (right) in the VV due to the PFV at the final time of the simulation (t=2.2 s).

3.5.2   TFV effects

The driving term in the TFV analyses is the plasma diamagnetic flux time history, whilst the vacuum field generated by the TF coils is taken into account as F_0/R with $F_0 = 32.86\ Tm$ for $R < 9m$.

Fig. III.16 shows the total poloidal current as computed by CARIDDI and compared with the result provided by a simple first order model lumped parameters: it results that the first peak given by CARIDDI is about 15% higher than that of the analytical model, whereas the agreement is better afterwards.
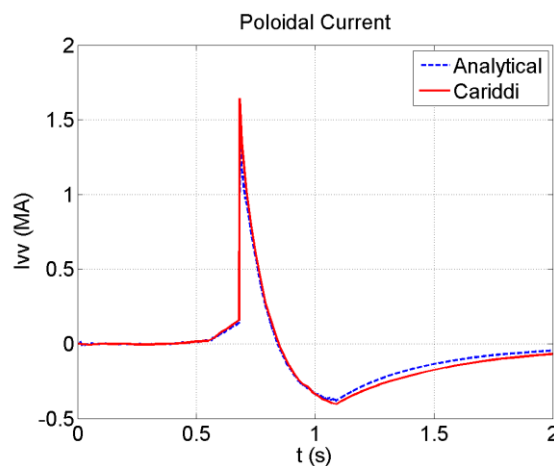
Fig. III.16: Total poloidal current induced in the passive structure by the TFV as computed by CARIDDI (I_{vvmax}=1.64 MA, I_{vvmin}=−0.40 MA) a simple 1st order model (L_{vvpol}=1.71 µH, R_{vvpol}=5.80 µΩ): I_{vvmax}=1.38 MA, I_{vvmin}=−0.38 MA).

These results can be explained by considering that:

- the value of the single turn inductance refers to an equivalent single shell having a slightly larger cross section;

- the poloidal currents are allowed to flow partially in the blanket modules through the straps and the divertor structure (see Fig. III.17), which are not taken into account into the analytical model.
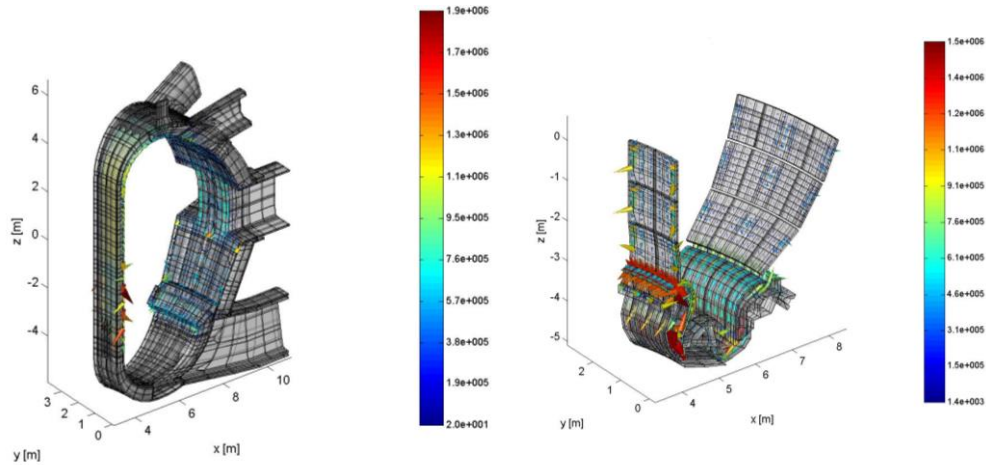
Fig. III.17: Eddy current distribution in the VV (left) and in the FW/divertor structures (right) due to the TFV just after the thermal quench.

Fig. III.17 shows that the currents flow in the inner shell, in the divertor structure, and partially in the blanket modules, thus reducing the effective value of the inductance with respect to the simple single vacuum vessel shell model.
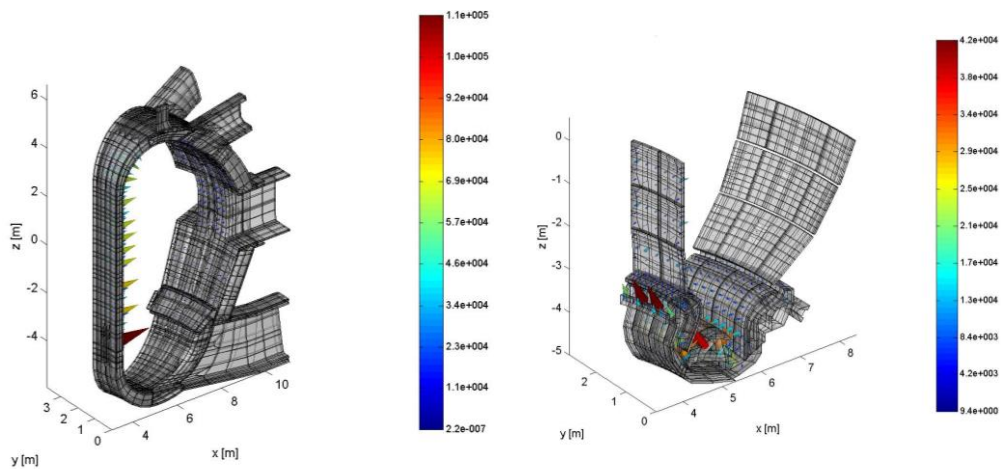
Fig. III.18: EM forces distribution in the VV (left) and in the FW/divertor structures (right) due to the TFV just after the thermal quench.

3.5.3 Axisymmetric halo current distribution and related electromagnetic loads

This analysis considers as driving term the only halo current flowing from the plasma into the structures, whose closure is guaranteed by the artificial shell that replaces the plasma. The only external field considered for the calculation of the forces is that of the TF coils, assumed as F_0/R with $F_0 = 32.86\,Tm$ for $R < 9m$.

The simplified model used for this analysis considers the halo current injected into the structure as driven by the 2-D axisymmetric plasma evolution, so that the dynamic behaviour of the total current is forced only by the external sources (just the distribution is slightly different because of the resistive and inductive parameters of the passive structure). Since this behaviour can be highlighted by analysing the total force in the passive structures, the effects of the axisymmetric halo currents were analysed using the following models and techniques:

- approximate resistive model (where the inductance matrix is neglected): it is faster to simulate (there is no need to invert the full inductance matrix) but is be valid only on the slow time scale;
- consistent model (taking account of the inductive effects) with an artificial shell having low resistivity (namely $\rho = 0.8 \cdot 10^{-7}\,\Omega m$);
- consistent model (taking account of the inductive effects) with an artificial shell having high resistivity (namely $\rho = 0.8 \cdot 10^{-5}\,\Omega m$).

Fig. III.19 and Fig. III.20 show that the current density distribution using the approximate resistive model differs from that of the consistent model, where the pattern is more concentrated near the plasma.
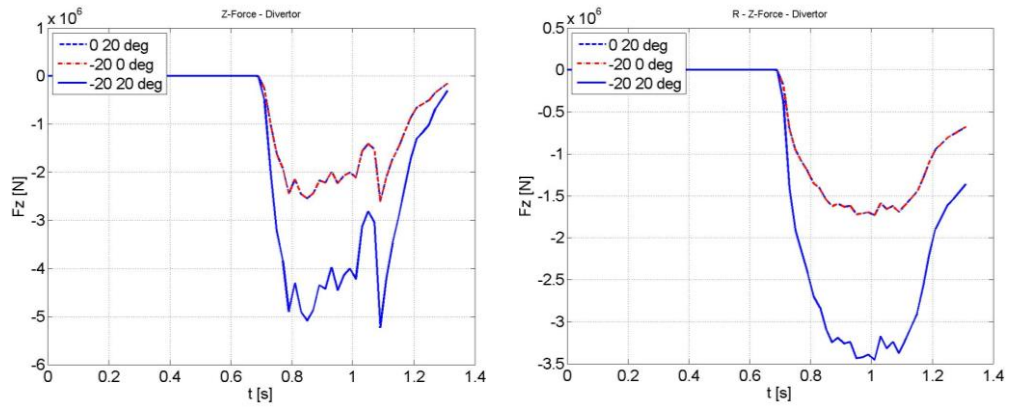
Fig. III.19: Axisymmetric halo currents: time history of the vertical force on one sector of the divertor (-20 deg < φ < 20 deg) computed with the consistent model (left) and the approximated resistive model (right)
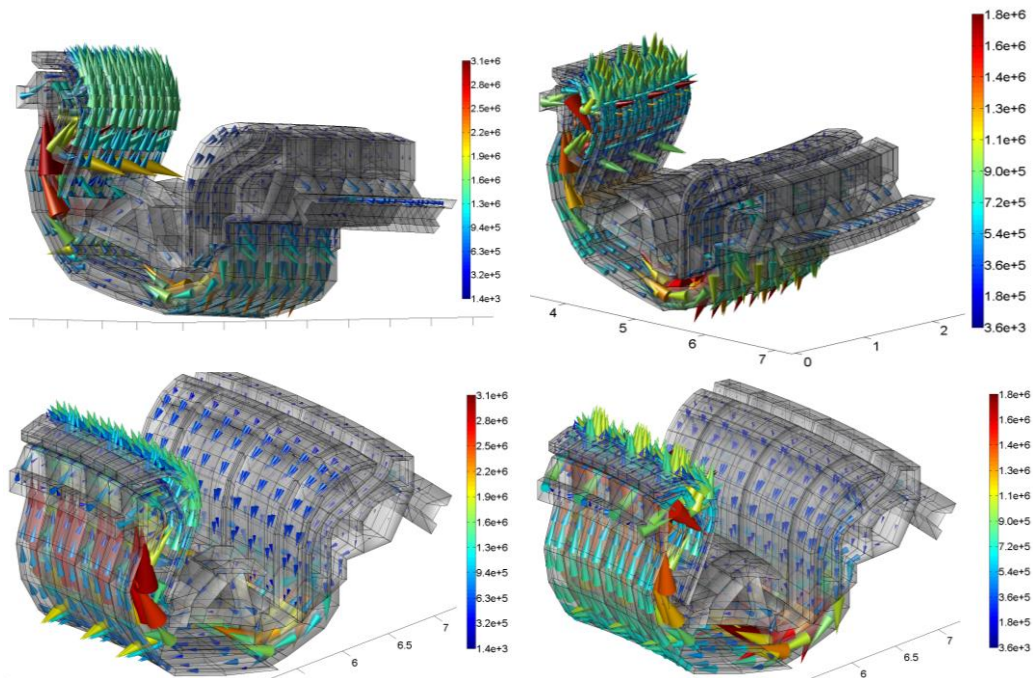
Fig. III.20: Axisymmetric halo currents: current density distribution when the maximum value of the vertical force is reached, computed with the consistent model (left, t = 1.09 s) and the approximated resistive model (right, t = 1.01 s)

The current density distribution is different also into the vacuum vessel, where the forces in the upper part of the structure are larger than those of the consistent model, (see Fig. III.21 and Fig. III.22).
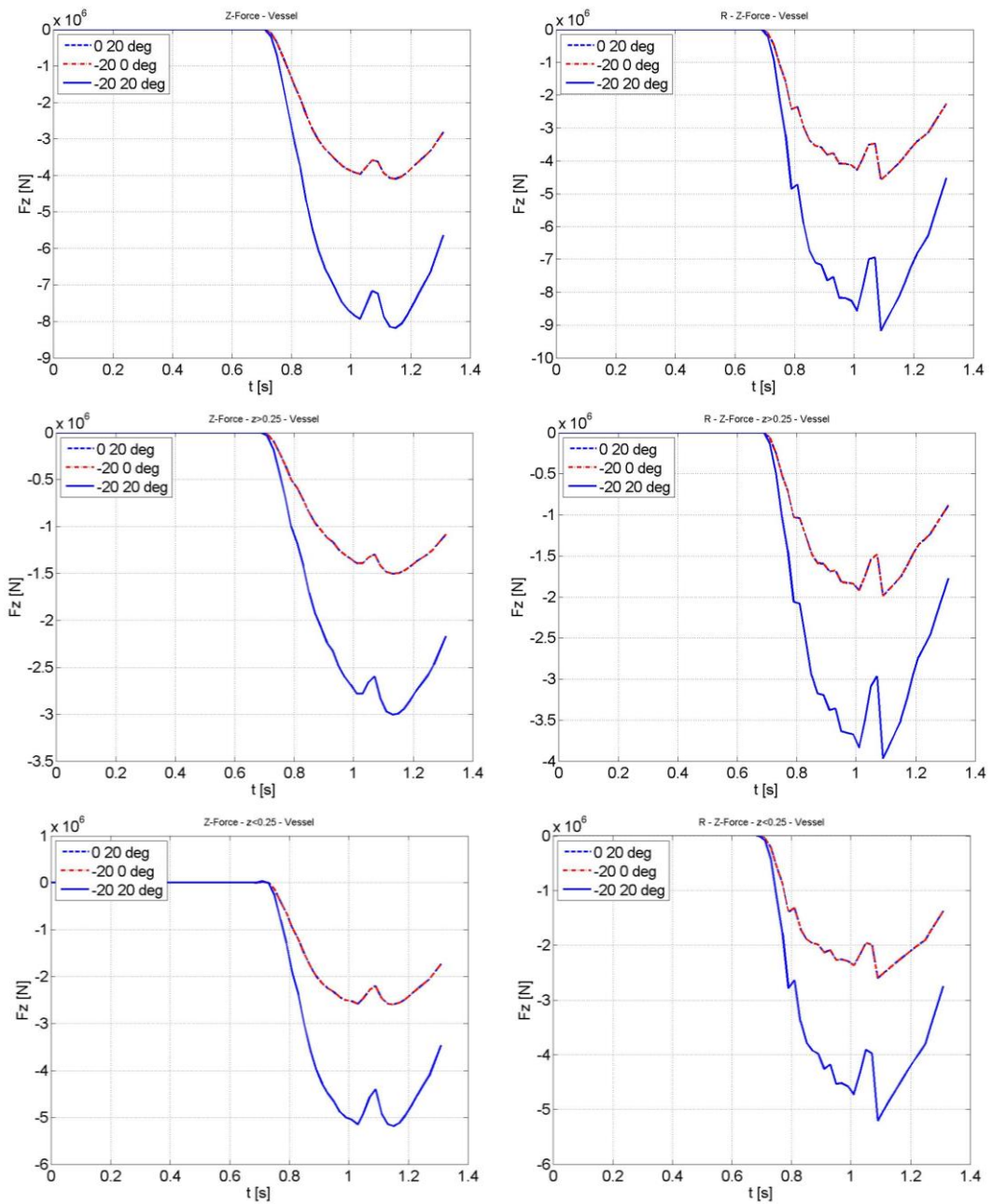
Fig. III.21: Axisymmetric halo currents: time history of the vertical force on one sector of the vessel (top row), on its upper part (center row) and on its bottom (bottom part), as computed by the consistent model (left) and the approximated resistive model (right).
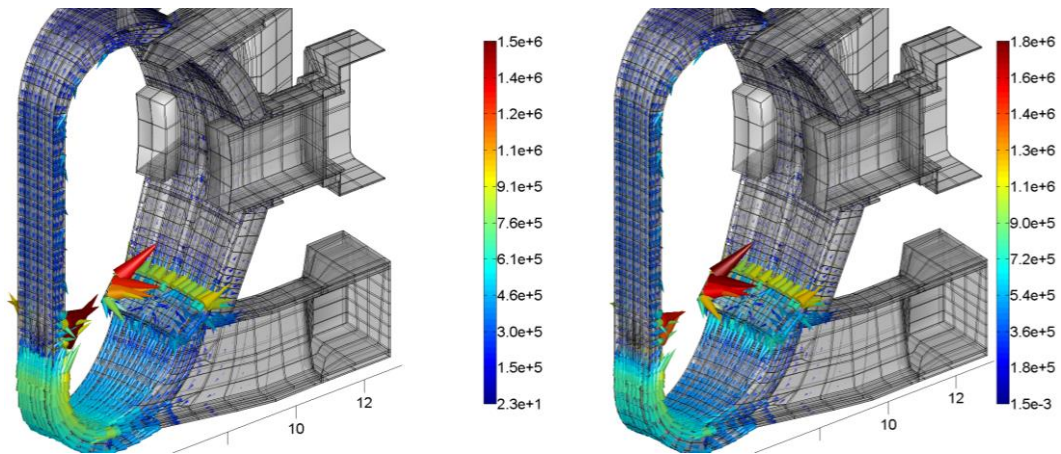
Fig. III.22: Axisymmetric halo currents: current density distribution on the vessel, at the time instant when the vertical force reaches its maximum value computed with the consistent model (left, t = 1.15 s) and the approximated resistive model (right, t = 1.09 s)

Basing on the results shown in Fig. III.19 to Fig. III.22, the upper part of the blanket modules was eliminated so that the mesh was coarser when using the full 360 deg mesh. As consequence, they are marginally affected by the induced current density during the considered load case.

Fig. III.23, Fig. III.24 and Fig. III.25 show the current density, the ohmic power and the force distribution respectively, obtained with the resistive model and the full 360 deg mesh at the time instant $t = 0.900\,s$. The results perfectly agree and the vertical force ($-88.5\,MN$, $-78.3\,MN$ on the vessel) is in good agreement with the calculation provided by the simple model consisting of the interaction between sheet currents on the first wall and the divertor and the vacuum toroidal field.

The results shown in Fig. III.25, Fig. III.26 and Fig. III.27 show that the artificial shell resistivity has no apparent effect.
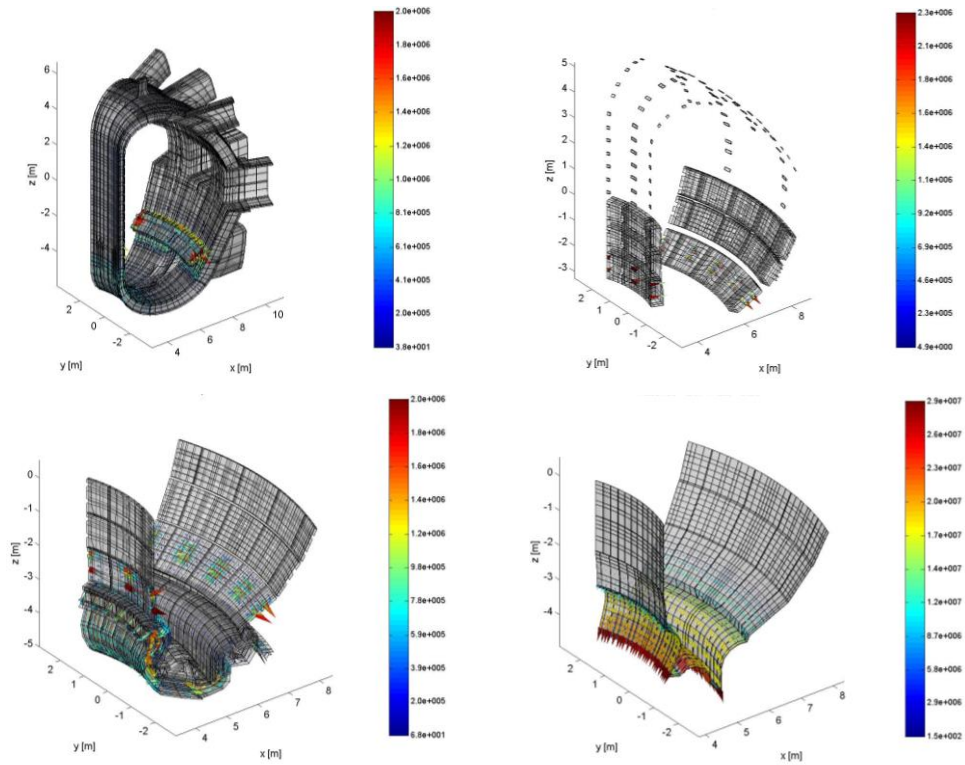
Fig. III.23: Axisymmetric halo currents: current density distribution obtained with the resistive model at the time instant t = 0.9 s: Vessel (up-left), Shielding blocks (up-right), Front panels (down-left) and Artificial shell (down-right)
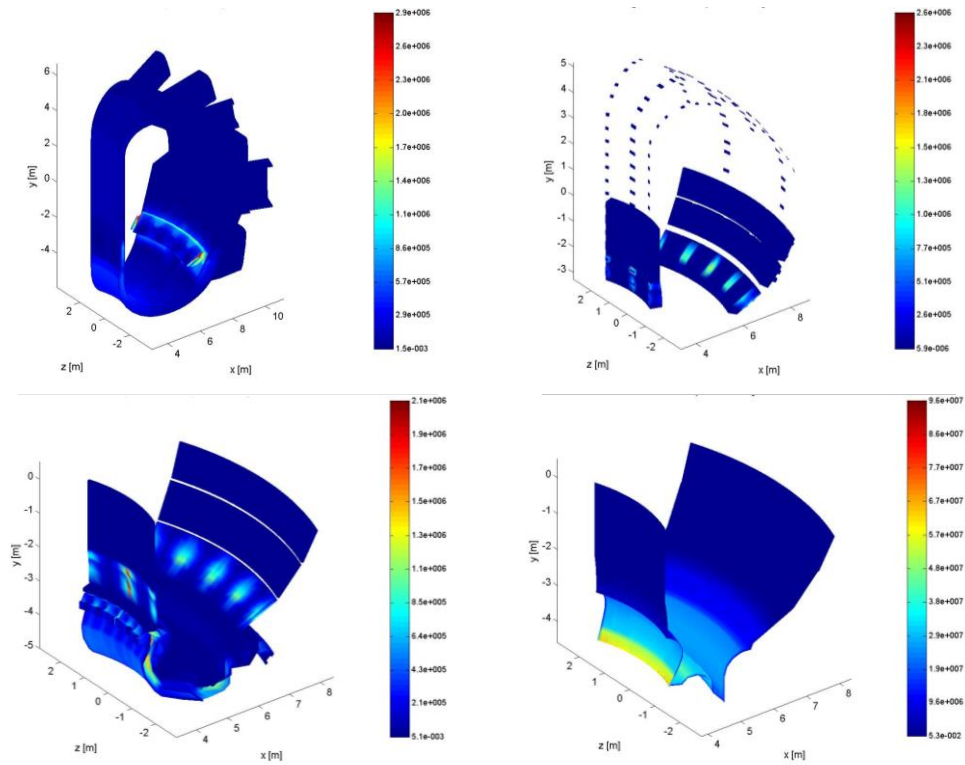
Fig. III.24: Axisymmetric halo currents: ohmic power distribution obtained with the resistive model at the time instant t = 0.9 s: Vessel (up-left), Shielding blocks (up-right), Front panels (down-left) and Artificial shell (down-right)
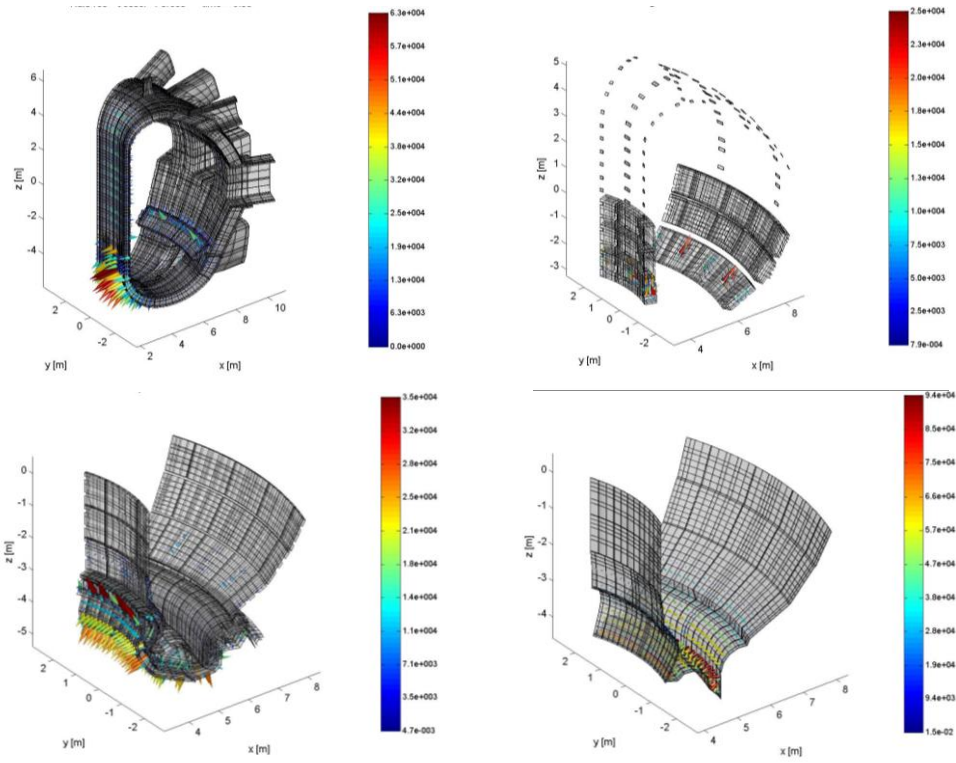
Fig. III.25: Axisymmetric halo currents: force distribution obtained with the resistive model at the time instant t = 0.9 s: Vessel (up-left), Shielding blocks (up-right), Front panels (down-left) and Artificial shell (down-right)
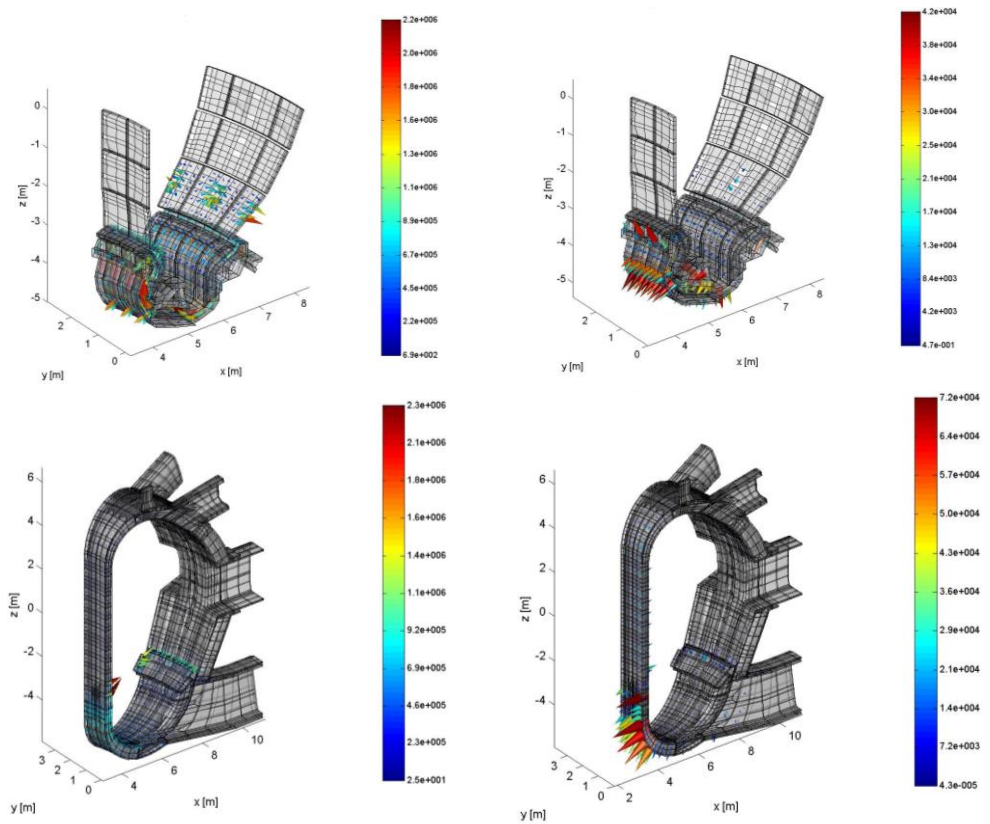
Fig. III.26: Axisymmetric halo currents: current density and force distribution obtained with the high resistivity artificial shell at the time instant t = 0.77 s (Front panels - up) and t = 1.13 s (Vacuum Vessel - down)
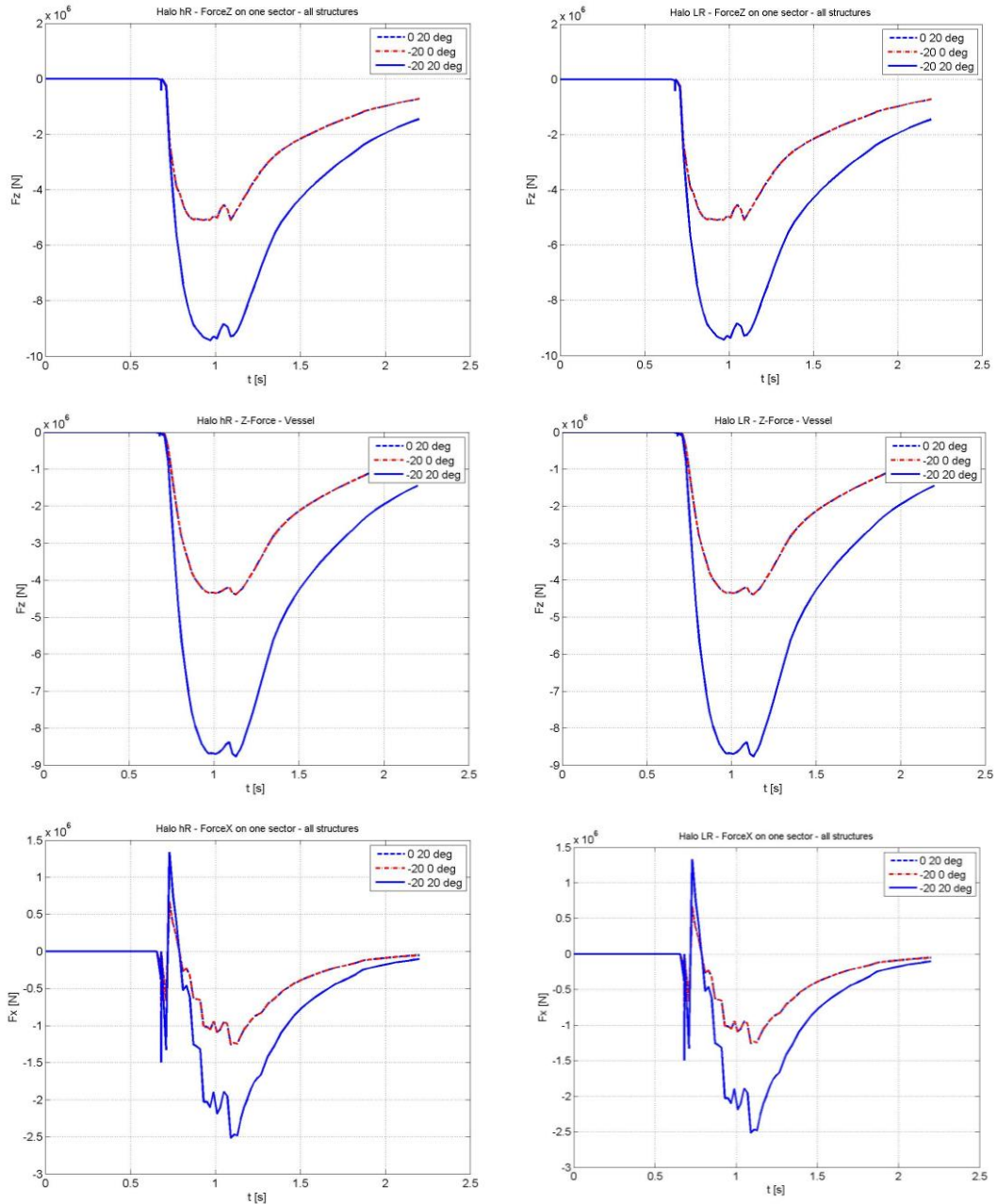
Fig. III.27: Axisymmetric halo currents: time history of the vertical and horizontal force on one sector as computed with the high (left) and low (right) resistivity artificial shell (the field generated by the halo currents is taken into account)

3.6 Asymmetric halo current effects and related loads on vacuum vessel and divertor structure

The analysis of the AVDE was carried out considering the halo current flowing from the plasma to the structures as driving term, allowing the current density path to close via the artificial shell replacing the plasma. The total field

considered for the calculation of the electromagnetic loads is axisymmetric and consists of the superposition of that generated by the:

- TF coils: assumed as F_0/R with $F_0 = 32.86\ Tm$ for $R < 9m$;
- PF/CS coils: assumed to be current driven with the DINA waveforms;
- Plasma: modelled as a set of equivalent filamentary conductors.

In the following, the problem of the analysis of the asymmetric halo current effects with the full $360\ deg$ mesh and using the consistent model (thus taking account of the inductive effects) is tackled; the artificial shell is considered with an high resistivity ($\rho = 0.8 \cdot 10^{-5}\ \Omega m$).

This kind of analysis requires a huge computational burden also because of the full inductance matrix that would need more than $1\ TB$ memory for the single precision computation. For this reason, suitable compression techniques and supercomputing resources were adopted, as:

- the parallel architecture available at the Cassino University, with 78 processors and a distributed 432 GB memory;
- the parallel facility *MareNostrum* available in Barcelona, with 10000 processors and a distributed 20 TB memory;
- the parallel facility *Helios* available in Japan, with 70000 processors and a distributed 280 TB memory.

The results here discussed were obtained with a CPU time higher than 7 hours on the Helios facility, showing a speed up (not taking into account the waiting time while queuing) of:

- about a factor of 1,33 vs MareNostrum;
- about a factor of 10 vs the Cassino facilities.

Fig. III.28 to Fig. III.31 show the current density, ohmic power and force distribution at various time instants (the effects generated by the asymmetric halo currents field are evaluated for sector #1, where the toroidal angle spans between $-20\ deg < \varphi < 20deg$).
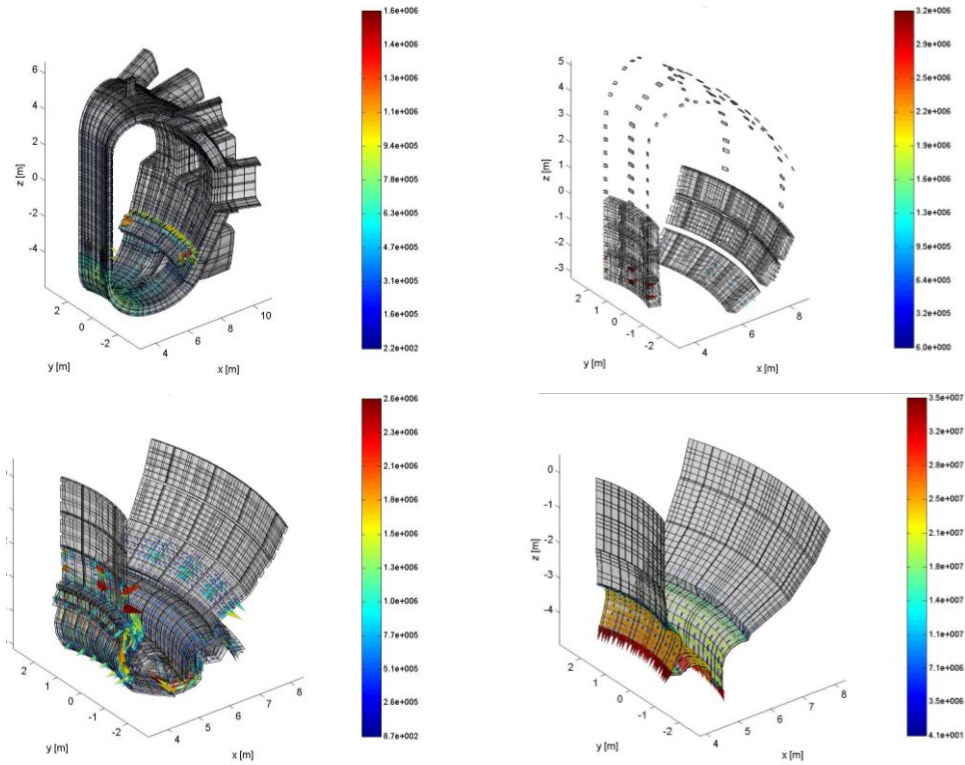
Fig. III.28: Asymmetric halo currents: current density distribution in Sector #1 at various time instants: Vessel (up-left, t = 1.155 s), Shielding blocks (up-right, t = 0.93 s), Front panels (down-left, t = 0.87 s) and Artificial shell (down-right, t = 1.1 s)
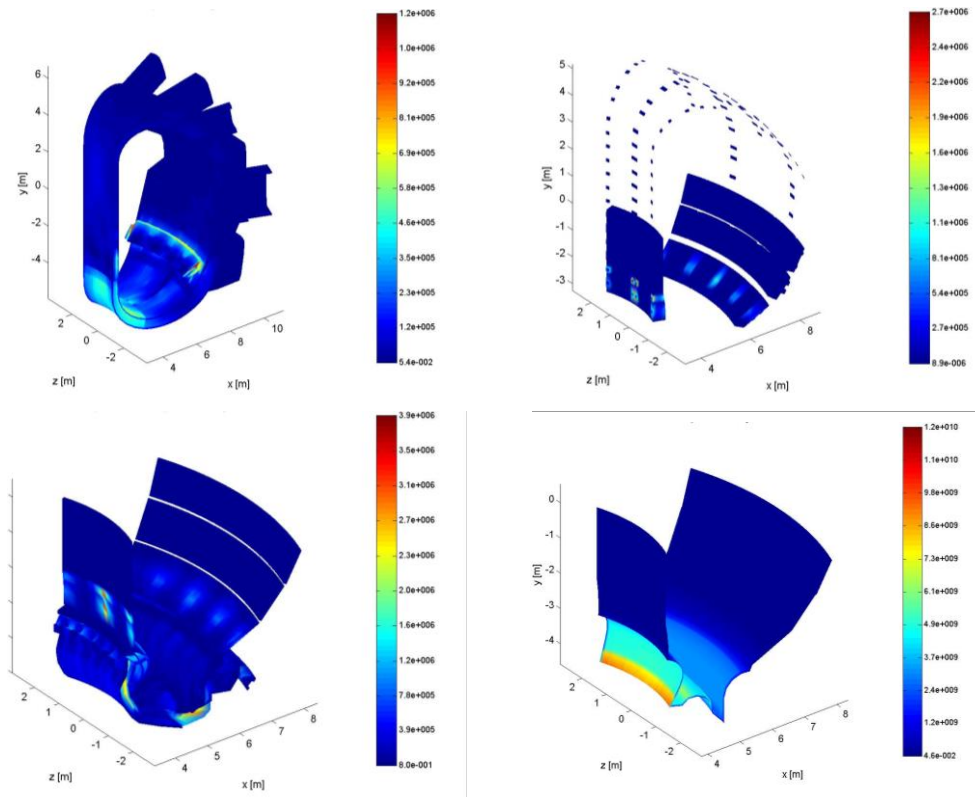
Fig. III.29: Asymmetric halo currents: ohmic power density distribution in Sector #1 at various time instants: Vessel (up-left, t = 1.155 s), Shielding blocks (up-right, t = 0.93 s), Front panels (down-left, t = 0.87 s) and Artificial shell (down-right, t = 1.1 s)
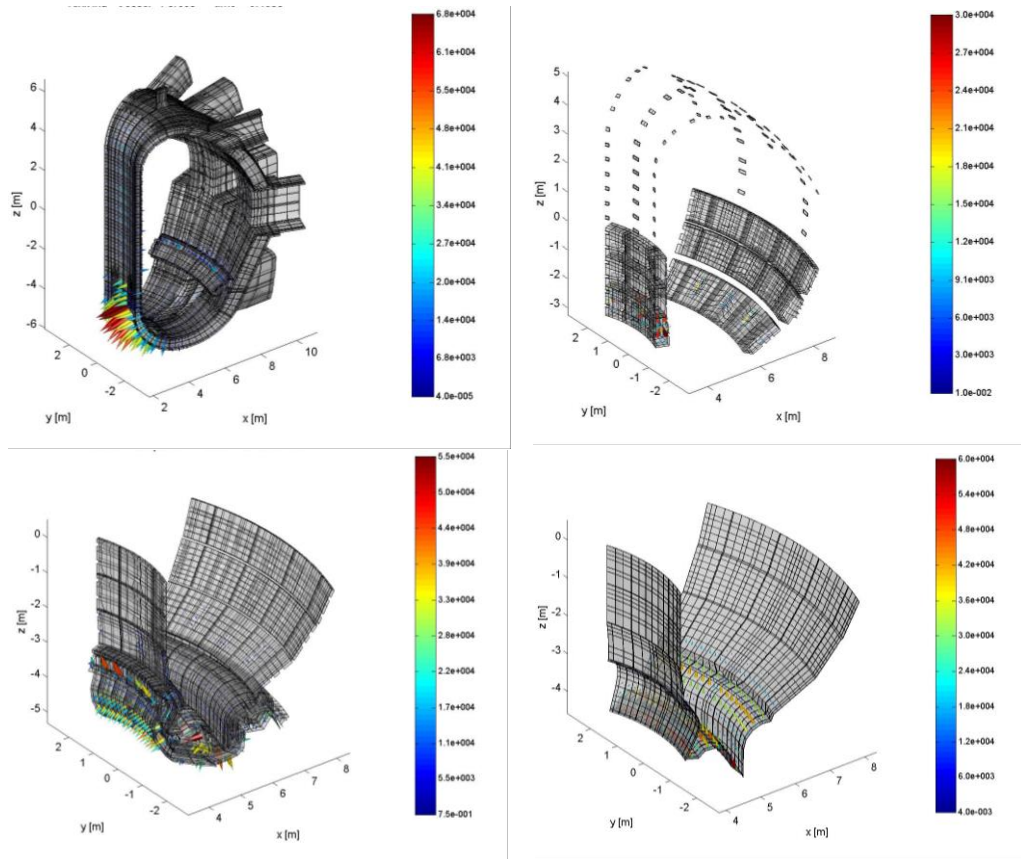
Fig. III.30: Asymmetric halo currents: force distribution on Sector #1 at various time instants: Vessel (up-left, t = 1.155 s), Shielding blocks (up-right, t = 0.93 s), Front panels (down-left, t = 0.87 s) and Artificial shell (down-right, t = 1.1 s)
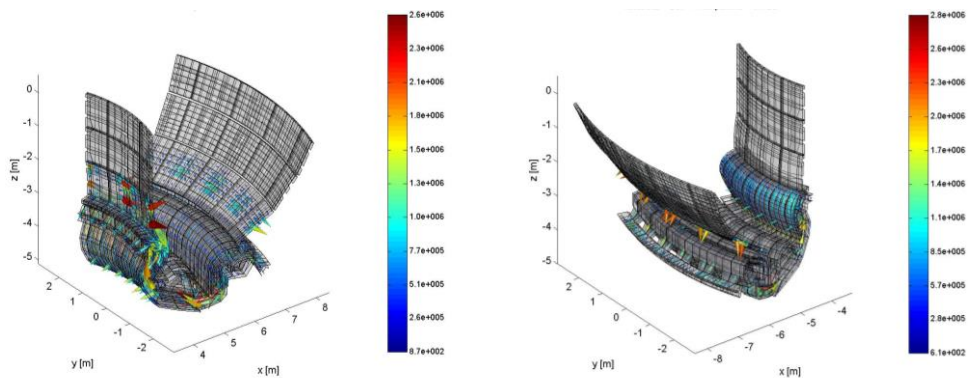
Fig. III.31: Asymmetric halo currents: current density distribution in the Front panels of Sector #1 (left, t = 0.87 s), and of the opposite part of the torus (right, t = 0.84 s)

Fig. III.32 and Fig. III.33 show the forces and the torques (the pivot point is the centre of the torus) on each sector, while Fig. III.34 shows the total force on the torus:
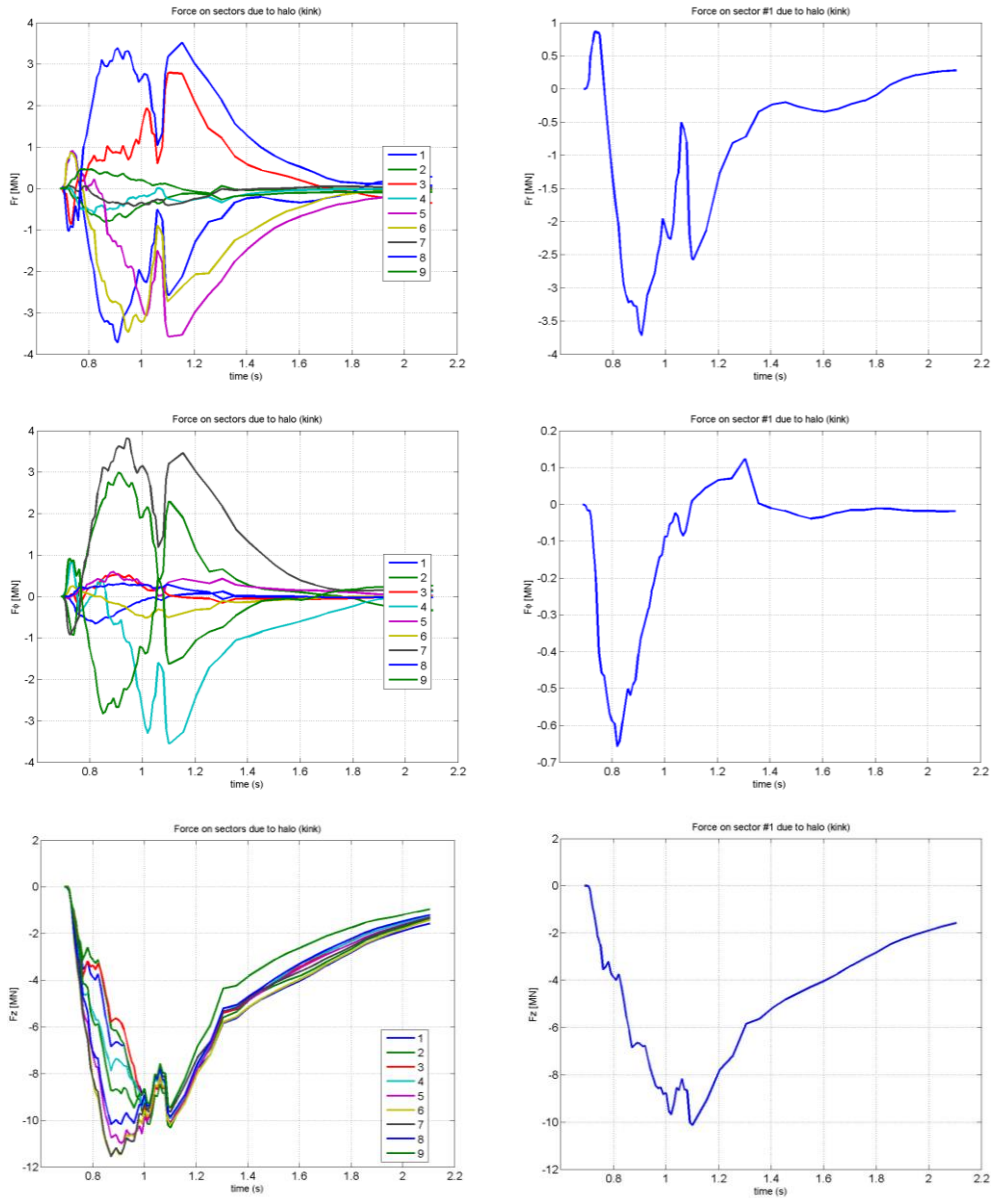
Fig. III.32: Asymmetric halo currents: time history of the radial, toroidal and vertical forces on each of the 9 sectors (left) and on Sector #1 (right)
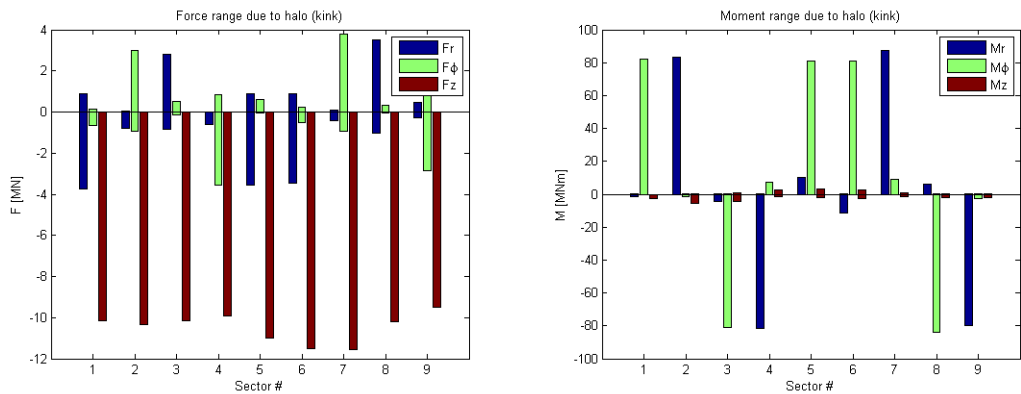
Fig. III.33: Asymmetric halo currents: forces and moments ranges in each of the 9 sectors
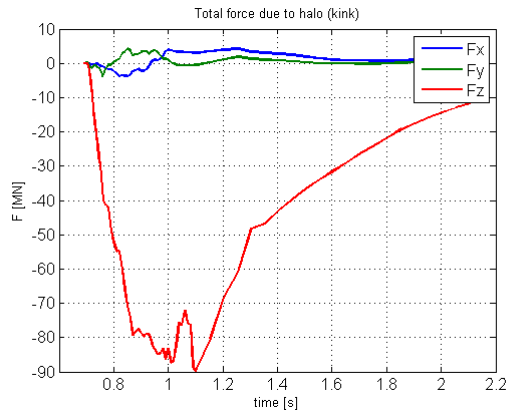
Fig. III.34: Asymmetric halo currents: time history of the total force on the passive structures

Fig. III.35 shows the range of the forces and the torques (the pivot point is the centre of the torus) on the divertor in each sector.

Fig. III.36 shows the total force on the divertor:
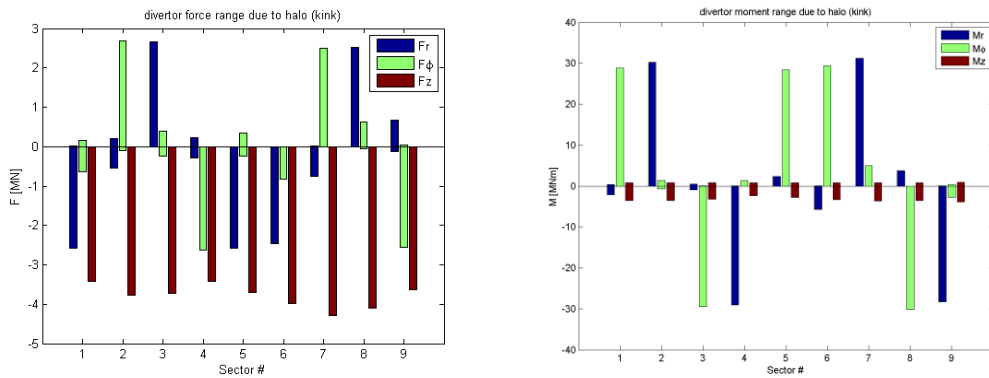
Fig. III.35: Asymmetric halo currents: forces and moments ranges on the divertor in each of the 9 sectors
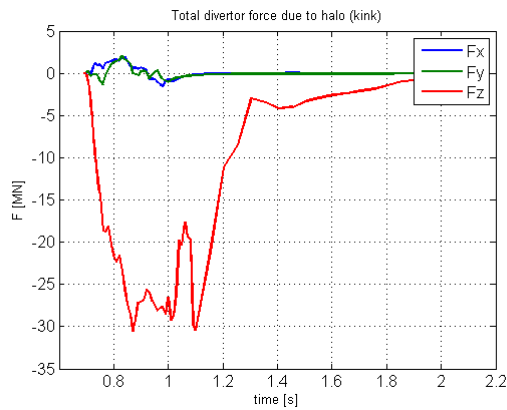
Fig. III.36: Asymmetric halo currents: time history of the total force on the divertor

At last, Fig. III.37 shows the approximation in the force calculation when neglecting the field generated by the halo currents:
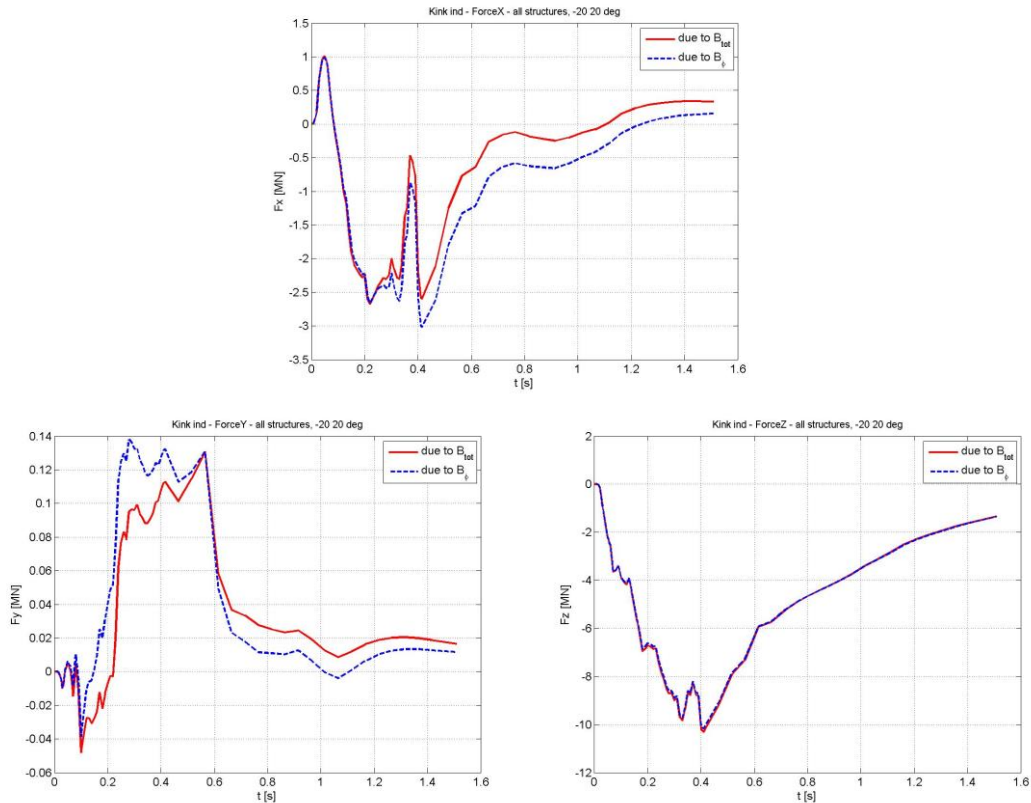
Fig. III.37: Asymmetric halo currents: time history of the forces on Sector #1 calculated including (solid) and neglecting (dashed) the magnetic field due to the halo currents.

Fig. III.37 shows that the approximation introduced when neglecting the field generated by the halo currents is less than 0.5 MN on Sector #1 (about 20% in this specific sector).

3.7 Kink inductive effects and related loads on vacuum vessel and divertor structure

Under the action of a kink, the plasma core starts moving thus making the mutual inductances between the plasma itself and the other surrounding conductors change.

To estimate these inductive effects, the plasma is modelled by means of a filamentary current located at the position of the plasma centroid at the time

instant $t = 0.85\,s$ (when $I_p = 11.7\,MA$ and $dI_p = 1.5\,MA$). The plasma motion is modelled two filamentary conductors:

1. one filament whose centre is located on the z-axis (i.e., not kinked) and whose poloidal coordinates are $R = 5.49m, Z = -2.13m$;

2. one filament tilted and shifted (i.e. kinked), with $R = 5.49m, Z = -2.13m$, $dx_2 = -0.15\,m, d\theta_{x_2} = 2.7\,deg$.

Since the effects of an axisymmetric plasma current were already depicted when studying the action of the PFV, the time evolution of the two currents $I_1(t)$ and $I_2(t)$ is prescribed as follows:

$$\begin{cases} I_1(t) = 11.7 \cdot 10^6 \dfrac{d\theta_x(t)}{d\theta_{x_2}(t)} \\ I_2(t) = -11.7 \cdot 10^6 \dfrac{d\theta_x(t)}{d\theta_{x_2}(t)} \end{cases} \qquad \text{(III.15)}$$

where $d\theta_x(t)$ is the same as in Fig. III.9.

With such definition, there is no effect when $d\theta_x(t) = 0$, whereas the filament carrying the current $I_1(t)$ partially compensates the effect of the axisymmetric plasma, when it attains its maximum value. In this way, the effective source is a kinked plasma when superposing the effects of these two filaments to the PFV effects.

It is worth noticing that the tilt is not around the x-axis as in the asymmetric halo case but another axis that is parallel to x-axis and passing at the point in the (y, z) plane having coordinates $y = 0\,m$ and $z = 2.13\,m$. However, the difference between the two assumptions is small, yielding a difference of about $2\,cm$ whereas the filament displacement is more than $25\,cm$ (Fig. III.38).
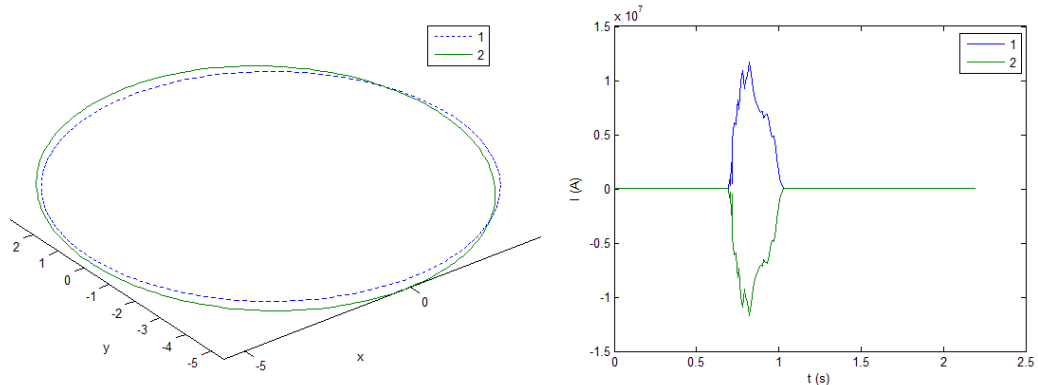
Fig. III.38: Location and currents of the two filaments for the computation of the inductive effects of the kink perturbation

As regards the electromagnetic loads, they were computed by considering the interaction of the axisymmetric magnetic field generated by the TF coils (static), the PF coils (dynamic) and the plasma (dynamic) with the induced currents.

Fig. III.39 shows the time history of the forces on each of the 9 sectors, whereas Fig. III.40 reports the range of the total forces and torques acting on each sector (the pivot point is taken at $x = y = z = 0$). Finally, Fig. III.41 shows the time behaviour of the total force.
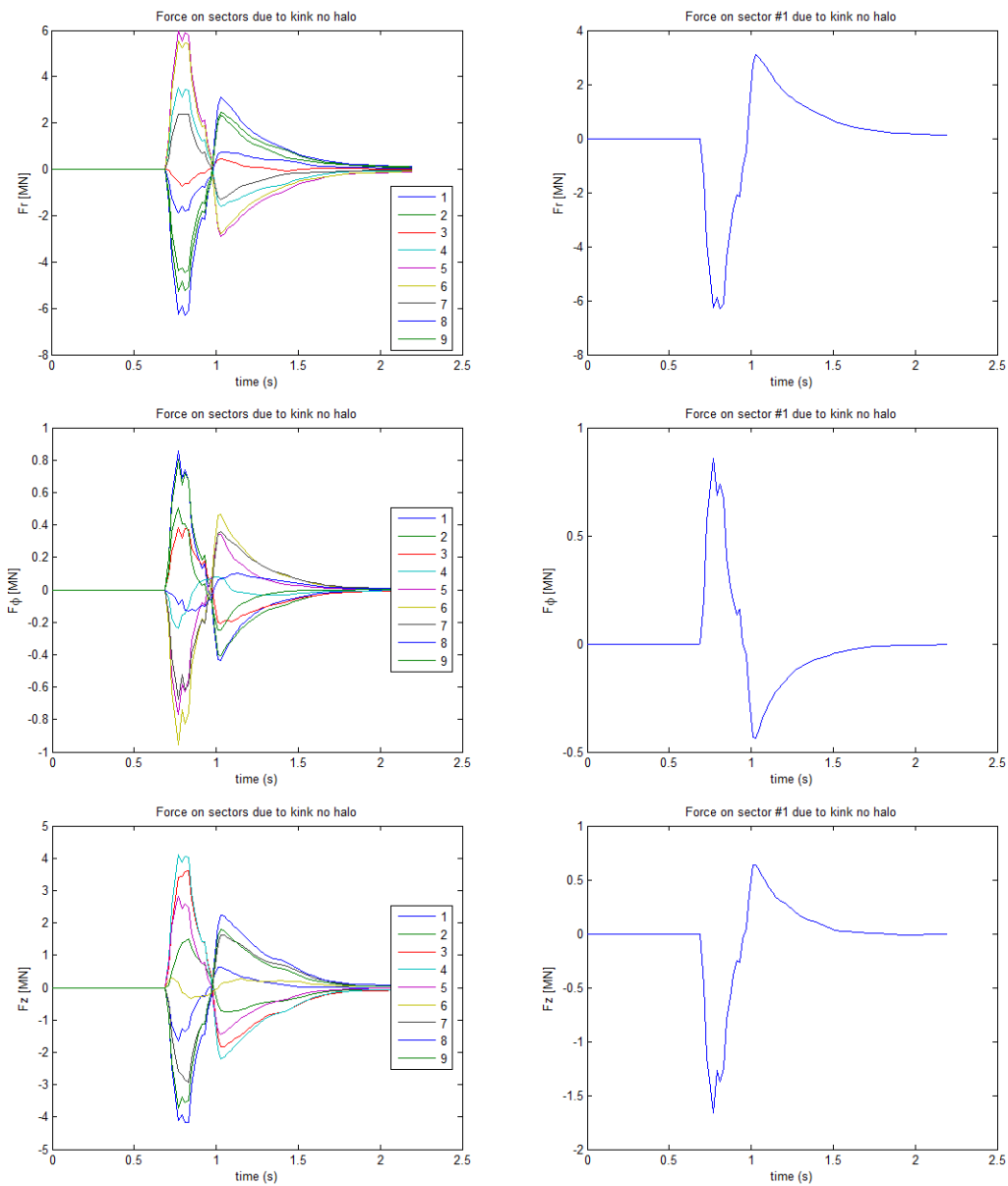
Fig. III.39: Kink inductive effect: time history of the radial, toroidal and vertical forces on each of the 9 sectors (left) and on Sector #1 (right)
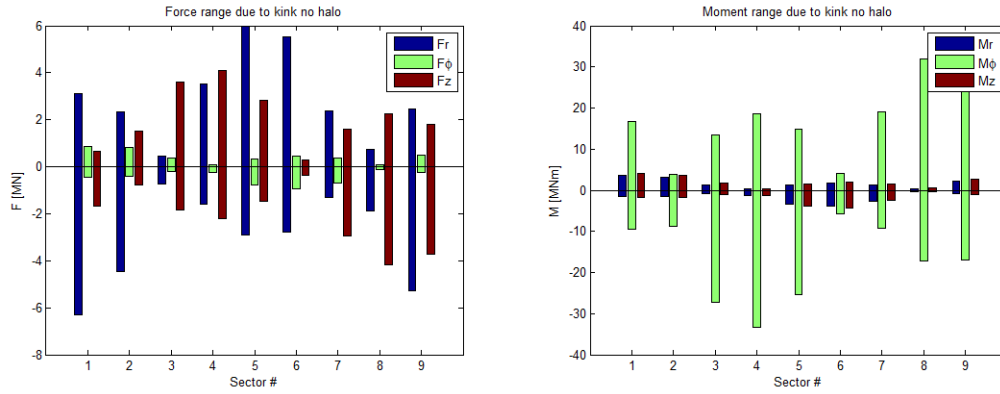
Fig. III.40: Kink inductive effect: forces and moments ranges on the divertor in each of the 9 sectors
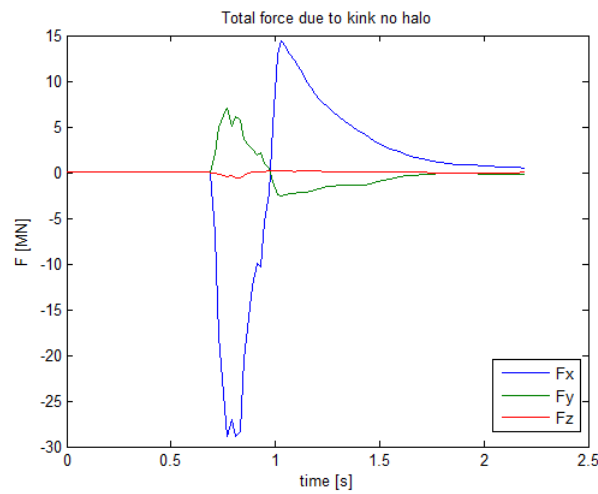
Fig. III.41: Kink inductive effect: forces: time history of the total force

3.8   Loads on TF coils

The calculation of the electromagnetic loads on the Toroidal Field Coils was carried out considering two different effects:

- the effects produced by the tilt of the plasma core;
- the asymmetric halo currents.

For the analysis of the plasma tilt without considering the halo currents, the same model described in Section 3.7 is used. The TF Coils are modelled as a single filamentary current having the shape of the actual windings and carrying the overall current $I_{TF} = 9.112$ MAturns. With such assumptions, a preliminary analysis by means of the COMPFLUX procedure (see Section 2.1) was performed to identify the most affected TF Coil in terms of electromagnetic loads.

The analysis was carried out firstly modelling the plasma as an axisymmetric filamentary current and evaluating the related electromagnetic loads on the coils, and then kinking it (the kink parameters are the maximum values attained by dx and $d\theta_x$ in Fig. III.9). The evaluation of the electromagnetic loads in terms of total net force and torque on each coil is carried out, then evaluating the difference between the two configurations:
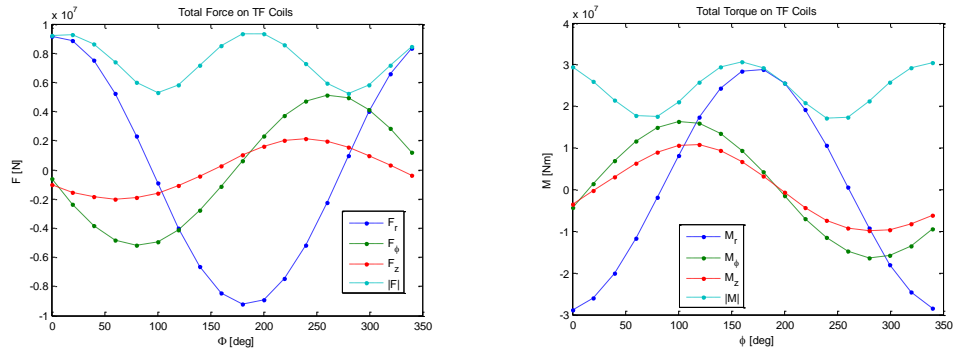
Fig. III.42: Load on TF Coils: Difference of forces and torques (the pivot point is the center of the torus) on each of the TF Coils between the axisymmetric and kinked configuration

Fig. III.42 shows that the most affected coils are in the poloidal sections with $\varphi = 0$ and $\varphi = \pi$. In Fig. III.43, the difference between the force distribution on the TF Coils in the axisymmetric and kinked configurations in the poloidal plane $\varphi = 0$ is exploited:
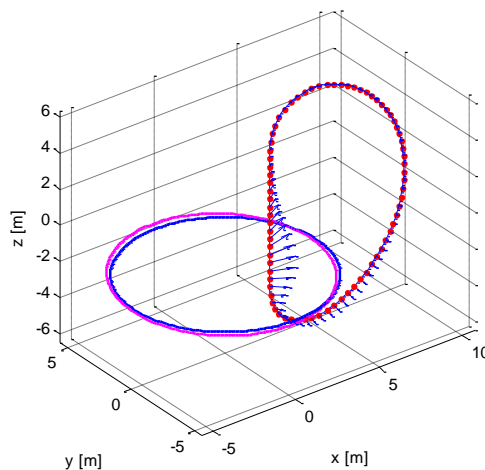
Fig. III.43: Force distribution on the TF Coil in the poloidal plane $\varphi = 0$; the axisymmetric filamentary plasma current (solid blue) and the kinked one (solid magent) are shown.

Basing on these results, the CARIDDI calculations were focused only on the TF Coil in Fig. III.43.

Fig. III.45 shows the effects of the halo currents, whereas Fig. III.44 shows the effects due to the tilt of the filament and the 3-D eddy currents induced by the tilt.
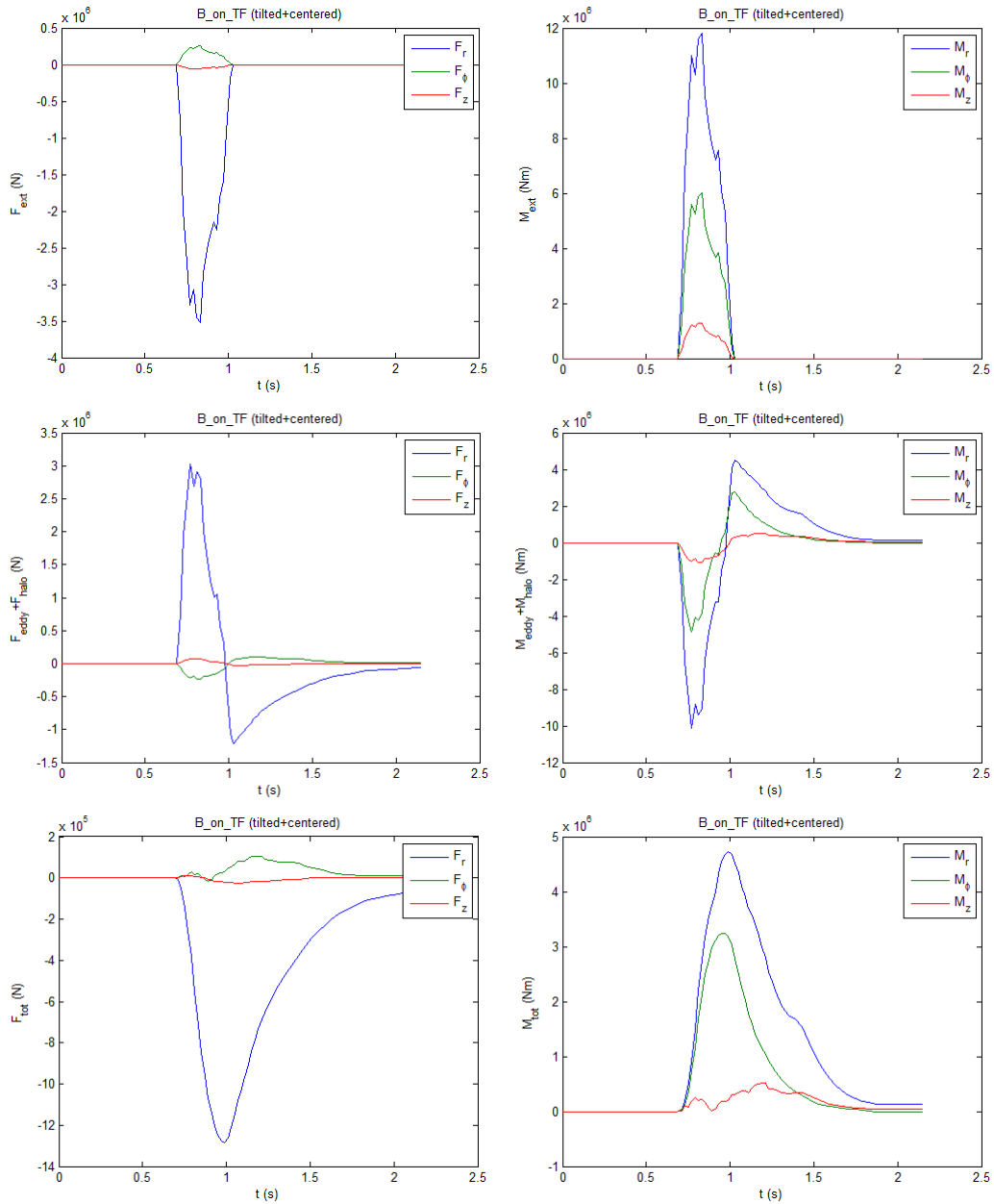
Fig. III.44: Effects on the TF coils due to the plasma kink in terms of forces (left) and moments (right): loads due to the field generated by the moving coil (top), loads due to the field of the eddy currents induced in the passive structure and the halo currents (center) and sum of the two contributions (bottom)
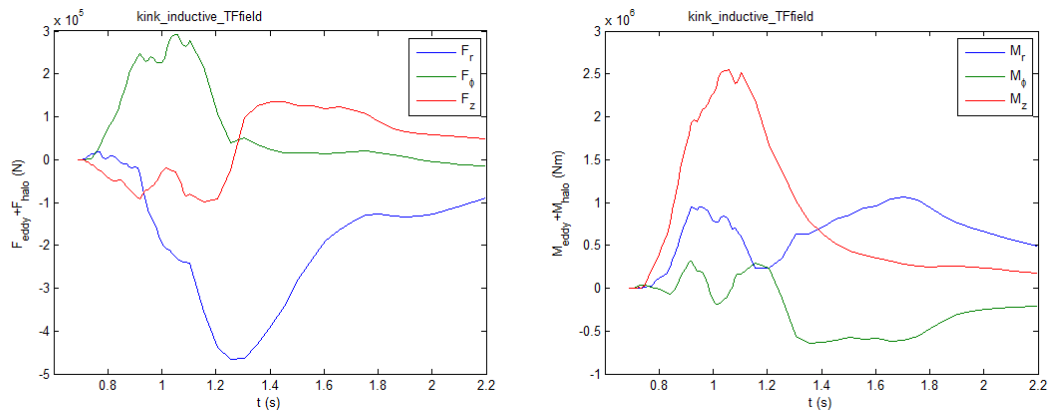
Fig. III.45: Effects in terms of forces (left) and moments (right) on the TF coil at $\phi = 0$ due to the 3-D halo currents distribution

Chapter 4

Field Lines Tracing and Identification of non-axisymmetric plasmas

The chapter is divided into three parts: the first part is devoted to the description of the CFTT procedure, designed and validated to trace the magnetic flux density field lines inside the tokamaks. The second part is aimed to the assessment of the algorithms for the plasma boundary reconstruction based on the field lines tracing, both for the axisymmetric and non-axisymmetric plasmas. At last, the chapter illustrates a new technique for the identification of non-axisymmetric plasmas and the study of their topology.

4.1   CFTT: a Numerical Suite for the 3-D Flux Density Field Lines Tracing in Tokamaks

The idea the Tokamak is based on, is the closure of the cylindrical solenoid to prevent the plasma particles to escape from the vacuum chamber. This particular geometry suggests a desirable condition for the operation of the plasma into tokamaks, that is the axisymmetry, very useful for many aspects of the tokamak engineering, e.g. the plasma modelling, the plasma stability and control or the mechanical and electromagnetic design.

Unfortunately, this ideal condition is so far to be verified while the plasma is burning: first, the structures surrounding the plasma are intrinsically non-axisymmetric (e.g., the Toroidal Field Coils are not a toroidally continuous solenoid, because of the need to have some space between two adjacent coils for the ports or other operations like remote handling). Then, the plasma itself is

often affected by many non-axisymmetric perturbations, e.g. a kink (as studied in Chapter III) or the ripple field generated by the TF Coils.

When an axisymmetric plasma has to be studied, we can solve the Grad-Shafranov equation, whose unknown is the poloidal flux per unit radian ψ. Using such formulation, this quantity is invariant on the flux density field lines, allowing to trace them by means of the isoflux lines in the poloidal plane.

If a non-axisymmetric perturbation affects the plasma, it is not possible to solve the Grad-Shafranov equation and the poloidal flux per unit radian is not invariant along the flux density field lines anymore. For this reason, the CFTT (CREATE Field Tracing in Tokamaks) procedure was set up, tested and validated with the aim to trace the flux density field lines both in axisymmetric and non-axisymmetric field configurations.

It consists of two main parts:

1. *Pre-processor*: its aim is to process the CREATE-NL or CREATE-L equilibria, performing an axisymmetric identification of the poloidal flux per unit radian, modelling the plasma by means of an equivalent set of axisymmetric filamentary currents.

2. *Processor*: it is the core of the procedure, devoted to the tracing of the magnetic flux density field lines and to the graphical processing of the results. The field data can be taken by:

    a. the numerical data available into the CREATE-NL or CREATE-L equilibrium files;

    b. the analytical reconstruction performed by the pre-processor;

    c. user-defined formulations.

4.1.1 CFTT Pre-processor

The pre-processor is aimed to the axisymmetric identification of the poloidal flux per unit radian, as known at the mesh points provided by the solution of the Grad-Shafranov equation. The following Fig. IV.1 shows a typical single-null equilibrium in DEMO tokamak, by means of the contour map of the magnetic flux per radian ψ:
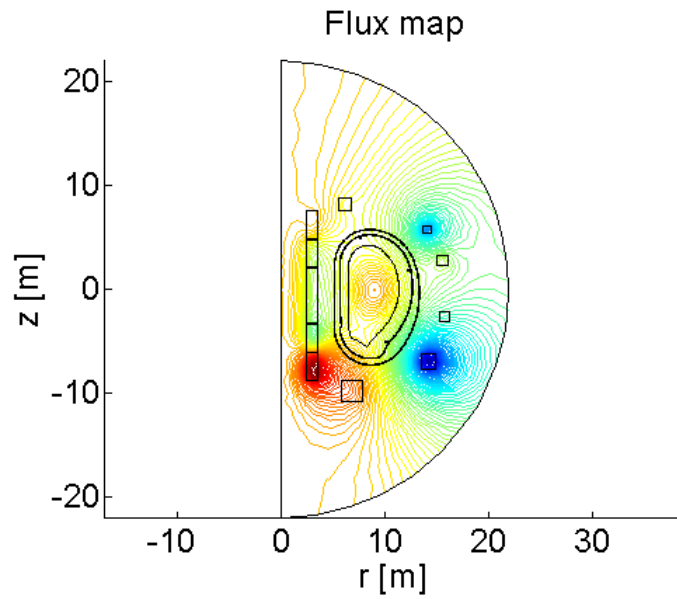
Fig. IV.1: Example of plasma equilibrium in DEMO tokamak (the solid black lines are the edges of the solid structures)

The plasma is modelled as a suitable set of equivalent axisymmetric filamentary conductor, whose positions and currents are calculated according to the best fit of ψ in a given set of points in the poloidal plane. Once the number of equivalent filament N_f is provided, their position is chosen in such a way that the convex hull of the polygon having the filamentary currents at its vertices has a similar shape to the plasma.

The separatrix geometry is provided by the equilibrium file so as the coordinates of its nodes; then, N_f nodes belonging to the plasma domain are chosen so to keep the ratio between the distance of two consecutive nodes of the plasma boundary and the distance of each filamentary current from the plasma boundary higher than a given value.

In this way, all the admissible filamentary currents are individuated, as shown in the following Fig. IV.2:
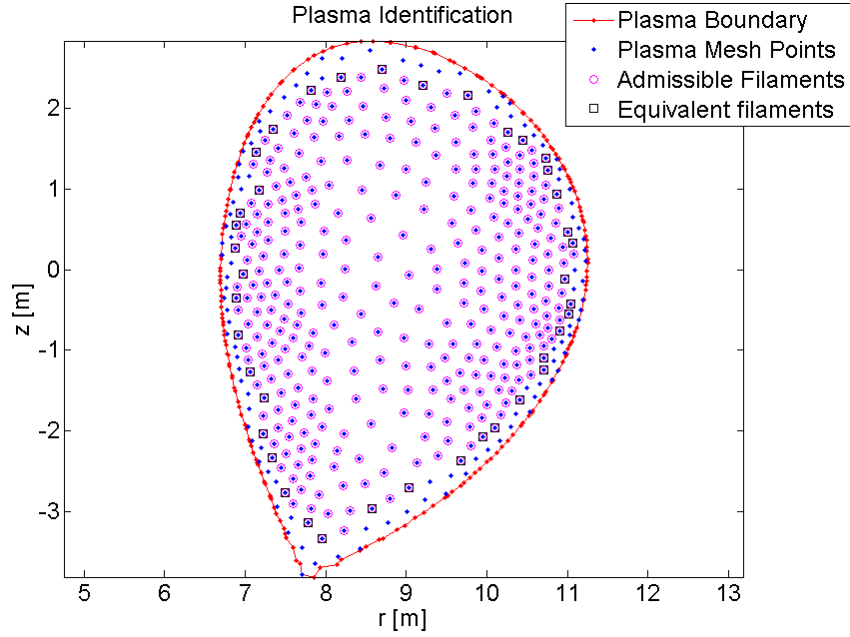
Fig. IV.2: Example of axisymmetric plasma identification

The choice of the filaments is based on the best fit of the values of the poloidal flux per unit radian at the plasma separatrix and at the first wall.

Once the positions of the filaments are fixed, the unknown of the identification problem are the currents carried by the sources. Therefore, the problem is linear and the value of the magnitude of the sources can be calculated via pseudo-inversion of the following linear model:

$$\underline{I} = \underline{\underline{M}} \cdot \underline{b} \qquad (\text{IV}.1)$$

where:

- $\underline{I}$ is the vector of the unknown currents;

- $\underline{\underline{M}}$ is the Green Matrix, that is the matrix of the poloidal flux per unit radian values generated at the plasma separatrix and at the first wall by each unitary source;

- $\underline{b}$ is the vector of the actual poloidal flux per unit radian values at the plasma separatrix and at the first wall.

A singular value decomposition of the Green matrix is performed to choice the most influent N_f currents, corresponding to highest N_f singular values.

The same procedure is then carried out to model the active coils surrounding the plasma: each coil consists of many mesh points, each carrying a

116

prescribed current, calculated from the specifications for the equilibrium. The active coil is thus modelled as a suitable set of equivalent filaments, carrying a current so to fit the actual values of poloidal flux per radian at the first wall point, generated by the actual sources.

The equivalent set of axisymmetric filamentary currents is the output of the pre-processor. An example is shown in the following Fig. IV.3:
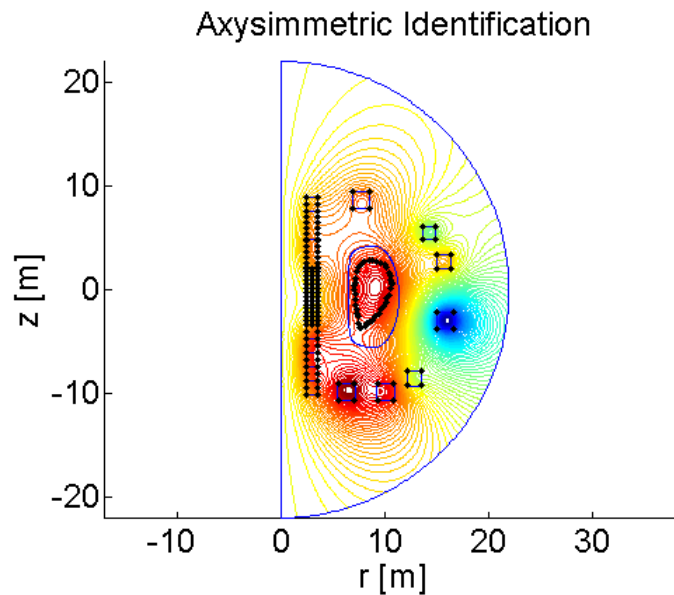
Fig. IV.3: Equivalent filamentary currents on the actual flux map

4.1.2   CFTT Processor

The main task of the CFTT Processor is to trace the flux density field streamlines inside the Vacuum Vessel, that is to calculate the coordinates of the points of the field lines.

The streamline of a given vector field is a family of curves defined into the 3-D space that are everywhere tangent to the vector field itself; their computation can be numerically performed by solving the following set of partial differential equations:

$$\begin{cases} \dfrac{\partial r}{\partial \varphi} = r \dfrac{B_r}{B_\varphi} \\[2ex] \dfrac{\partial z}{\partial \varphi} = r \dfrac{B_z}{B_\varphi} \end{cases} \tag{IV.2}$$

where B_r, B_φ and B_z are the radial, toroidal and vertical component of the flux density field respectively. The choice of using the cylindrical coordinate frame (r, φ, z) guarantees the toroidal angle φ to be a continuous function along the whole integration.

The structure of the equation (IV.2) can be simplified if we note that the magnetic flux density field $\boldsymbol{B}$ is divergence-free as well as the velocity vector field for incompressible fluids in stationary conditions $(\nabla \cdot \boldsymbol{B} = 0 \leftrightarrow \nabla \cdot \boldsymbol{v} = 0)$. Therefore, the flux density field line tracing problem into the problem is analogous to that of tracing the trajectories of the particles of a Lagrangian fluid in stationary conditions.

Therefore, the problem in equation (IV.2) can turned into the following autonomous Cauchy Problem:

$$\begin{cases} \dfrac{\partial r}{\partial \tau} = B_r(r, \varphi, z) \\[2ex] \dfrac{\partial \varphi}{\partial \tau} = \dfrac{1}{r} B_\varphi(r, \varphi, z) \\[2ex] \dfrac{\partial z}{\partial \tau} = B_z(r, \varphi, z) \\[1ex] (r, \varphi, z)|_{\tau=0} = (r_0, \varphi_0, z_0) \end{cases} \tag{IV.3}$$

where τ is not a physical time (its unit is $\frac{m}{T}$), but is the integration parameter.

The CFTT processor is so devoted to the numerical solution of the Ordinary Differential Equation (ODE) in (IV.3), starting from a specified initial condition. It is worth noticing that the general form of the problem in (IV.3) is not dependent on any symmetry condition of the flux density field configuration, that is, the same problem is solved for both the axisymmetric and the non-axisymmetric fields.

The procedure allows to perform a very flexible integration because it is possible to set:

1. the initial condition: the starting point can be chosen in several ways:
   a. manually, providing a given set of starting points;
   b. evenly spaced along a prescribed direction;

c. evenly spaced along the radial and angular directions over a circumference, whose centre is given;

d. at the points of a rectangular grid inside the first wall on the poloidal plane;

2. the type of integrator among:

a. built-in MATLAB standard integrators (e.g. ODE23, ODE45, ODE113 and others);

b. properly designed integrators by the user (e.g. geometric integrators);

3. the vector field to integrate defined:

a. numerically, as given by the values of ψ on the mesh points provided by the CREATE-NL/CREATE-L equilibrium files;

b. by calculating the flux density field generated by a set of axisymmetric filamentary currents;

c. by user-defined expressions for the flux density field components.

4. all the integration parameters (e.g. Integration Step, Integration Length and Accuracy).

Once the integration is terminated, the data are processed to calculate many other quantities related to the integrated field lines, as the Connection Length: by definition, the *Connection Length* is the length of the trajectory covered by the plasma particles overall a magnetic field line up to its eventual intersection against the first wall, from a given starting point.. If the Larmor radius (see equation (I.7)) is neglected (about $10^{-4}\ m$ for the protons and about $10^{-6}\ m$ for the electrons), the trajectory covered by the plasma particle is coincident with the flux density field line. Therefore, the connection length is the length of the traced field line from the initial condition (the starting point) up to its eventual intersection with the first wall.

Another very important output for the study of the topological properties of the flux density field configuration is the Poincaré Map: by definition, a *First Recurrence Map* or *Poincaré Map* is the intersection of a periodic orbit in the state space of a continuous dynamical system with a given lower–dimensional subspace (namely *Poincaré Section*), transversal to its flow. More precisely, considering a periodic orbit having the initial condition within a section of the

space, the Poincaré Map consists of the collection of all the points, which the orbit returns to that given section at. The property of the Poincaré Section to be transversal means that the periodic orbits starting on a given subspace flow through it and not parallel to it.

A Poincaré map can be interpreted as a discrete dynamical system with a state space that is one dimension smaller than the original one. It preserves many properties of periodic and quasi-periodic orbits of the original dynamical system and has a lower-dimensional state space; for this reason, it is often used to analyse it, as for the plasma shape in non-axisymmetric field configurations.

In fact, if the flux density field configuration is 2-D axisymmetric, the plasma shape (that is the shape of the plasma boundary) is exactly the same in any poloidal section ($0 \leq \varphi \leq 2\pi$). Therefore, if the plasma shape is known for one poloidal section, it is everywhere. If the flux density field configuration is 3-D, in principle, the plasma shape is different in all the poloidal sections (except for periodic perturbations or other particular configurations), but it can be easily reconstructed if the field line tracing algorithm is exploited with the Poincaré Maps (see Section 4.3).

At last, if the plasma equilibrium configuration is loaded, both from CREATE-NL/CREATE-L files, the processor performs a precision analysis too, basing on the concept that the poloidal flux per unit radian ψ is invariant along the field lines. This analysis basically consists of the evaluation of ψ overall the points of the traced field line and the subsequent calculation of the maximum absolute error on the flux values: obviously, the lower is the difference value, the more accurate is the integration.

At this stage, the data are ready to be processed by the graphical processor, devoted to the graphical elaboration of all the main results provided by the pre-processor and processor. In particular, after showing the flux map in the poloidal plane (as in Fig. IV.1 and in Fig. IV.3, for the axisymmetric field configurations only), the traced field line into the three-dimensional space and its projection on the poloidal plane is drawn.
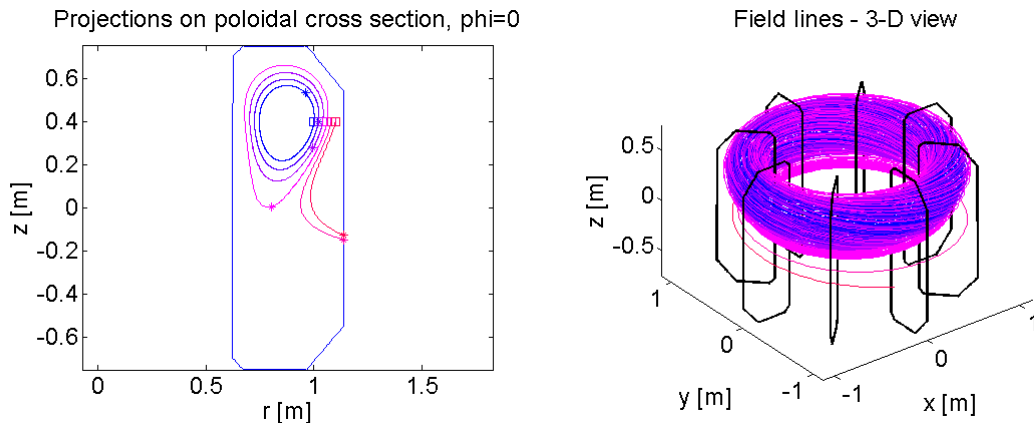
Fig. IV.4: Field Line Traced: Projection on the Poloidal cross section of many traced lines (blue-red transition), starting points (squares) and final points (stars) and 3-D view

Fig. IV.4 shows many traced lines and their different topology: in particular it is possible to see that the blue to magenta drawn lines do not intersect the first wall, whilst the magenta to red drawn lines do. The same topology is evidenced in the 3-D view.

In the following Fig. IV.5, an example of Poincaré map is shown: the integrated flux density field consists of the superposition of that of a toroidal solenoid surrounding the Vacuum Vessel and that of an axisymmetric filamentary current, located at $(r, z) = (9,0)$ and affected by a $0.5\ m$ shift along the x axis:
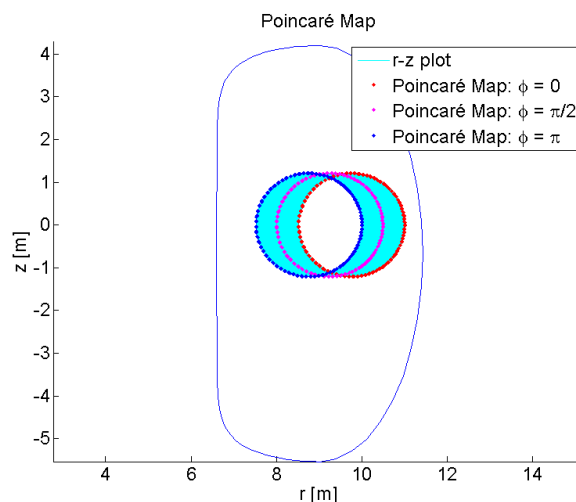
Fig. IV.5: Example of Poincaré maps for a non-axisymmetric configuration

4.1.3   Test Cases and Assessment of the CFTT Procedure

4.1.3.a   Plasma Breakdown in JET Tokamak

The following case refers to the plasma breakdown in JET Tokamak (pulse #78369) [53].

The breakdown is the initial phase when the plasma column starts creating inside the vacuum vessel. Therefore, the more the plasma particles interact each other, the more energy can yield to the plasma, letting it burn. This condition is turned into the need for the plasma particles to have high connection lengths, so to be contained into the plasma as much as possible. For these reasons, it is necessary to calculate the connection length of the plasma particles as well as their trajectory inside the vacuum vessel.

Fig. IV.6 shows the projection of the traced field line on the poloidal plane and its 3-D view.
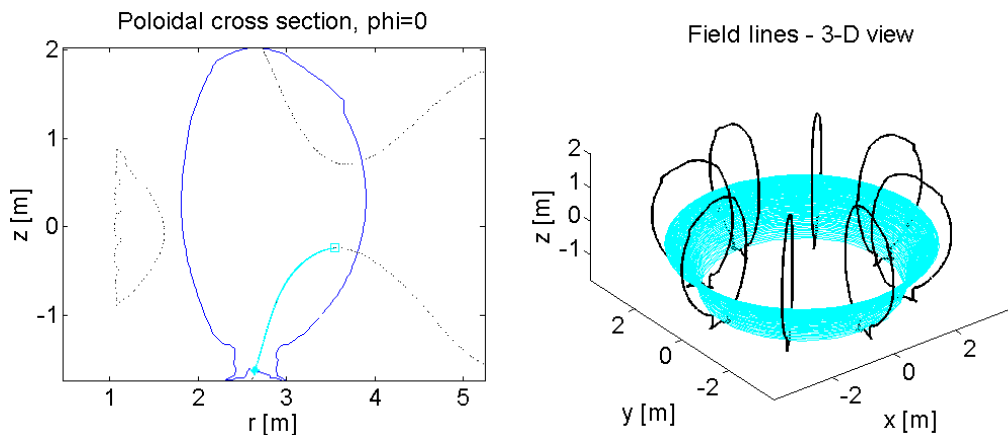
Fig. IV.6: Projection on the Poloidal cross section of a flux density field line in breakdown in JET Tokamak (pulse #78369) and its 3-D view

For the traced field line, the connection length is about $1000\ m$ from the starting point at $(r_0, \varphi_0, z_0) = (3.54, 0, -0.24)$. This parameter can be used as a design constraint for future breakdown configurations in the currently operative tokamaks (as the JET tokamak in this test case), as well as for the optimal design of the future ones (as for DEMO and DTT).

In Fig. IV.7, the numerical null point and the analytic null point (given by the ψ map generated by the axisymmetric filamentary currents) are compared:
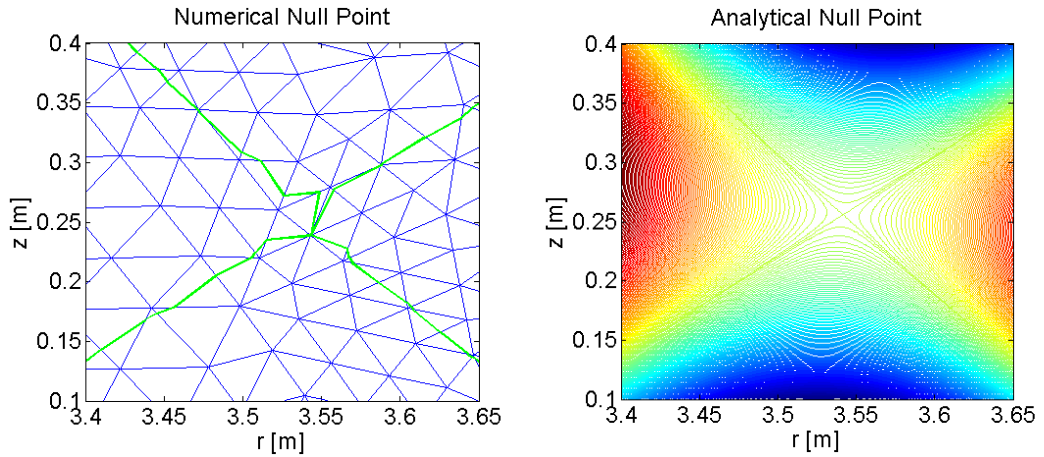
Fig. IV.7: Null Point in Pulse #78369 both in the numerical and analytical reconstruction

4.1.3.b   Scrape-Off Layer analysis in DEMO Tokamak

DEMO Tokamak will be a milestone in the nuclear fusion research because it will be the first nuclear fusion power plant. Moreover, one of its aims will be to exploit the advanced configuration of the plasma, as for many other tokamaks currently operated (e.g. TCV in Lusanne).

Contrary to the previous test case, the presence of the plasma inside the vacuum vessel makes of crucial importance the calculation of the connection length of the flux density field lines along both the clockwise and counterclockwise directions. This need is due to the presence of a *Stagnation Point* (a point inside the vacuum vessel where the plasma parallel speed to the flux density field $v_\parallel$ is zero) in the configurations with an X-point, located in the lower part of the chamber [54].

When the heat loads are to be evaluated (e.g. on the divertor tiles and on the other components of the vacuum vessel), it is crucially important to trace the flux density field lines outside the plasma, from the stagnation point in both the two directions, so to calculate the *Strike Points* (intersection point between the field line and the first wall) and the subsequent thermal flux per unit surface.

Assuming the stagnation point lying on the equatorial plane, and the Scrape-Off Layer (SOL) depth at the same plane $\lambda_q = 20\ mm$ [55], the following Fig. IV.8 shows the traced trajectories in both the directions. The starting point set is chosen using a logarithmic spacing along the SOL depth on the poloidal plane $\varphi = 0$:
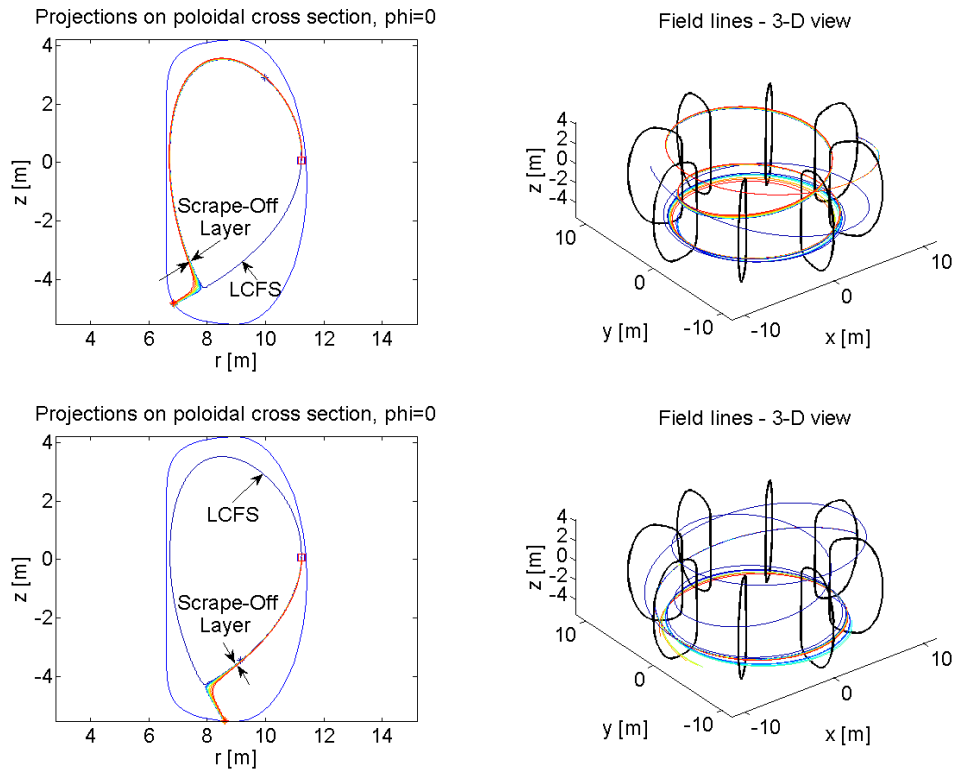
Fig. IV.8: Equilibrium "*Equil_EOF_betapol0d8_li0d7_11coils_final2*" - Field line tracing in a Scrape-Off Layer of 20 mm at the outer plasma boundary: Projection on the Poloidal cross section and 3-D view for the clockwise (upper row) and counterclockwise (lower row) field configuration with specification to the Scrape-Off Layer and to the Last Closed Flux Surface (LCFS).

The following Tab. IV.1 shows the results in terms of Connection Length for all the traced field lines in both the directions and the poloidal coordinates of their Strike Points:

Tab. IV.1: Connection Lengths in clockwise and counterclockwise directions

Start Points		Connection Length Clockwise [m]	Connection Length Counterclockwise [m]	Strike Point (clockwise)		Strike Point (counterclockwise)	
R [m]	Z [m]			R [m]	Z [m]	R [m]	Z [m]
11.2247	0.061	108.1	179.7	8.572	-5.520	6.882	-4.851
11.2253	0.061	107.6	176.8	8.574	-5.520	6.880	-4.848
11.2261	0.061	106.7	176.1	8.576	-5.520	6.850	-4.848
11.2270	0.061	103.9	171.6	8.579	-5.521	6.876	-4.843
11.2283	0.061	102.4	165.2	8.580	-5.521	6.874	-4.840
11.2299	0.061	85.8	155.4	8.587	-5.521	6.870	-4.835
11.2320	0.061	85.3	154.9	8.592	-5.522	6.866	-4.830
11.2347	0.061	84.2	154.1	8.599	-5.522	6.861	-4.823
11.2382	0.061	79.8	149.4	8.612	-5.523	6.855	-4.812
11.2427	0.061	74.9	143.6	8.625	-5.524	6.846	-4.797

4.1.3.c   Three-Dimensional Non-Axisymmetric Field

The chosen three-dimensional test cases refers to a Stellarator Plasma, where the field configuration is intrinsically non-axisymmetric even during normal operations, because of the non-axisymmetric coils surrounding the Vacuum Vessel.

The aim of this kind of simulations is to exploit the Poincaré Maps to study the topological properties of the magnetic flux density field configuration. Hereafter, a typical field configuration is shown by means and the 3-D view of a field line of the Poincaré Maps:
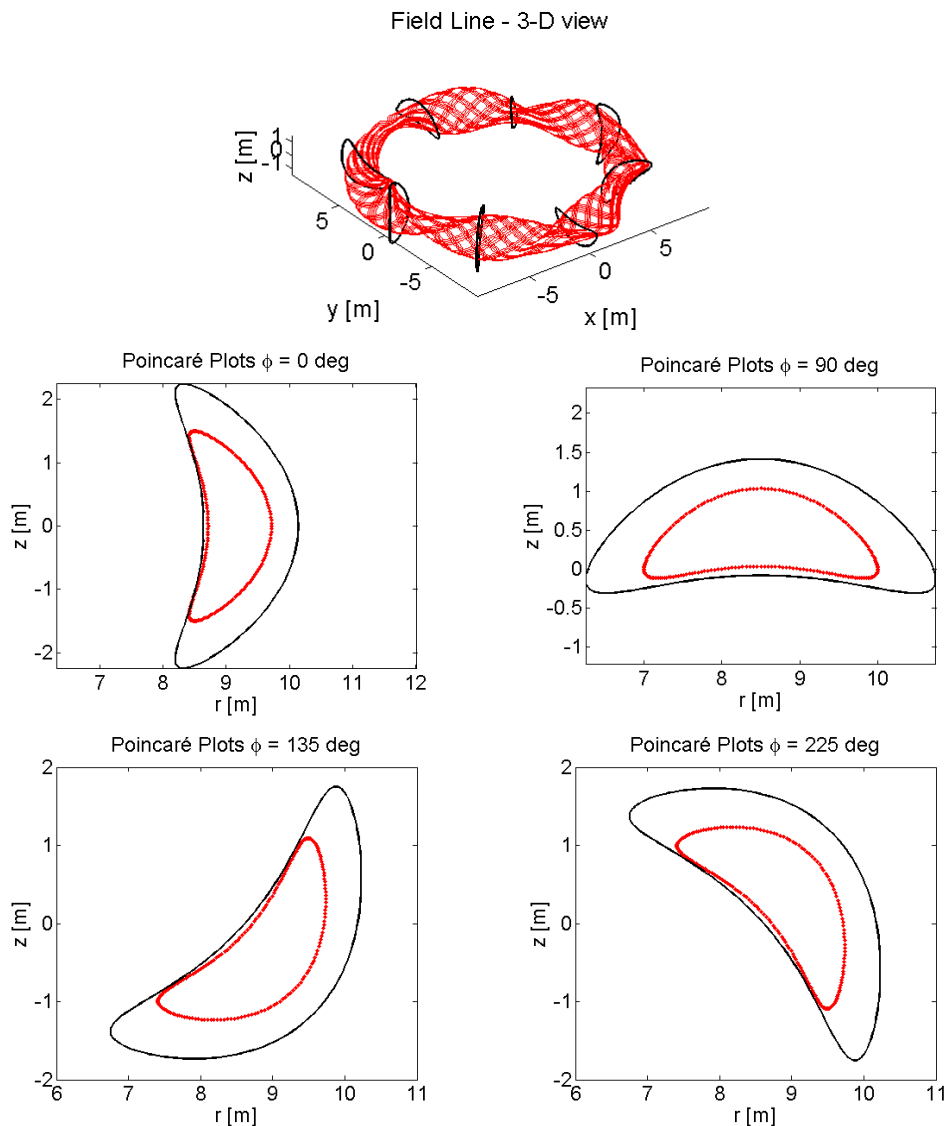
Fig. IV.9: Example of a three dimensional plasma configuration: Three-dimensional view of the field line (red dots) inside the Vacuum Vessel (top) and four examples of Poincaré Plots (middle and bottom)

It is worth noticing that the Poincaré Plots are all different because of the non-axisymmetry of the field configuration, so as the geometry of the Stellarator first wall, that is also intrinsically non-axisymmetric.

4.2   Geometric Integration of Flux Density Field Lines in Tokamaks

The problem of the tracing of the flux density field lines has a crucial importance when realistic estimations of 3-D plasmas are to be carried out, in terms of plasma shape, plasma-wall gaps or heat loads on the structures.

It is worth recalling that the hypothesis of axisymmetry is actually broken by many three dimensional effects present during normal operations too (e.g. ripple field generated by the Toroidal Field Coils, Eddy Currents into the Vacuum Vessel, ferromagnetic inserts, not to mention the non-axisymmetric control coils, as the ELM Coils). For this reason, the setup of a reliable numerical procedure able to trace very long flux density field lines is mandatory for the study of the 3-D configuration [53]-[56]-[57]-[58]-[59]-[60]-[61].

The problem may be in principle trivial, if recognized as the solution of the ODE flow in (IV.3), but is actually challenging if considering the very long field lines to trace (up to $10^3 \ m$) at an affordable computational cost [62] and showing high performances (an error lower than $10^{-3} \ m$ overall the integration length), thus achieving a relative precision of 10^{-6}.

The problem of long-term integration of ODE sets is faced in several science areas, devoting many efforts to improve the performances and the properties of the numerical algorithms and mainly of the so-called *Geometric Integrators* [62]-[63]-[64]-[65]-[66]-[67]. Their task is to integrate the given vector field while preserving in the numerical solution some average properties the analytical flows shows.

Besides these considerations, a high accuracy of each single line traced is mandatory for a reliable estimation of the quantities under investigation. For this reason, it is very important to assess the performances of the integrators called to the task of tracing the flux density field lines in full 3-D field configurations.

4.2.1 Volume-Preserving Integrators for divergence-free vector fields

In section 4.1.2, the problem of tracing the flux density field lines was turned into the solution of a Cauchy Problem thanks to the property of the flux density field to be divergence-free. Therefore, an accurate solution of (IV.3) is needed, also for very long integration lengths, at an affordable computational burden, once the required spatial resolution for the plasma boundary reconstruction is assigned.

Standard ODE integrators could be used to solve this problem, but a strict control and verification of the integration error is needed to ensure reliable results, as well as the preservation of intrinsic invariant properties in the numerical solution, as the divergence-free structure of the flux density field. The correct solution of equation (IV.3) is *Volume Preserving*, like for Lagrangian trajectories in incompressible fluids. Such similarity can be used to explain what Volume Preservation means:

"Consider the fluid molecules which initially form a certain figure F_0; when these molecules are displaced, their ensemble forms a new figure which will be deformed in a continuous manner, and at the instant t the envisaged ensemble of molecules will form a new figure F."

J.H. Poincaré, Celestial Mechanics, 1899

If the transformation that moves the fluid molecules along the time line is volume preserving, the new figure F can be obtained via a similitude transformation acting on the initial figure F_0 and is characterized by the same volume.

The ODE set in equation (IV.3) is divergence-free (or source-free) if the divergence of the source term is zero everywhere. Let $\underline{dB} = \left\{ \frac{\partial B_i}{\partial x_j} \right\}$ be the derivative of the field and $\underline{\underline{A}} = \frac{\partial \varphi_\tau}{\partial x}$ the Jacobian of its flow, evolving accordingly the following equation:

$$\begin{cases} \dfrac{dA}{d\tau} = dBA \\ A(0) = I \end{cases} \qquad\qquad \text{(IV.4)}$$

where I is the identity matrix.

It is possible to show that:

$$\frac{d}{d\tau} det(A) = tr(dB)det(A) \qquad\qquad \text{(IV.5)}$$

and so, if $\nabla \cdot \boldsymbol{B} = 0$, then: $det(A) = 1$ overall the integration and the flow is volume preserving. Therefore, the numerical integrator is volume preserving (VP) if:

$$det\left(\frac{\partial \psi_\tau}{\partial x_j}\right) = 1 \qquad\qquad \text{(IV.6)}$$

where ψ_τ is the mapping of the numerical method.

A way to implement volume preserving integration schemes, thus guaranteeing a priori the volume invariance is the *Generating Function* approach. It exploits some properties of the given source field, in order to generate many auxiliary vector fields to be integrated, and so to guarantee the invariance of the volume. In particular, a *Vector Potential Splitting Method* was set up: following its procedure, the 3-D flux density field is split as the sum of three 2-D divergence-free vector fields as properly obtained from a vector potential $\boldsymbol{B} = \nabla \times \boldsymbol{A}$ (with the Coulomb gauge), which are then integrated via any symplectic method. Since the property to be symplectic implies the algorithm to be volume preserving for 2-D flows (thus *Area Preserving*), the invariance of the volume overall the integration is guaranteed.

The expression of both the flux density field and the vector potential in the Cartesian coordinates frame makes possible to consider the following splitting:

$$\begin{cases} \boldsymbol{B}_1 = \nabla A_x \times \hat{x} \\ \boldsymbol{B}_2 = \nabla A_y \times \hat{y} \Rightarrow \boldsymbol{B} = \boldsymbol{B}_1 + \boldsymbol{B}_2 + \boldsymbol{B}_3 \\ \boldsymbol{B}_3 = \nabla A_z \times \hat{z} \end{cases} \qquad\qquad \text{(IV.7)}$$

Each $\boldsymbol{B}_i$ component is 2-D because the stream function of the i-th ODE set has no component along one axis ($\hat{x} \cdot \boldsymbol{B}_1 = 0$, $\hat{y} \cdot \boldsymbol{B}_2 = 0$ and $\hat{z} \cdot \boldsymbol{B}_3 = 0$) and the corresponding ODE set is Hamiltonian (with A_x, A_y and A_z the respective Hamiltonians). As consequence of the Liouville Theorem, the area is preserved in the phase space of each 2-D ODE set. Therefore, each $\boldsymbol{B}_i$ field is divergence-

free and so the ODE set can be integrated via any symplectic (area preserving) numerical integrator, thus assuring the preservation of the solenoidal structure of the initial ODE set.

For such problem, the Midpoint Rule (MR) with step h is symplectic (area preserving) [64]-[65]:

$$x_{i,k+1} = x_{i,k} + h B_i \left(\frac{x_{i,k+1} + x_{i,k}}{2} \right) \tag{IV.8}$$

where $x_{i,k}$ and $x_{i,k+1}$ are the positions at the steps k and $k+1$ for the integration of the i-th B_i component of the field.

This can be easily verified by calculating the Jacobian Matrix associated to the vector transformation in equation (IV.8):

$$J_i = \frac{\partial x_{i,k+1}}{\partial x_{i,k}} = \left(1 - \frac{h F_i}{2} \right)^{-1} \left(1 + \frac{h F_i}{2} \right), F_i = \frac{\partial B_i}{\partial x_{i,k}} \tag{IV.9}$$

and verifying that it has unitary determinant (the subscript i identifies the corresponding field component), being $Tr(F_i) = \nabla \cdot B_i = 0$:

$$\det(J_i) = \frac{1 + \dfrac{h}{2} Tr(F_i) + \dfrac{h^2}{4} \det(F_i)}{1 - \dfrac{h}{2} Tr(F_i) + \dfrac{h^2}{4} \det(F_i)} = \frac{1 + \dfrac{h^2}{4} \det(F_i)}{1 + \dfrac{h^2}{4} \det(F_i)} = 1 \tag{IV.10}$$

The following composition of symplectic mappings for the solution of the given ODE set:

$$x_{k+1} = \varphi_{\tau_{1,k+1}}(x_{i,k}, h) \circ \varphi_{\tau_{2,k+1}}(x_{1,k+1}, h) \circ \varphi_{\tau_{3,k+1}}(x_{2,k+1}, h) \tag{IV.11}$$

is a 3-D volume preserving mapping, since the total Jacobian determinant is the product of the unitary Jacobian determinants associated to each of the three integration sub-steps (IV.8). To improve the order of accuracy of such scheme, it is possible to formulate a second order accuracy multistep algorithm, by means of the following five 2-D mappings:

$$
\begin{aligned}
x_{k+1} = &\varphi_{\tau_{1,k+1}} \left(x_{i,k}, \frac{h}{2} \right) \circ \varphi_{\tau_{2,k+1}} \left(x_{1,k+1}, \frac{h}{2} \right) \circ \varphi_{\tau_{3,k+1}}(x_{2,k+1}, h) \\
&\circ \varphi_{\tau_{2,k+1}} \left(x_{3,k+1}, \frac{h}{2} \right) \circ \varphi_{\tau_{1,k+1}} \left(x_{4,k+1}, \frac{h}{2} \right)
\end{aligned}
\tag{IV.12}
$$

The need to use a Generating Function Approach and to set up a cascaded scheme as in (IV.12) is due to the Midpoint Rule that is area preserving for two-dimensional flows but is not volume preserving. The Jacobian determinant of the mapping (IV.8) for three-dimensional flows:

$$J = \frac{1 + \dfrac{h^2}{4} Q(\boldsymbol{F}) - \dfrac{h^3}{8} \det(\boldsymbol{F})}{1 + \dfrac{h^2}{4} Q(\boldsymbol{F}) + \dfrac{h^3}{8} \det(\boldsymbol{F})} = 1 + O(h^3) \tag{IV.13}$$

$$Q(\boldsymbol{F}) = F_{11}F_{22} + F_{22}F_{33} + F_{33}F_{11} - F_{12}F_{21} - F_{23}F_{32} - F_{31}F_{13}$$

is not unitary and constant as for 2-D ODEs, but approaches to 1 with the cube of the integration step.

4.2.2 Assessment of the Geometric Integration of the Flux Density Field

4.2.2.a Analytical Calculation of the Split Fields

Because of the need to know the Magnetic Vector Potential inside the entire Vacuum Vessel, we choose to represent the flux density field by means of the superposition of the field generated by:

- a set of axisymmetric filamentary currents (e.g., as calculated by CFTT's Pre-processor), as regards the poloidal field modelling;
- a toroidally continuous solenoid as regards the toroidal field modelling.

In this way, an analytical expression of the magnetic vector potential is available for the generation of the auxiliary 2-D fields to be integrated.

Let us consider a current density distribution directed along the toroidal direction: $\boldsymbol{J}(r,\varphi,z) = J(r,z)\hat{\varphi}$; the Biot-Savart law gives:

$$\boldsymbol{B}(r,\varphi,z) = \frac{\mu_0}{4\pi} \int_0^{+\infty} dr' \int_0^{+\infty} dz' \int_0^{2\pi} \left(\boldsymbol{J}(r',\varphi',z') \times \frac{\boldsymbol{R} - \boldsymbol{R}'}{\|\boldsymbol{R} - \boldsymbol{R}'\|^3} \right) r' d\varphi' \tag{IV.14}$$

where: $\boldsymbol{R} = r\hat{r} + z\hat{z}$ and $\boldsymbol{R}' = r'\widehat{r'} + z'\widehat{z'}$.

The coordinate frame (r',φ',z') can be obtained from the frame (r,φ,z) via a rigid rotation around the z axis:

$$\begin{cases} \widehat{r'} = cos(\varphi' - \varphi)\hat{r} + sin(\varphi' - \varphi)\hat{\varphi} \\ \widehat{\varphi'} = -sin(\varphi' - \varphi)\hat{r} + cos(\varphi' - \varphi)\hat{\varphi} \\ \widehat{z'} = \hat{z} \end{cases} \qquad \text{(IV.15)}$$

and so:

$$\boldsymbol{R} - \boldsymbol{R'} = [r - r'\,cos(\varphi' - \varphi)]\hat{r} - r'\,sin(\varphi' - \varphi)\,\hat{\varphi} + (z - z')\hat{z}$$
$$\|\boldsymbol{R} - \boldsymbol{R'}\| = \sqrt{r^2 + r'^2 - 2rr'\,cos(\varphi' - \varphi) + (z - z')^2} \qquad \text{(IV.16)}$$

Taking into account the relations between the unit vectors belonging to the same coordinate frame:

$$\begin{cases} \hat{r} = \hat{\varphi} \times \hat{z} \\ \hat{\varphi} = \hat{z} \times \hat{r} \\ \hat{z} = \hat{r} \times \hat{\varphi} \end{cases} \qquad \text{(IV.17)}$$

the Biot-Savart Law can be re-written as follows:

$$\boldsymbol{B}(r, \varphi, z) = \frac{\mu_0}{4\pi} \int_0^{+\infty} dr' \int_0^{+\infty} dz' \int_0^{2\pi} J(r', z')\widehat{\varphi'} \times$$

$$\times \frac{[r - r'\,cos(\varphi' - \varphi)]\hat{r} - r'\,sin(\varphi' - \varphi)\,\hat{\varphi} + (z - z')\hat{z}}{(r^2 + r'^2 - 2rr'\,cos(\varphi' - \varphi) + (z - z')^2)^{\frac{3}{2}}} r'd\varphi' \qquad \text{(IV.18)}$$

Taking into account the following relationships:

$$\begin{cases} \widehat{\varphi'} \times \hat{r} = -cos(\varphi' - \varphi)\,\hat{z} \\ \widehat{\varphi'} \times \hat{\varphi} = -sin(\varphi' - \varphi)\,\hat{z} \\ \widehat{\varphi'} \times \hat{z} = sin(\varphi' - \varphi)\,\hat{\varphi} + cos(\varphi' - \varphi)\,\hat{r} \end{cases} \qquad \text{(IV.19)}$$

we get:

$$\widehat{\varphi'} \times (\boldsymbol{R} - \boldsymbol{R'}) = (z - z')\,cos(\varphi' - \varphi)\,\hat{r} + (z - z')\,sin(\varphi' - \varphi)\,\hat{\varphi} + [r' - r\,cos(\varphi' - \varphi)]\hat{z} \qquad \text{(IV.20)}$$

and so:

$$B(r, \varphi, z) = \frac{\mu_0}{4\pi} \int_0^{+\infty} dr' \int_0^{+\infty} dz' \int_0^{2\pi} r' d\varphi' \cdot J(r', z') \cdot$$

$$\cdot \left\{ \frac{(z - z') \cos(\varphi' - \varphi)}{(r^2 + r'^2 - 2rr' \cos(\varphi' - \varphi) + (z - z')^2)^{\frac{3}{2}}} \hat{r} + \right.$$

$$+ \frac{(z - z') \sin(\varphi' - \varphi)}{(r^2 + r'^2 - 2rr' \cos(\varphi' - \varphi) + (z - z')^2)^{\frac{3}{2}}} \hat{\varphi} +$$

$$\left. + \frac{[r' - r \cos(\varphi' - \varphi)]}{(r^2 + r'^2 - 2rr' \cos(\varphi' - \varphi) + (z - z')^2)^{\frac{3}{2}}} \hat{z} \right\} \qquad \text{(IV.21)}$$

If we sort the integrals over the toroidal angle, we get:

$$B(r, \varphi, z) = \frac{\mu_0}{4\pi} \int_0^{+\infty} r' dr' \int_0^{+\infty} dz' \cdot J(r', z') \cdot$$

$$\cdot \left\{ \left[\int_0^{2\pi} \frac{(z - z') \cos(\varphi' - \varphi)}{\|R - R'\|} d\varphi' \right] \hat{r} + \right.$$

$$+ \left[\int_0^{2\pi} \frac{(z - z') \sin(\varphi' - \varphi)}{\|R - R'\|} d\varphi' \right] \hat{\varphi} +$$

$$\left. + \left[\int_0^{2\pi} \frac{[r' - r \cos(\varphi' - \varphi)]}{\|R - R'\|} d\varphi' \right] \hat{z} \right\} \qquad \text{(IV.22)}$$

It is clear that the integrand that generates the flux density field component along the toroidal direction is odd, hence the corresponding integral is zero. This implies that the flux density field generated by an axisymmetric current density consists only of the poloidal components whose analytical expressions are:

$$B(r, \varphi, z) = B_r(r, z)\hat{r} + B_z(r, z)\hat{z} \qquad \text{(IV.23)}$$

$$B_r = \frac{\mu_0}{4\pi} \int_0^{+\infty} r' dr' \int_0^{+\infty} dz' \cdot J(r', z') \int_0^{2\pi} \frac{(z - z') \cos(\varphi' - \varphi)}{\|R - R'\|} d\varphi' \qquad \text{(IV.24)}$$

$$B_z = \frac{\mu_0}{4\pi} \int_0^{+\infty} r' dr' \int_0^{+\infty} dz' \cdot J(r', z') \int_0^{2\pi} \frac{[r' - r \cos(\varphi' - \varphi)]}{\|R - R'\|} d\varphi' \qquad \text{(IV.25)}$$

As regards the magnetic vector potential:

$$A(r, \varphi, z) = \frac{\mu_0}{4\pi} \iiint_{\Omega_s} \frac{J(r', z')}{\|R - R'\|} dV \qquad \text{(IV.26)}$$

where Ω_s is the sources region, it can be re-written as follows:

$$A(r, \varphi, z) = \frac{\mu_0}{4\pi} \int_0^{+\infty} dr' \int_0^{+\infty} dz' \int_0^{2\pi} J(r', z') \cdot$$

$$\cdot \frac{-\sin(\varphi' - \varphi)\hat{r} + \cos(\varphi' - \varphi)\hat{\varphi}}{\sqrt{(r^2 + r'^2 - 2rr'\cos(\varphi' - \varphi) + (z - z')^2)}} r' d\varphi' \qquad \text{(IV.27)}$$

If we sort the integrals over the toroidal angle into the expression of the magnetic vector potential, we get:

$$A(r, \varphi, z) = \frac{\mu_0}{4\pi} \int_0^{+\infty} r' dr' \int_0^{+\infty} dz' \cdot J(r', z') \cdot$$

$$\cdot \left\{ \left[-\int_0^{2\pi} \frac{\sin(\varphi' - \varphi)}{\|R - R'\|} d\varphi' \right] \hat{r} + \left[\int_0^{2\pi} \frac{\cos(\varphi' - \varphi)}{\|R - R'\|} d\varphi' \right] \hat{\varphi} \right\} \qquad \text{(IV.28)}$$

The integrand that generates the radial component of the magnetic vector potential is an odd function, thus its integral over the set $\varphi \in [0, 2\pi]$ is zero. Consequently, the magnetic vector potential consists of the only toroidal component, whose analytical expression is:

$$A_\varphi(r, z) = \frac{\mu_0}{4\pi} \int_0^{+\infty} r' dr' \int_0^{+\infty} dz' \cdot J(r', z') \int_0^{2\pi} \frac{\cos(\varphi' - \varphi)}{\|R - R'\|} d\varphi' \qquad \text{(IV.29)}$$

At this stage it is possible to introduce the poloidal flux per unit radian ψ in terms of the vector potential as follows: $\psi(r, z) = r \cdot A_\varphi(r, z)$, hence obtaining:

$$\psi(r, z) = \frac{\mu_0}{4\pi} \int_0^{+\infty} rr' dr' \int_0^{+\infty} dz' \cdot J(r', z') \int_0^{2\pi} \frac{\cos(\varphi' - \varphi)}{\|R - R'\|} d\varphi' \qquad \text{(IV.30)}$$

If we define the Kernel of the integral in (IV.30):

$$G(r, r', z, z') = \frac{\mu_0}{2} \int_0^{2\pi} \frac{rr'\cos(\varphi' - \varphi)}{\|R - R'\|} d\varphi' = \mu_0 \int_0^{\pi} \frac{rr'\cos(\varphi' - \varphi)}{\|R - R'\|} d\varphi' \qquad \text{(IV.31)}$$

we get:

$$\psi(r, z) = \frac{1}{2\pi} \int_0^{+\infty} dr' \int_0^{+\infty} G(r, r', z, z') \cdot J(r', z') dz' \qquad \text{(IV.32)}$$

Finally, if we introduce the angle θ defined as: $\varphi' - \varphi = \pi - 2\theta$ and substitute the relation: $\cos(\varphi' - \varphi) = 2\sin^2\theta - 1$ in equation (IV.31), we get:

$$G(r, r', z, z') = -2\mu_0 rr' \int_0^{\frac{\pi}{2}} \frac{1 - 2\sin^2\theta}{\sqrt{(r + r')^2 + (z - z')^2 - 4rr'\sin^2\theta}} d\theta \qquad \text{(IV.33)}$$

The following parameter:

$$m = k^2 = \frac{4rr'}{(r + r')^2 + (z - z')^2} \tag{IV.34}$$

is called *Elliptic Parameter* and allows to rewrite the equation (IV.33) as follows:

$$G(r, r', z, z') = -\mu_0 k \sqrt{rr'} \int_0^{\frac{\pi}{2}} \frac{1 - 2 \sin^2 \theta}{\sqrt{1 - k^2 \sin^2 \theta}} d\theta =$$

$$= -\mu_0 k \sqrt{rr'} \int_0^{\frac{\pi}{2}} \frac{\left(1 - \frac{2}{k^2}\right) + \frac{2}{k^2}(1 - k^2 \sin^2 \theta)}{\sqrt{1 - k^2 \sin^2 \theta}} d\theta = \tag{IV.35}$$

$$= -\mu_0 \sqrt{rr'} \left[\left(k - \frac{2}{k}\right) \int_0^{\frac{\pi}{2}} \frac{d\theta}{\sqrt{1 - k^2 \sin^2 \theta}} + \frac{2}{k} \int_0^{\frac{\pi}{2}} (1 - k^2 \sin^2 \theta) d\theta \right]$$

The following addends:

$$K = \int_0^{\frac{\pi}{2}} \frac{d\theta}{\sqrt{1 - k^2 \sin^2 \theta}} \tag{IV.36}$$

$$E = \int_0^{\frac{\pi}{2}} (1 - k^2 \sin^2 \theta) d\theta \tag{IV.37}$$

are the *Complete Elliptic Integral of the First Kind* (IV.36) and *Complete Elliptic Integral of the Second Kind* (IV.37). They are defined only if $k \in [0,1[$ and can be calculated by means of an iterative procedure [68], obtaining the following diagrams:
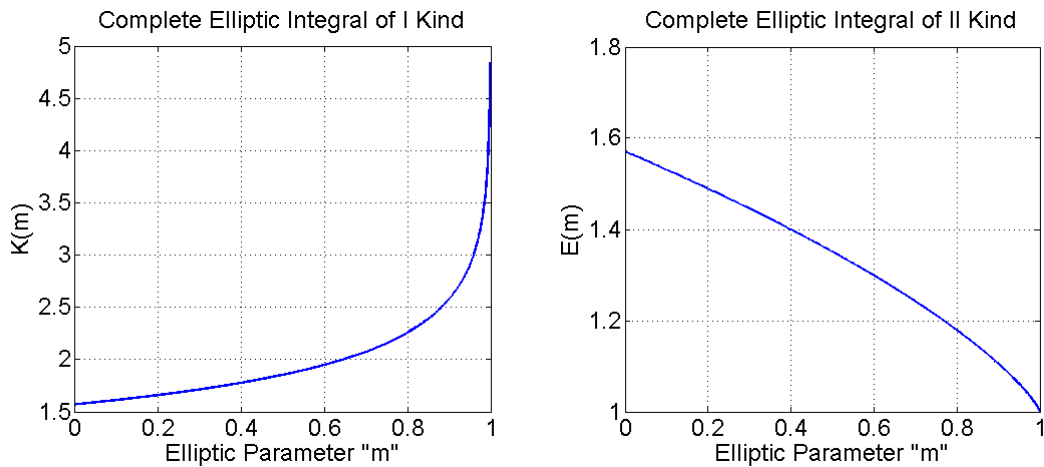
Fig. IV.10: Complete Elliptic Integrals of the First and Second Kinds in terms of the Elliptic Parameter "m"

Therefore, it is possible to rewrite the (IV.35) in terms of the Complete Elliptic Integral as follows:

$$G(r, r', z, z') = -\frac{2\mu_0}{k}\sqrt{rr'}\left[\left(1 - \frac{k^2}{2}\right)K(k^2) - E(k^2)\right] \qquad \text{(IV.38)}$$

and the poloidal flux per unit radian can be rewritten as:

$$\psi(r, z) = \frac{\mu_0}{\pi}\int_0^{+\infty} dr'\int_0^{+\infty}\frac{\sqrt{rr'}}{k}\left[\left(1 - \frac{k^2}{2}\right)K(k^2) - E(k^2)\right]\cdot J(r', z')dz' \qquad \text{(IV.39)}$$

Let us consider that the toroidal current consists of a set of axisymmetric conductors:

$$J(r, z) = \sum_{n=1}^{N_{fil}} I_n \delta(r - r'_n, z - z_n') \qquad \text{(IV.40)}$$

where $\delta(r - r'_k, z - z_k')$ is the Dirac distribution shifted at the point $P \equiv (r'_n, z_n')$. If the property of the measure μ_P generating the Dirac distribution is exploited, the integral (in the Stieltjes-Lebesgue sense) in (IV.39) gives the following results in terms of poloidal flux per unit radian and magnetic vector potential:

$$\psi(r, z) = \frac{\mu_0}{\pi}\sum_{n=1}^{N_{fil}} I_n\frac{\sqrt{rr_n'}}{k_n}\left[\left(1 - \frac{k_n^2}{2}\right)K(k_n^2) - E(k_n^2)\right] \qquad \text{(IV.41)}$$

$$A_\varphi(r, z) = \frac{\mu_0}{\pi}\sum_{n=1}^{N_{fil}}\frac{I_n}{k_n}\sqrt{\frac{r_n'}{r}}\left[\left(1 - \frac{k_n^2}{2}\right)K(k_n^2) - E(k_n^2)\right] \qquad \text{(IV.42)}$$

Once the magnetic vector potential is known, the construction of the three auxiliary fields shown in (IV.7) is finally possible. For this reason, let us recall that the derivatives of the complete elliptic integrals with respect to the square root of the integral parameter $k = \sqrt{m}$ are [69]:

$$\frac{dK}{dk} = \frac{E(k^2)}{k(1 - k^2)} - \frac{K(k^2)}{k} \qquad \text{(IV.43)}$$

$$\frac{dE}{dk} = \frac{E(k^2) - K(k^2)}{k} \qquad \text{(IV.44)}$$

and calculate the following derivatives:

$$\frac{\partial k}{\partial r} = \frac{r'[(r + r')^2 + (z - z')^2] - 2rr'(r + r')}{[(r + r')^2 + (z - z')^2]^{\frac{3}{2}}\sqrt{rr'}} \qquad \text{(IV.45)}$$

$$\frac{\partial k}{\partial z} = -\frac{2(z - z')\sqrt{rr'}}{[(r + r')^2 + (z - z')^2]^{\frac{3}{2}}}$$

(IV.46)

At this stage it is possible to calculate the partial derivatives of the magnetic vector potential with respect of the geometrical coordinates in the Cartesian frame. For sake of simplicity, a single axisymmetric filamentary current is considered hereafter:

$$\frac{\partial A_\varphi}{\partial x} = \frac{\mu_0 I}{\pi k}\sqrt{\frac{r'}{r}}\left\{-\left[\frac{1}{k'}\frac{\partial k}{\partial r} + \frac{1}{2r}\right]\cdot\left[\left(1 - \frac{(k')^2}{2}\right)K - E\right] + \right.$$

$$\left. +\left[-k\frac{\partial k}{\partial r}K + \left(1 - \frac{(k')^2}{2}\right)\frac{\partial K}{\partial r} - \frac{\partial E}{\partial r}\right]\right\}\frac{x}{\sqrt{x^2 + y^2}}$$

(IV.47)

$$\frac{\partial A_\varphi}{\partial y} = \frac{\mu_0 I}{\pi}\sqrt{r'}\left\{-\left[\frac{1}{(k')^2\sqrt{r}}\frac{\partial k}{\partial r} + \frac{1}{2kr\sqrt{r}}\right]\cdot\left[\left(1 - \frac{(k')^2}{2}\right)K - E\right] + \right.$$

$$\left. +\frac{1}{k\sqrt{r}}\left[-k\frac{\partial k}{\partial r}K + \left(1 - \frac{(k')^2}{2}\right)\frac{\partial K}{\partial r} - \frac{\partial E}{\partial r}\right]\right\}\frac{y}{\sqrt{x^2 + y^2}}$$

(IV.48)

$$\frac{\partial A_\varphi}{\partial z} = -\frac{\mu_0 I}{\pi k}\sqrt{\frac{r'}{r}}\left\{\frac{1}{k}\frac{\partial k}{\partial z}\left[\left(1 - \frac{k^2}{2}\right)K - E\right] + \right.$$

$$\left. +\left[\left(k\frac{\partial k}{\partial z}\right)K - \left(1 - \frac{k^2}{2}\right)\frac{\partial K}{\partial z} + \frac{\partial E}{\partial z}\right]\right\}$$

(IV.49)

Recalling that:

$$\begin{cases} A_x = -A_\varphi \sin\left(atan\left(\frac{y}{x}\right)\right) \\ A_y = A_\varphi \cos\left(atan\left(\frac{y}{x}\right)\right) \\ A_z = 0 \end{cases}$$

(IV.50)

the gradient of the components of the magnetic vector potential is:

$$\nabla A_x = \begin{bmatrix} -\frac{\partial A_\varphi}{\partial x}\sin\left(atan\left(\frac{y}{x}\right)\right) + A_\varphi \cos\left(atan\left(\frac{y}{x}\right)\right)\frac{y}{x^2 + y^2} \\ -\frac{\partial A_\varphi}{\partial y}\sin\left(atan\left(\frac{y}{x}\right)\right) - A_\varphi \cos\left(atan\left(\frac{y}{x}\right)\right)\frac{x}{x^2 + y^2} \\ -\frac{\partial A_\varphi}{\partial z}\sin\left(atan\left(\frac{y}{x}\right)\right) \end{bmatrix}$$

(IV.51)

$$\nabla A_y = \begin{bmatrix} \dfrac{\partial A_\varphi}{\partial x} \cos\left(atan\left(\dfrac{y}{x}\right)\right) + A_\varphi \sin\left(atan\left(\dfrac{y}{x}\right)\right) \dfrac{y}{x^2 + y^2} \\[2mm] \dfrac{\partial A_\varphi}{\partial y} \cos\left(atan\left(\dfrac{y}{x}\right)\right) - A_\varphi \sin\left(atan\left(\dfrac{y}{x}\right)\right) \dfrac{x}{x^2 + y^2} \\[2mm] \dfrac{\partial A_\varphi}{\partial z} \cos\left(atan\left(\dfrac{y}{x}\right)\right) \end{bmatrix} \qquad (IV.52)$$

$$\nabla A_z = \begin{bmatrix} 0 \\ 0 \\ 0 \end{bmatrix} \qquad (IV.53)$$

Therefore, the three auxiliary fields for that of an axisymmetric filamentary conductor are:

$$\mathbf{B}_1 = \nabla A_x \times \hat{x} =$$

$$= \begin{bmatrix} 0 \\[2mm] -\dfrac{\partial A_\varphi}{\partial z} \sin\left(atan\left(\dfrac{y}{x}\right)\right) \\[2mm] \dfrac{\partial A_\varphi}{\partial y} \sin\left(atan\left(\dfrac{y}{x}\right)\right) + A_\varphi \cos\left(atan\left(\dfrac{y}{x}\right)\right) \dfrac{x}{x^2 + y^2} \end{bmatrix} \qquad (IV.54)$$

$$\mathbf{B}_2 = \nabla A_y \times \hat{y} =$$

$$= \begin{bmatrix} -\dfrac{\partial A_\varphi}{\partial z} \cos\left(atan\left(\dfrac{y}{x}\right)\right) \\[2mm] 0 \\[2mm] \dfrac{\partial A_\varphi}{\partial x} \cos\left(atan\left(\dfrac{y}{x}\right)\right) + A_\varphi \sin\left(atan\left(\dfrac{y}{x}\right)\right) \dfrac{y}{x^2 + y^2} \end{bmatrix} \qquad (IV.55)$$

$$\mathbf{B}_3 = \nabla A_z \times \hat{z} = \begin{bmatrix} 0 \\ 0 \\ 0 \end{bmatrix} \qquad (IV.56)$$

Thanks to the linearity of the relation between the magnetic vector potential and the current carried by its sources, the superposition principle can be exploited, whether many axisymmetric currents are present.

The same procedure has to be carried out for the toroidal component of the flux density field, generated by the toroidal solenoid:

$$B_\varphi = \begin{cases} \dfrac{\mu_0 N I}{2\pi r} & in\ \Omega \\[2mm] 0 & elsewhere \end{cases} \qquad (IV.57)$$

$$A_r = \begin{cases} \dfrac{\mu_0 N I}{2\pi r} z & in \ \Omega \\ 0 & elsewhere \end{cases} \tag{IV.58}$$

where N in the number of turns of the toroidal winding and Ω is the region inside the solenoid. The expression of the magnetic vector potential in the Cartesian frame is:

$$\begin{cases} A_x = \dfrac{\mu_0 N I}{2\pi\sqrt{x^2 + y^2}} z \cos\left(atan\left(\dfrac{y}{x}\right)\right) \\ A_y = \dfrac{\mu_0 N I}{2\pi\sqrt{x^2 + y^2}} z \sin\left(atan\left(\dfrac{y}{x}\right)\right) \\ A_z = 0 \end{cases} \tag{IV.59}$$

Therefore, the three auxiliary fields for the toroidal component of the flux density field are:

$$\mathbf{B_1} = \nabla A_x \times \hat{x} =$$

$$= \frac{\mu_0 N I}{2\pi} \begin{bmatrix} 0 \\ \dfrac{1}{\sqrt{x^2 + y^2}} \cos\left(atan\left(\dfrac{y}{x}\right)\right) \\ -\dfrac{z}{(x^2 + y^2)^{\frac{3}{2}}} \left[y \cdot \cos\left(atan\left(\dfrac{y}{x}\right)\right) + x \cdot \sin\left(atan\left(\dfrac{y}{x}\right)\right) \right] \end{bmatrix} \tag{IV.60}$$

$$\mathbf{B_2} = \nabla A_y \times \hat{y} =$$

$$= \frac{\mu_0 N I}{2\pi} \begin{bmatrix} \dfrac{1}{\sqrt{x^2 + y^2}} \sin\left(atan\left(\dfrac{y}{x}\right)\right) \\ 0 \\ -\dfrac{z}{(x^2 + y^2)^{\frac{3}{2}}} \left[x \cdot \sin\left(atan\left(\dfrac{y}{x}\right)\right) - y \cdot \cos\left(atan\left(\dfrac{y}{x}\right)\right) \right] \end{bmatrix} \tag{IV.61}$$

$$\mathbf{B_3} = \nabla A_z \times \hat{z} = \begin{bmatrix} 0 \\ 0 \\ 0 \end{bmatrix} \tag{IV.62}$$

Once these split fields are superposed to those of the axisymmetric filamentary conductors, it is possible to implement a proper cascade scheme, aimed to their integration.

4.2.2.b   Integration Assessment in Axisymmetric Geometry

After having discussed about the principles which the flux density field line tracing is based on, it is necessary to assess the performances of the ODE integrators, to be sure to get reliable results within a prescribed accuracy. Hereafter, a comparison of the performance of standard ODE integrators based on Runge-Kutta method [70] versus the Volume Preserving Midpoint Rule scheme (IV.8) is depicted.

The error assessment for this class of problems is not trivial in tokamaks because:

- the error has to be bounded after a long integration, in order to perform an accurate tracing;
- analytical invariants for plasma equilibria, such as the poloidal magnetic flux per unit radian ψ, are usually available only for the axisymmetric field configurations;
- the transverse (poloidal plane) components of the flux density field (and therefore the related error) are usually much smaller than the toroidal one.

For axisymmetric plasmas, a way to provide an error estimation for these 3-D integrators is based on the property of the poloidal magnetic flux per unit radian ψ to be an invariant for the flux density field and so to be constant along its streamlines [71]-[72]. The more ψ is kept constant, the higher are the performances of the integrator in terms of integration error. Moreover, the Jacobian determinant of the mapping is also an invariant (see Section 4.2.1) for such field configuration, even for non-axisymmetric plasmas. Therefore, its conservation in the 3-D integration can be also used as a figure of merit.

The latter estimation is based on the conjecture that the combination of high flux accuracy (related to the poloidal component of the flux density field) and high volume preservation guarantees a good accuracy level for toroidal component too.

On such bases, the following DEMO [73] configuration was taken as reference case to trace 1000 m long flux density field lines within the plasma:

- Plasma Current: $I_p = 16\ MA$;

- Major Radius: $R_0 = 9\ m$;

- Minor Radius: a = 2.25 m;

- Poloidal Beta: $\beta_p = 0.8$;

- Plasma Internal Inductance: $l_i = 0.7$;

- Toroidal Field at the Major Radius: $B_\varphi\big|_{r=R_0} = 7\ T$.

On this reference case, the compared algorithms were tested in terms of accuracy and computational time as functions of the integration step-size. Fig. IV.11 shows the relative error on the poloidal flux per unit radian conservation $\frac{\Delta\psi}{\psi}$, in terms of the integration step-size:
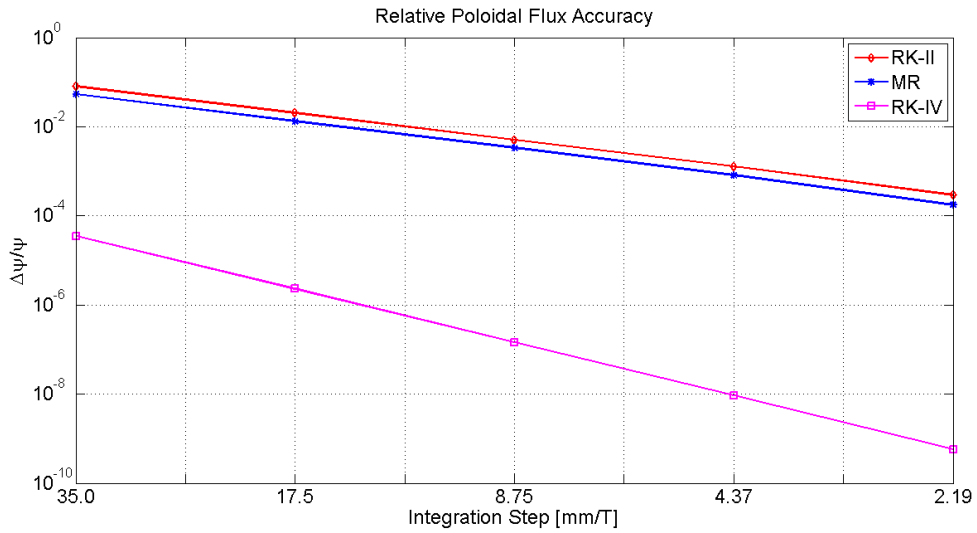
Fig. IV.11: Flux accuracy in terms of integration step-size for the considered algorithms: mid-point rule (MR), Runge-Kutta 2nd (RK-II) and 4th (RK-IV) order

It is worth noting that the relative error $\frac{\Delta\psi}{\psi}$ scales with the integration step in perfect agreement with the algorithm order, proving that the considered integration step-sizes are large enough to neglect the round-off error with respect to truncation one.

Fig. IV.12 shows the relative variation of Jacobian determinant in terms of the curvilinear abscissa along the traced field line:
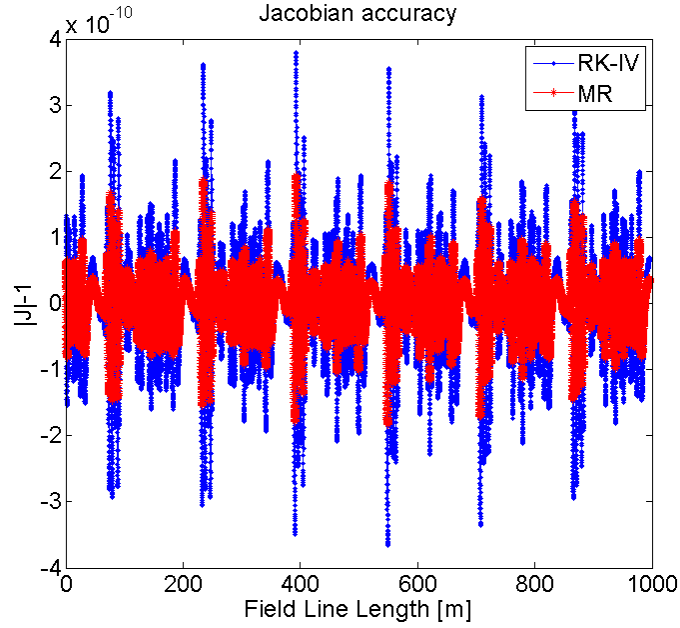
Fig. IV.12: Volume preserving condition along the flux density field integration for the Runge-Kutta 4th order (RK-IV) and the Midpoint Rule (MR)

The local volume preserving condition $det(J) - 1 = 0$ is verified at the round off error limit and is limited within the accuracy of 10^{-10} for both the compared integrators. Even though the latter is not volume-preserving, the good result in Fig. IV.12 is mainly due to the small integration step selected to meet the accuracy requirements.

The evaluation of numerical accuracy in the volume preservation is affected by another error that is the numerical evaluation of the partial derivatives in the Jacobian matrix (IV.9) by means of central point derivation rule with a second order approximation. Therefore, a second order extrapolation can be used to get a more precise estimation of the volume preservation:

$$\frac{\det(J(\tau))}{\det(J(0))} = 2 \frac{\det\left(J_{\frac{h}{2}}(\tau)\right)}{\det\left(J_{\frac{h}{2}}(0)\right)} - \frac{\det(J_h(\tau))}{\det(J_h(0))} + O(h^2) \qquad \text{(IV.63)}$$

where h is the step-size used for the numerical calculation of the entries of the Jacobian Matrix. Considering a step-size $h = 320\,\mu m$, the extrapolated accuracies are $0.460 \cdot 10^{-12}$ for MR and $3.302 \cdot 10^{-12}$ for the RK-IV, respectively.

Tab. IV.2 gives a general comparison of the tested algorithms in terms of flux accuracy and computing time.

Tab. IV.2: Flux accuracy in terms of integration step-size for a field line 1000 m long, for the considered algorithms: mid-point rule (MR), Runge-Kutta 2nd (RK-II) and 4th (RK-IV) order

$\Delta\tau$ [mm/T]		MR	RK-II	RK-IV
35.0	$\Delta\Psi$ [Vs]	0.911	1.382	5.986e-4
	CPU_time [s]	239	60	116
17.5	$\Delta\Psi$ [Vs]	0.225	0.346	3.907e-5
	CPU_time [s]	480	118	241
8.75	$\Delta\Psi$ [Vs]	0.057	0.087	2.492e-6
	CPU_time [s]	923	245	489
4.37	$\Delta\Psi$ [Vs]	0.014	0.022	1.574e-7
	CPU_time [s]	1594	493	990
2.19	$\Delta\Psi$ [Vs]	0.003	0.005	9.876e-9
	CPU_time [s]	2749	996	1992

4.2.2.c Clebsch Representation of a Divergence-Free Vector Field and Integration Assessment in Non-Axisymmetric Configurations

Since the poloidal flux per unit radian is not an invariant for the non-axisymmetric magnetic flux density fields, analytical invariants for a general three-dimensional flux density field can be found into the *Clebsch Decomposition* of a divergence-free vector field.

Let us recall the Helmholtz theorem for vector fields:

*Let **F** be any continuous vector field with continuous first partial derivatives. Then **F** can be expressed in terms of the negative gradient of a scalar potential* Φ *and the curl of a vector potential **A**.*

This means that the vector field **F** can be split as follows:

$$\boldsymbol{F} = -\nabla\Phi + \nabla \times \boldsymbol{A} \qquad (IV.64)$$

If the vector field is divergence-free as the flux density field is, the scalar potential Φ is everywhere zero. Moreover, if two additional scalar potentials U and V are introduced and the vector potential is reformulated as follows:

$$\boldsymbol{A} = U\nabla V \qquad (IV.65)$$

we get the following expression for the flux density field:

$$\boldsymbol{B} = \nabla U \times \nabla V \qquad\qquad\qquad (IV.66)$$

Equation (IV.66) is called *Clebsch Decomposition* of the flux density field and the scalar potential U and V are named *Clebsch Potentials*.

The lack of spreading of such representation is mainly due to the non-linear relation between the flux density field and the two Clebsch potentials [74]. For this reason, the only local uniqueness of such decomposition was demonstrated, but not the global one, because many other couples of Clebsch Potentials $\tilde{U}$ and $\tilde{V}$ can be obtained by means of Volume-Preserving Transformations [75].

However, such representation is useful when describing the magnetic field lines as a Hamiltonian flow [76]. Thanks to the this particular decomposition, two analytical invariants are available also for 3-D flux density field configurations, i.e. the Clebsch Potentials, which are constant along the flux density field lines:

$$\begin{cases} \boldsymbol{B} \cdot \nabla U = \nabla U \times \nabla V \cdot \nabla U = 0 \\ \boldsymbol{B} \cdot \nabla V = \nabla U \times \nabla V \cdot \nabla V = 0 \end{cases} \qquad\qquad (IV.67)$$

Therefore, a magnetic flux density field line is the intersection of the two $U = const.$ and $V = const.$ surfaces.

Using such fundamental properties, an accuracy estimation of the numerical tracing of 3-D magnetic field lines may be the evaluation of the relative error on the constancy of U and V potentials along the traced field lines, as well as for the magnetic poloidal flux per unit radian in the axisymmetric case.

This information can be also turned into a geometrical error, that is the minimal distance $\|\delta P\|_{min}$ between the exact field line $U = U_0 \cap V = V_0$ and the traced line. The minimum distance between the two lines can be calculated by solving in the least square sense the following underdetermined set:

$$\begin{cases} \nabla U \cdot \delta P = U - U_0 \\ \nabla V \cdot \delta P = V - V_0 \end{cases} \qquad\qquad (IV.68)$$

where:

- U and V are the actual values of the Clebsch potentials at each point of the traced field line;
- ∇U and ∇V are the actual values of the gradient of the Clebsch potentials at each point of the traced field line;

- U_0 and V_0 are the values of the Clebsch potentials on the analytical field line.

To choose a couple of Clebsch potentials in such a way that the corresponding lines resemble those of a typical axisymmetric plasma, we refer to the parametric equations of the toroidal surface with elliptic cross section (IV.69) and to the helicoid (IV.70):

$$\begin{cases} r = R_0 + a \cdot cos(\alpha) \\ z = Z_0 + b \cdot sin(\alpha) \quad \alpha \in [0,2\pi], \beta \in [0,2\pi] \\ \varphi = \beta \end{cases} \tag{IV.69}$$

$$\begin{cases} r = R_0 + \alpha \cdot cos(\beta) \\ z = Z_0 + \alpha \cdot sin(\beta) \quad \alpha \in [0,+\infty], \beta \in [0,+\infty] \\ \varphi = q \cdot \beta \end{cases} \tag{IV.70}$$

thus obtaining:

$$\begin{cases} U = \left(\dfrac{r - R_0}{a}\right)^2 + \left(\dfrac{z - Z_0}{b}\right)^2 + U_0 \\ V = q\theta - \varphi + V_0 \end{cases} \tag{IV.71}$$

where:

- R_0 and Z_0 are the radial and vertical coordinates of the helix elliptic cross section;
- a and b are the radial and vertical axes of the helix elliptic cross section;
- q is the safety factor;
- θ is the poloidal angle, calculated by: $(r - R_0)\,tan(\theta) = z - Z_0$ using the four quadrants inverse tangent;
- U_0 and V_0 are arbitrary constants.

The two Clebsch surfaces with their intersection are shown in the following Fig. IV.13:
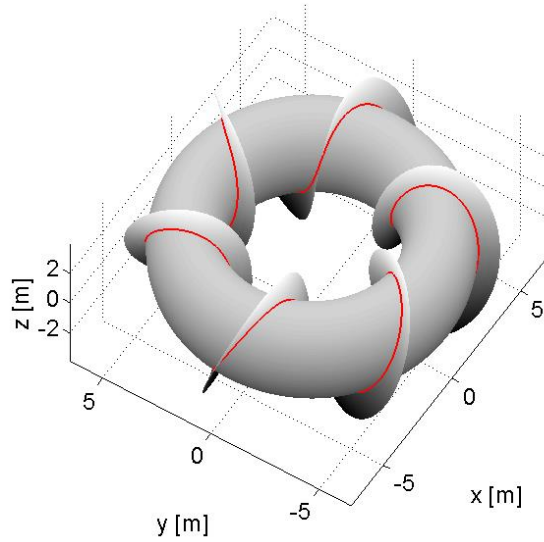
Fig. IV.13: Clebsch surfaces generating a toroidal helix (the solid line is their intersection)

Such axisymmetric field configuration can be easily modified by adding perturbing non-axisymmetric terms in the expressions of U and V. Two kinds of perturbation will be hereafter considered, namely a global perturbation (GP), and a local perturbation (LP).

As regards the global perturbation, a toroidal mode resembling a 3-D *Sausage Instability* may be generated by:

$$\begin{cases} U = \left(\dfrac{r - R_0}{a + \delta U}\right)^2 + \left(\dfrac{z - Z_0}{b + \delta U}\right)^2 + U_0 \\ V = q\theta - \varphi + V_0 \end{cases} \qquad \text{(IV.72)}$$

$$\delta U = \delta r \cdot cos(n\varphi)$$

where: δr is the amplitude of the perturbation and n is the mode number of the perturbation. The following Fig. IV.14 shows this configuration when: $R_0 = 9\,m$, $Z_0 = 0$, $a = 0.75\,m$, $b = 1.25\,m$, $q = 2\pi$, $\delta r = 0.25\,m$ and $n = 18$:
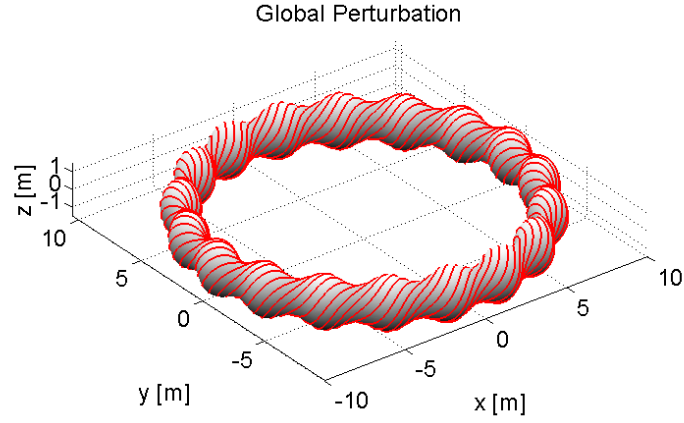
Fig. IV.14: Ergodic surface covered by a field line in a globally perturbed field configuration ($V = const.$ surface is omitted)

As regards the Jacobian conservation, the same extrapolation as for the axisymmetric test case was carried out, obtaining $det(J) - 1 = 0$ of $0.4918 \cdot 10^{-11}$ for the MR and $0.3190 \cdot 10^{-11}$ for the RK-IV algorithms.

As regards the local perturbation, the perturbing term consists of a smooth function $\delta U \subset \Omega_p$, defined as follows:

$$\begin{cases} U = \left(\dfrac{r - R_0 + \delta U}{a}\right)^2 + \left(\dfrac{z - Z_0}{b}\right)^2 + U_0 \\ V = q\theta - \varphi + V_0 \end{cases}$$

(IV.73)

$$\delta U = \delta r \cdot e^{\frac{a_1}{\Delta z} - \frac{a_1}{\sqrt{\Delta z^2 - (Z_1 - z)^2}}} \cdot e^{\frac{\alpha}{\Delta \varphi} - \frac{1}{\sqrt{\Delta \varphi^2 - (\varphi_1 - \varphi)^2}}} u(r - R_0)$$

where $u(r - R_0)$ is the step function, and:

$$\Omega_p = \begin{cases} |z| < z_1 \\ |\varphi - \varphi_1| < \Delta \varphi \end{cases}$$

(IV.74)

Fig. IV.15 shows this field configuration when: $R_0 = 9\,m$, $Z_0 = 0$, $a = 0.75\,m$, $b = 1.25\,m$, $a_1 = 10\,m$, $\alpha = 1\,rad$, $q = 2\pi$, $\delta r = 1\,m$, $\Delta z = 0.5\,m$, $X_1 = 1.56\,m$, $Y_1 = 8.86\,m$, $Z_1 = Z_0$, $\Delta \varphi = 10\,deg$ and $\varphi_1 = -90\,deg$:
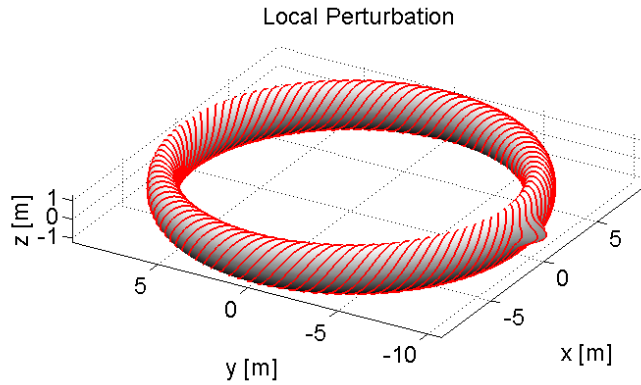
Fig. IV.15: Ergodic surface covered by a field line for a locally perturbed field configuration ($V = const.$ surface is omitted)

The following Tab. IV.3 summarizes the accuracy assessments results, carried out both in the axisymmetric and in the two full 3-D configurations mentioned above by means of Clebsch Decomposition, for the MR, RK-II and RK-IV algorithms.

Tab. IV.3: Tracing accuracy for MR, RK-II and RK-IV estimated using Clebsch potentials for an integration length of 1000 m and a step size of 2.18 mm/T

	$|U - U_0|/U_0$			$|V - V_0|/V_0$			$\delta P\ [m]$		
	AXI	GP	LP	AXI	GP	LP	AXI	GP	LP
MR	8.0e-3	4.4e-1	3e-3	7.0e-3	2.3e-1	2.0e-2	3.0e-4	1.5e-2	8.0e-4
RK-II	2.3e-5	2.1e-3	8.0e-4	1.3e-5	2.0e-4	4.0e-4	8.9e-7	1.0e-4	4.6e-5
RK-IV	2.1e-12	4.3e-8	1.0e-7	1.1e-11	2.0e-9	5.3e-9	6.9e-13	4.0e-9	5.5e-9

This analysis suggests that standard integrators, e.g. Runge-Kutta, are extremely accurate in terms both of integration precision and of volume preservation (basically at the round-off error limit), when appropriate accuracy requirements (step-size) are selected. Moreover, they are by far simpler and less expensive than volume preserving algorithms from a computational point of view.

A final consideration about the Runge-Kutta algoritms: even if adaptive ODE solvers might be expected to show better performances than fixed-step integrators in terms of trade-off between accuracy and computation time, the use of step-adaptivity may not preserve spatial symmetries with drastic consequences [64]. For this reasons, fixed step Runge-Kutta algorithms were chosen for the comparison with the Volume Preserving integrator.

4.3 Plasma Boundary Reconstruction via Field Line Tracing

After discussing about the assessment of the numerical integrators when called to trace very long flux density field lines, their use for the reconstruction of the plasma boundary is now depicted, both in axisymmetric and non-axisymmetric configurations.

The plasma boundary is defined as the outermost closed magnetic surface entirely contained in the vacuum vessel. This is justified by the consideration that a plasma particle follows the magnetic field lines in its motion. As a consequence, the plasma particles following a magnetic field line which is inside this surface will remain in the plasma interior, while a particle following a magnetic field line external to this surface will collide with the mechanical structures surrounding the plasma.

The lack of analytical invariants for three-dimensional flux density fields (unfortunately, nowadays a Clebsch decomposition does not exist neither for axisymmetric and non-axisymmetric fields) can be circumvented if exploiting the *Connection Length*.

The plasma particles characterized by an infinite value of the connection length lay on field lines do not intersecting the wall (periodic or ergodic), are by definition within the plasma core and cover a closed field line ($q \in \mathbb{Q}$) or an ergodic surface ($q \in \mathbb{R} - \mathbb{Q}$). On the contrary, plasma particles characterized by a finite value of the connection length lay on field lines that will definitively touch the first wall and are to be considered outside the plasma core [77].

Exploiting such properties, it is possible to reconstruct the plasma boundary by means of a grid of starting points, dense enough according to the prescribed precision which the plasma boundary is requested to be known with. The problem of tracing infinitely long lines can be practically circumvented by assuming that a line is closed when:

- it comes back to the initial point within a given small distance, or
- the length of the traced field line is greater than a defined threshold (i.e., the admissible length expected for lines to intersect the wall).

Following such connection length approach, an iterative procedure aimed to the calculation of the connection length for successive initial positions along a given direction was designed. Once a prescribed accuracy in the plasma boundary reconstruction is assigned and the scanning direction is given with the starting point on the first wall, the connection length is calculated in terms of the distance of the integration initial point from the wall, thus to calculate the plasma-wall gap [78]-[79].

In the following, several cases are discussed, both for axisymmetric and non-axisymmetric plasmas.

4.3.1   Axisymmetric Plasma

As regards the axisymmetric plasmas, the possibility to formulate the flux density field components in terms of the magnetic poloidal flux per unit radian provides the plasma boundary as a level line for ψ: $\psi = \psi_b$. Therefore, the results obtained for this case can be used as a benchmark and as a proof of principle of the viability of 3-D plasma boundary reconstruction by means of accurate field lines tracing and connection length evaluation.

The equilibrium here considered is the end of a flat-top in DEMO Tokamak: *Equil_EOF_betapol0d8_li0d7_11coils_final2*. The gap reconstructed is at the outboard on the equatorial plane and the distance between two consecutive starting points along the unit normal vector to the first wall is $10\ mm$. Fig. IV.16 shows the results in terms of 3-D view of the traced field lines and their projection on the poloidal plane:
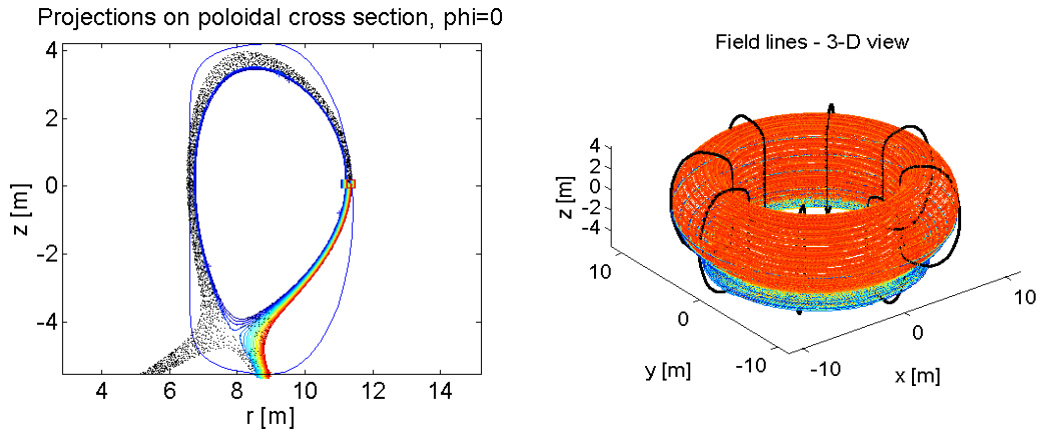
Fig. IV.16: Plasma-wall gap calculation in axisymmetric configuration: Projection on the Poloidal cross section of many traced lines (transition from red to blue) for the plasma-wall gap calculation, starting points (squares) and end points (stars) and 3-D view

Fig. IV.17 shows the Connection Length in terms of the distance from the first wall:
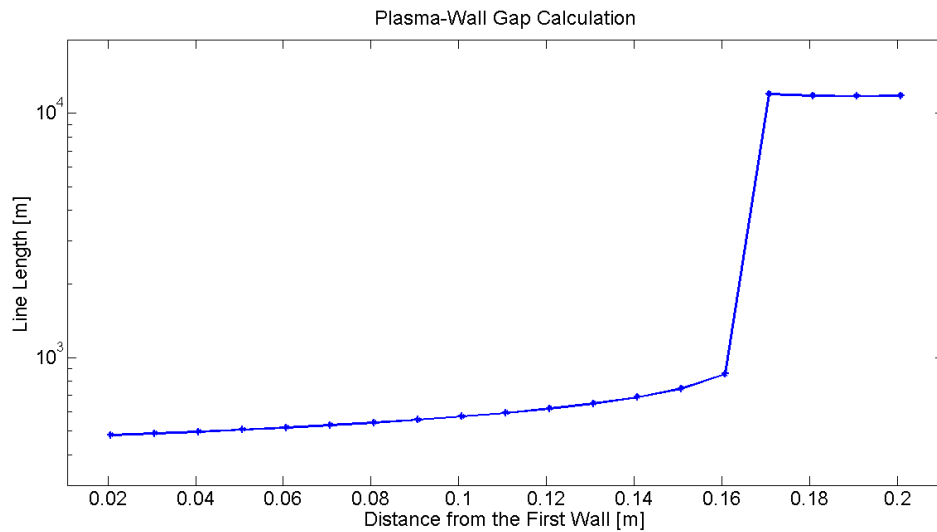
Fig. IV.17: Connection Length in terms of the distance from the First Wall

The sharp change in the connection length diagram shown in Fig. IV.17 is typical of the transition from the outer to the inner plasma region. The plasma separatrix is conventionally located at the average distance between the starting point of the last field line touching the wall and that of the first field line inside the plasma core (namely, *Last Closed Flux Surface - LCFS*). Therefore, the plasma-wall gap is: $Gap = 0.17 \pm 0.05\ m$

There is no need to clarify that the higher accuracy in the plasma-wall gap calculation is required, the smaller is step-size the numerical integrator needs,

so to prevent that the truncation error pushes away from the plasma the confined particles or vice versa, pulls the non-confined particles inside the core.

This implies a much higher computational burden because of the higher number of steps per each traced field line and the higher number of lines to be traced. For such problems, parallel computing is mandatory for a fast reconstruction of the plasma boundary, especially in non-axisymmetric configurations [80].

In Fig. IV.18 the quadrisection parallel computing algorithm is shown:
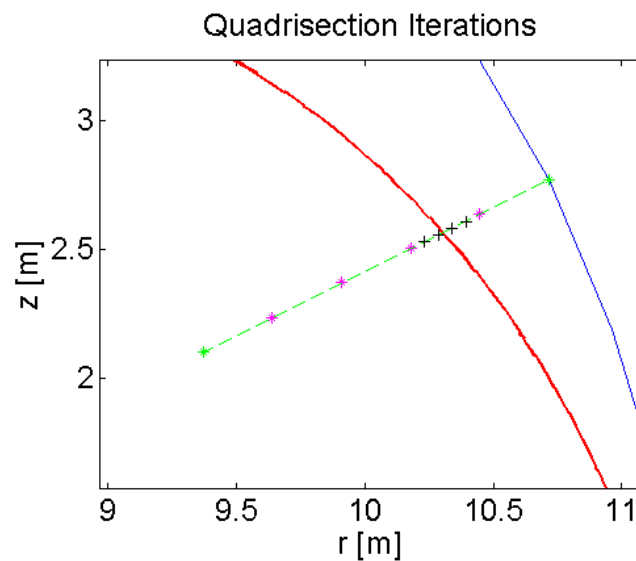
Fig. IV.18: The Quadrisection parallel computing algorithm (magenta stars are the starting points at the first iteration and black crosses are at the second iteration)

The parallel procedure in Fig. IV.18 is an enhanced version of the bisection algorithm, better suited for computers having four local workers. The procedure is based on the partition in five parts (i.e. positioning four evenly spaced points) of a segment having the two extrema in two points which are known to be outside and inside the plasma core respectively; then, each point is addressed to a different processor. Once the tracing is completed for the first step, two new extrema are individuated, so repeating the iterative procedure until the distance between the last internal and the last external points evaluated is lower than the prescribed tolerance in the plasma boundary reconstruction.

This procedure provides a speed up in the plasma-wall gap calculation because the distance between the last internal point and the last external point

is reduced by a factor of $\left(\frac{1}{5}\right)^k$, instead of $\left(\frac{1}{2}\right)^k$ as for the bisection procedure (k is the iteration number). In principle, this procedure can be even enhanced if a higher number of parallel CPUs is available on the workstation, thus placing a higher number of evenly spaced points along the exploration direction.

The application of this iterative procedure for the axisymmetric case in Fig. IV.16 gives the following results (the resolution in the plasma-wall gap calculation is $0.5\ mm$):
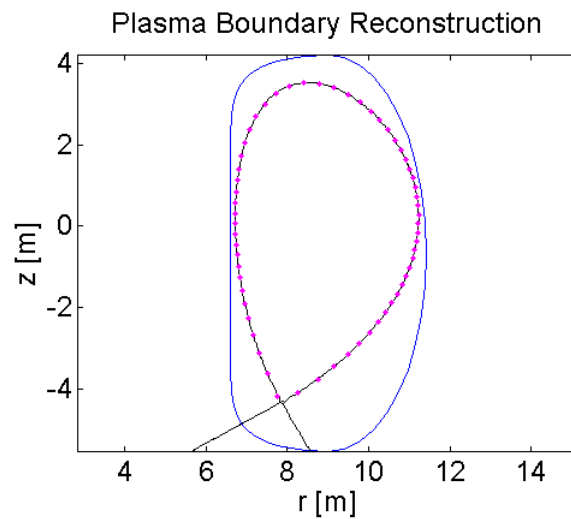
Fig. IV.19: Plasma boundary reconstruction in axisymmetric configuration (solid line: actual boundary as from the solution of the Grad-Shafranov equation; magenta stars: reconstructed plasma boundary)

The quadrisection parallel algorithm performs with a speed up that is about 2.67 with four local workers on a DUAL CORE workstation. The speed-up is defined as the ratio between the time need to run the algorithm using one processor and the time need if using more than one processor. This implies that the calculations were carried out by virtual processors, thus showing a speed up lower than the ideal value.

4.3.2 Non-Axisymmetric Plasma

Differently from the axisymmetric plasma configuration, where the reconstructed plasma boundary is perfectly replicated at each poloidal section,

the non-axisymmetric configuration needs the calculation at many toroidal angles, thus resulting in a much higher computational burden.

Therefore, a different technique for the plasma boundary reconstruction is presented: it is based on the calculation of just one plasma-wall gap within a prescribed accuracy, so to get one point of the Last Closed Magnetic Surface and then to carry out a very long integration (up to tens of kilometers), so to ergodically cover it. At last, the plasma-boundary is reconstructed in all the poloidal sections by exploiting the Poincaré Maps.

Fig. IV.20 refers to the axisymmetric CREATE-NL equilibrium *Equil_EOF4_betapol0d1_li1d0_11coils_nc*. After its identification via a suitable number of axisymmetric filamentary conductors, the non-axisymmetric plasma configuration is obtained by perturbing them. In particular, each filamentary conductor is affected by a 100 *mm* shift along the x-axis and a 5 *deg* tilt around the same axis. Moreover, the toroidal field is referred to the new coordinate frame where the actual filamentary conductor are axisymmetric.
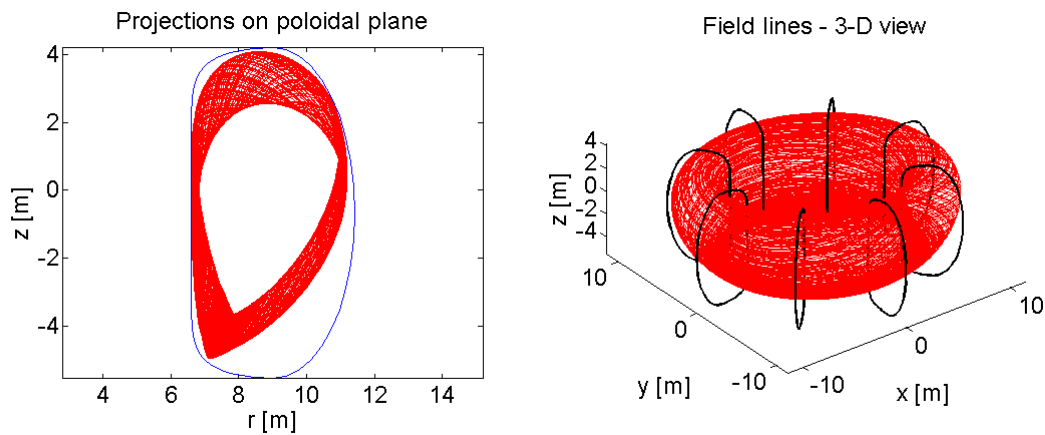
Fig. IV.20: Plasma-wall gap calculation in non-axisymmetric configuration: Projection on the Poloidal cross section and 3-D view of the field line covering the Last Closed Magnetic Surface

The field line in Fig. IV.20 covers the Last Closed Magnetic Surface for about 25 *km*. It is reconstructed within an accuracy of 5 *mm* for the calculation of the gap in the poloidal plane at $\varphi = 0$ on the outboard at the poloidal plane.

Fig. IV.21 shows the Poincaré Maps for the poloidal planes located at $\varphi = 0$, $\varphi = \frac{\pi}{2}$, $\varphi = \pi$ and $\varphi = \frac{3}{2}\pi$, that are the sections where the highest perturbation is expected to affect the plasma:
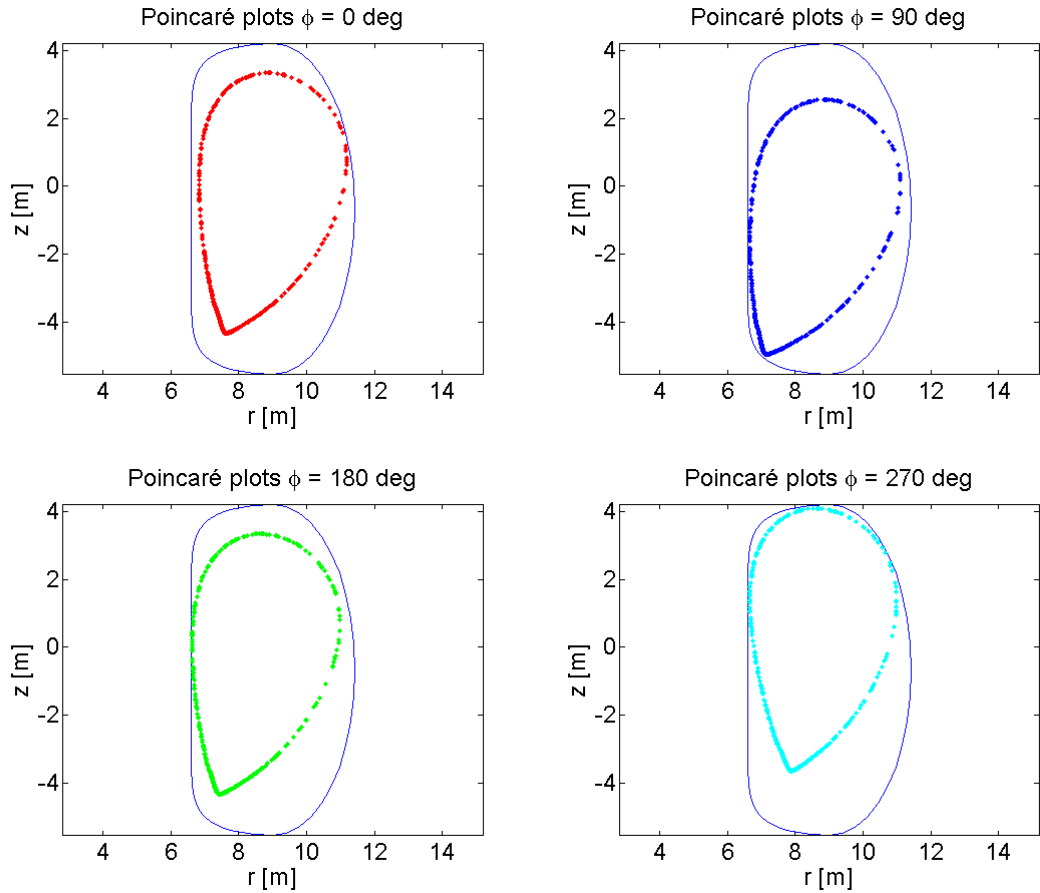
Fig. IV.21: Poincaré Maps at $\varphi = 0$, $\varphi = \frac{\pi}{2}$, $\varphi = \pi$ and $\varphi = \frac{3}{2}\pi$ for a kinked plasma

The Poincaré Maps in Fig. IV.21 show how the plasma boundary changes at each poloidal section, accordingly with the perturbation affecting the flux density field sources. This technique has the further advantage to calculate the Poincaré Maps at all the poloidal sections as a post-process of the field line tracing so taking few tens of milliseconds per each of them.

Therefore, a 3-D surface enclosing the plasma core can be drawn inside the vacuum vessel, by merging the many Poincaré Maps:
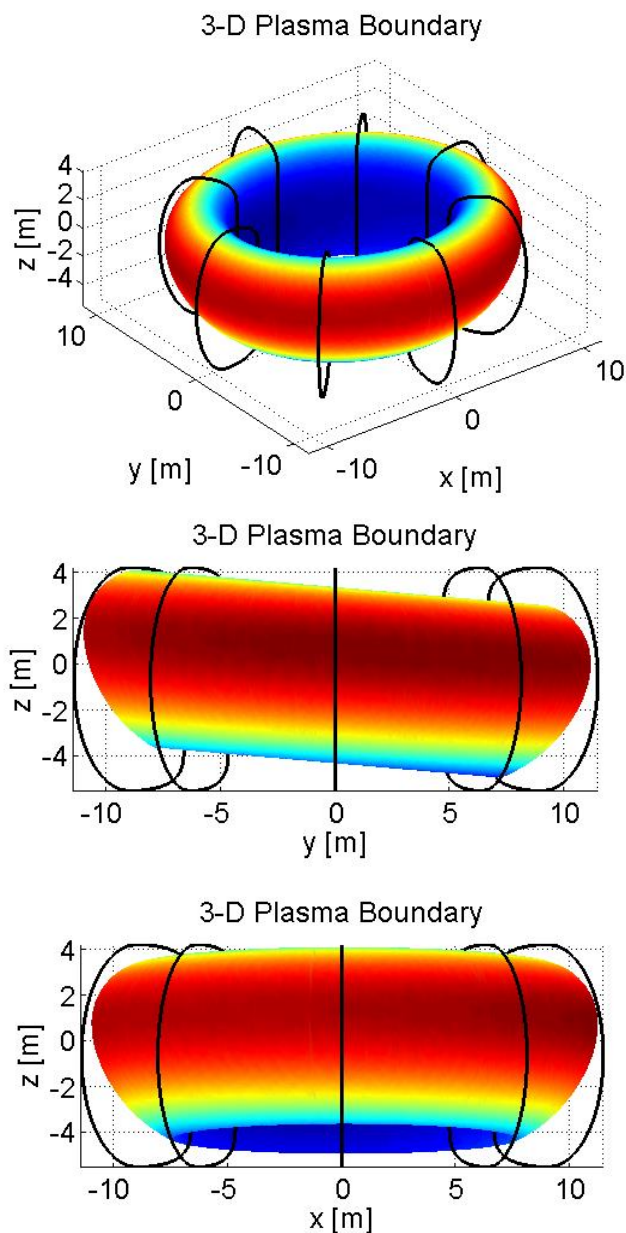
Fig. IV.22: Kinked plasma shape

Parallel computing is also suitable for this procedure, because:

- the quadrisection algorithm can be exploited for the calculation of the plasma-wall gap, or

- each processor is devoted to the calculation of one plasma-wall gap and then to the tracing of one field line for the ergodic covering of the plasma boundary, thus reducing the length of each traced field line.

At last, the same procedure is applied for a non-axisymmetric configuration expressed by means of the Clebsch decomposition. In particular, the two Clebsch Potentials U and V are those expressed in (IV.73).

Thanks to the shape of the first wall and of the $U = const.$ Clebsch surface, it is possible to know the exact coordinates of one of the boundary points, that is the very point touching the first wall: $(r_{tch}, \varphi_{tch}, z_{tch}) = \left(10.395, \frac{\pi}{2}, 0\right)$. The Clebsch potentials get the following values: $U_b = -9.7226 \, mT^{\frac{1}{2}}, V_b = 5.25 \, mT^{\frac{1}{2}}$ at the contact point.

Fig. IV.23 shows the Poincaré Maps for such field configuration:
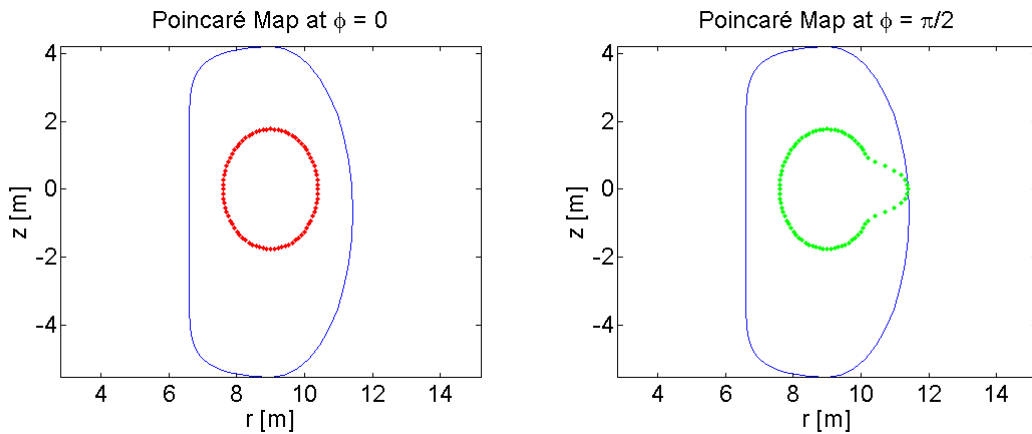
Fig. IV.23: Poincaré Maps for at $\varphi = 0$ and $\varphi = \frac{\pi}{2}$ for a locally perturbed plasma

4.4   Identification of Non-Axisymmetric Plasmas

4.4.1   Introduction

The need to have elongated plasmas inside the vacuum vessel with their intrinsic instability highlights the need to set up a feedback control system acting on the plasma position and shape. A very important component of this kind of control systems is the subsystem generating the values of the geometrical parameters related to the plasma boundary to control, on the basis of the magnetic measurements. Unfortunately, these parameters cannot be directly measured, but can only be estimated in real-time via a proper processing of the available magnetic measurements.

Fig. IV.24: Examples of Pick-up Coils for the flux density field measurement (Courtesy of JET-EFDA Organization)

As recalled, the problem of the *Plasma Boundary Identification* for axisymmetric plasmas can be solved by solving the Grad-Shafranov Equation for the axisymmetric plasmas, or by using other techniques [81]-[82] better suited for the real-time control issues, thanks to their high speed (some milliseconds, as well as the sampling time of the control system).

Unfortunately, these techniques are not exploitable for full three-dimensional plasma configurations, because of the lack of symmetry (as for the identification based on the axisymmetric filamentary currents, since it exploits the poloidal flux per unit radian that is intrinsically axisymmetric). Therefore, new techniques are to be developed and set up when dealing with 3-D plasmas.

Once the plasma is identified, it is possible to study its topology by tracing the flux density field lines and reconstructing the boundary exploiting the techniques presented in Section 4.3. In fact, they require the knowledge of the flux density field at each point inside the Vacuum Vessel or at the nodes fine enough mesh, so to interpolate the *B* field values at the other points within a given accuracy.

4.4.2   Methods

The identification of a three dimensional plasma is based on the magnetic measurements provided by the diagnostic system. Conceptually, the sensors consist of an open coil; the voltage across its terminals is measured by means of

a differential amplifier and is proportional to the to the time derivative of the total magnetic flux linked with it, according with the Faraday-Neumann-Lenz law.

A measure of the magnetic field can be obtained by using so called *pick-up coils* (see Fig. IV.24): this kind of sensors consists of multiple windings of small radius wires, located at a given point of the tokamak. The flux linked with this solenoid is proportional to the component of the magnetic field parallel to the sensor axis:

$$V = -NA \frac{\partial}{\partial t} B_a(\boldsymbol{r}, t)$$
$$B_a(\boldsymbol{r}, t) = -\frac{1}{NA} \int_{t_0}^{t} V(\tau) d\tau + B_a(\boldsymbol{r}, t_0)$$

(IV.75)

where:

- N is the number of turns of the pick-up coil;
- A is the cross section area of the pick-up coil;
- B_a is the flux density field component along the axis of the pick-up coil.

For sake of simplicity, in the following, the pick-up coils will be considered as ideal local tri-axial sensors, able to measure all the radial, vertical and toroidal components of the magnetic flux density field at a point. Moreover, the measurement performed will not be affected by any integration drift or statistical errors.

Additional magnetic measurements are given by full flux loops and saddle coils, which provide the total magnetic flux linked with a closed line. Although these measurements can also be considered in the 3-D identification procedure, for the sake of simplicity, here we just consider local pick-up coil measurements.

In principle, this kind of identification of a 3-D plasma means to approximate the flux density field with an equivalent distribution obtained via best fit of the magnetic measurements. The equivalent flux density field distribution is obtained via a proper combination of a family of basis functions, which are the flux density fields generated by equivalent sets of electromagnetic sources, able to model both the axisymmetric field and the three-dimensional perturbation.

The axisymmetric poloidal flux density field is generated by an equivalent set of axisymmetric conductors, whilst the perturbations breaking the axisymmetry of the configurations are modelled by superposing the fields

generated by a set of magnetic dipoles, characterized by a proper value of the magnetic moment.

$$\boldsymbol{B}_{axi} = \nabla \left(\frac{\mu_0}{\pi} \sum_{n=1}^{N_{fil}} I_n \frac{\sqrt{rr_n'}}{k_n} \left[\left(1 - \frac{k_n^2}{2} \right) K(k_n^2) - E(k_n^2) \right] \right) \times \nabla \varphi \qquad \text{(IV.76)}$$

$$\boldsymbol{B}_{dip} = \frac{\mu_0}{4\pi |\boldsymbol{r}|^3} \left(\frac{3\boldsymbol{r}(\boldsymbol{m} \cdot \boldsymbol{r})}{|\boldsymbol{r}|^2} - \boldsymbol{m} \right) \qquad \text{(IV.77)}$$

Fig. IV.25 shows a sketch of the two equivalent sources:
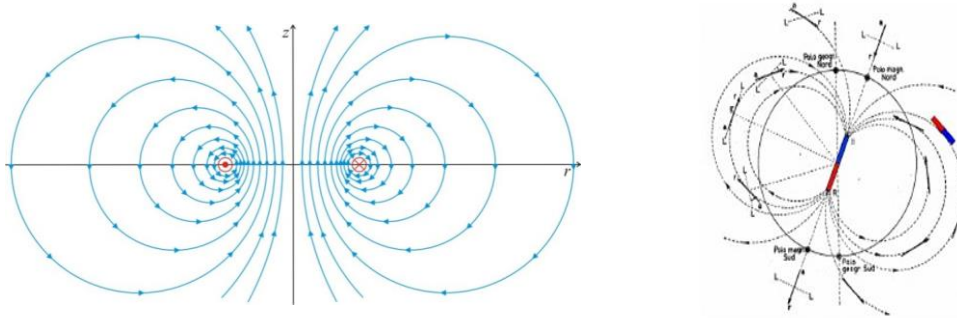
Fig. IV.25: Equivalent sources for the three-dimensional identification (axisymmetric filamentary conductor on the left and magnetic dipole on the right)

For each axisymmetric filamentary current, the parameters to calculate to get the best approximation of the axisymmetric flux density fields are the poloidal position in the poloidal plane, as well as the current it carries. On the other hand, the magnetic dipoles have to be characterized by their spatial position, the orientation of the magnetic moment and the magnetic moment amplitude. Therefore, the total number of degrees of freedom is $3 \cdot N_{fil} + 7 \cdot N_{dip}$.

Being $\mathcal{S} \subseteq \mathbb{R}^{3 \cdot N_{fil} + 7 \cdot N_{dip}}$ the subspace of the vector space of the solutions, the mathematical model of the identification problem can be formulated as:

$$\min_{\underline{x} \in \mathcal{S}} \left\| \underline{B} - \underline{B}_{id} \right\| \qquad \text{(IV.78)}$$

where $\underline{B}$ is the vector of the actual flux density field measurements and $\underline{B}_{id}$ is the identified flux density field measurements.

The problem formulated as in (IV.78) is intrinsically non-linear, being so the relation between the flux density field and the geometry of the electromagnetic sources. A different linearized formulation can be implemented, where the poloidal position of the axisymmetric filamentary currents is fixed as

well as the spatial position and the orientation of the magnetic moments of the magnetic dipoles. Moreover:

- the magnetic dipoles are placed at the poloidal position of the axisymmetric filamentary currents, along the toroidal direction;
- three distributions of magnetic dipoles are placed at each poloidal position, directed along the radial, vertical and toroidal direction respectively;
- the magnetic moments of each distribution of dipoles having the same poloidal position is sinusoidal and the toroidal frequency depends on the kind of perturbation to identify.

Therefore, the solution vector belongs to the following vector subspace $\tilde{\mathcal{S}} \subseteq \mathcal{S} \cap \mathbb{R}^{7 \cdot N_{fil}}$, where the degrees of freedom are:

- the current of the axisymmetric filaments;
- the amplitudes of the sine and cosine distributions of the $\boldsymbol{m}_r$ sinusoidal distribution;
- the amplitudes of the sine and cosine distributions of the $\boldsymbol{m}_z$ sinusoidal distribution;
- the amplitudes of the sine and cosine distributions of the $\boldsymbol{m}_\varphi$ sinusoidal distribution.

Using such formulation, the unknown vector consists of the amplitudes of the magnetic sources. Their relation with the flux density field is now linear, allowing to rewrite the (IV.78) as follows:

$$\underline{\underline{G}} \cdot \underline{x} = \underline{B} \tag{IV.79}$$

where $\underline{\underline{G}}$ is the Green Matrix, and G_{ij} is the measure performed by the i-th sensor when the only j-th source is active is characterized by an unitary magnitude (an unitary current, for the axisymmetric filamentary currents or an unitary magnetic moment for the magnetic dipoles).

Assuming that the Green matrix is left-invertible, that is equivalent to say that the available measurements are independent, it follows that a unique solution into the subspace $\tilde{\mathcal{S}}$ can be found if the measurement vector is in the range of the matrix $\underline{\underline{G}}$. In practice, this is extremely improbable because nothing guarantees that the solution of the (IV.79) lies in $\tilde{\mathcal{S}}$. Moreover, it is worth noticing

that the noise corrupting the measurements is another cause for the solution vector not to belong to the subspace $\tilde{\mathcal{S}}$.

For these reasons, the solution of (IV.79) is obtained by choosing the vector $\underline{x}$ as:

$$\underline{x} = \left(\left(\underline{\underline{G}}^T \cdot \underline{\underline{G}} \right)^{-1} \cdot \underline{\underline{G}} \right) \cdot \underline{B} = \underline{\underline{G}}^\dagger \cdot \underline{B} \qquad \text{(IV.80)}$$

where $\underline{\underline{G}}^\dagger$ states the Moore-Penrose Green Pseudoinverse Matrix [83], that is the solution of the following linear optimization problem:

$$\min_{\underline{x} \in \tilde{\mathcal{S}}} \left\| \left(\underline{B} - \underline{\underline{G}} \cdot \underline{x} \right)^T \cdot \left(\underline{B} - \underline{\underline{G}} \cdot \underline{x} \right) \right\| \qquad \text{(IV.81)}$$

The solution of (IV.80) needs to take into account that the matrix $\underline{\underline{G}}$ may be ill-conditioned [84], making the evaluation of its pseudoinverse unreliable; this problem can be easily circumvented if a singular value regularization is performed [85].

Moreover, it is worth noticing that the different dimensions of the axisymmetric currents and the magnetic dipoles might also affect the Green matrix making it badly scaled or nearly singular. For this reason, the identification procedure is split in two sub-steps:

1. an axisymmetric identification, considering the average value of the sensors placed at the same poloidal position;
2. a non-axisymmetric identification, considering only the perturbing flux density field contribution on the pick-up coils measurements.

4.4.3 Assessment and application to a kinked plasma

Before applying the identification procedure depicted in Section 4.4.2 to a plasma configuration, it was validated and tested on several cases, each of them characterized by a different perturbation affecting the axisymmetric filamentary currents. Hereafter, the main results are reported.

The sensors used for the cases illustrated below are specified in Fig. IV.26, where their poloidal positions are shown:
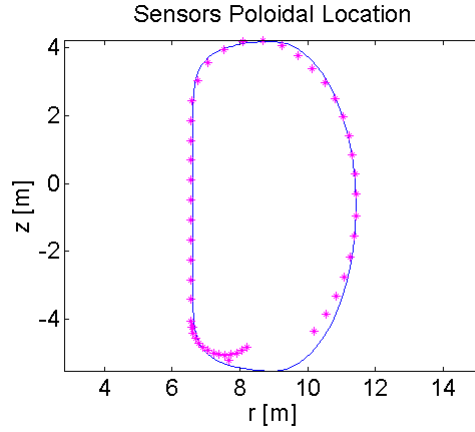
Fig. IV.26: Poloidal positions of the pick-up coils used for the identification

The sensors in are then replicated in six poloidal cross sections evenly spaced (every sixty degrees along the toroidal direction).

Moreover, taking into account the sinusoidal distribution along φ of the magnitude of the magnetic moments, the class of perturbations hereafter considered consists of harmonic deformations of the axisymmetric currents:

$$\begin{cases} x = (r_0 + a \cdot \cos(N\varphi)) \cos(\varphi) \\ y = (r_0 + a \cdot \cos(N\varphi)) \sin(\varphi) \\ z = z_0 + b \cdot \sin(N\varphi) \end{cases} \tag{IV.82}$$

The following test case refers to a $N = 2$ perturbation acting on a filamentary current, whose amplitude is $0.01\ m$; the axisymmetric filament carries a $1\ MA$ current and is placed at $(r_0, z_0) = (9,0)$ in the poloidal plane, as shown in the following Fig. IV.27:
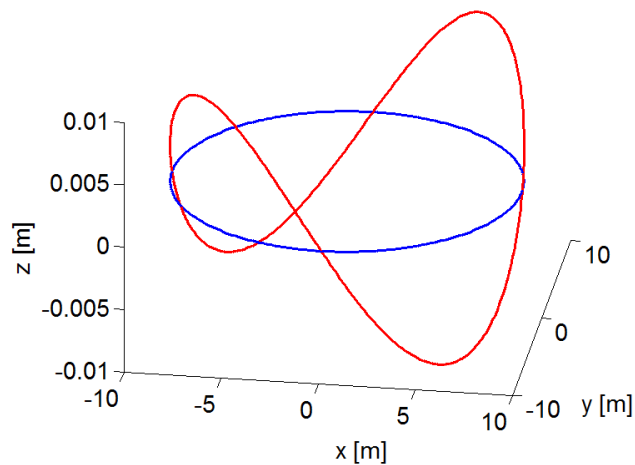
Fig. IV.27: Deformed filamentary conductor (solid red) and equivalent axisymmetric filamentary conductor (solid blue)

As regards the axisymmetric identification sub-step, the equivalent source is the axisymmetric filament (solid blue line in Fig. IV.27). The goal of this sub-step is to get the current circulating into the axisymmetric filament, that it is the same of the deformed wire, thanks to the geometry of the magnetic sources.

The identification problem (IV.80) can be rewritten as follows:

$$\begin{cases} m_1 = g_{11}I_{axi} \\ m_1 = g_{12}I_{axi} \\ \quad\vdots \\ m_{N_{sens}} = g_{1N_{sens}}I_{axi} \end{cases} \qquad (IV.83)$$

The solution of the set in (IV.83) in the least square sense gives the axisymmetric current value within a relative error less than $1\ p.p.m.$, and a high accuracy is also obtained for the flux density field. The identification error on the flux density field components is defined as the average value of the absolute error on each sensors measurement, over the flux density field magnitude at the sensors location.

Fig. IV.28 and Fig. IV.29 show the comparison between the actual and the identified axisymmetric field, related only to the set of sensors located at $\varphi = 0$, thanks to the axisymmetry:
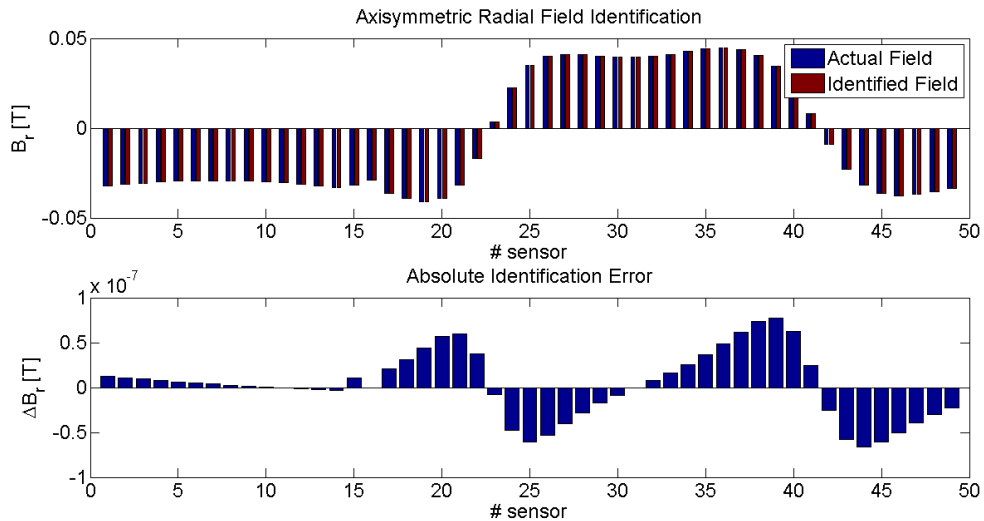
Fig. IV.28: Radial Field Identification
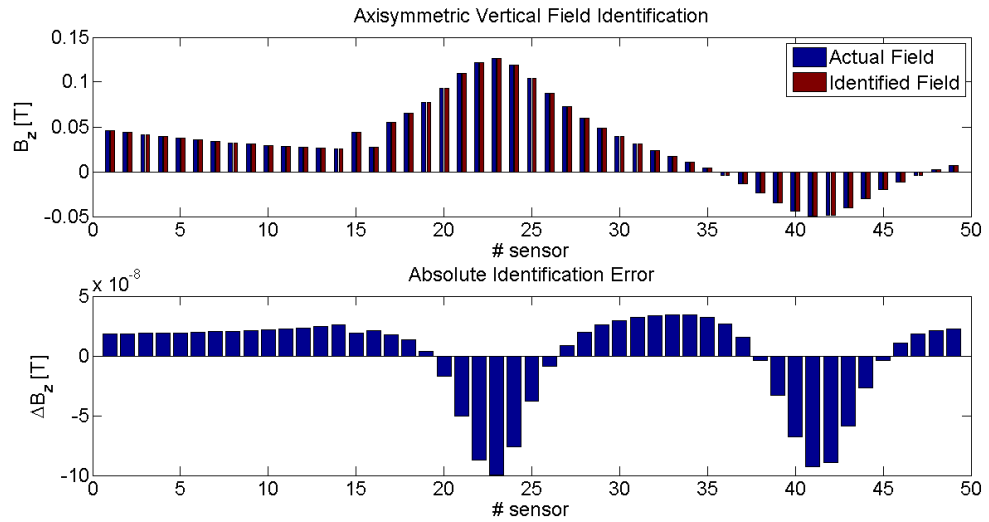
Fig. IV.29: Vertical Field Identification

As regards the identification of the three-dimensional contribution, the three magnetic dipoles distributions are placed along the solid blue line in Fig. IV.27. The field the magnetic dipole are called to identify is the perturbation due to the deformation of the current, with respect to the axisymmetric geometry. Fig. IV.30, Fig. IV.31 and Fig. IV.32 show the results in terms of flux density field components identification:
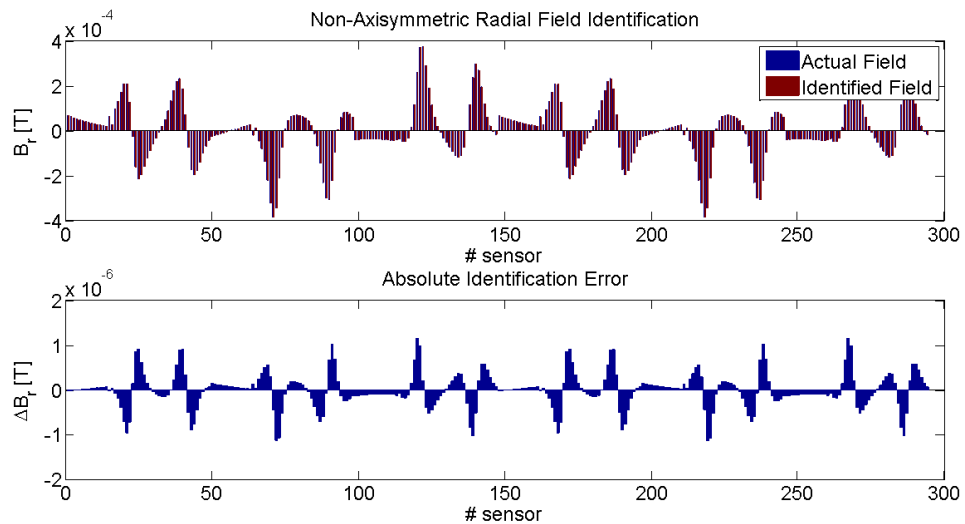
Fig. IV.30: Radial Field Identification
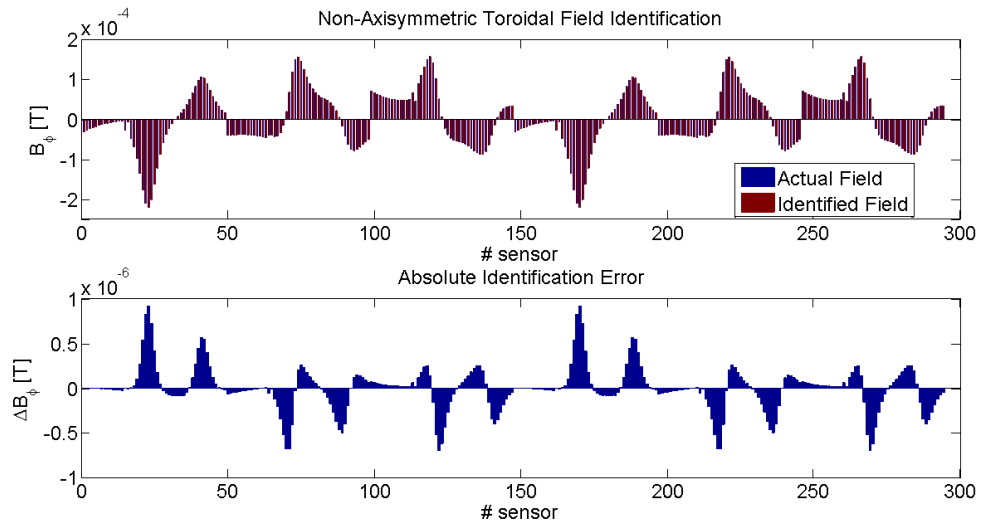
Fig. IV.31: Toroidal Field Identification
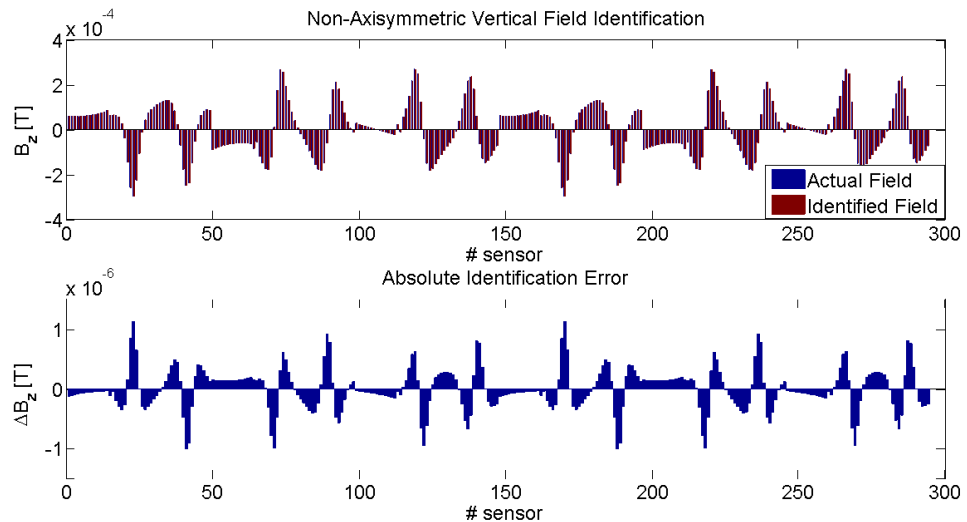
Fig. IV.32: Vertical Field Identification

Since the identification procedure generates the values of the axisymmetric currents and the magnetic moments in such a way to get the best fit of the magnetic measurements, it is necessary to check the value of the flux density field also in a validation set of points, outside the location of the sensors used for the identification. This additional check is necessary because it may occur that the identification procedure verifies the constraints at the sensors points, with however a high error on the field distribution elsewhere.

The validation set is chosen taking the points along several circumferences placed in various the poloidal planes, whose centre coincides with the poloidal coordinates of the equivalent sources.

Fig. IV.33 shows the validation points set:
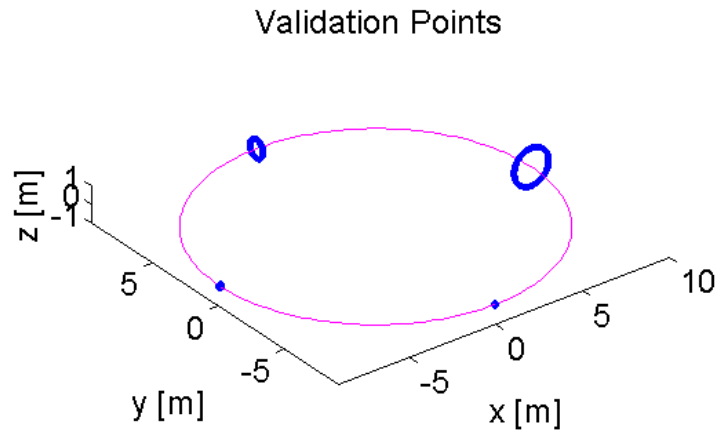
Fig. IV.33: Validation Points set

The radii of the circumferences are $1\ m, 0.5\ m, 0.1\ m, 0.05\ m$ respectively. The results obtained comparing the actual, and the identified components of the flux density field are hereafter shown:
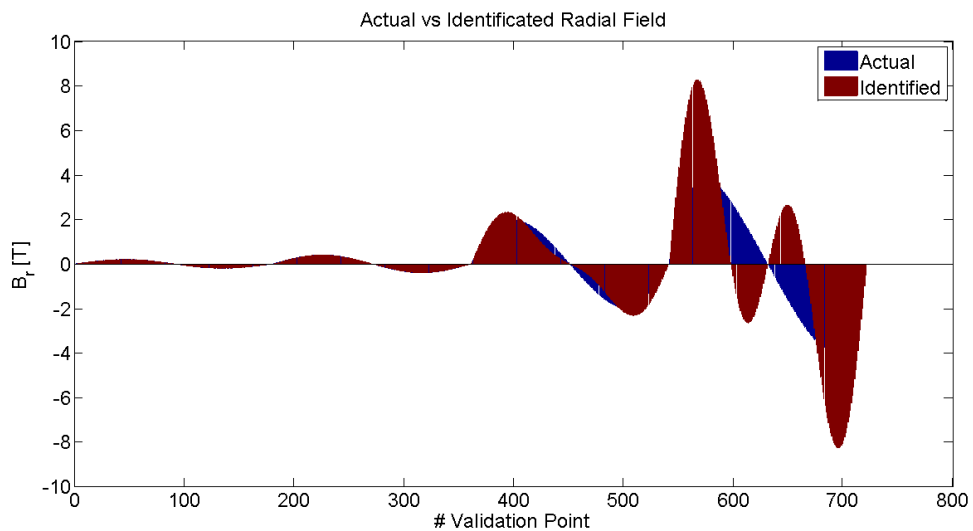
Fig. IV.34: Radial Field Identification
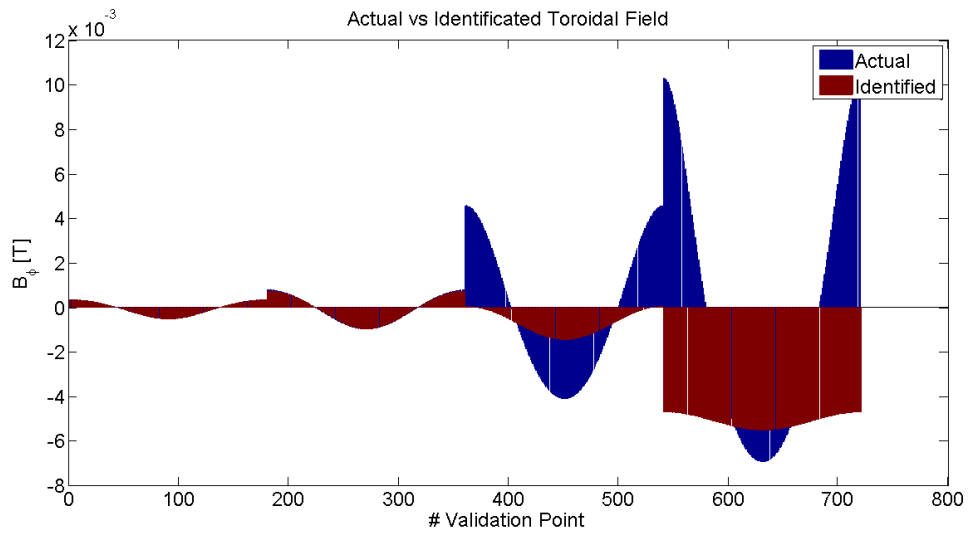
Fig. IV.35: Toroidal Field Identification
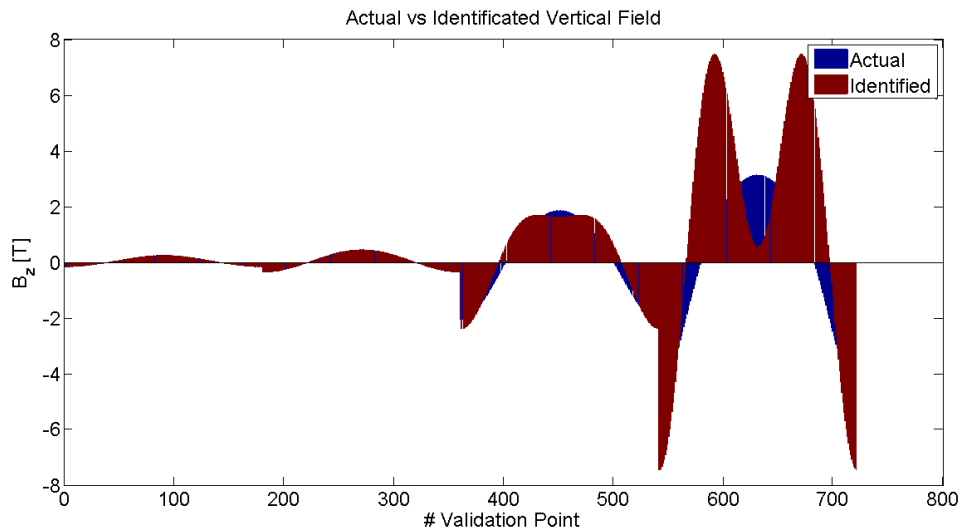
Fig. IV.36: Vertical Field Identification

It is worth noticing that the considered deformation acts like an $M = 1$ poloidal mode into the poloidal plane, even though the toroidal mode is $N = 2$. Moreover, the flux density field components at the last points in Fig. IV. 34, Fig. IV.35 and Fig. IV.36 are affected by a ripple that makes unreliable the identification results. On the other hand, this phenomenon is shown only on the closest validation points to the equivalent sources and the closer they are, the higher the ripple is. For this reason, it is necessary to evaluate the flux density field at a high enough distance from the sources, not to be affected by this perturbation and so to get a reliable identification. This condition is not

restrictive when pursuing the goal to identify a three-dimensional plasma, because the equivalent sources are placed inside the plasma core and the flux density field is to be calculated into the vacuum vessel region bounded by the first wall and the plasma separatrix.

After having assessed the identification procedure, it is then applied to a non-axisymmetric plasma configuration: the three-dimensional perturbation identified in the following is an $N = 1$ kink mode affecting the plasma, as considered in Chapter III for the electromechanical analysis.

The non-axisymmetric field is generated by kinking (i.e. shifting along a direction and rotating around an axis) the axisymmetric currents obtained by the identification of a plasma equilibrium configuration (*Equil_SN_17condR3_SOF_betapol_1d2_li_0d7*). Fig. IV.37 shows the unperturbed plasma equilibrium in terms of poloidal flux per unit radian distribution:
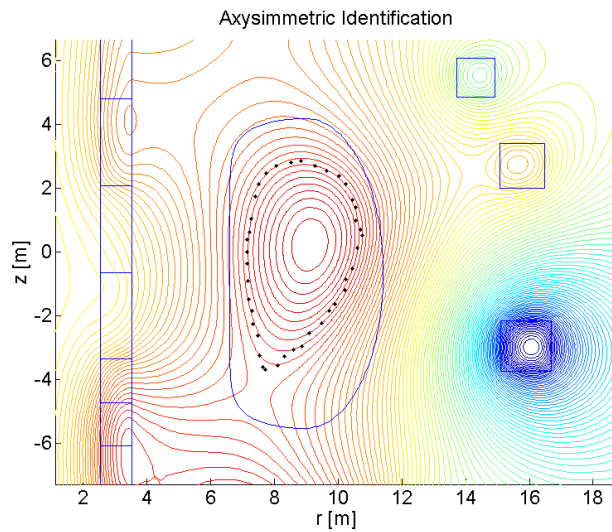
Fig. IV.37: Axisymmetric plasma configuration in terms of Poloidal Flux per unit radian and axisymmetric filamentary currents

Every axisymmetric filament is affected by a 5 *cm* rigid displacement along the x axis and by a 0.5 *deg* rotation around the same axis:
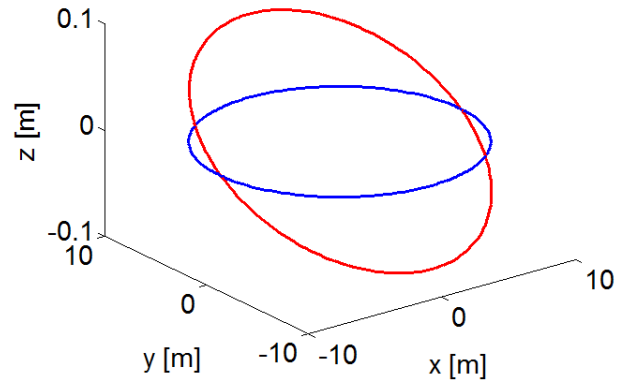
Fig. IV.38: Example of axisymmetric filamentary current affected by a kink

As regards the poloidal position of the equivalent sources, they would be too much close to the axisymmetric plasma separatrix if the position of the axisymmetric filamentary currents were chosen, as in Fig. IV.37. For this reason, the latter was shrunk by a factor of $\frac{1}{3}$ so to avoid the ripple effects observed in in Fig. IV. 34, Fig. IV.35 and Fig. IV.36.

The radial, toroidal and vertical components of the flux density field were identified, applying the approach illustrated above:
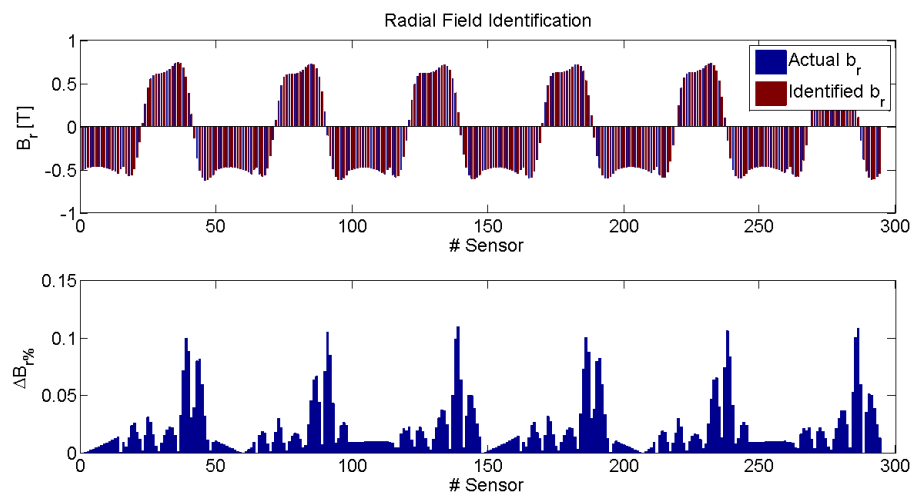
Fig. IV.39: Radial Field Identification
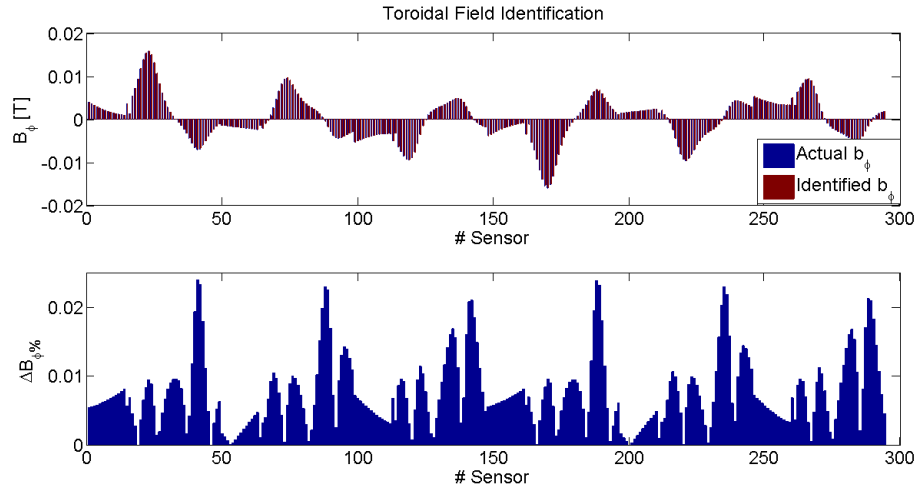
Fig. IV.40: Toroidal Field Identification
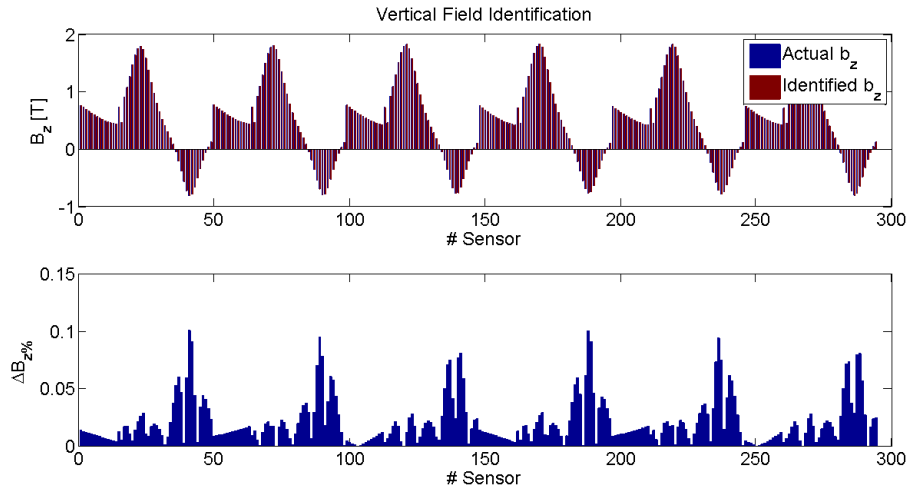
Fig. IV.41: Vertical Field Identification

On such identification, the errors on three components of the flux density field are: $\Delta B_{r_\%} = 0.0211\%$, $\Delta B_{\varphi_\%} = 0.0076\%$ and $\Delta B_{z_\%} = 0.0214\%$ respectively.

An additional figure of merit to assess the performances of the identification procedure can be pursued by reconstructing the plasma boundary in both the actual and the identified configurations and then comparing them, exploiting the Poincaré Maps as shown in Section 4.3. Using such technique, the plasma boundary was reconstructed within an accuracy of 1 mm.

In Fig. IV.42, the plasma boundary is shown by means of the field line covering it in ergodic way. Fig. IV.43 shows the comparison of the Poincaré Maps of the plasma boundary and of the last traced field line touching the first wall, in four poloidal sections for both the two configurations.
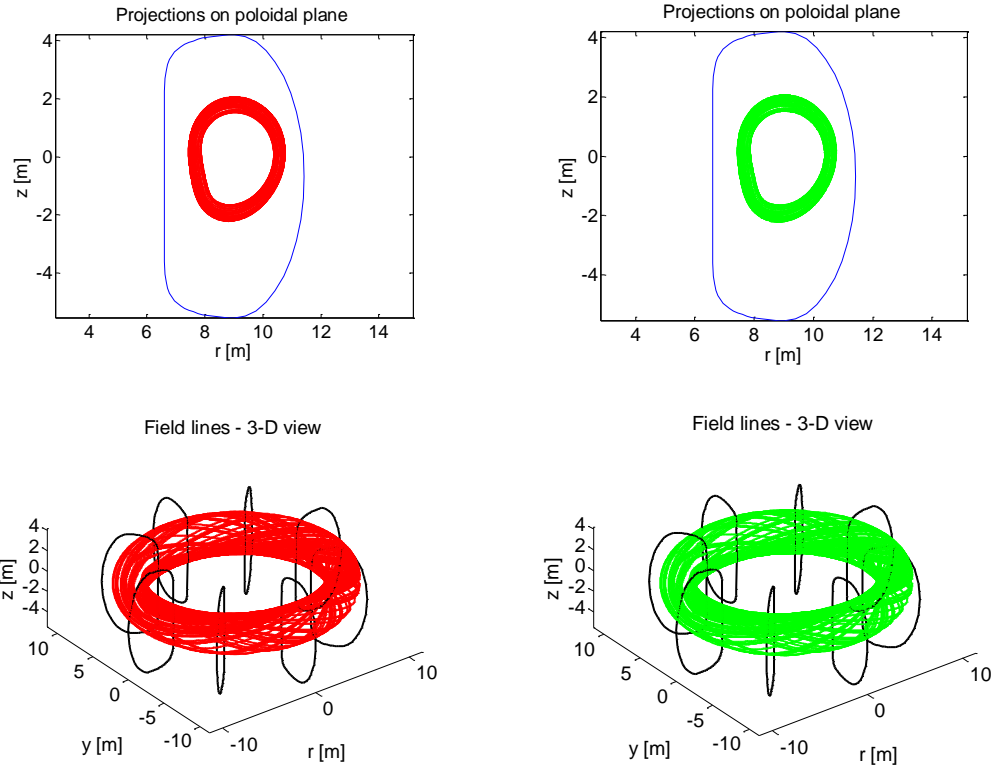
Fig. IV.42: Plasma Boundary Field Line in Actual (left) and Identified (right) Configurations
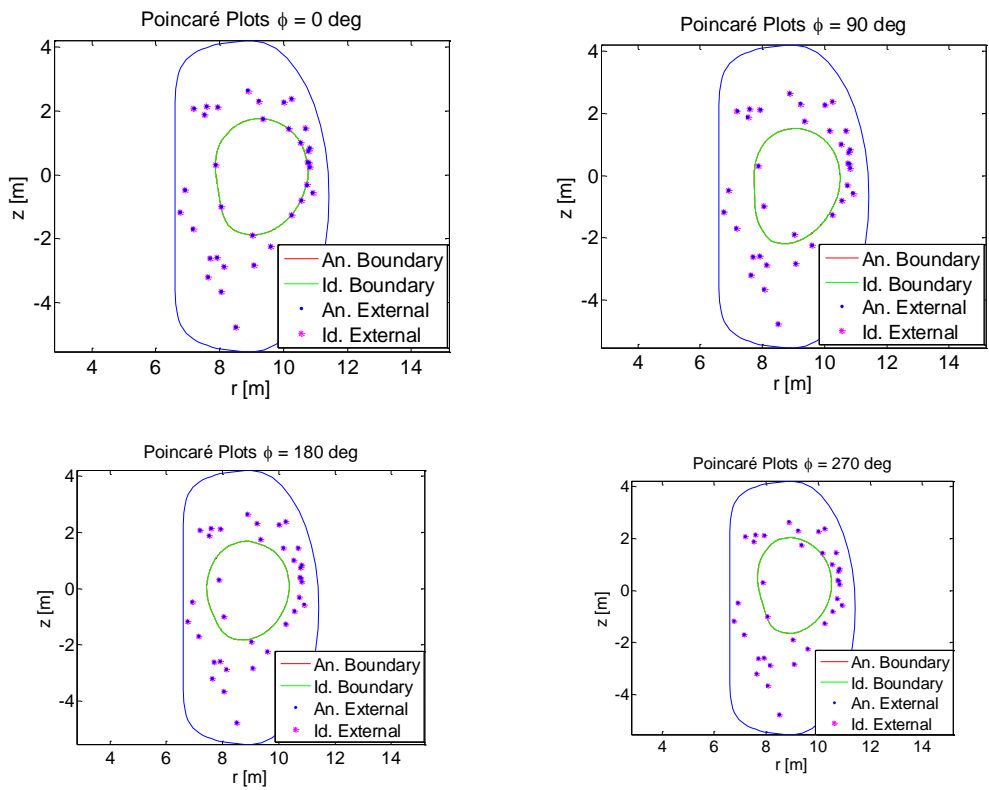
Fig. IV.43: Plasma Boundary in Actual (left) and Identified (right) Configurations at $\varphi = 0$, $\varphi = \frac{\pi}{2}$, $\varphi = \pi$ and $\varphi = \frac{3}{2}\pi$

Fig. IV.43 shows that the identified and the actual plasma boundaries are practically coincident, demonstrating that the proposed identification procedure is well suited for the considered class of plasma perturbations, as the plasma kink.

At last, the comparison between the actual and the identified plasma boundaries is shown in the following Fig. IV.44:
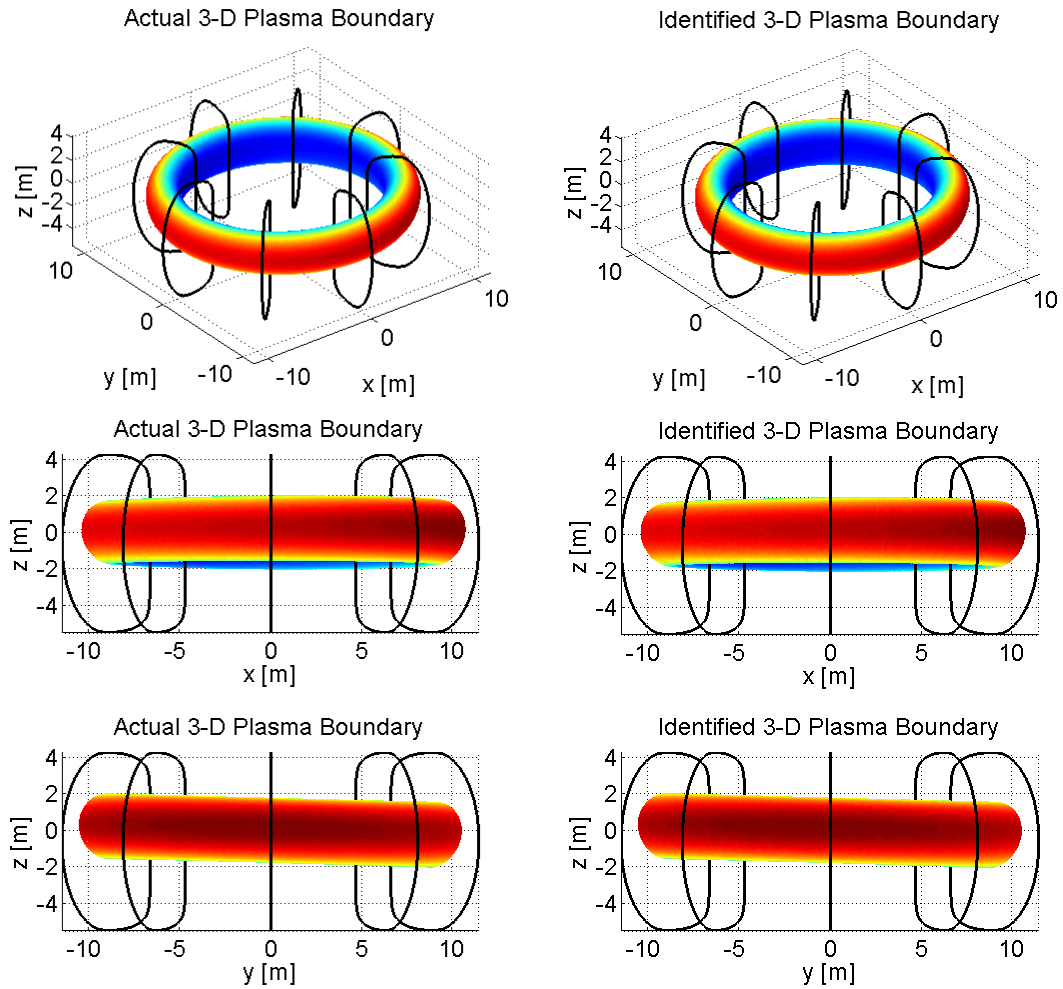
Fig. IV.44: Actual (left) vs Identified (right) Plasma Shape

The assessment of the accuracy of such reconstruction can be pursued by calculating and comparing the plasma-wall gaps for the two configurations. Being available the plasma boundary by means of the Poincaré Maps, the plasma-wall gap can be easily calculated as shown in the following Fig. IV.45:
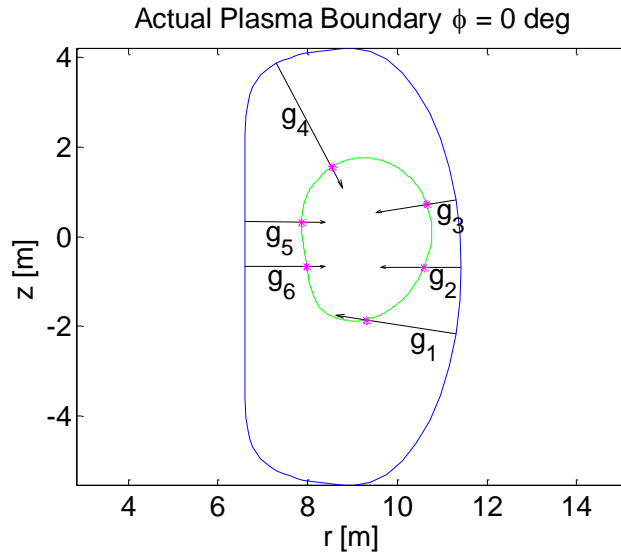
Fig. IV.45: Plasma-Wall Gaps

The following Tab. IV.4 shows the values of the plasma-wall gaps in Fig. IV.45 calculated at the four poloidal sections in Fig. IV.43:

Tab. IV.4: Plasma-Wall Gaps in Actual ($\mathcal{A}$) and Identified ($\mathcal{I}$) Configuration

	Plasma-Wall Gaps [m]							
	0 *deg*		90 *deg*		180 *deg*		270 *deg*	
	$\mathcal{A}$	$\mathcal{I}$	$\mathcal{A}$	$\mathcal{I}$	$\mathcal{A}$	$\mathcal{I}$	$\mathcal{A}$	$\mathcal{I}$
g1	2.036	2.034	1.799	1.803	2.366	2.371	-	-
g2	0.883	0.888	1.015	1.019	1.313	1.310	1.142	1.141
g3	0.660	0.662	0.983	0.977	1.073	1.074	0.865	0.865
g4	2.667	2.666	2.761	2.761	2.544	2.548	2.229	2.231
g5	1.274	1.274	1.164	1.165	0.867	0.870	1.077	1.074
g6	1.385	1.381	1.146	1.150	0.962	0.960	1.313	1.310

The results in Tab. IV.4 show that it is possible to reconstruct the plasma boundary by means of an equivalent set of axisymmetric filamentary currents and magnetic dipoles with a geometrical error on the plasma-wall gaps up to few millimetres.

Conclusions

Basic equilibria in tokamaks are mostly 2-D axisymmetric, but in principle the 3D perturbations may occur in any moment of the tokamak operations, breaking the symmetry of the field distribution and making the plasma stability and control more difficult.

As well as for the 2-D axisymmetric equilibria, for these reasons, the study of the property of a 3-D plasma (field distribution, boundary, Scrape-Off Layer etc.) is mandatory for the stable and reliable long-term operation of the machine, as the principal part of a Fusion Power Plant.

Therefore, several aspects related to the 3-D perturbations affecting the thermonuclear plasmas were dealt; hereafter the main conclusions are reported for each of them.

Diamagnetic flux measurement for Poloidal Beta estimation in presence of non-axisymmetric effects in ITER tokamak:

A new tool for the electromagnetic analysis in tokamak, COMPFLUX, is presented; it is designed for the analysis of the effects related to geometrical imperfection of both magnetic field sources and sensors and spurious sources in fusion devices.

The main feature of this procedure is the interpolation procedure based on the computation of the magnetic field and magnetic vector potential for the nominal and auxiliary sensors, allowing to carry out extensive and fast sensitivity analyses in the presence of misalignments and manufacturing errors of sensors and sources.

The procedure was validated for several test cases, showing about 10 ppm accuracy, fulfilling the usual requirements for fusion tokamaks.

The procedure was used for the analysis of the diamagnetic measurements in ITER tokamak to estimate effects of various error sources.

The effects due to thermal expansion and sensor/magnetic field sources deformation can mostly be compensated. In particular, the effects of Poloidal Field Coils, Central Solenoid and Toroidal Field coils can mostly be compensated because their deformation is caused by assembly and manufacturing deviations and so well-known once the actual geometry either is.

The effect of the toroidal plasma current can also be known by means of the experimental measurement with two similar plasmas with opposite helicity; once it is known, it can be partially compensated for the other pulses. Its effect upon a 0.1 deg tilted main diamagnetic loop is about 30 mVs.

The thermal expansion yields a 360 mVs perturbation upon the main diamagnetic loop measurement.

As for the ferromagnetic components of the tokamak, the largest effect is generated by the ferromagnetic inserts (about 250 mVs). This effect can experimentally be estimated, with suitable test pulses at different values of the toroidal field and then partially compensated. However, the time integration of the Diamagnetic Loop voltage starts at the beginning of the pulse and so this effect is limited to about 50 mVs due to the rotation of the magnetization vector when the poloidal field changes.

As regards the non-axisymmetric coils, the effect of the bus bars and feeders on the diamagnetic flux is very low (about 5 mVs), whilst the ELM coils have a larger effect. In fact, a 15 kAt current in a middle ELM coil yields about 20 mVs spurious pick up on the closest diamagnetic loop and then 7 mVs on the toroidal average of the three sensors at steady state (frequency below 2 Hz). On the other hand, because of the eddy currents flowing in the proximity of the sources and the sensors, higher frequencies lead to a lower effects (about 2 mVs at 500 Hz).

A TF coil discharge is the operational condition used to test the compensation formulas; during the fast transients, the eddy current contribution is about 13.5 Vs (18 Vs due to the external TF source in 200 ms). The

compensation formulas based on the inner and upper outer compensation coils provide estimations of the polluting contribution within an error of 220 mVs, being so performant when the toroidal currents flowing into the Vacuum Vessel are significant (L-H and H-L transitions, ELMs, plasma heating, disruptions).

During breakdown and ramp up the eddy currents affect the diamagnetic loop measurement in a very negligible way (about 2 mVs); note that the use of the compensation formulas increases its effect on the signal (about 33 mVs) because of the use of the compensation coils.

The noise effect on the diamagnetic flux measurement at full plasma current is very small ($2\sigma = 5\ mVs$) in static (no eddy) conditions, but also in this case its effects are larger if the compensation formulas are used ($2\sigma = 33\ mVs$).

During the disruption the spurious signal is high (1.6 Vs, i.e. about 70% of the diamagnetic flux) with no compensation, but it can be decreased to 380 mVs if the compensation formulas are adopted. The spurious signals during ELMs are about 30 mVs and could be reduced to 3 mVs in the absence of noise.

Summarizing:

- in static (no eddy) conditions, as during a flat top, the accuracy requirements are met without compensation;

- during breakdowns, ramps-up and other phases with significant toroidal eddy currents, the accuracy requirements are also met without compensation;

- during fast disruptions, the compensation formulas are needed to meet the accuracy requirements, estimating that the compensation coil misalignments and manufacturing errors are within 0.2 deg.

Electromechanical effects of non-axisymmetric Halo Currents on ITER tokamak components

To carry out the electromechanical analysis of ITER tokamak subjected to halo currents, two kind of analyses were carried out: a Vertical Displacement Event Analysis and an Asymmetric Vertical Displacement Event Analysis.

As regards the effects of the asymmetric halo currents, the total vertical force on the structure is about 90 MN downwards (about one third part on the

divertor), the horizontal net force is about 48 MN in the direction of the axis of the kink (about one third part loading on the divertor).

The radial loads on the various sectors are very different from each other (from $-14\ MN$ to 11 MN), as well as the moments (from $-89\ MNm$ to 85 MNm), whilst the distribution of the vertical force on the sectors is nearly uniform (from 9.5 MN to 11.5 MN).

As regards the inductive effects of the kink of the plasma core, a net horizontal force of about 28 MN is generated in the direction of the axis of the kink, but with the sign opposite with respect to the one generated by the halo currents. The radial loads on the various sectors are very different from each other (from $-5\ MN$ to 6 MN).

Finally, the loads on the TF coils were analysed: the total force and the total moments loading on the TF coils generated by the halo currents are respectively about 0.5 MN and 3 MNm, respectively.

On the other hand, the effects of the plasma kink generate about 1.2 MN and 5 MNm; note that these values would be higher in absence of the shielding effect of the vacuum vessel, being about 3.5 MN and 12 MNm respectively.

Field Line Tracing and Identification of non-axisymmetric plasmas

A new tool for the tracing of magnetic field lines in fusion tokamaks, was built up, assessed and validated for several test cases. It allows to pre-process a CREATE-NL equilibrium, performing an axisymmetric identification of the sources, generating a set of equivalent axisymmetric currents, to be used by the processor, as well to work on the flux map included in the equilibrium file. Then, a full 3-D field line tracing is performed by the processor, both on the axisymmetric configurations, mentioned above, treated as non-axisymmetric fields, as well on full 3-D configurations, generated via analytical perturbations of the flux density field components, or via Clebsch potentials.

The procedure allows choosing the integrator among the built-in Matlab procedures as well to build new integrators, based on different integration rules, as Volume Preserving Geometric Integrators, setting the accuracy requirements for the analysis.

The error assessment was carried out by means of:

- 2-D axisymmetric configurations by evaluating the preservation of the flux per radian along the field line;

- 3-D configurations by using the Clebsch decomposition and evaluating both the preservation of the Clebsch potentials along the integrated field line and the spatial distance between the analytical field line and the actual one.

The relative accuracy required for tokamaks is 10^{-6} (1 mm error after 1 km long integration). The procedure provides a relative accuracy of 10^{-9} with a reasonable computational time.

As for Geometrical Integration, a Volume Preserving Mid-Point Rule was built and compared with the standard Runge-Kutta routines for the ODE integration. Standard Runge-Kutta schemes are not geometrical integrators, thus not preserving the divergence-free structure of the ODE set. However, the accuracy with which the Jacobian determinant of the vector transformation is preserved during the integration is comparable with the Mid-Point Rule. Even if adaptive ODE solvers might be expected to show better performances than fixed-step integrators in terms of trade-off between accuracy and computation time, the use of step-adaptivity may not preserve spatial symmetries with drastic consequences. The conclusions are remarkable; for very long integrations too, the fixed step Runge-Kutta schemes are:

- extremely accurate;

- not expensive in terms of computational time;

- extremely accurate in volume preservation too.

These features make this scheme feasible for plasma boundary reconstructions in 3-D configurations, as well for the plasma-wall gap calculations. The absence of analytical invariants as the poloidal flux in the axisymmetric configuration, can be easily circumvented by using the Connection Length technique, thus calculating each gap within a prescribed precision (even lower than the micrometre) and then exploiting the Poincaré maps. In this way, there is no need to calculate each plasma-wall gap by means of the field line tracing, since the plasma-boundary reconstruction can be obtained from the

Poincaré Maps as post-process results, taking no more than few tens of milliseconds.

Parallel computing is strongly recommended for these analyses, especially when a high number of gaps are to be calculated or very long trajectories are to be integrated; in these cases, the computational burden scales linearly with the number of processors.

As regards the identification of the non-axisymmetric plasmas, a new set of basis functions was proposed ad used for the kink perturbation. The results are extremely positive: the $n = 1$ mode is well identified with an average error in the field identification of 1% on the toroidal field and 0.05% on the poloidal one, while the calculation of the plasma-wall gaps is affected by an error lower than $1\ cm$.

Future efforts will be devoted to the extension of the use of such basis functions to other kind of perturbations, e.g. higher toroidal modes or local perturbations.

References

[1] T. J. M. Boyd, J. J. Sanderson, **The Physics of Plasmas**, *Cambridge University Press* (2003)

[2] V. P. Smirnov, **Tokamak foundation in USSR/Russia 1950-1990**, *Nuclear Fusion*, **50** (2010)

[3] S. Azteni, J. Meyer-Ter-Vehn, **The Physics of Inertial Fusion: Beam Plasma Interaction, Hydrodynamics, Hot Dense Matter**, *Oxford University Press* (2004)

[4] https://www.euro-fusion.org/fusion/spot-on-jet-operations/maintaining-the-plasma/heating-the-plasma

[5] R. Cashmore et al., **R&D Needs and Required Facilities for the Development of Fusion as an Energy Source**, *Report of the Facilities Review Panel* (2008)

[6] F. Romanelli et al., **Fusion Electricity A roadmap to the realization of fusion energy** (2013)

[7] P. Batistoni et al., **Report of the ad hoc group on DEMO activities**, CCE-FU 49/6.7 (2010)

[8] R. Fresa et al., **COMPFLUX: a tool for the analysis of the effects of spurious sources and geometrical imperfections on the magnetic measurements in fusion devices**, submitted for publication on *COMPEL - The international journal for computation and mathematics in electrical and electronic engineering*

[9] R: Albanese, R. Fresa, **D2.7: Diamagnetic flux computer model and demonstration case, including any input files, output files and any source code developed**, Technical Report on F4E Grant No. F4E-2009-GRT-047(PMS-DG) CREATE_047_D2.7-D2.10_7_v_d003, F4E UID= 24LF7R, v.1.0 (2011)

[10] R. Fresa et al., **Sensitivity of the diamagnetic sensor measurements of ITER to error sources and their compensation**, accepted for publication on *Fusion Engineering and Design*

[11] R. Albanese and G. Rubinacci, **Integral formulation for 3D eddy current computation using edge-elements**, *IEE Proceedings 135 Part A*, 457– 462 (1988)

[12] R. Albanese and G. Rubinacci, **Finite elements methods for the solution of 3D eddy current problems**, *Advances in Imaging and Electron Physics*, 102, 1–86 (1998)

[13] R. Fresa, G. Rubinacci and S. Ventre, **An eddy current integral formulation on parallel computer systems**, *International Journal for Numerical Methods in Engineering*, 62, 1127-1147 (2005).

[14] A. G. Chiariello, A. Formisano and R. Martone, **Fast magnetic field computation in fusion technology using GPU technology**, *Fusion Engineering and Design*, 88, 1635-1639 (2013)

[15] R. Albanese et al., **Coupling plasmas and 3D passive structures in the JET tokamak**, *International Journal of Applied Electromagnetics and Mechanics* 33, 533–540 (2010)

[16] R. Albanese R. Fresa and R. Martone, **Accurate computation of electromagnetic fields in the presence of conducting and magnetic materials**, *International Journal of Applied Electromagnetics in Materials*, 6, 1, 73-88 (1995)

[17] www.comsol.com

[18] F. W. Grover, **Inductance Calculations**, *Dover Phoenix Editions* (1946)

[19] A. Salar Elahi and M. Ghoranneviss, **Measurement of Plasma Energy Confinement Time in Presence of Resonant Helical Field in IR-T1 Tokamak**, *Journal of Fusion Energy*, 28, 4, 394-397 (2009)

[20] Shen, B. et al., **Poloidal beta and internal inductance measurement on HT-7 superconducting tokamak**, *Review of Scientific Instruments*, 093501, DOI 10.1063/1.2779213 (2007)

[21] E. J. Strait et al., **Magnetic Diagnostics**, *Fusion Science and Technology*, 53, 2, 304-334 (2008)

[22] J. M. Moret et al., **Fast single loop diamagnetic measurements on the TCV**, *Review of Scientific Instruments*, 74, 11, 4634-4643 (2003)

[23] J. M. Moret, **Final Report on ITER Magnetic Diagnostic Design Study on contract EFDA/04-1208, Part 1: Diamagnetic Loop System** (2006)

[24] A. Quercia, **Flux Linkage in Helical Windings and Application to Pick-up Coils**, *IEEE Transactions on Magnetics*, 49, 5692–5697 (2013)

[25] E. P. Gorbunov, K. A. Razumova, **The effect of a strong magnetic field on the magnetohydrodynamic stability of plasma and the containment of charged particles in the "Tokamak"**, *Sovietic Atomic Energy*, 15,5,1105-1112 (1963)

[26] M.G. Bell, et al., **Measurements of Plasma Diamagnetism in NSTX**, Bull. of American Physicists Society, 46, 264 (2001)

[27] R. Albanese, R. Fresa, S. Minucci, **R2.7-5: Final Report on Diamagnetic flux**, Technical Report on F4E Grant No. F4E-2009-GRT-047 (PMS-DG) CREATE_047_R2.7-5_v_d03 (2013)

[28] G. Vayakis, et al. **Development of the ITER magnetic diagnostic set and specification**, *Review of Scientific Instruments*, 83, 10D712 (2012)

[29] S. Peruzzo, **Review of the baseline magnetic diagnostic system**, ITER magnetic sensors database (Annex of the "Report on the preliminary list of magnetic sensors and their positions"), Technical Report on F4E Grant No. F4E-2009-GRT-047 (PMS-DG), v.3.0 (2012)

[30] B. Lim et al., **Design of the ITER PF Coils**, *IEEE Transactions on Applied Superconductivity*, 21, 3, 1918-1921 (2011)

[31] J. Knaster et al., **ITER non-axisymmetric error fields induced by its magnet system**, *Fusion Engineering and Design*, 86, 6–8, Pages 1053-1056 (2011)

[32] Reich, J. et al., **Three dimensional tolerance investigations on assembly of ITER vacuum vessel**, presented at *23rd IEEE/NPSS Symposium on Fusion Energy* (2009)

[33] A. Costley et al, **Measurement Requirements and the Diagnostic System on ITER: Modifications Following the Design Review**, presented at *22nd IAEA Fusion Energy Conference*, Geneva (2008)

[34] L. C. Appel et al., **A unified approach to equilibrium reconstruction**, presented at *33rd EPS conference on plasma physics*, Rome (2006)

[35] Lao L. L., et al., **Reconstruction of current profile parameters and plasma shapes in tokamaks**, *Nuclear Fusion*, 25, 1611-1622 (1985)

[36] A. Pironti, L. Appel, **Reconstruction code incorporating description of the ITER machine and demonstration cases**, Technical Report on F4E Grant No. F4E-2009-GRT-047 (PMS-DG), CREATE_047_R2.5_v_d01 (2011)

[37] W. A. Cooper, A. J. Wotton, β_p **Analysis for Tokamak Plasma with Anisotropic Pressure and Mass Flow**, *Plasma Physics*, 24, 9, 1183-1185 (1982)

[38] V. D. Shafranov, **Determination of the parameters β_p and l_i in a Tokamak of arbitrary shape of plasma pinch cross-section**, *Plasma Physics*, 13, 9 (1971)

[39] L. Lao, **Separation of β_p and l_i in Tokamaks of non-circular cross-section**, *Nuclear Fusion*, 25, 11 (1985)

[40] A. Pironti et al., **R3.2.D: Final report on the evaluation of the estimation error on Poloidal Beta**, Technical Report on F4E Grant No. F4E-2009-GRT-047 (PMS-DG), CREATE_047_R3.2.D_v3 (2012)

[41] R. Albanese et al, **Effects of asymmetric vertical disruptions on ITER components**, accepted for publication on *Fusion Engineering and Design*

[42] M. Buzio et al., **Axisymmetric and non-axisymmetric structural effects of disruption-induced electromechanical forces on the JET Tokamak**, *Joint European Torus Publications* (1996)

[43] C. Bachmann et al., **Specification of asymmetric VDE loads of the ITER tokamak**, *Fusion Engineering and Design*, 86, 9–11, 1915-1919 (2011)

[44] V. Riccardo, P. Noll and S. P. Walker, **Forces between plasma, vessel and TF coils during AVDEs at JET**, *Nuclear Fusion*, 40, 10, 1805-1810 (2000)

[45] G. Rubinacci et al., **A fast technique applied to the analysis of resistive wall modes with 3D conducting structures**, Journal of Computational Physics, 228, 5, 1562–1572 (2009)

[46] R. Albanese et al., **Computational techniques for efficient analysis of large halo current models in fusion devices**, presented at *IX IET International Conference on Computation in Electromagnetics*, Izmir, Turkey (2013)

[47] C. Bachmann, **Asymmetric Loads on the ITER Tokamak Components due to the Sink and Source Model**, ITER_D_356AD2 v 1.0

[48] P. Bettini et al., **Numerical modeling of 3D halo current path in ITER structures**, *Fusion Engineering and Design*, 88, 6–8, 529-532 (2013)

[49] D. A. Humphreys, and A. G. Kellman, **Analytic modeling of axisymmetric disruption halo currents**, *Physics of Plasmas*, 6, 2742-2756 (1999)

[50] P. Testoni, et al., **F4E studies for the electromagnetic analysis of ITER components**, *Fusion Engineering and Design*, 89, 7–8, 1854-1858 (2014)

[51] R. R. Khayrutdinov and V. E. Lukash, **Studies of Plasma Equilibrium and Transport in a Tokamak Fusion Device with the Inverse-Variable Technique**, *Journal of Computational Physics*, 109, 2, 193-201 (1993)

[52] R. Albanese et al., **Electromechanical analysis of ITER components**, Final Report, F4E-2008-OPE-06 (ES-AC), LOT 1, TASK ORDER No. 09: Vacuum Vessel electro-magnetic analyses, Issue 2.0 (2012)

[53] F. Maviglia et al., **Electromagnetic Models of Plasma Breakdown in the JET Tokamak**, *IEEE Transactions on Magnetics*, 50, *2*, 937 (2014)

[54] T. Takizuka et al., **Two-dimensional full particle simulation of the flow patterns in the scrape-off-layer plasma for upper- and lower-null point divertor configurations in tokamaks**, *Nuclear Fusion*, 49, 075038, (2009)

[55] R. P. Wenninger et al., **DEMO divertor limitations during and in between ELMs**, *Nuclear Fusion*, 54, 114003 (2014)

[56] R. MAINGI et al., **Magnetic Field Line Tracing Calculations for Conceptual PFC Design in the National Compact Stellarator Experiment**, presented at *33rd EPS conference on plasma physics*, Rome (2006)

[57] M. W. Jakubowski, S. S. Abdullaev, K. H. Finken and the TEXTOR Team, **Modelling of the Magnetic Field Structures and First Measurements of Heat Fluxes for TEXTOR-DED Operation**, *Nuclear Fusion,* 44, S1–S11 (2004)

[58] A. Punjabi and H. Ali, **Symplectic Approach to Calculation of Magnetic Field Line Trajectories in Physical Space with Realistic Magnetic Geometry in Divertor Tokamaks**, *Physics of Plasmas*, 15, 122502 (2008)

[59] M. Shoji et al., **Investigation of the Helical Divertor Function and the Future Plan of a Closed Divertor for Efficient Particle Control in the LHD Plasma Periphery**, *Fusion Science and Technology*, 58, 1, 208-219 (2010)

[60] T. K. Mau et al., **Divertor Configuration and Heat Load Studies for the ARIES-CS Fusion Plant**, *Fusion Science and Technology*, 54, 3, 771-786 (2008)

[61] A. Bruschi et al., **A New Launcher for Real-Time ECRH Experiments on FTU**, *Fusion Science and Technology*, 55, 1, 94-107 (2009)

[62] B. D. Blackwell et al., **Algorithms for Real Time Magnetic Field Tracing and Optimization**, *Computer Physics Communications*, 142, 243(2001)

[63] R. I. McLachlan, G. Reinout and G. R. W. Quispel, **Geometric Integrators for ODE's**, *Journal Physics A: Mathematical and General*, 39, 5251 (2006)

[64]   R. I. McLachlan and G. R. W. Quispel, **Six Lectures on Geometric Integration**, *Foundations of Computational Mathematics, Cambridge University Press*, 155 (2001)

[65]   J. M. Finn and L. Chacon, **Volume Preserving Integrators for Solenoidal Fields on a Grid**, *Physics of Plasmas*, 12, 054503, 1 (2005)

[66]   D. Bonfiglio et al., **Magnetic Chaos Healing in the Helical Reversed-Field Pinch: Indications from the Volume-Preserving Field Line Tracing Code NEMATO**, *Journal of Physics: Conference Series*, 260, 012003(2010)

[67]   G. Ciaccio et al., **Numerical Verification of Orbit and Nemato Codes for Magnetic Topology Diagnosis**, *Physics of Plasmas*, 20, 062505 (2013)

[68]   M. Abramowitz and I. A. Stegun, **Handbook of Mathematical Functions**, *Dover Publications* (1965)

[69]   P. F. Byrd and M. D. Friedman, **Handbook of Elliptic Integrals for Engineers and Physicists**, *Springer-Verlag* (1954)

[70]   J. R. Dormand and P. J. Prince, **A Family of Embedded Runge-Kutta Formulae**, *Journal of Computation and Applied Mathematics*, 6, 19 (1980)

[71]   R. Albanese et al., **Numerical Formulations for Accurate Magnetic Field Flow Tracing in Fusion Tokamaks**, presented at *IX IET International Conference on Computation in Electromagnetics*, London, UK (2014)

[72]   R. Albanese et al., **Accuracy Assessment of Numerical Tracing of 3-D Magnetic Field Lines in Tokamaks with Analytical Invariants**, accepted for publication on *Fusion Science and Technology*

[73]   G. Federici et al., **Overview of EU DEMO design and R&D activities**, *Fusion Engineering and Design*, 89, 7–8, 882-889 (2014)

[74]   T. E. Raptis, **A Closed Algebra of Clebsch Forms Derived from Whittaker Super-potentials and applications in electromagnetic research,** *arXiv preprint arXiv:1308.3932* (*2013*)

[75]   C. Barbarosie, **Representation of Divergence-Free Vector Fields,** *Quarterly of applied mathematics* (*2011*)

[76]   S. V. BULANOV et al., **Current Sheet Formation in Three-Dimensional Magnetic Configurations**, *Physics of Plasmas*, 9, 9 (2002)

[77]   M. Itagaki et al., **Use of a Twisted 3D Cauchy Condition Surface to Reconstruct the Last Closed Magnetic Surface in a Non-Axisymmetric Fusion Plasma**, *Plasma Physics and Controlled Fusion*, 54, 125003 (2012)

[78]   M. Ariola and A. Pironti, **Plasma shape control for the JET tokamak: an optimal output regulation approach**, *IEEE Transactions on Control Systems*, 25, 5, 65-75 (2005)

[79]   R. Albanese et al., **Design, implementation and test of the XSC extreme shape controller in JET**, *Fusion Engineering and Design*, 74,1-4,627-632 (2005)

[80]   R. Tsuji, **Parallel computing for tracing torus magnetic field line**, Presented at *International Conference on Parallel Computing in Electrical Engineering*, Trois-Rivieres, Quebec, Canada, (2000)

[81]   M. Ariola et al., **Plasma current and shape control in tokamaks using H∞ and μ-synthesis**, presented at *XXXVI IEEE Conference on Decision and Control* (1997)

[82]   M. Ariola, A. Pironti, **Magnetic Control of Tokamak Plasmas**, *Springer-Verlag* (2008)

[83]   P. Courrieu, **Fast Computation of Moore-Penrose Inverse Matrices**, *Neural Information Processing - Letters and Reviews*, 8, 2, 25-29 (2005)

[84]   A. N. Tikhonov and V. Y. Arsenin, **Solutions of Ill-Posed Problems**, *V. H. Winston & Sons* (1977)

[85]   G. H. Golub and C. Reinsch, **Singular Value Decomposition and Leas Square Solutions**, *Numerische Mathematik*, 15, 5, 403-420 (1970)